Dissertation zur Erlangung des Doktorgrades der Fakultät
für Chemie und Pharmazie der
Ludwig-Maximilians-Universität München

From biology to material sciences: a combined multimodal micro-spectroscopy platform for *in vivo* and *in situ* analysis.

Adrian Fuchs

aus

München, Deutschland

2022

Erklärung

Diese Dissertation wurde im Sinne von §7 der Promotionsordnung vom 28. November 2011 von Herrn Prof. Don C. Lamb, PhD betreut.

Eidesstattliche Versicherung

Diese Dissertation wurde eigenständig und ohne unerlaubte Hilfe erarbeitet.

München, den 20.06.2022

Adrian Fuchs

Dissertation eingereicht am	20.06.2022
1. Gutachter:	Prof. Don C. Lamb, PhD
2. Gutachterin:	Dr. Evelyn Plötz (Vertretungsprofessorin)
Mündliche Prüfung am	21.07.2022

Any sufficiently advanced technology is indistinguishable from magic.

(Arthur C. Clarke)

The reason why truth is so much stranger then fiction is that there is no requirement for it to be consistent.

(Mark Twain)

There are no turtles anywhere!

(Sir Terry Pratchett, Science of the Discworld)

Abstract

Multimodal optical microscopy correlated with spectroscopy (micro-spectroscopy) is a powerful tool, known for a wide variety of method combinations and sample systems reported in literature [1–10]. The combination of different modalities from the fields of fluorescence, nonlinear optical microscopy, and spectroscopy on the same platform, enables the simultaneous monitoring of multiple parameters, such as tracking endogenous fluorophores with respect to the surrounding collagen network [1–4]. Therefore the investigation of correlations in highly complex sample systems becomes possible such as detailed studies of the cellular metabolism or the process of collagen deposition during wound healing [5–7]. However, most reported systems are specialized for a specific combination of techniques only [1–10], which limits their flexibility. Moreover, most multimodal methods focus on biological systems only. A combined multimodal optical micro-spectroscopy platform, capable of investigating systems with biological and inorganic background *in vivo* and *in situ* in equal fashion, has not yet been reported.
In this thesis, a prototype of such a multimodal setup is presented. It is dedicated for ***M****ultimodal* ***O****ptical* ***S****pectroscopy* ***A****nd* ***I****maging* ***C****orrelation* analysis, or MOSAIC analysis in short. First, the potential of multimodal analysis for correlating particle morphology-property relationships in inorganic samples will be demonstrated. The fast growing material class of metal-organic framework (MOF) was studied, focusing on the uptake of guest molecules into the carrier structures. In particular, the influence of defects and heterogeneities in MOF crystals on the application of atmospheric water harvesting was the focus of the research leading to the development of a novel Raman scattering based method for obtaining single crystal isotherms. In the second part of the thesis, projects with biological sample systems will be presented. The sensitivity of the setup was pushed from large tissue sections to single cells. A combination of label-free imaging and Raman spectroscopy enabled localization and identification of embedded inorganic particles, such as microplastic, in maritime sponge tissue. The suitability of the platform for fluorescence imaging was demonstrated by measuring the import of the Yes-associated protein (YAP) in HeLa cell spheroids. The feasibility of the platform for state of the art live-fluorescence techniques was shown by monitoring a fluorescent cGAMP analogue in single THP-1 cells using Phasor-fluorescence lifetime imaging microscopy (FLIM). The presented projects demonstrate the wide varieties of applications of the developed analysis platform ranging from material science to biological systems, from water adsorption at defect sites in single crystals to FLIM studies in single cells. The multimodal study unveiled correlations that are not accessible otherwise, highlighting the potential of the technique for further investigations on similar systems, such as guest-host interactions of gases in reticular frameworks [11, 12] and particle-cell interactions in drug-delivery processes [13].

Contents

List of Abbreviations

1PE one-photon excitation

2PE two-photon excitation

APD avalanche photdiode

BF bright-field

BPDC biphenyl-4,4'-dicarboxylate

CARS coherent anti-Stokes Raman scattering

CSRS coherent Stokes Raman scattering

CLSM confocal laser scanning microscopy

CRS coherent Raman scattering

cw continuous wave

FLIM fluorescence lifetime imaging microscopy

FWM four-wave mixing

GFP green fluorescent protein

IRF instrument response function

IR infra-red

laser light amplification by stimulated emission of radiation

MOF metal-organic framework

MOSAIC Multimodal Optical Spectroscopy And Imaging Correlation

NIR near infra-red

NLO nonlinear optics

NMR nulear magnetic resonance

pCARS polarization coherent anti-Stokes Raman scattering

PCF photonic crystal fiber

RBITC Rhodamine B isothiocyanate

RH relative humidity

SF6 Schwer-Flint 6

SFG sum-frequency generation

SHG second harmonic generation

SRL stimulated Raman loss

SRG stimulated Raman gain

SRS stimulated Raman scattering

TCSPC time-correlated single-photon counting

UV ultraviolet

VIS visible

YAP Yes-associated protein

List of Figures

Chapter 1.

Motivation

When asked to describe a microscope, most people will picture an optical light microscope. And for good reason: optical microscopy has been the most prominent tool in research for at least three centuries [14]. It is based on the enhancement of images created by illumination with light. This bright-field (BF) microscopy enabled the observation of microorganisms like microfungi, protozoa, and bacteria (between 1665-83, by R. Hooke and A. Leeuwenhoek [15]), the first recording of living cells (1913, Comandon et al. [16]), and other fundamental building blocks of life on the microscopic level.

In the following years, microscopes were continuously advanced in the optical materials that are available and in their design. Illuminating the complete field-of-view at once (widefield) has the disadvantage of high signal contribution from out-of-focus planes and the requirement of high average field intensities. Focusing the laser light onto a single spot in the sample vastly reduces the required excitation power. Images can then be acquired by scanning the sample point-by-point. When the emission signal from the focus is refocused onto a pinhole in front of the detector, out-of-focus contributions are almost completely blocked (see section 2.4.1). Since both the sample and the pinhole are simultaneously in focus, the technique is named confocal microscopy [17]. In parallel, new optical microscopy methods, based on a variety of light-matter interactions, were developed. In non- or low light-absorbing materials the originally applied, broad light sources interact with the sample matter almost non-specific regarding the material. This made the distinction between different types of materials very challenging. To accomplish higher specificity for a material of interest, staining dyes were developed[1]. A deeper understanding of the nature of light and its spectral composition enabled monochromatic excitation and multiplexing of staining materials [19]. The so-called Stokes shift occurring in the fluorescence emission of dyes can be exploited in the vast field of fluorescence microscopy (section 2.2.1 [20]): the development of pulsed light sources made it possible to monitor the fluorescence decay over time with high spatial resolution, enabling fluorescence lifetime imaging microscopy FLIM. Fluorescence methods, like Phasor-FLIM [21], raster image correlation spectroscopy (RICS) [22], fluorescence (cross) correlation spectroscopy (F(C)CS) [23], or pulsed-interleaved excitation (PIE) [24] pushed the sensitivity for investigation in live science applications.

The development of high-intensity light field sources (section 2.1) in combination with

[1]The first dye applied for staining, was saffron in 1673 by the Dutchman Anton van Leeuwenhoek. [18]

confocal microscopes expanded optical analysis methods by enabling significant higher-order light-matter interactions, referred to as nonlinear optics (NLO) microscopy [25]. Fluorescent imaging with NLO microscopy is possible via multi-photon excitation of fluorescent compounds. The simplest example is two-photon excitation (2PE). Many of these techniques allow for the blue-shifted emission of the fluorescent signal of a dye or an auto-fluorescent specimen [26, 27]). A further NLO technique, that also leads to spectral signatures at higher frequencies but without the requirement of a fluorescent label is second harmonic generation (SHG) (see section 2.2.2 [28]). SHG is used to monitor non-centrosymmetric materials or surfaces based on the frequency-doubling of the incident light. Both the fluorescent and the label-free NLO techniques frequently employ light sources in the infra-red (IR), which provide high penetration depths in tissue and a lower risk of photodamage [29] while still enabling detection in the ultraviolet (UV)-visible (VIS) spectral range. Further information can be acquired by analysing the interaction of the sample with the excitation light in a spectral manner. Newton was the first reported scientist to show that light, which appears white, consists of a superposition of different wavelength [30]. The analysis of the spectral composition of light after interaction with a sample is the field of optical spectroscopy. Its methods are numerous and belong to the staples of research methodology (section 2.4 [30]). The subcategory of vibrational optical spectroscopy, namely Raman [31] and IR spectroscopy, utilize the interaction of light with molecular bond vibrations for substance identification. The combination of Raman spectroscopy with confocal microscopy enables a spatial analysis of the chemical composition of a sample. This approach, termed hyperspectral Raman imaging, is a powerful, label-free characterization method applied, for example, to study the chemical composition of HeLa cells depending on the external pH around the cells [32]. The technique is limited by the relatively weak Raman signal strength, requiring high excitation powers and long measurement durations per image (section 2.3.3 [33]). It is possible to enhance the effect by several orders of magnitude, either by resonance to electronic transitions or by applying additional electric fields in close proximity (see section 2.3.4 [34]). The enhanced Raman scattering enables chemically sensitive imaging without the need for additional staining, with methods like coherent anti-Stokes Raman scattering (CARS) [35, 36] and stimulated Raman scattering (SRS) [37, 38].

The optical micro- and spectroscopy techniques are powerful, established methods with individual advantages but also limitations: fluorescence enables chemically specific imaging with a good signal-to-noise ratio, but requires labels or auto-fluorescent processes. SHG is label-free, but restricted to non-centrosymmetric materials and surfaces. Raman spectroscopy is chemically sensitive, but requires long measurement times and high laser intensities. Therefore, a single optical characteristic is often not sufficient to resolve complex processes. The combination of multiple optical modalities allows one to (1) correlate the acquired information and resolve multiple influences in an interaction and (2) counter-check one modality with another method to validate the results. The combination makes it possible to study processes in a highly heterogeneous environment using multiple parameters to correlate the measured informations. Biological processes

have, almost exclusively, a high level of complexity and highly heterogeneous environments, especially when studying cells or cell clusters. Multimodal optical microscopy is therefore a prominent tool for the study of biological systems. A common combination is simultaneous detection of 2PE and SHG since excitation sources and microscopes are very similar. The combination allows the observation of endogenous fluorophores, like NADH, flavins, or retinol [1–4, 7] with respect to the surrounding collagen network, imaged by SHG. This enabled detailed studies of cellular metabolism and collagen deposition during wound healing [5–7]. The correlation of SHG and CARS images can provide insight into the internal structure and molecular organization of tissue, as shown by the study of starch grains by Slepkov et al. [7, 10]. The benefit of combining a high-speed modality like fluorescence with a highly-specific modality, like Raman spectroscopy, was demonstrated by Kong et al. [39, 40]. Barcal cell clusters were scanned with autofluorescence imaging and areas of interest were identified. Raman spectra were collected at the selected points and compared with classification models of basal cell carcinoma. The combination achieved an objective, label-free classification of potentially cancerous tissue in 20-60 minutes, significantly faster than conventional histopathology. The power of this approach was demonstrated by identifying small residual tumors on the surface of breast excision specimens intra-operativo [39, 41]. Similarly, Lin et al. developed an approach for the *in vivo* identification of tumor sites in nasopharyngeal tissue [39, 42]. Current platforms have demonstrated the benefit of correlated multimodal analysis, but most of the reported systems are optimized for a specific modality (e.g. SRS [7, 10]) or a specific combination of modalities [39, 40]. This limits the accessible information that can be correlated and, therefore, the sample systems that can be investigated. The need for an analysis platform, where all major modalities (fluorescence, non-linear and spectroscopy-based) can be selected and combined according to the sample's requirements, has not yet been (fully) addressed. Additionally, most systems are optimized for biological samples only, rendering the correlated investigation of systems containing inorganic and biological material challenging.

While biological systems can be monitored with live cell-imaging, the influence of the inorganic materials requires a material science analysis. Heterogeneity can massively alter inorganic material properties [43]. Therefore, it would be necessary to characterize not only the cellular environment but also the heterogeneity of the inorganic material on the microscopic level. Especially the interaction of inorganic particles with biological system is an important field of modern research [13]. It can be involuntary, such as with microparticulate pollutants (see project 3, section 5.1), or by design, as in the field of drug delivery [44, 45]. Drug delivery requires the development of efficient nanometer sizes particles for drug delivery and ideally also diagnostic monitoring of the transport process. Here, porous materials including covalent- (COF) and metal-organic framework (MOF) particles have been introduced as an exciting new class of carriers [13]. These crystalline, porous materials possess a high active surface area per volume ratio, and, therefore, play an important role in a variety of applications such as heterogeneous catalysis [46]. Originally, zeolites, an aluminiosilica mineral which can be synthetically synthesised and altered [47], and ordered mesoporous silica [46] were applied as the

reticular framework to host the catalyst. However, their adaptation capabilities were limited, leading to the search for a more utilitarian crystalline material [48]. In 1995, Yaghi et al. published the idea of constructing crystalline networks based on metal (oxide)-centers connected by coordinated organic linkers [49]. These materials, referred to as metal-organic frameworks (MOFs) allow for a wide variety of linker-metal combinations. Their exact properties can be tuned by altering their topology, the morphology, the chemistry of their constituents, and by post-synthetic modifications (either internal or surface-only) [48]. The high degree of flexibility allows essentially limitless possible combinations [50]. The strong coordination bonds of the charged linkers to the metal center make MOFs stable even in harsh environments [51]. Their crystalline reticular framework results in very high active surface areas. Over 7000 m^2/g have been reported in literature [52]. MOF materials were applied to various fields ranging from catalysis [53–55], over CO_2 storage [56], to biomedical applications, such as drug delivery [44], photodynamic therapy [57], or biodiagnostics [58].

Since topology and morphology of the particles can heavily influence their properties, the study of particle heterogeneity is of paramount importance [43]. However, most common characterization techniques average over a multitude of particles to achieve a high signal-to-noise ratio [59]. These bulk measurements makes studies of the influence of heterogeneity on the individual particle properties difficult. To reveal the correlation, *in situ*, single particle methods are required. While high-resolution diffraction methods are unsurpassed in their spatial resolution, they are not suited for fast, *in situ*, multiple-particle screening. Optical microscopy can also provide the required spatial resolution in the higher nano to micrometer regime and is well-known for *in situ* studies. Photothermal induced resonance was applied to map the chemical complexity of multivariant MIL-68(In) by Katzenmayer et al. [60]. The combination of atomic-force microscopy (AFM) and IR spectroscopy allowed their team to spatially analyse the chemical composition of the MOF crystals with nanoscale resolution. A similar approach represented the combination of Tip-enhanced Raman scattering (TERS) with AFM [61] for studying crystalline heterogeneous catalysts, which posses high surface areas per volume ratios comparable to MOFs. Jayachandrababu et al. [8] published a novel combination of fluorescence confocal microscopy with nulear magnetic resonance (NMR) spectroscopy. It allowed to study mixed MOF crystals of ZIF-8 and ZIF-90. SRS was used for fast chemical mapping in Zn-exchanged ZSM-5 (zeolite) reticular framework particles. For defect localization in the H-KUST-1 framework, Ameloot et al. [9] exploited the fact that furfuryl alcohol becomes fluorescent during polymerization. Since only open metal sites provide a polymerization seed for the alcohol, fluorescence imaging revealed their location inside crystals after incubation with furfuryl alcohol. Schrimpf et al. monitored the lifetime of labeled UiO-67(Zr) crystals to localize open metal sites [62]. In the presence of defect sites, the dyes are partly quenched resulting in a lower apparent lifetime. Wolf et al. provided a label-free alternative for fast defect-site localization based on NLO microscopy [63]. They applied a combination of NLO methods with Raman spectroscopy to visualize and classify defects in MOF-177, CoTPT, and γ-CD MOF. The interaction with guest molecules was monitored with vibrational spectroscopy. [64, 65]

The published work mentioned above, highlights the potential of spectroscopic methods for *in situ* studies of MOF systems. However, similar to the presented applications in biological systems, most research is focused on either a very specific sample system or a specific technique. The general applicability of correlative *in situ* spectroscopy and multimodal optical microscopy for a wider variety of MOFs has not yet been demonstrated in its full potential.

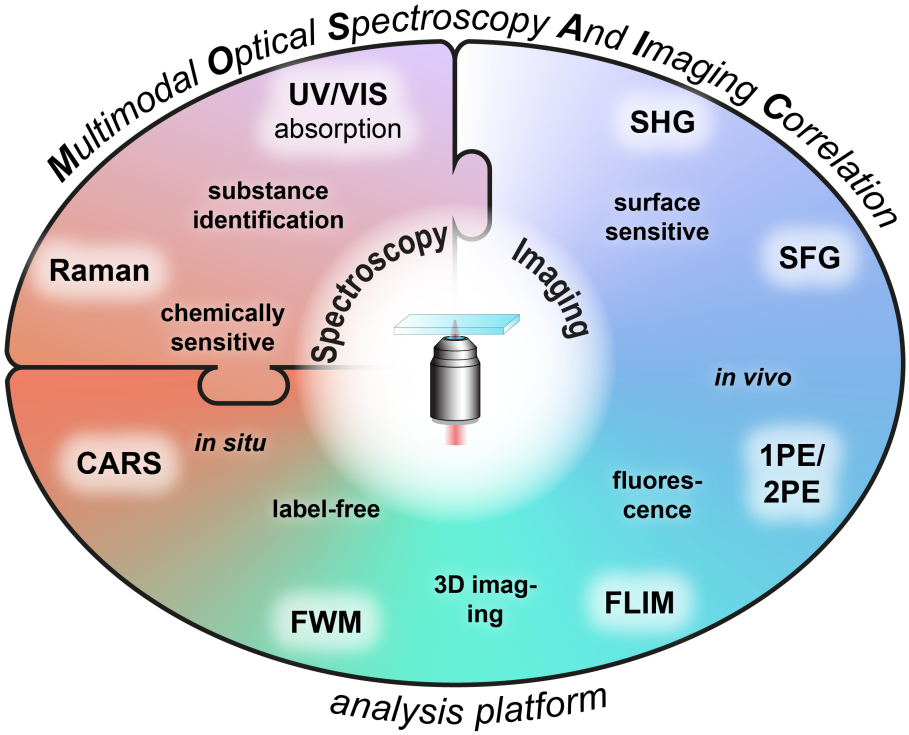

Figure 1.1.: Overview over the outlined selected requirements and the respective modalities combined for the MOSAIC analysis platform. Abbreviations: SHG: second-harmonic generation; SFG: sum-frequency generation; 1PE/2PE: one-/two photon excitation; FLIM: fluorescence lifetime imaging microscopy; FWM: four-wave mixing; CARS: coherent anti-Stokes Raman scattering; UV/VIS: ultraviolet to visible absorption;

Multimodal optical micro-spectroscopy has great potential for the correlative and label-free characterization of heterogeneous biological and inorganic systems. Therefore, the aims of this work are:

- to design and construction of a multimodal optical analysis platform combining state of the art fluorescence methods with NLO imaging and spectroscopic modalities.
- to demonstrate the potential of such a platform to investigate heterogeneity in a variety of MOF systems.

- to investigate reticluar particles as well as biological systems on the same microscope to prove the flexibility regarding sample systems of the analysis platform.

To address the first aim, the platform design should be capable of label-free and fluorescence based imaging (including FLIM). To analyse heterogeneity in MOFs, surface-specific imaging correlated with 3D imaging is needed to distinguish between effects on material interfaces and heterogeneity inside a certain material. Chemically-sensitive imaging allows for a label-free substance localization. Additionally, highly-sensitive substance identification and quantification modalities are required. All modalities would have to be combined on a singular micro-spectroscopy platform, to correlate the acquired information with sub-micrometer resolution.

In this thesis, the prototype of such a multimodal setup is presented. It is dedicated for ***M****ultimodal* ***O****ptical* ***S****pectroscopy* ***A****nd* ***I****maging* ***C****orrelation* analysis, or MOSAIC analysis in short. Figure 1.1 illustrates the selected methods for the platform. The modalities are based on a variety of light-matter interaction. The first part of the thesis provides a short introduction to the theoretical and technical backgrounds of the platform and discusses the selected modalities in detail (chapter 2). The general design and the technical realization of MOSAIC are laid out in chapter 3. The next chapters of the thesis describes the application of MOSAIC analysis on reticular (chapter 4) and biological systems (chapter 5):
First, the potential of the method for MOF materials was investigated (section 4.1). To demonstrate the feasibility of multimodal analysis on MOF systems, UiO-67, a well known MOF was investigated with all selected modalities. The influence of defect sites and heterogeneity on extrinsic properties was exemplary investigated for light absorption in MIL-88A microcrystals. The intrinsic property of guest-host interaction was studied in MOF crystals of MOF-801, an atmospheric water harvesting material. The limited techniques in researching heterogeneity of water adsorption in these systems lead to the development of a novel Raman scattering based method for single crystal isotherms (section 4.2). Following this work, projects with a biological background are presented. The analysis platform can identify embedded inorganic particles in tissue (section 5.1) and is well suited for state of the art fluorescent imaging in cell spheroids (section 5.2) as well as in single cells (section 5.3).

Chapter 2.

Multimodal Optical Microscopy

Optical microscopy is based on the interaction of light with a specimen. When the excitation photon flux is sufficiently high, higher-order interactions become significant and can be exploited in microscopy and spectroscopy. Since a sample can exhibit a multitude of linear and nonlinear interactions simultaneously, one can probe multiple properties at the same time. This multimodal approach requires knowledge of the physical background of the interactions, a good characterization of the sample and high control over the technical realization of the micro-spectroscopy platform. This chapter gives a brief introduction to light-matter interactions in a historical context and provides a short overview of nonlinear optics. Afterwards, the physical background of the modalities implemented in our microscope will be discussed based on the order of the interaction. In the last section, the underlying technical concepts of our analysis platform will be introduced.

2.1. Interaction of light and matter

2.1.1. The nature of light - a brief excurse

In the very first lines of the book Genesis, during the act of creation of the heavens and the earth, God declared "Let there be light;" (Genesis 1:3 [66]) and separated light from darkness. Unfortunately, the following text does not state the nature of light, resulting in a discourse between scientists for over two millennia.[1] The earliest recorded systematic studies about the nature of light are from the Hellenistic period until ca. 320 BC. They can be roughly divided into atomists, who believed that light consists of atoms emitted by matter, and supporters of the extramission theory, where light consisted of rays emitted by the eyes. The latter theory was stated by Plato and his supporters and did last over a thousand years before it could be dismissed by one of the leading optical scientists during the prime of the Islamic period, Alhazen in 1027. He could show that light sources, here lanterns, create the light instead of the eye, but did not further specify the nature of light. In the western world, after the dark ages faded away around the 15^{th} century, the scientific revolution dawned. With Copernicus, Galileo and Kepler, scientific methods were held in high regard again while scientists like Snell, Descartes and Fermat continued expanding the knowledge about the behaviour of light [67]. Sir

[1] The following paragraph is a summary of *A Very Brief History of Light*, the first chapter in *Optics in our time* by Zubairy, Al-Amri et al. [67]

Isaac Newton could first prove that light itself has an apparent color and that white light is composed of all colors [30]. He proposed that light consists of small corpuscles while matter consists of bigger corpuscles, postulating light as particles. His theory was in opposition to the concept of light propagating as a wave, put forth by Grimaldi, Young, and Fresnel who all observed distinct wave-like features of light propagation in their experiments [67]. James Clerk Maxwell could describe light as an electromagnetic wave in the equations named after him, explaining all previous experimental observations [68]. His description was proven experimentally by Hertz in 1888 [69], leading to the conclusion that light indeed is an electromagnetic wave. But the question remained: a wave in what medium? Already in Newton's time, the concept of a luminiferous ether was proposed, similar in function as air for sound waves but unknown in nature [70]. However, the existence of such an ether could never be proven, deeming its existence highly unlikely. Additionally, more experiments [67] were published hinting at the particle nature of light. The apparent duality was explained by Einstein in 1905 [71]. He applied the mathematical constant that Max Planck derived to describe the so-called black body experiments [72], the Plank's constant h, to postulate the relation $E = h \cdot \nu$ for describing the energy of light. Light was postulated as an electro-magnetic wave that behaves as a particle. This particle-wave duality could finally settle the millennia-old dispute over the nature of light and opened the field of quantum mechanics enabling a deeper understanding of light-matter interactions.

To introduce the underlying physical principles for the selected multimodal effects in this thesis, I will use the classical description[2] of light as an electromagnetic wave with a time-dependent, photon induced electric field $\mathbf{E}(t)$:

$$\mathbf{E}(t) = \mathbf{E} \cdot e^{-i\omega t} \tag{2.1}$$

$\mathbf{E}$ is the absolute electric field strength, ω is the frequency, and t is the time. Variables in bold indicate that the property is a vector. In the following chapters, a classical description based on Boyd et al. [74] is employed to describe the selected effects.

2.1.2. Interaction with matter

Matter consists of atoms, which have electric and magnetic properties. Electric and magnetic fields can, therefore, influence the charge and the magnetic moment of a material. Maxwell developed the expressions to describe the entanglement of electric and magnetic physical properties in his famous four *Maxwell equations*:

[2] The presented description follows Chapter 1 of *"Electromagnetic Waves and Antennas"* by S. Orfanidis [73] and *Nonlinear Optics* by Boyd et al. [74]

$$\nabla \times \mathbf{E} = -\frac{\delta \mathbf{B}}{\delta \mathbf{t}} \tag{2.2}$$

$$\nabla \times \mathbf{H} = \mathbf{J} + \frac{\delta \mathbf{D}}{\delta \mathbf{t}} \tag{2.3}$$

$$\nabla \cdot \mathbf{D} = \rho \tag{2.4}$$

$$\nabla \cdot \mathbf{B} = 0 \tag{2.5}$$

where $\mathbf{E}$ and $\mathbf{H}$ are the electric and magnetic field intensities, $\mathbf{D}$ and $\mathbf{B}$ are the electric and magnetic flux densities, and ρ and $\mathbf{J}$ refers to the volume charge density and the current density.

Static electric and magnetic field intensities are related to the induced respective flux densities via the so-called *constitutive relations*:

$$\mathbf{D} = \epsilon \mathbf{E} \tag{2.6}$$

$$\mathbf{B} = \mu \mathbf{H} \tag{2.7}$$

with ϵ and μ being the permittivity and the permeability of the material, in which the flux densities are located. For a field intensity in a vacuum, permittivity and permeability are constants (ϵ_0 and μ_0). This allows the materials' permittivity and permeability to be connected to its electric and magnetic susceptibility χ and χ_m.

$$\epsilon = \epsilon_0(1 + \chi) \tag{2.8}$$

$$\mu = \mu_0(1 + \chi_m) \tag{2.9}$$

The susceptibilities are dimensionless material properties. In isotropic materials they are material constants while in anisotropic environments, they are tensors mediating the direction-depending interaction between electric fields and matter. The following paragraphs apply the more general vector notation for the susceptibility. By combining equations 2.1, 2.6, and 2.8, one can derive an expression describing the time-dependent electric flux $\mathbf{D}(t)$ induced by a light-induced electric field $\mathbf{E}(t)$ (the time-dependent magnetic flux can be derived in the same way):

$$\mathbf{D}(t) = \epsilon_0 \cdot (1 + \boldsymbol{\chi}) \cdot \mathbf{E} \cdot e^{-i\omega t} \tag{2.10}$$

The electric interaction is influenced by three main components: the material properties (here described by the electric susceptibility $\boldsymbol{\chi}$), the frequency ω of the incident light and the field strength $\mathbf{E}$. For example, in dispersive materials, the electric susceptibility is a function of the frequency $\boldsymbol{\chi}(\omega)$ resulting in the different refractive indexes for different frequencies. To a good approximation, all sample systems studied in this thesis can be described as non-magnetic, dielectric matter with a negligible magnetic-field contribution. In dielectric materials, the electric susceptibility can depend on the excitation

frequency and the excitation field strength. Equation 2.10, describing the interaction, can be written as:

$$\mathbf{D}(t) = \epsilon_0 \cdot \mathbf{E}(t) + \epsilon_0 \cdot \boldsymbol{\chi}(\omega, \mathbf{E}) \cdot \mathbf{E}(t) \tag{2.11}$$

The second part of the equation can be identified as the time-dependent polarization of the dielectric material $\mathbf{P}(t)$.

$$\mathbf{P}(t) = \epsilon_0 \cdot \boldsymbol{\chi}(\omega, E) \cdot \mathbf{E}(t) \tag{2.12}$$

Light-matter interactions in dielectric materials are connected via the polarization. In the following we will restrict ourselves to monochromatic excitation light sources. For low photon fluxes, i.e. low $\mathbf{E}$, the relation between $\mathbf{P}(t)$ and $\mathbf{E}(t)$ can be approximated as linear. However, for high field intensities, this approximation is no longer sufficient and equation 2.12 needs to be adapted accordingly. It can be expanded by a power series of $\mathbf{P}$(t) with the electric field $\mathbf{E}(t)$:

$$\begin{aligned} \mathbf{P}(t) &= \epsilon_0[\boldsymbol{\chi}^{(1)}\mathbf{E}(t) + \boldsymbol{\chi}^{(2)}\mathbf{E}^2(t) + \boldsymbol{\chi}^{(3)}\mathbf{E}^3(t) + ...] \\ &\equiv \mathbf{P}^{(1)}(t) + \mathbf{P}^{(2)}(t) + \mathbf{P}^{(3)}(t) + ... \end{aligned} \tag{2.13}$$

with $\boldsymbol{\chi}^{(n)}$ being the *n-th* order susceptibility. Since the *n-th* order effects depend on the excitation field strength with the power of n, high intensities are required to induce non-negligible nonlinear effects. Broadly speaking, the higher the non-linearity of the optical effect, the more power is needed for a significant contribution. In this work, only effects up to the third order are considered. Higher order effects would require laser intensities that could cause photodamage in the specimens studied in this work.

The expression for dielectric samples, derived from *Maxwell equations*, allows one to describe an observed light-matter interaction via its order of dependency on the excitation field intensity. The nonlinear interactions are the foundation of the developed multimodal optical microscopy setup. To induce a specific nonlinear effect, the excitation light source must possess a high field intensity in a relatively narrow spectral window. This requirement exceeds classical light sources like candles, the sun or electric light bulbs.

In the year 1916, Albert Einstein published a re-evaluation of Planck's law of radiation [75] based upon the so-called Einstein coefficients. In this work, he described the processes of photon-absorption and photon-emission (spontaneous and stimulated), based on the formulas developed by Planck [76] and Maxwell [77]. The stimulated emission, where a photon that hits an electronically excited system will create another photon with the same properties, was the basis for his proposal for a monochromatic light source, which would be capable of intense field strengths. Such a device was technically challenging, needing 44 years until Maiman et al. published their work about the first so-called light amplification by stimulated emission of radiation (laser) device

in 1960 [78]. The invention of the laser is commonly known as the starting point of nonlinear physics (although some nonlinear effects were reported before, such as the observation of saturation effects in the luminescence of dyes by Lewis et al. in 1941 [79]). Only a year after the first laser system was published, the system was already successfully applied to observe frequency-doubled light in quartz crystals by Franken et al. [28](SHG is discussed in more detail in 2.2.2). The laser paved the way for nonlinear, multimodal microscopy by allowing high control over the triggered effects.

The developed MOSAIC analysis platform (chapter 3) combines a suite of imaging and spectroscopy methods. Light-matter interactions can result in a multitude of fundamentally different signals. For this work, five modalities were selected: the surface-specific, label-free sum-frequency generation (SFG) and SHG (1), the label-free four-wave mixing (FWM) for unspecific imaging (2), Raman spectroscopy for substance identification and quantification (3), and CARS for chemically sensitive imaging (4). These were combined with the fluorescence emission based methods after one-photon excitation (1PE) and 2PE (5). Figure 2.1 displays the energy diagrams for the different modalities according to their dependence on the number of interacting light fields. The order n of light-matter interaction is given by the number of electric fields due to the incident light fields that lead to a modulation of the material's polarization $\mathbf{P}^{(n)}$ serving as source of the newly created light field. It is frequently described by the order n of the electric susceptibility $\boldsymbol{\chi}^{(n)}$, as laid out above. While absorption and consecutively emission (1PE) depend linearly on the electric field (figure 2.1a) of the incident light source, SFG and SHG (figure 2.1b) are second order processes, i.e. they depend on the interaction of two incident light fields with the sample. FWM, CARS and spontaneous Raman scattering (figure 2.1c) result from third order interactions. Analog to Raman scattering, 2PE induced absorption (2PE; figure 2.1a) is a dissipative process resulting in a excitation of the involved material. For both processes, no direct excitation from the ground state to the (vibrational or electronically) excited state are happening. The transition requires a two-step process. It populates the excited state via an intermediate, virtual state leading to a third-order interaction. A full description of both processes requires a quantum electrodynamic model [74, 80].

In the following, the selected effects are presented in detail, related to their order of light-matter interaction.

2.2. First and second order effects

The MOSAIC microscope utilizes the effect of 1PE fluorescence as a modality based on a first-order light-matter interaction. It will be discussed in the following chapter with a focus on multiplexing capabilities and lifetime analysis in fluorescence imaging which are applied for projects 4 and 5 respectively. The second effect presented here will be the surface-sensitive SFG and SHG as a derivative thereof.

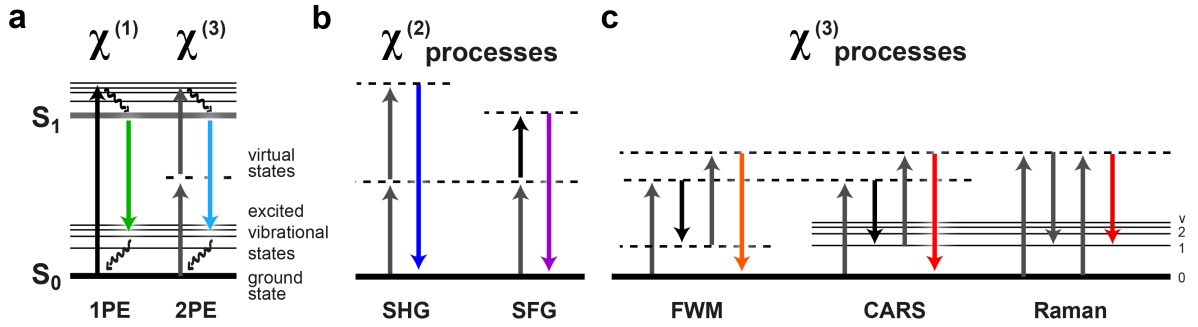

Figure 2.1.: Energy diagrams of the spectral signatures selected for MOSAIC. **a)** 1PE and 2PE induced fluorescence are first and third-order interactions, respectively. The straight arrows indicate photons and the curved arrows energy transfer without photon emission by internal conversion. **b), c)** Selected second- (b) and third order (c) interactions of light and matter. Here, the straight arrows represent electric fields. The horizontal solid and dashed lines represent the molecular and virtual energy levels, respectively. Figure adapted from [81].

2.2.1. Fluorescence

The emission of a photon by an electronic system after absorbing a photon refers to the process of photoluminescence. Figure 2.2 displays the process schematically using a Jablonski diagram [82]. Electrons from the electronic ground state S_0 can be excited by photoabsorption to a higher electronic state, here S_1 (figure 2.2, green). The excited electron can convert energy into heat via vibrational relaxation (yellow). It can then fall back to the ground state, emitting a photon with lower energy than the incident absorbed photon. Consecutively, it relaxes to the vibrational ground state of S_0. Since the emission occurs from the lowest sub-state of the excited electronic state the shape of the absorption and emission spectrum of a fluorescent system roughly mirror each other, with a shift to lower energy in the emission compared to the excitation spectrum, due to the vibrational relaxation (see figure 2.2). This spectral red-shift was first described by Goerge G. Stokes in 1852 [20]. When absorption and emission can occur without a change in the electron spin, the process is called fluorescence. Stokes observed it in fluorspar and uranium glass. He coined the term based on fluorspar, similar to opalescence is named after the gem opal [20].
Usually transitions with spin-inversion are forbidden. However, it is possible that an electron converts from the excited singlet to an energetically close excited triplet state T_1. The process is referred to as inter-system crossing. The relaxation and photon emission from the triplet state is called phosphorescence (figure 2.2, black). The relaxation to the ground state from either excited state can also occur without photon emission, referred to as non-radiative decay or quenching.

Molecules where fluorescence can be observed are referred to as fluorophores (generally absorbing in the UV to VIS regime). High-performance synthetic fluorophores (e.g., Atto or Alexa dye series) and the discovery of native fluorescent proteins (first and foremost the green fluorescent protein (GFP) [83]) greatly advanced the large field of

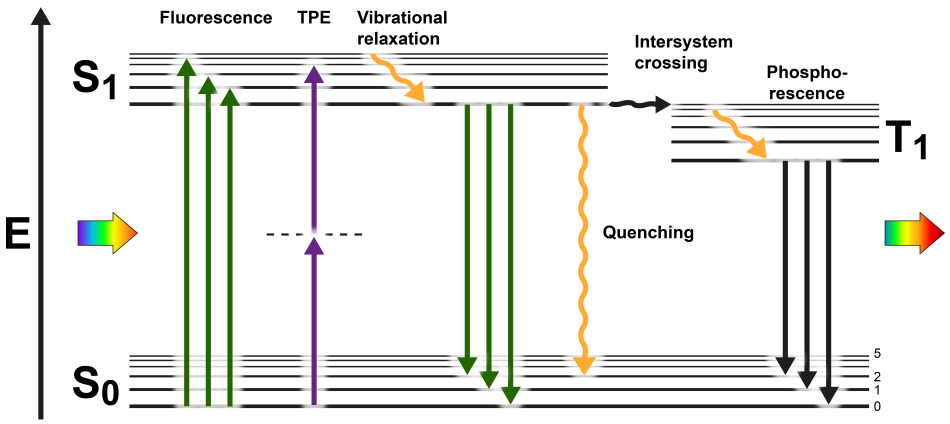

Figure 2.2.: A Jablonski diagram showing processes involved in photoluminescence and quenching. Straight arrows indicate photon absorption / emission processes, while curved arrows indicate energy transfer or energy loss without photon emission. Solid lines are real states, dotted lines are virtual energy levels. "S" and "T" represent the singlet and triplet electronic states and sub-states. The two-photon excitation (2PE, lilac) is discussed in section 2.3.2.

fluorescence microscopy. A powerful option is to label site-specific multiple targets with different dyes and correlate the acquired information. This multiplexing requires that the emission spectra of the fluorophores have little to no spectral overlap. Since the emission spectra are usually relatively broad, it is challenging to have more than three different labels per experiment. In project 4, we monitored the import of a photo-switchable YAP correlated to the nucleus position, demonstrating the multiplexing capabilities of our setup (chapter 5.2).

Fluorescence lifetime

The average time the system stays in the excited electronic state is the fluorescence lifetime τ, described by the inverse sum of radiative and non-radiative emission rates $k_{(n)r}$.

$$\tau = (k_r + k_{nr})^{-1} \tag{2.14}$$

Typically, fluorescent lifetimes are between 1 to 10 nanoseconds, while phosphorescence is decaying on a significantly longer time-scale (ranging from microseconds to hours or even days) since the transition requires a spin-inversion. The fluorescence intensity decay after excitation $I(t)$ is representative of the dye and the current local environment. A histogram of a single decay process ($S_1 \rightarrow S_0$) can be described by eq.2.15 as a mono-exponential decay:

$$I(t) = I_0 \cdot e^{\frac{-t}{\tau}} \tag{2.15}$$

where I_0 is the initial fluorescence intensity and t the time. When scanning an image point by point, one can extract a lifetime for every pixel. The resulting fluorescent life-

time image allows access to the spatial distribution of the fluorescence lifetimes [84]. The technique called FLIM is a powerful tool that expands the intensity-based fluorescent imaging. For example, by applying FLIM in MOF materials it was shown that defect sites in single crystals decrease the lifetime [62]. Defect localization in UiO-67 crystals was possible by exploiting the lifetime reduction due to quenching in the proximity of uncoordinated metal sites.

The Phasor approach

Fluorescence lifetime analysis provides information about the nano-environment around the fluorophore with high sensitivity. It can monitor an accumulation of multiple fluorescent decay processes, where every component possesses a (different) mono-exponential lifetime. The simultaneous detection of only two decay processes will already lead to an apparent bi-exponential decay. When multiple components are contributing to the detected lifetime histogram, the distinction between the different components by lifetime fitting alone becomes challenging. It requires either prior knowledge of the system or a high signal-to-noise ratio, usually leading to long measurement times. An alternative is presented in the Phasor approach, introduced by the Weber group [86]. Here, the lifetime is Fourier-transformed using eq. 2.16 and 2.17 (figure 2.3a, b).

$$s = \int_0^T I(t) \cdot sin(n\omega t)dt / \left(\int_0^T I(t)dt \right) \tag{2.16}$$

$$g = \int_0^T I(t) \cdot cos(n\omega t)dt / \left(\int_0^T I(t)dt \right) \tag{2.17}$$

The lifetime is projected from the time domain in the Fourier space, represented by angular coordinates inside or on a unit half circle. In FLIM, this results in one point per pixel of the image (figure 2.3c-e). Mono-exponential decays appear on the unit half circle line. Bi-exponential decays are weighted vector additions of the two pure species vector representations (figure 2.3f). The exact bi-exponential vector location is dependent on the ratio of the two species. This holds true for multi-component systems. Figure 2.3f and g show a schematic for a two- and three-component system respectively. The advantage of the Phasor technique is a high sensitivity for identifying contributions of a substance even at low concentrations and low signal-to-noise ratios. If the substance of interest has a distinct lifetime population in or on the half circle compared to the other components of a mixture, it's presence will result in a detectable shift towards the pure compound location (figure 2.3g, purple dot). We applied this technique in the analysis of the import of c^{th}GAMP in THP1 cells (see project 5).

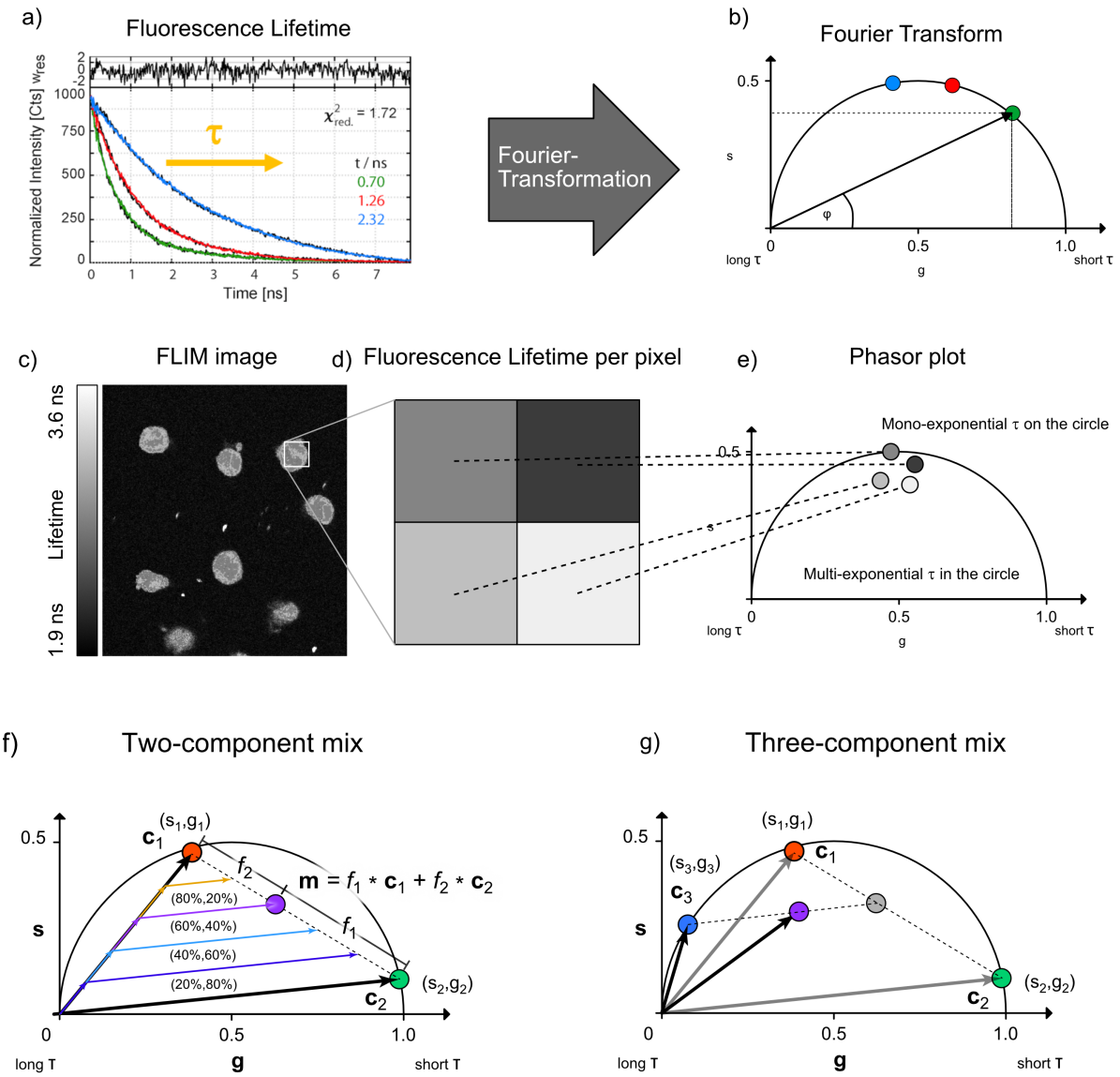

Figure 2.3.: A Phasor analysis of fluorescence lifetime imaging data. **a)** Fluorescence lifetime decays with different mono-exponential rates. **b)** A Phasor plot of the Fourier transformed fluorescent curves in (a). **c)** A FLIM image of the autofluorescence of HeLa cells (color-coded according to the lifetime extracted from the phasor plot). **d)** A schematic zoom into the FLIM image in (c). The color value of every pixel is a representation of its position in the Phasor plot. **e)** A schematic Phasor plot of the pixel wise lifetimes measured in a confocal fluorescence microscope image using time-correlated single-photon counting (TCSPC) based on the selection in panel (d). **f)** A theoretical phasor plot for a two-component mix of component c_1 and c_2 with the ratio f_1 to f_2. The mixture (purple dot) is the weighed vector sum and located on a line between the pure species locations. The position is dependent on the ratio f_1 to f_2. **g)** A theoretical phasor plot of a three component mix upon addition of a third fluorescent species c_3 with long lifetime. The purple population would be observed as mixed population between all three components. Figure adapted from the publication Veth, Fuchs et al. [85], see section 5.3.

2.2.2. Sum-frequency generation

In materials where the second order susceptibility $\boldsymbol{\chi}^{(2)}$ is non-zero, light fields can interact with each other to create a field with another frequency, derived from the incident ones. An example of this effect is sum-frequency generation (SFG): two light fields with the frequencies ω_1 and ω_2 are annihilated in a non-linear material and create a new light field with the frequency $\omega_{SFG,1} = \omega_1 + \omega_2$. Contrary to fluorescence no energy transfer from light to matter occurs, therefore, no real energy levels are required apart from the ground state. Eq. 2.18 shows the second-order polarization in the case of SFG [74]:

$$\mathbf{P}^{(2)}_{SFG}(t) \propto \epsilon_0 \chi^{(2)} 2\mathbf{E}_1 \mathbf{E}_2 e^{-i(\omega_1+\omega_2)t} \tag{2.18}$$

When the two interacting fields have the same frequency ω_1 (i.e. the laser field interacts with itself), the created light field possess double the frequency of the incident light fields. This effect is refereed to as second harmonic generation (SHG) and is a special degenerated case of SFG. Eq. 2.19 shows the second-order polarization in case of SHG [74]:

$$\mathbf{P}^{(2)}_{SHG}(t) \propto \epsilon_0 \chi^{(2)} \mathbf{E}_1^2 e^{-i2\omega_1 t} \tag{2.19}$$

where $\omega_{SHG} = 2\omega_1$. The power dependency of the respective signals is therefore:

$$I_{SFG} \propto I_1, I_2 \tag{2.20}$$
$$I_{SHG} \propto I_1^2 \tag{2.21}$$

The effect is based on a significant $\boldsymbol{\chi}^{(2)}$, which requires a non-inversion symmetric material. Independent of the material, surfaces can never have inversion symmetry. Therefore, SFG and SHG imaging are well suited for surface imaging in general, and for specific substances with a high $\boldsymbol{\chi}^{(2)}$ in particular. A common example from the field of life science is label-free collagen imaging [87–89]. In this work, SFG and SHG were demonstrated on MOF crystals for surface specific imaging (section 3.1).

2.3. Third order effects

Most techniques employed for our system are based on third order non-linear interactions, where three light fields interact. A wide variety of interaction can occur. In the following, I will describe the modalities implemented on the presented setup: FWM allows for (mostly) unspecific 3D imaging, 2PE for fluorescence excitation with IR laser sources. Space-resolved chemical characterization is carried out using different implementations of Raman scattering. The suitability of spontaneous Raman micro- spectroscopy for quantitative analysis is the base for the developed method presented in section 4.2. While label-free imaging with only spontaneous Raman spectroscopy is possible (referred to as hyperspectral Raman imaging), it is slow (hours to days) and

has a high risk of causing photodamage to the sample. Therefore, we additionally implemented enhanced Raman methods for fast, label-free imaging, discussed in the last paragraph of this section.

2.3.1. Four-wave mixing

In a nonlinear medium with a third-order susceptibility $\boldsymbol{\chi}^{(3)}$, up to three light fields with different frequencies can interact with each other. Inelastic scattering in this medium can lead to frequency mixing of all light fields, creating a fourth field with a new frequency ω_{FWM} [74]. When the three incident fields have distinct frequencies from each other $(\omega_1, \omega_2, \omega_3)$, nine distinct frequencies are generated by the FWM process. The number m of possible frequencies based on the FWM interaction of n fields with distinct excitation frequencies is [90]:

$$m = \frac{(n^2 \cdot (n-1))}{2} \tag{2.22}$$

At a sufficiently high photon flux the generated fields can also interact with each other, leading to new FWM processes. This effect is exploited to generate spectrally broad light fields in a photonic crystal fiber (PCF), as implemented in our setup to create the probe beam [91].
When applying FWM for nonlinear imaging, typically only two different excitation sources are applied. Theses incident light fields with the frequencies ω_1 and ω_2 create the degenerated FWM signals at the frequencies:

$$\omega_{FWM1} = 2\omega_1 - \omega_2 \tag{2.23}$$
$$\omega_{FWM2} = 2\omega_2 - \omega_1 \tag{2.24}$$

When one of the laser fields intensities is significantly higher than the other, e.g. $I_1 \gg I_2$, it will result in $I_{FWM1} \gg I_{FWM2}$. On our microscope, this relation is exploited for the FWM imaging modality.
The FWM signal intensity is proportional to $\boldsymbol{\chi}^{(3)}$ and the excitation fields intensity I_1 and I_2 [74]:

$$I_{FWM1} \propto I_1^2, I_2, \boldsymbol{\chi}(\omega_1, \omega_2) \tag{2.25}$$
$$I_{FWM2} \propto I_2^2, I_1, \boldsymbol{\chi}(\omega_2, \omega_1) \tag{2.26}$$

FWM is a universal, often unspecific tool for imaging, since it is possible to induce FWM in (almost) every material. In homogeneous, crystalline materials, FWM imaging maps the spatial distribution of $\boldsymbol{\chi}^{(3)}$ in the material. It is not restricted to surfaces, making it a valuable modality for label-free, unspecific 3D imaging. Moreover, changes in $\boldsymbol{\chi}^{(3)}$ caused by material inhomogeneities (such as defects in MOF crystals for example) will result in local changes in the detected FWM intensity. This enables defect-localization

in crystals, as shown by Wolf et al. [63]. In this work, the FWM modality was employed for label-free imaging and to localize defects in MOF crystals, as discussed in projects 1 and 2 (chapter 4).

2.3.2. Two-photon excitation

The application of pulsed laser sources with high intensities provides the possibility that the examined system absorbs two photons within a period of femtoseconds. Both photons contain approximately half the energy needed for a transition into an excited state. Two-photon excitation (2PE) allows the usage of near infra-red (NIR) excitation sources for fluorescence imaging. Since biological matter absorbs and scatters less in the NIR range [92], this enables deep tissue imaging and reduces the risk of photodamage [92] from out-of-focus absorption. An additional advantage stems from the fact, that the 2PE signal I_{2PE} scales quadratically with the excitation power [74]:

$$I_{2PE} \propto I_{exc}^2 \tag{2.27}$$

Only the photon flux in the focal plane is sufficient to induce 2PE and thereby creates a detectable fluorescence signal. This massively reduces the out-of-focus excitation compared to 1PE. Despite the increase in spatial resolution, 2PE suffers from a small cross section [93]. Therefore, it requires high excitation field strengths, which are usually achieved by exploiting the confocal beam geometry and applying pulsed laser sources in the NIR region. The effect was theoretically predicted in 1931 by Göppert-Mayer [26], but could, as mentioned, only be observed after the laser was invented (1961 by Kaiser et al. [27]).

2.3.3. Spontaneous Raman scattering

Spontaneous Raman scattering is an inelastic interaction, where energy transfer between a light field and matter occur, causing a vibrational transition of the material and a frequency shift in the scattered light. Every distinct vibrational transition caused by the inelastic scattering will create a unique frequency, referred to as Raman signal. The amount and likelihood of vibrational transitions is correlated to the chemical composition of the sample. The scattering pattern can therefore be used to identify substances enabling its application as Raman spectroscopy. The effect was first postulated in 1923 by A. Smekal [94] and 5 years later verified by Chandraskhara Venkata Raman [31]. It is a common characterization tool in modern science due to the high information content and the relatively easy implementation. It can be applied *in situ*, *in vivo* (usually in the IR regime), and on solid, liquid, or gaseous samples. The scattering process can be described with a classical approach, which will be laid out in the following paragraphs [74]:

The angular frequency notation ω will be employed as a representation of the frequency, with its relationship to the actual frequency ν as $\omega = 2\pi\nu$. The frequency ν and the wavelength λ of a photon are connected with $\nu = \frac{c}{\lambda}$ (c equals the speed of light).
Lets now consider a diatomic molecule. The dipole moment $\mathbf{p}$(t) of the molecule oscillates in the presence of an electric field $\mathbf{E}$(t), based on its polarizability $\boldsymbol{\alpha}$(t):

$$\mathbf{p}(t) = \boldsymbol{\alpha}(t) \cdot \mathbf{E}(t) \tag{2.28}$$

The polarizability $\boldsymbol{\alpha}$(t) depends on the vibration of the atom coordinates of a given chemical bound. It can be approximated as the sum of a constant $\boldsymbol{\alpha}_0$ and a time dependent contribution, induced by the change in atomic positions of the molecule during the vibration.

$$\boldsymbol{\alpha}(t) = \boldsymbol{\alpha}_0 + (\frac{\delta\boldsymbol{\alpha}}{\delta\mathbf{Q}})_0 \cdot \mathbf{Q}(t) \tag{2.29}$$

The latter part is dependent of the strength and frequency of the atomic displacement $\mathbf{Q}(t)$. We can describe this periodic atom displacement $\mathbf{Q}(t)$ as a damped, harmonic oscillator:

$$\mathbf{Q}(t) = 2 \cdot \mathbf{Q}_0 \cdot cos(\omega_\nu t + \theta) = \mathbf{Q}_0 \cdot (e^{-i\omega_\nu t - i\theta} + e^{-i\omega_\nu t + i\theta}) \tag{2.30}$$

$\mathbf{Q}_0$ is the vibration amplitude tensor, ω_ν the resonance frequency of the bond and θ the phase. When a light field with the frequency ω_1 is scattered at the material, a description of the process can be derived by inserting eq. 2.1, eq. 2.29, and 2.30 in eq. 2.28:

$$\mathbf{p}(t) = (\boldsymbol{\alpha}_0 + (\frac{\delta\boldsymbol{\alpha}}{\delta\mathbf{Q}})_0 \cdot \mathbf{Q}_0 \cdot (e^{-i\omega_\nu t - i\theta} + e^{-i\omega_\nu t + i\theta})) \cdot \mathbf{E} \cdot e^{-i\omega_1 t}) \tag{2.31}$$

This can be simplified to eq. 2.32:

$$\mathbf{p}(t) = \boldsymbol{\alpha}_0 \cdot \mathbf{E} \cdot e^{-i\omega_1 t} + (\frac{\delta\boldsymbol{\alpha}}{\delta\mathbf{Q}})_0 \cdot \mathbf{Q}_0 \cdot (e^{-i(\omega_1+\omega_\nu)t - i\theta} + e^{-i(\omega_1-\omega_\nu)t + i\theta}) \cdot \mathbf{E} \tag{2.32}$$

The description of the scattering process reveals three possible frequency combinations: elastic Rayleigh scattering without energy transfer $\omega_{out} = \omega_1$ (first term) and inelastic Raman scattering (second term). The light field can receive energy from a molecule vibration in an excited state, so that the frequency of the scattered light ω_{out} is $\omega_{out} = \omega_1 + \omega_\nu$ (referred to as Anti-Stokes scattering). Alternatively, a photon can excite a vibration by transferring energy to the material. The scattered photon then has the frequency $\omega_{out} = \omega_1 - \omega_\nu$ (referred to as Stokes scattering). Since vibrational levels are thermally populated according to the Boltzmann distribution [95], Raman scattering on the Anti-Stokes Side is less likely to occur than on the Stokes side. This leads to a spectral intensity difference in the scattering pattern below and above the excitation wavelength, i.e. a higher average Raman intensity towards lower frequencies than towards higher frequencies relative to the incident excitation frequency.

The frequency of the Raman scattered photons is centred around the excitation frequency ω_1. Since Raman scattering is usually exploited for substance identification, i.e. as a spectroscopic method, an excitation independent notation of the Raman spectrum is needed. Here, the relative wavenumber $\tilde{\nu}$ is introduced with:

$$\Delta\tilde{\nu} = \frac{(\omega_{out} - \omega_1)}{c} \cdot \frac{1}{2\pi} = \frac{1}{\lambda_{out}} - \frac{1}{\lambda_1} \tag{2.33}$$

By converting the measured Raman peak positions from wavelength in $[nm]$ into rel. wavenumbers in $[cm^{-1}]$, Raman spectra can be compared independent of the excitation wavelength.

The intensity of a Raman signal I_R depends on several parameters outlined in detail in the publication to project 2 (section 4.2). In brief, it depends linearly on the laser field intensity I_E and the concentration of the scattering substance c:

$$I_R \propto I_E, c \tag{2.34}$$

Typically, the probability of a Raman scattered photon is low compared to the absorption probability in fluorescent dyes. Even good Raman scatterer have a low occurrence for inelastic scattering compared to fluorescent materials. Therefore, high excitation field intensities are necessary, usually tens of milliwatts average power, whereas confocal fluorescent methods operate between <1 to tens of microwatts [93]. Since the Raman signal intensity scales linear with the excitation source intensity, photodamage occurs when the excitation power exceeds the damage threshold of the sample. This can lead to long measurement times, especially in hyperspectral Raman imaging [93]. Since the data collection per pixel ranges in the second regime, the overall time per image can be several hours. While our hyperspectral datasets were usually recorded in ca. 2 1/2 hours, up to 38 hours per field of view can be found in literature [33].

2.3.4. Enhanced Raman scattering

The main hindrance for employing the Raman effect for chemically sensitive, label-free imaging is the low probability of the process to occur. Hence, several strategies have been developed to enhance its likelihood and, therefore, increase the achievable sensitivity and acquisition speed. These processes exploit the enhancement by electronic resonance, plasmonic and metal surface enhancement, or laser coherence:[3]:

- Resonant Raman scattering
- Surface-enhanced Raman scattering (SERS) / Tip-enhanced Raman scattering (TERS)
- Coherent Raman scattering (CRS)

[3]Paragraph follows the review by Jones et al. [34]

Resonant Raman scattering occurs when the energy of (at least) one of the electric fields involved in the Raman scattering process is in close proximity to the energy gap of an electronic transition of the sample material. The Raman bands which are energetically close to the transition experience an increase in scattering probability and a subsequent enhancement in intensity up to 10^6 [34]. The enhancement is usually confined to a small spectral region of a Raman spectrum. The study of resonant Raman substances can be performed at low concentrations [96].

A less substance-specific approach is SERS. Here, nanostructures excited by a light field can induce local surface plasmons. The plasmons generate an additional electric field, where the local field strength is defined by the nanostructure shape. Apexes and sharp edges can locally concentrate the plasmonic field strength. Raman scatterers in close proximity experience a strong enhancement of the scattering process. SERS can be combined with atomic force microscopy (AFM) where a small metal tip is close to the sample surface [97]. While this tip-enhanced Raman scattering (TERS) enables fast surface imaging and enhanced Raman spectroscopy combined with nanometer resolution, the technique is limited to surface analysis only and is technically challenging to implement. Moreover, even stronger enhancement can be found when Raman scatterers are located between two or more nanostructures close to one another [98]. These create electric fields with very high local strength, so called "hot spots". In addition to the plasmon induced field enhancement, the close proximity of the scattering particle to the nanostructure can result in hybridization of orbitals, enabling a resonant Raman enhancement on top [34]. This contribution is mainly reported for organic molecules close to noble metal nanostructures. With both effects present, SERS increases the Raman signal up to a factor of 10^{11} [34]). The strong enhancement make even single Raman scatterer detectable [99]. Therefore, SERS is ideal for screening and sensing applications, such as detection of pathegeneous materials [100], aerosol pollutants [101], or unmodified DNA [102].

While SERS provides single-molecule sensitivity, the method requires multiple nanostructures in close proximity to the substance of interest. A completely label-free alternative is provided by methods based on coherent Raman scattering (CRS): when the difference in energy of two light fields matches the energy of a vibrational transition, the probability of Raman scattering at this bond vibration is increased. This enhanced Raman scattering is now coherent to the driving excitation light fields in contrast to the incoherent spontaneous Raman scattering. coherent Raman scattering (CRS) is a resonant FWM process and therefore also requires high photon fluxes and high field strengths.

The coherently enhanced Raman scattering on the Stokes and Anti-Stokes transitions are referred to as coherent Stokes Raman scattering (CSRS) (pronounced "scissors") and CARS respectively. In CARS, photons are blue-shifted with respect to the excitation lasers making the technique ideal for combination with biological fluorescent imaging

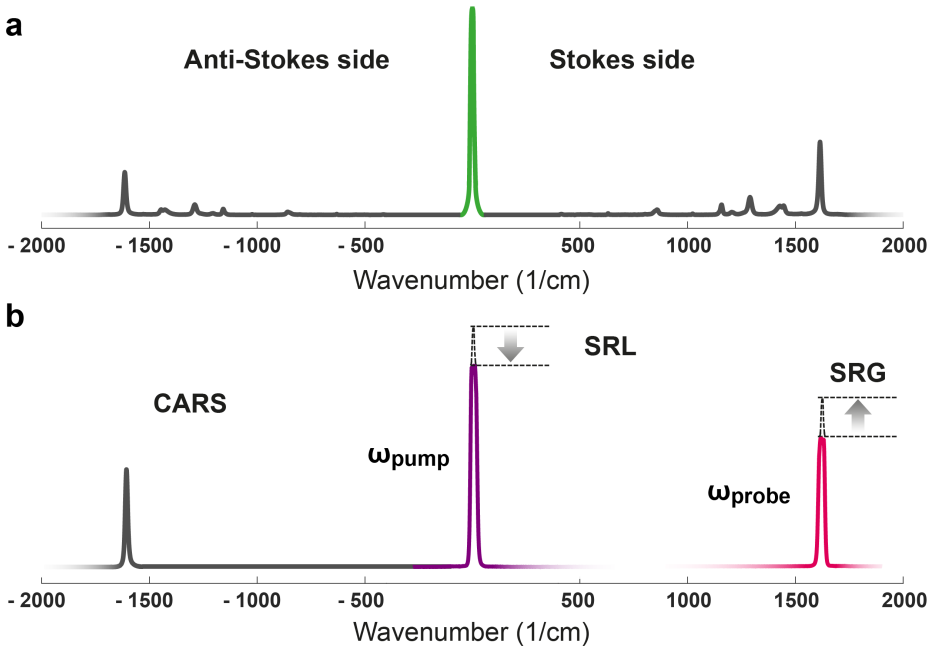

Figure 2.4.: Schematic spectra for Raman scattering, CARS, and SRS. **a)** Spontaneous Raman scattering. The green curve represents a schematic excitation laser signal, the grey curves a typical spontaneous Raman scattering spectrum (selected peaks from the polystyrene spectrum). **b)** Resonant, degenerate FWM as the basis for CARS and SRS effects. When the difference in energy between the wavelength of the pump (ω_{pump}, lilac curve) and probe beam (ω_{probe}, pink) is equivalent to a Raman active transition, the resonant CARS signal is created. In addition, the pump beam intensity experiences stimulated Raman loss (SRL) and the probe beam the equivalent stimulated Raman gain (SRG) (indicated by the dotted lines). The latter process is referred to as SRS. Intensities of the signals are chosen for clarity since the Raman scattering signals are much less intense and would not have been visible in this representation.

(see figure 2.4b). Since its revival[4] in 1999 by Zumbusch et al. [36], CARS has been applied to a multitude of research projects, i.e. in brain tumour detection [103], to study skeletal stem cells [104], and to track organelles in living cells [105]. Over the last two decades, CARS has proven to be a robust and flexible tool for label-free, chemically-sensitive imaging. It is well suited for biological and inorganic imaging and therefore an important addition to the platform presented here. Nevertheless, both CSRS and CARS can be extremely challenging to apply for the quantitative analysis of unknown sample substances. This is, one the hand, due to the quadratic dependence on the sample concentration and, on the other hand, due to non-resonant signal contribution: since CARS is a FWM process, the generated signal is composed of a resonant component and a non-resonant background. Both are created at the same time in the same

[4]Although Duncan et al. published a working CARS microscope in 1982 [35], the visible lasers he applied were introducing high backgrounds, rendering a broader application impossible. Zumbusch et al. solved this problem, by switching to excitation sources in the NIR, allowing a significantly better signal-to-noise ratio.

confocal volume at the same wavelength, rendering the distinction of the signal origin challenging. One option is the separation them via the signal phase, applying the *Kramers-Kronig* relation [106–108]. However, these techniques are technically highly demanding and restrict applications of the excitation sources for other modalities. Another approach is to exploit differences in the polarization of the signals [109, 110]. The CARS signal The polarization of the non-resonant and the resonant components depends on the polarization of the excitation laser fields. Linearly polarized excitation lasers result in linear polarization of both, the resonant and non-resonant component. The angle between these components is a function of the angle between the excitation laser polarizations. When adjusting this angle between the excitation lasers to 71.6°, the resonant and non-resonant component polarizations are perpendicular to each other. By blocking the linearly polarized, non-resonant component with a polarizer in front of the detector it becomes possible to transmit only the resonant signal contribution, the CARS signal. The technique is referred to as polarization coherent anti-Stokes Raman scattering (pCARS) [110] and is implemented on our microscopy platform. When blocking the non-resonant signal, we acquired the CARS images. By rotating the polarizer by 90° the resonant component is blocked and the non-resonant FWM signal is transmitted. The polarizer position allows us to map the same area in both modalities and compare the resonant, chemically-sensitive image to the unspecific, non-resonant $\chi^(3)$ mapping. We applied the combination to localize water molecules in a MOF framework in chapter 4 and correlate them to defect site positions.

While the non-resonant background can be minimized, the quadratic dependence on the sample concentration still limits the application of CARS for quantitative analysis [37]. Another CRS effect holds more promise: stimulated Raman scattering SRS. When the two laser fields interact in resonance with a Raman vibration, energy is transferred from the higher energy pump to the probe laser field. This results in a SRL for the pump and a SRG for the probe beam (see figure 2.4b), known as SRS [37, 38]. The power dependence is linear with the concentration and no non-resonant background is present. SRS could be combined with the presented methods, and has been shown in literature to pair very well with fluorescence imaging [111]. The SRS induced change in intensity is very small compared to the total intensity of the laser fields and is challenging to detect against background noise. Retrieval of the SRS signal requires a specific electronic detection scheme, revolving around a Lock-In Amplifier (LIA) [37, 38]. Here, one of the laser lines is modulated with a distinct frequency f_{rep}. The LIA filters the detected signal after the sample for intensity fluctuations at f_{rep}. The noise-induced random fluctuations can, therefore, be vastly reduced. This detection scheme allows to apply SRS as an effective imaging modality. The required electronical components are already implemented in the setup and first test measurements were performed. However, for the presented projects CARS was more then sufficient for chemically-sensitive imaging of the sample systems investigated in this thesis (chapters 4 and 5). The additional implementation of SRS will be the prospect of future development.

The selected effects are based on a variety of light-matter interactions. However, the

requirements regarding instrumentation are relatively similar: high photon densities, excitation in the VIS to NIR range, and a high control over the spectral composition of excitation and emission light. The next section describes the key technical concepts that can be applied to combine the described modalities onto a singular platform.

2.4. Instrumentation for optical microscopy

Optical microscopy and spectroscopy have a wide variety in technical realizations. The developed setup is composed of two modular units: a confocal optical microscope combined with a spectrometer enabling the spectral analysis with spatial resolution. The microscope base, an inverted confocal microscope, and the spectrometer are presented in this section in context to optical microscopy in general and with respect to their spatial and spectral resolution.

2.4.1. The optical microscope

Microscopy is the field of studying microscopic systems, literally meaning images, that cannot be seen by the naked eye. The oldest known form of microscopy is optical microscopy based on enhancing images created by illumination with visible light [19]. The optical image enhancement here is founded on the lensing effect. Lenses were employed already early in human history, e.g. the Assyrian "Nimrud lens" [112], sculpted out of crystalline rock with a focal length of ca. 12 cm, can be dated to ca. 700 BC.[5] The earliest documented use of lenses for magnifying glasses, the most simple form of a microscope, dates back to the 13^{th} century. The widespread popularity of spectacles, starting in Italy shortly before, had resulted in the fabrication of high quality glass lenses [14] required for the magnifying glass. The microscope developed over the following years with the compound microscope where multiple lenses further enhanced the maximum magnification. The actual inventor of the first optical compound microscope is still under debate. Many potential candidates claim this title [14] (including Galileo Galilei [113]). Due to conflicting sources regarding the inventor one can only be certain that the first functioning devices were finished between 1590 and 1619. The origin of the term "microscope", however, is known being coined by Giovanni Faber in 1625 as analogue to the term "telescope" [14]. A compound microscope consists of at least two lenses [14]: the *objective lens* focusses light onto the sample, and a *ocular lens* to create the image for the observer. Our multimodal optical microscope includes a classic bright field BF modality, wherein a spectrally broad light source shines on the object, is collected by the objective and redirected onto the eyepiece. This approach, basically the same design as in the 17^{th} century, provides a fast and robust way to visualize the sample in wide field geometry.

The investigation of complex systems in the micrometer to sub-micrometer regime with optical microscopy required the development of more refined methods and optical elements (see chapter 1). The spatial resolution of the microscope defines the lower limit of teh objects that can still be directly visualized. It depends on the numerical aperture (NA) of the objective lens:

[5] Although whether it was actually applied for magnification, lighting fires, or just as a decorative inlay can't be verified with certainty, due to a lack of reliable sources from that time period.

$$NA = sin(\alpha) \cdot n \tag{2.35}$$

Here, α is the half-opening angle of the objective and n the reflective index of the transmitting medium. The Rayleigh criterion [114] allows an estimate of the maximum possible resolution laterally Δx and axial Δz to the illumination path of the incident light [115]:

$$\Delta x = 0.61 \cdot \frac{\lambda}{NA} \tag{2.36}$$

$$\Delta z = 2 \cdot \frac{\lambda}{(NA)^2} \tag{2.37}$$

Eq. 2.36 describes the minimum distance the centers of two point emitters need to be apart to be considered resolvable by the Rayleigh criterion [114]. Typical resolutions achievable using light microscopy with illumination sources in the visible spectral region (ca. 380-750 nm) [116] and high NA objectives (NA $>$ 1) are between ca. 200 to 350 nm. The axial resolution is significantly lower, around 1 µm. Moreover, out of focus light blurs the acquired images. To minimize this distortion and increase the signal-to-noise ratio in the so-called point microscopy, the incident light is focused on only one point in the sample at a time instead of large sections. An image is created by raster-scanning the sample and collecting the intensity at every point. Scanning can be either performed by moving the sample with a stage or by moving the excitation source, typically with electronically adjustable mirrors (galvanic mirrors). When the recollected signal is focused onto a pinhole in the detection path the out-of-focus contributions can be additionally reduced (see figure 2.5).
The so-called confocal principle was first published by Minsky et al. in 1961 [17]. The excitation beam is focused onto the sample by the objective. The signal can be either collected by a second objective on top of the first (*forward detection*) or by the same objective (*epi detection*, see figure 2.5). The signal is then focused onto the detection pinhole before being focused again onto the detector. Signal contributions from outside of the focal volume are not focused onto the pinhole, leading to a significant reduction of their contribution to the intensity measured by the detector. Since the selected sample region and the pinhole are simultaneously in focus, the method is known as confocal principle. The combination of confocal microscopy, laser excitation, and raster scanning enabled high contrast, substance-specific, multiplexing imaging, making confocal laser scanning microscopy (CLSM) a staple in modern optical microscopy.
Confocal microscopy is based on focusing the excitation laser light onto the diffraction limited volume (typically in the range of femtolitre in modern microscopes), where high field intensities can be created in the focal spot. Since high field intensities are a necessity for the significant occurrence of the nonlinear interactions, we based our platform on a CLSM. Additionally, the spatial confinement of the focal volume enables a point-by-point spectral characterization, adding an additional dimension to the analysis options.

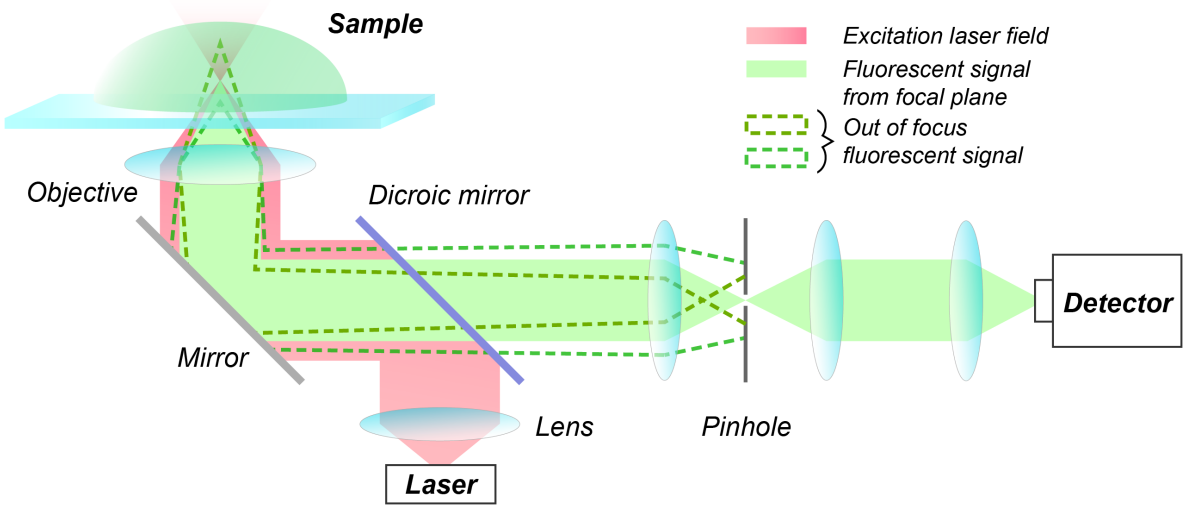

Figure 2.5.: Schematic of confocal microscopy. The emission after laser excitation from the sample is separated from the excitation light by a dicroic mirror. Signal from the focal plane is focused through a pinhole with negligible loss in intensity and projected onto the detector. Emission from out-of-focus regions is predominantly blocked by the pinhole, increasing the image contrast.

2.4.2. Spectrum acquisition

To extend the CLSM from a singular modality to a multimodal setup it is desired to distinguish between different spectral signatures. This can be achieved with dispersive optical elements. While lenses manipulate light of every color in the same fashion, optical elements like dichroic mirrors, prisms, and gratings are separating light depending on the wavelength. Optical filters and dichroic mirrors transmit certain wavelength regions and reflect the complementary regions. They are employed to separate different spectral signatures according to their spectral range. Prisms and gratings spatially disperse spectral components of light in space, with a wavelength dependent diffraction angle. The effect enables the analysis of the spectral composition of an optical signal, a field known as spectroscopy.[6] A device to record spectra in a quantitative manner is a spectrometer. It is comprised out of a spectrograph, which spatially divides a signal into its spectral components, and a detector for recording the light. In early versions, the detector was the eye of the observer whereas modern systems typically apply a multi-pixel line detector.
Spectrometer can be realized in a variety of different designs. The spectrometer in our microscope is based on the Czerny-Turner design (see figure 2.6a, [117]), which will be exemplary presented in the following:
The collected light from the focal volume of the microscope is first focused onto the entrance slit of the spectrometer. The light is recollimated by a focus mirror and reflected onto a diffraction grating at an angle α relative to the norm. Diffraction gratings

[6]From "spectrum" and "scope", meaning "observing the spectrum".

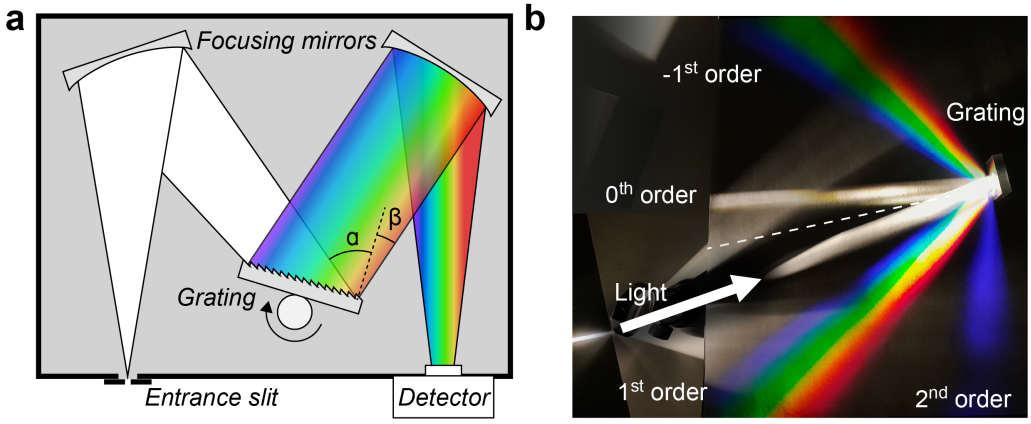

Figure 2.6.: A Czerny-Turner spectrometer based on optical gratings. **a)** A schematic of a Czerny-Turner Spectrometer. Light is focused through the entrance slit and recollimated by the first focusing mirror. It is directed onto a grating with the angle α against the grating norm (indicated by the dotted line). The diffraction angle β changes with respect to the wavelength. The spectrum is projected onto the detector by a second focusing mirror. **b)** Spectrum of a filament lamp diffracted by a blazed grating (blazed for 780 nm, 500 l/mm). The diffraction orders are marked and the dotted line indicates the grating norm.

possess periodic, equally spaced, parallel grooves. The dispersion effects originates from wavefront division and interference of the reflected radiation due to the periodic structures. One observe typically multiple reflection orders (figure 2.6b). While the zero order reflection has no dispersion, the diffraction angle β of non-zero order reflections is wavelength dependent. Usually, the first order reflection is focused by a second focusing mirror onto the detector. By rotating the grating, different spectral components can be imaged onto the limited detector area, significantly enhancing the available spectral range at constant spectral resolution. Based on the desired application, a variety of gratings are available. Commonly, blazed gratings are employed, due to their high intensity in the first order of the reflection and the high total reflectivity. The shape of the groove, the *blaze angle*, defines the wavelength with the maximum efficiency. The total grating size and the grating line density define the grating resolution or the spectrometer.

The spectral chromatic resolution of a spectrometer, R, is defined as [118]:

$$R = |\frac{\lambda}{\Delta\lambda}| \tag{2.38}$$

The spectral resolution is influenced by the focal length of the focus mirrors F in the spectrograph, the incident angle onto the grating α, the optical properties of the grating, and the detector pixel size.F and α are defined by the spectrograph design and are typically constant. If the detector is chosen with a significantly smaller pixel size than the optical resolution defined by the other parameters, R is directly proportional to the angular dispersion D of the grating [118]:

$$D = \frac{\delta\beta}{\delta\lambda} = \frac{G \cdot m}{cos(\beta)} \tag{2.39}$$

where G is the line density of the grooves and m the diffraction order (typically $m = 1$). The part of the spectrum that can be acquired without rotating the grating itself $\lambda_{max} - \lambda_{min}$, is also dependent on the groove density [118]:

$$\lambda_{max} - \lambda_{min} = n \cdot W_p \cdot \frac{cos(\beta)}{F \cdot G \cdot m} \tag{2.40}$$

where n is the number of pixels or pixel columns in the detector and W_p the pixel width. When selecting a spectrograph and detector combination, the grating line density G connects the possible spectral resolution R and the spectral window $\lambda_{max} - \lambda_{min}$:

$$R \propto G \propto \frac{1}{\lambda_{max} - \lambda_{min}} \tag{2.41}$$

When selecting a spectrometer for a multimodal, optical microscope, the implemented grating is integral: lower line densities allow fast acquisition over a relatively wide spectral range whereas high line densities enable high spectral resolutions. For example, a grating with 300 lines per mm and an excitation wavelength of 532 nm can acquire spectral ranges of $> 1000\,\mathrm{cm}^{-1}$, but the resolution will be higher than $10\,\mathrm{cm}^{-1}$ (for a focal length of 328 mm for the spectrograph and a detector pixel size of 16 µm). Therefore, multiple peaks can be monitored directly in relation to each other allowing for faster substance identification and direct interpretation of processes. However, small changes in single peak shapes or the development of side shoulders is usually not observable at this resolution, limiting the sensitivity for smaller changes in the sample system. For a grating with 1200 lines per mm, the range reduces to several $100\,\mathrm{cm}^{-1}$, but the spectral resolution typically increases ideally fourfold, enabling studies of spectral regions sensitive to small changes. An automated turret, which can switch between different gratings, provides the advantages of both and is one key component to a flexible spectroscopy unit within our multimodal microscope (see section 3.2 for a detailed description).

Chapter 3.

MOSAIC Analysis Platform

The following chapter describes the main focus of this thesis: the design and the technical realization of the developed MOSAIC setup, as published in:

Fuchs, A., Mannhardt, P., Hirschle, P., Wang, H., Zaytseva, I., Ji, Z., Yaghi, O., Wuttke, S.*, Ploetz, E.*, **Single Crystals Heterogeneity Impacts the Intrinsic and Extrinsic Properties of Metal–Organic Frameworks.** *Adv. Mater.* 2022, 34, 2104530.

The application of the developed multimodal system to study particle-property relations in MOF systems, also presented in the publication above, will be shown in section 4.1. Here, the combination and implementation of the selected imaging and spectroscopic modalities (whose theoretical backgrounds were presented in the last chapter) on a microscopy platform will be presented. First, we show the general design of the microscope and the spectral windows selected for the excitation sources and the subsequent modalities. After the broad, general overview, the key components for the technical realization of the microscope are highlighted in more detail.

3.1. General design of the microscope

All selected effects can provide imaging contrast in confocal microscopy. Therefore, an inverted confocal microscope with a spectrometer extension was used as the basis for the developed platform.

Basic microscope design

Figure 3.1 depicts the general design: continuous wave (cw) and pulsed laser sources (details in the next sections) are combined and coupled into the microscope. The sample can be scanned with a three-axis piezo stage. For detection of the different imaging modalities, an APD records the intensity at each scan point. In combination with a TCSPC card, APDs provide single photon sensitivity and access to lifetime information. Here, FLIM analysis can be performed. The detected signal is divided between two APDs by a 610 nm short pass dicroic mirror, effectively splitting the signal between green and red channels. This allows the simultaneous collection of different modalities, e.g. SHG and CARS. In addition to the discussed modalities, a bright field (BF) channel

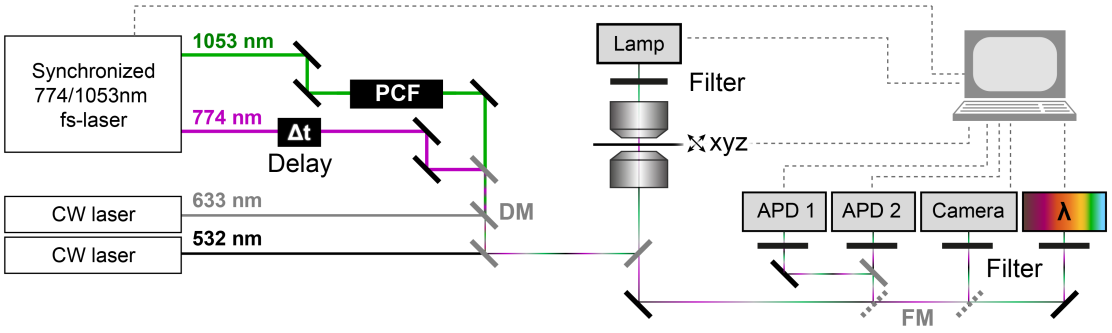

Figure 3.1.: A schematic of the MOSAIC microscope design. The setup consists of three parts: the excitation sources, the scanning confocal microscope, and the detection unit. The first comprises two types of light sources: cw lasers and a synchronized, dual-output fs-laser for nonlinear-imaging. They are all coupled into an inverted scanning microscope. The microscope is equipped with a lamp and a camera for bright field (BF) imaging and two avalanche photdiode (APD) for scanning images. The detection path can also be redirected onto the spectrometer. The microscope is controlled with home-written software. Legend: APD: avalanched photodiode; λ: Spectrometer; xyz: piezo-stage; Δt: temporal delay unit; DM: dichroic mirror; FM: flipping mirror; cw: continuous wave; PCF: photonic crystal fiber. Figure adapted from [81].

was implemented. A Xenon lamp illuminates the sample from above and is projected onto a sCMOS camera. It provides a BF image of the sample area for ease of navigation. A flip mirror can be applied to switch between the APDs and the BF channel. To obtain spectral information, an automatic flip mirror can be applied to switch the output to the spectrometer instead of the imaging detectors or the BF channel. The spectrometer is discussed in detail in section 3.2. It is equipped with three different grating options to provide the best compromise between acquisition speed and spectral resolution depending on the requirements of the measurement.

The next step in combining fluorescence and Raman spectroscopy with non-linear imaging modalities on the microscope was to select the excitation sources in a way that every modality occurs in a similar spectral range but can still be separated.

Spectral design

The excitation sources and detected spectroscopic signatures were chosen to occur in the VIS to NIR range of the spectrum based on the typical requirements for live-cell measurements. For non-linear excitation (2PE, CARS, FWM, and SHG/SFG), a spectrally narrow light source in the NIR range at 774 nm[1], as well as a spectrally broad source from circa 770 to 1100 nm, were implemented. According to the naming conventions in the field of non-linear optics, the light source at 774 nm is referred to as the "pump beam" or the "pump", while the broad light source is termed the "probe beam" in the following. Additionally, a set of common cw lasers (532, 561, and 633 nm) is employed for fluorescence excitation and Raman scattering. Usually, the 532 nm laser line serves

[1]The pulsed laser sources will be discussed in detail in section 3.2.

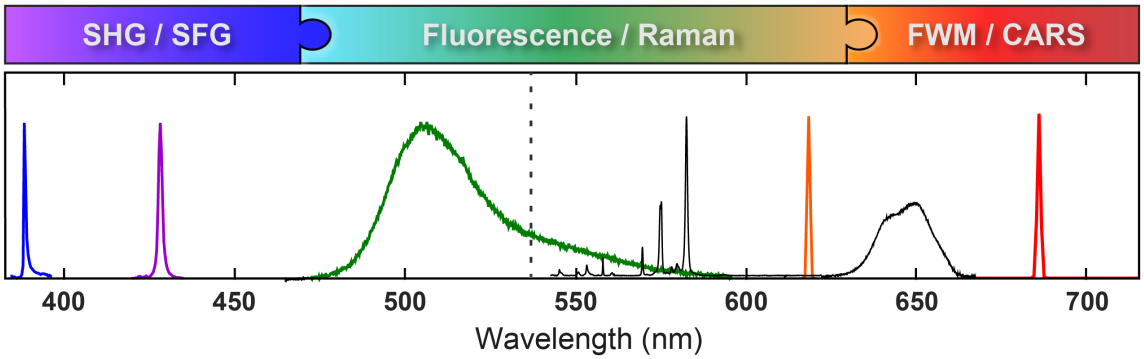

Figure 3.2.: Spectral ranges for the employed modalities. SHG, SFG, and FWM (blue, purple, and orange) were measured at the interface of a silica crystalline surface. The fluorescence emission spectrum of Rhodamine B isothiocyanate (RBITC) after 2PE with the pump laser is shown in green. The Raman spectrum between ca. 540 - 600 nm belongs to UiO-67 MOF, and the broad peak around 650 nm to water (black). The CARS signal is represents the CO stretch in UiO-67 (red). Figure adapted from [81].

as the excitation source for Raman spectroscopy in the presented projects, although all cw lasers are implemented as potential Raman excitation sources. The optics necessary for implementing additional laser lines at 488 nm and 785 nm have been included in the cw beam path.

Figure 3.2 depicts the spectral regions selected for the addressed modalities: starting from the UV, the frequency doubled SHG signal of the pump laser appears at 387 nm. The SFG can be tuned between the two pulsed NIR laser lines, i.e. between 387-526 nm.[2] Around 510 nm, the emission spectrum of a RBITC dye solution after 2PE is displayed (green). Although fluorescence is a powerful tool, it is limited for multiplexing applications due to spectral broadness as can be observed here. In black, the Raman spectrum of a MOF UiO-67 crystal after illumination with the 532 nm laser line (spectral position of excitation indicated as dotted line) between ca. 500-1800 cm^{-1} is plotted. Additionally, the typical water OH stretch vibration around 650 nm, is shown. This Raman signature of water will be further addressed in the water adsorption related to projects 1 and 2 (chapter 4). The spectral range from 532 to ca. 750 nm corresponding up to 4800 cm^{-1}, providing access to the usual frequency range measured with Raman spectroscopy. The current optics for separating the excitation source from the induced signals within the microscope body are limiting the range from 500 to 4400 cm^{-1}, which presents a hindrance especially in the study of iron-based MOFs since iron-oxide vibrations usually occur between 50 and 500 cm^{-1} [119]. An IR laser source in combination with spectrum collection in forward direction instead of the current backward detection, can resolve this limitation.

[2]Based on the driving laser for creating the broad spectrum at 1053 nm, see also next section 3.2 for more detail.

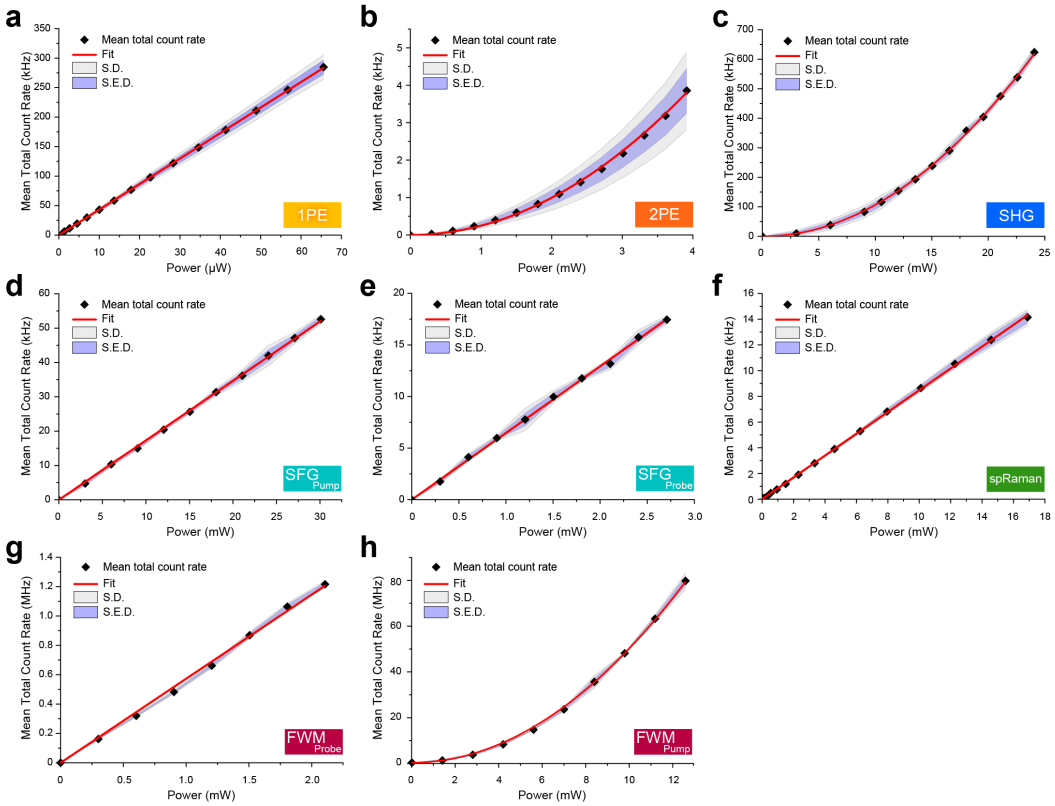

Figure 3.3.: The power dependencies of the different spectral signatures. The respective intensities as function of the laser power were either fitted with a linear or quadratic fit function with respect to their theoretical dependence as described in chapter 2. **a-b)** Fluorescence emission of 5 μM Atto532 in PBS as function of a) direct excitation at 532 nm and b) two-photon excitation at 774 nm. **c)** Quadratic dependence of SHG intensity at 774 nm excitation. **d-e)** Linear dependence of SFG intensity on the pump and probe power d) with fixed probe power of 25.6 mW at 1053 nm and e) with a fixed pump power of 22.3 mW at 774 nm measured in front of the microscope. **f)** Linear dependence of spontaneous Raman scattering at 520 cm^{-1} determined at 532 nm excitation. **g-h)** Quadratic and linear dependence of FWM intensity on the pump and probe power g) with fixed probe power of 17.4 mW at 1050 nm and h) fixed pump power of 120.2 mW at 774 nm at the sample. Mean values, standard deviations, and standard error of the mean represent the average of triplicates. Figure adapted from [81].

For label-free imaging, the FWM modality is usually tuned to 612 nm, corresponding to the interaction of the pump at 774 nm and the 1053 nm contribution in the probe beam. The spectrally broad probe beam, originating from the PCF, is powered by the pulsed laser line at 1053 nm. In the resulting broad spectrum, the highest laser power per spectral window remained around this fundamental wavelength. Therefore, by addressing the spectral window around 153 nm, it allows us to split the required laser power for FWM quite evenly between the pump and the probe beam. Experiments showed, that this reduces the risk of photo-damage among long measurements. A rotatable polarizer in front of the detectors enables us to either block the FWM signal and measure pCARS

Table 3.1.: Overview of the selected MOSAIC spectral signatures.

Modality	Excitation source(s)	Spectral region	Power dependency
Fluo. 1PE	cw 532/560/633 nm	ca. 350-750 nm	$\propto I_{cw}$
Fluo. 2PE	774 nm (pump)	ca. 350-750 nm	$\propto I^2_{pump}$
SHG	774 nm (pump)	387 nm	$\propto I^2_{pump}$
SFG	774 nm (pump) + 770-1100 nm (probe)	387-527 nm	$\propto I_{pump}, I_{probe}$
Raman	cw 532 nm	535-750 nm	$\propto I_{532}$
FWM/CARS	774 nm (pump) + 770-1100 nm (probe)	610-750 nm	$\propto I^2_{pump}, I_{probe}$

or transmit the FWM signals onto the detectors. Both effects occur between circa 610 and 750 nm, enabling CARS imaging for Raman peaks between 400 and 3500 cm^{-1}.

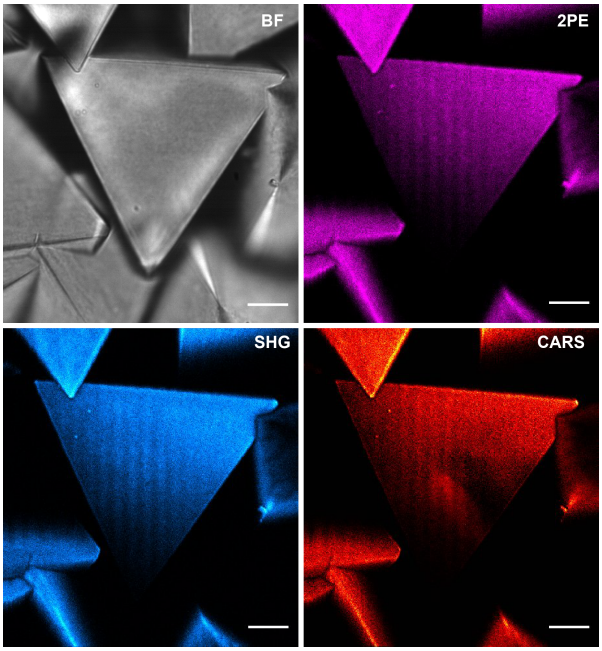

Figure 3.4.: Multi-modal, nonlinear imaging on unlabeled UiO-67-MOFs. Bright-field, 2PE induced autofluorescence and SHG show a smooth surface and well-defined edges of the particles. Together with CARS imaging, spectral information on MOFs can be obtained over the spectral range between 395 and 775 nm simultaneously. The chemical response is very even as expected. Excitation power after the objective: pump: 3.8 mW, probe 4.2 mW (measured at 1050 nm). All images are summed up over triplets with an integration time of 720 ns/pixel. 2PE emission was detected using a 685/150 bandpass filter in combination with 750 SP and 785/10 Notch filter to block the laser excitation. SHG was detected at 387 nm using a 377/50 bandpass filter in combination with 680 SP to block the laser excitation. CARS at 1615 cm^{-1} (688.2 nm) was measured consecutively to 2PE and with identical detection settings. All scale bars are 10 μm. Figure taken from [81]

The spectral orthogonality of the different modalities is the basis for the multimodal analysis. The acquired information for the selected modalities can be correlated and even

combined in an modular manner. To ensure the correct assignment of the signals to the underlying physical processes, a power series for every effect in isolation was measured (figure 3.3). Table 3.1 shows the expected power dependency as derived from the physical discussion in chapter 2. All power series can be well represented by polynomial fits with either strictly linear or quadratic exponents, in accordance with expectations. The series are averaged over three repeats, the standard deviation is shown as shaded background. We found a perfect overlay with the theoretical predictions, showing the clear distinction between the different modalities in our system. With the presented design, it is possible to excite and detect all desired modalities, as demonstrated for MOF UiO-67 (see figure 3.4, and project 1 in section 4.1).

3.2. Technical realization

In this section details regarding the employed nonlinear light source, the developed acquisition software, and the implemented electronics for multimodal experiments are presented. It will focus on the key components of the microscope in context to the advantages and challenges of the technical realization for this MOSAIC analysis platform. An extended summary can be found in the supplementary information file of [81].

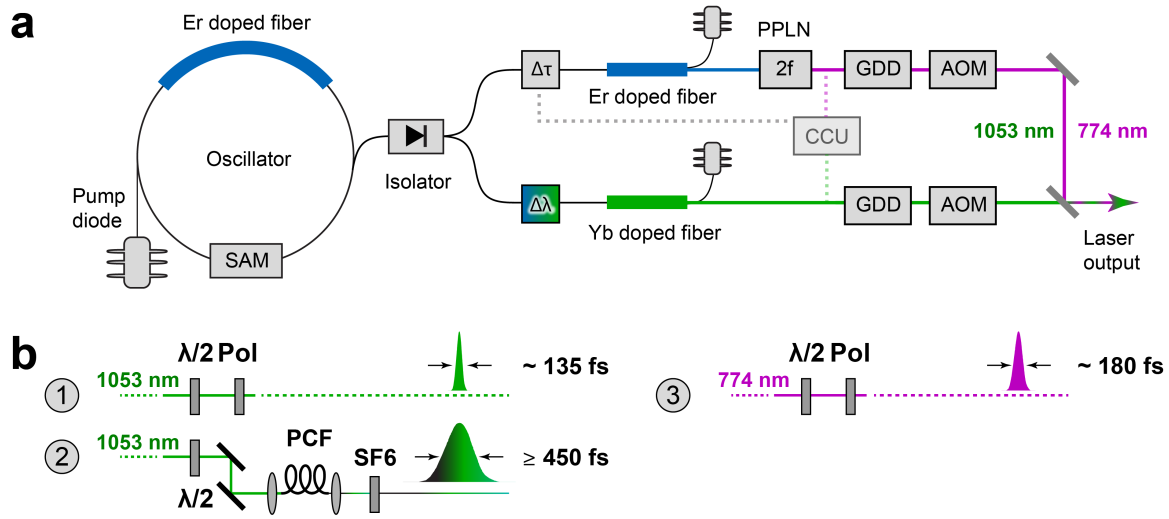

Figure 3.5.: Schematic of the pulsed nonlinear excitation source of the MOSAIC microscope. **a)** Schematic of the fiber-based fs-laser source based on a SESAM mode-locked ring oscillator as a master oscillator that seeds two polarization-maintaining, high-power fiber amplifier. **b)** Schematics of the available excitation sources. The direct excitation (Path 1 and 3) is used for SHG, SFG, and 2PE imaging. Super-continuum generation at 1053 nm is achieved in a PCF (Path 2) and serves as probe pulse for FWM/CARS applications. The white light is chirped in an SF6 glass rod for spectral focusing. Legend: AOM: accusto-optical modulator; CCU: cross-correlation unit; $\Delta\tau$: internal temporal delay unit; DM: dichroic mirror; FM: flipping mirror; GDD: group-dispersion delay unit; PCF: photonic crystal fiber; POL: polarizer; $\lambda/2$: half-wave plate; PPLN: periodically poled Lithium Niobate crystal; SAM: saturable absorber mirror; SF6: Schwer-Flint 6 (SF6) glass rod. Figure adapted from [81].

Nonlinear excitation laser

The nonlinear modalities FWM and CARS require two pulsed laser sources, synchronised in time and space. For such a purpose, the company Toptica Photonics developed a dual-color, femtosecond laser source prototype named *FemtoFiber dichro bioMP*. Figure 3.5a displays the internal architecture of the laser. An erbium (Er) doped fiber oscillator seeds a ytterbium (Yb)- and a second erbium- doped fiber. The former produces a laser line centred at 1053 nm, while the second laser line emits at 774 nm. Since both laser lines are based on the same oscillator the emitted pulses possess the same repetition rate (80 MHz) and an initial intrinsic temporal overlap. To control the temporal overlap at

the sample the 774 nm laser line is equipped with a delay stage, allowing a temporal delay of the pulses of up to 500 ps. The output power can be adjusted by two acusto-optical modulators (AOMs). A group dispersion delay (GDD) unit, consisting of a series of chirped mirrors, can be applied to adjust the temporal shape of both laser pulses. The maximum average output power is ca. 1 W and 1.5 W for the 774 nm and 1053 nm outputs, respectively, with pulse durations of ca. 180 and 135 fs (figure 3.5b, paths (3) and (1)). To adjust the linear polarization angle and the power on the table in front of the microscope both laser lines pass a lambda half-wave plate ($\lambda/2$) and a polarizer (Pol). A more detailed description of the laser can be found in the supplementary information of the publication to project 1 (section 4.1).

CARS signals can only be created when the difference in energy between two light fields matches the energy gap of a Raman transition. Therefore, the spectral difference between the laser lines defines the Raman band(s) that can be addressed with CARS. To switch the CARS between specific Raman bands in a Raman spectrum of a sample, one of the laser fields need to be spectrally broad while the other has a fixed wavelength. This was achieved, by coupling the 1053 nm laser line into a photonic crystal fiber (PCF) for super-continuum generation between 740 and 1100 nm (figure 3.5b, path (2)). The output beam from the PCF will be addressed in the following as the probe beam, while the laser line at 774 nm acted as the pump beam accordingly. To distinguish between Raman bands of a sample, we need to control the interacting spectral components of the probe and the pump beam. If all spectral components of the probe beam would interact with the pump beam at the same time the resulting image would be an overlay of all Raman bands present and no longer be specific for just one Raman band of interest. By inducing a strong positive chirp in the probe (here, by a 20 cm SF6 glass rod), the probe beam is stretched from $\sim$450 fs to $>$15 ps, while the pump beam possess a length of 180 fs. By tuning the temporal overlap of the two beams different spectral regions of the probe beam can be tuned to interact with the probe beam and thereby addres different regions in the Raman spectrum for CARS imaging (see figure 3.6). This spectral focusing approach [120] provides a theoretical resolution of $\sim$25 cm^{-1} over the full CARS spectrum.

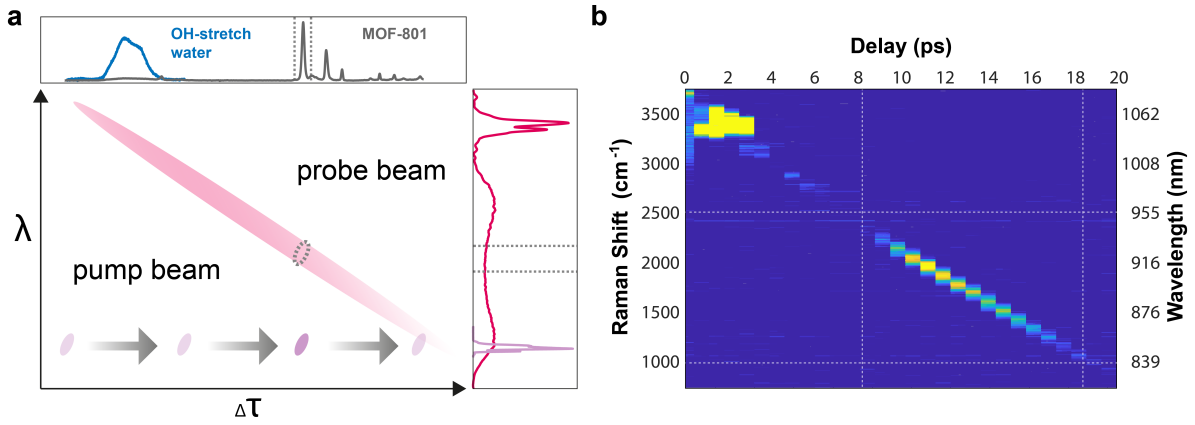

Figure 3.6.: Spectral focusing defines spectral resolution in CARS microscopy. **a)** Schematic of spectral focusing as function of the wavelength (λ) against relative delay between the probe and pump beam ($\Delta\tau$). The probe beam possess a broad spectrum and is strongly chirped. By delaying the pump relative to the probe (grey arrows), different spectral regions of the probe beam are interacting (dotted circle, dotted lines in right panel). The targeted spectral region of the sample Raman spectrum can be selected (indicated by dotted lines in upper panel). **b)** Temporal behaviour of the super continuum derived at 1053 nm after a 20 cm SF6 glass rod.

Confocal detection and image construction

For lifetime acquisition, it is necessary to implement fast detectors with single-photon sensitivity. We decided on two avalanche photodiodes (APDs, Count Blue / Count Red; LaserComponents), one optimized for the blue to green region of the spectrum and one for the red to NIR region. While other types of photodiodes possess a more defined instrument response function (IRF) and are therefore superior in the detection of short lifetimes, APDs provide the highest dynamic range of all available single-photon counting detectors. In addition, the selected APDs have an automatic safety shut-off, protecting the detection electronics against damage at high count rates. This was a necessary requirement for our detectors, since the non-linear modalities require very high photon-flux and can create large signal strength in some materials (especially for FWM).

The APD signals are collected by a time-correlated single photon counting (TCSPC) card. The basis of TSCPC is the determination of photon arrival times with respect to an external clock. The external signal is connected to the pulse rate of the excitation laser source. The laser sends a start signal to the TCSPC card when releasing a pulse. The card then counts the time until a photon arrives and converts it from an analogue into a digital signal, the number of internal ticks n_{int}. It stores this information and resets for the next photon. Since the internal binning size Δt_{int} is a known constant the photon arrival time after sample excitation, the so-called *Microtime*, can be calculated. Additionally, the number of external clock ticks since the start of the experiment n_{ext} is recorded. By determining the excitation laser repetition frequency f_{rep}, one can calculate the total photon arrival time relative to the start of the experiment, termed the *Macrotime* as:

$$Macrotime = \frac{n_{ext}}{f_{rep}} + n_{int} \cdot \Delta t_{int} \tag{3.1}$$

Since the storage buffer on the card is limited, the main program has to constantly read and save the data from the TCSPC buffer. For every detected photon, a Microtime and a Macrotime are available. The Microtime histogram of all photons from a region of interest allows one to determine the lifetime (see section 2.2.1. When the scanning timing is precisely known, we can calculate when the stage arrives and leaves a certain pixel relative to the start of the measurement. This allows us to sort all photons into the corresponding pixels based on their Macrotime. By combing the two pieces of information lifetime imaging is possible. In our system, we implemented the dual-channel TCSPC card TH260 pico dual from PicoQuant.

There are two main challenges regarding the image reconstruction when raster-scanning. The first is a timing uncertainty induced by the execution time of the code by the software. While the scanning code written in Labview 2018 (National Instruments) is deterministic, the surrounding C# (VisualStudio 2010, Microsoft) code is not. This results in an uncertainty in the exact measurement start, leading to a constant pixel shift within one frame and a variable pixel shift between the frames. This is solved, by inserting artificial photon signals as markers into the recorded photon stream by the scanning program itself. This marker signals can be inserted either at the start of a frame, the first pixel of every line, at every pixel, or in any combination thereof. For high accuracy without overloading the photon stream, we usually apply frame and line marker signals. The artificial photons are marked by a special event marker in the stream, making it possible to create a precise pixel time map and rduce the distortion in the image. Figure 3.7 displays an example with and without line markers.

Figure 3.7 also displays the second challenge during image acquisition: while the piezostage is very accurate in movement precision, it's response time is relatively slow. Every line is scanned from the left side of the image in figure 3.7 to the right side. The image construction routine already starts the acquisition for the first pixel of the next line while the stage is still in transition to the start. The result is the highly condensed mirror image on the left border of the right panel in figure 3.7. In addition, the movement response of the piezo-crystals to changes in applied voltage is nonlinear in the beginning of a new movement. This causing an additional "stretching" on the left side of the image even at moderate scanning times. Both are a well known artefact of piezostages and is usually dealt with by just omitting the affected region. We also applied this approach, since we already planned to upgrade to galvanic mirrors for faster 2D scanning. They can reach significantly faster imaging times without causing major distortions in the image. The galvanic mirrors are currently implemented onto the microscope.

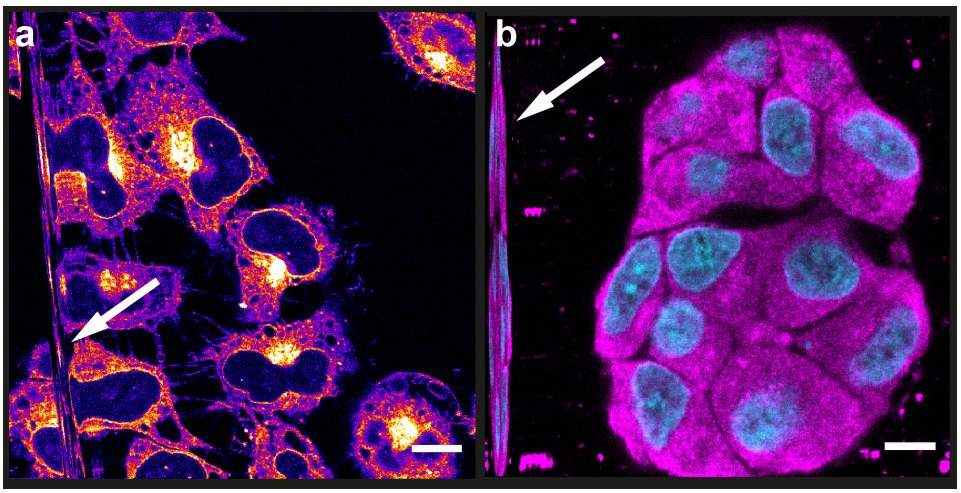

Figure 3.7.: Influence of line marker signal on raster scan images. **a)** HeLa cells, stained with WGA488 (Image taken by Simon Wanninger) without line start synchronisation. The delay at line start times is variable even between frames. A removal of the artefact (white arrow) is very challenging, a comparability between scan images cannot be guaranteed. **b)** 2PE images of HeLa cell cluster, nucleus stained with Hoechst dye (cyan) and cytosol with Alexa Fluor 647 (magenta). Acquisition and scanning are synchronized at every line start. The artefact is confined to the left image border and can be easily removed. Scale bars 10 µm

Spectrometer

An electronic flip mirror changes the detection path from the APDs to the spectrometer. To ensure the maximum detection efficiency, the f-number of the spectrometer needs to be matched. The spectrometer is a Kymera 328i from Andor, with a f-number of 4.1. The focal length f_{lens} of the lens for focusing into the spectrometer was chosen to be 30 mm. The relation to the f-number is defined by equation 3.2 [118]:

$$f = \frac{f_{lens}}{d_{beam}} \tag{3.2}$$

To match the f-number, we implemented a telescope system to adjust the beam diameter d_{beam} of the light emitted from the focal volume. In addition, a set of notch filters, one for each possible Raman excitation laser, was implemented on a variable filter wheel in front of the spectrometer. The spectrometer has a Czerny-Turner design, with three gratings and a silver mirror on a rotatable turret. We chose blazed gratings, optimised for 500 nm (Raman excitation at 532 nm). The gratings have 300, 600, and 1200 lines/mm corresponding to spectral resolutions of 15.4, 8.1, and 6.0 cm^{-1} for the Raman band of a silica wafer at 520 cm^{-1}. A grating with higher lines per mm will not significantly enhance the spectral resolution since the detector pixel size becomes the bottleneck. Therefore, we did not include a 1800 lines/mm grating. As a general approach, the grating was selected according to the sample requirements: for high quality spectra of unknown substances, we choose the 1200 lines/mm, while, for fast spectra where a good signal to noise ratio was crucial, the 300 lines/mm grating was selected. The flexibility regarding grating and excitation wavelength makes the spectrometer a

robust and sensitive device well suited for our platform.

An electron-multiplying charge coupled device camera (emCCD camera) was chosen as the detector for the spectrometer. The camera is an Andor iXon 512 emCCD from Andor with a 512x512 pixel grid as the detector. emCCD cameras allows for a detection with very high sensitivity even at relatively fast frame rates, well suited for our purpose. As a trade-off for the boost in sensitivity, however, a multiplicative noise is induced by the amplification mechanism. The result is a non-linear background in the collected spectra, that can be reasonably well described by a quadratic function. Since the background is (mostly) dependent on the chosen settings (mainly gain and acquisition time), subtracting the spectrum of a region on the sample slide without the substance of interest was usually sufficient to correct for the multiplicative noise. When the exact Raman peak strength was crucial, for example for the quantitative analysis in chapter 4.2, we fitted the spectral regions without Raman peaks with a quadratic function and subtracted the background prior to further analysis. This extended procedure negated the influence of multiplicative noise and enabled the quantitative determination of guest molecules in host frameworks.

Software
Image acquisition on the MOSAIC platform is controlled by a home-written software in C#, based on a software package from the group called *FabSurf*. Since precise timing and analogue output is non-ideal in C#, we implemented a *Field-Programmable Gate Array* (FPGA, cRIO-9063; National Instruments) for the stage control, programmed in Labview. The Labview program controls scanning and timing of the imaging modalities, based on the intrinsic timing of the FPGA. I implemented a variety of scanning options, including automated Z-stacks for 3D images and hyperspectral Raman imaging. The Labview code is implemented in the C# framework as a *dynamic link library* (dll). TCSPC data handling and saving is performed in C# and saved in a custom-desined format. The TCSPC data analysis is performed in PAM [121], a Matlab (Matlab 2018b, The MathWorks, Inc; Natick, MA, USA) based software, developed by the group. It allows to add custom read-in routines, to import our specific file format in the software and convert the recorded photon-stream into image files. In addition, the lifetime information per pixel is calculated. With the developed software the Phasor FLIM analysis for project 5 (section 5.3) was performed. Exported images could then be analysed with Image J [122].

All spectra were recorded with the Andor Solis software package *Andor Solis for Imaging V4.30* (Oxford Instruments). As described, the spectrometer is a Kymera 328i with an Andor Solis iXon 512 emCCD camera as the detector. The camera requires a specific hardware PCI card for the read-out, that could not be implemented on Windows 10 due to the unavailability of the correct drivers. Therefore, all spectra needed to be recorded on a different computer running Windows 7. This posed a challenge for the implementation of hyperspectral Raman imaging, since direct communication between a commercial program on Windows 7 and our home-written in Windows 10 is not possible.

The problem was solved by direct communication between the FPGA and the camera detector. The contribution of the program of the spectrometer is written in Andor Basic, a programming language created for Andor Solis. Spectra are saved as plain text and analysed with home-written programs in Matlab (Matlab 2018b, The MathWorks, Inc; Natick, MA, USA). This made it possible to customize the spectrum analysis. For example, the analysis software for the quantitative water uptake, is automatized by one Matlab function for ease of execution and can be implemented in other Matlab based software routines.

The software necessary just for controlling the main MOSAIC platform spans over two computers (Windows 10 and 7), three programming languages (C#, Labview, and Andor Basic), and two separate programs (FabSurf and Andor Solis for Imaging). This was necessary due to how the project developed but is not the ideal basis for a robust and easily expendable platform. Therefore, we already laid the groundwork for a Labview based replacement.

In summary, the spectral design was chosen in a way that the nonlinear spectral signatures are detected in the UV/VIS/NIR range of the spectrum, for a high compatibility with common live cell fluorescence imaging measurements. All imaging modalities were combined on a single confocal microscope platform, which was extended to include Raman spectroscopy. The technical realization of the design, while challenging, relied on common and robust techniques. This allowed us to adapt the developed MOSAIC analysis platform with ease to new sample requirements while still allowing high control over the triggered light matter interaction. Spatial control over the sample in combination with the correlated modalities enables the study of complex sample systems as described in the motivation. The following chapters 4 and 5 of this thesis presents five projects over a variety of sample systems, where the different modalities of the MOSAIC analysis platform were applied.

Chapter 4.

Adsorption in Metal-organic Frameworks

The MOSAIC analysis platform is capable of the combined chemical and spectral characterization of synthetic materials *in situ*. To highlight the potential of the platform for material science, correlated investigations of metal-organic frameworks (MOF) were performed. The field of synthetic materials was accelerated by the recent advancements in reticular chemistry, especially with the development of MOFs. The number of publications regarding MOFs has been growing rapidly since the first publication in 1995 [49], from only 37 publications in the five years till 2000, up up until >27500 in the following two decades [51]. While the number of reported frameworks is steadily growing, their characterization on the single-particle level is limited. Typical characterization methods either look at the nanometer scale or the bulk material [51], rendering the study of the influence of particle heterogeneity on the material properties challenging. Since MOF nanoparticles are a promising tool for a myriad of applications, such as drug delivery [123–125], water harvesting [126–128] or catalysis [129], the potential of multimodal analysis on the single-crystal level was demonstrated for the selected MOF systems UiO-67, MIL-88A, and MOF-801. For the study of the water harvesting MOF system MOF-801, there is currently no quantitative, single-particle sensitive method available to compare crystal properties directly to the bulk performance. In the follow-up publication, such a methodology was developed based on Raman spectroscopy.

4.1. Project 1: "*Single Crystals Heterogeneity Impacts the Intrinsic and Extrinsic Properties of Metal-Organic Frameworks*"

In this work, a multimodal, optical micro-spectroscopy platform for unveiling particle diversity-property relations was presented. UiO-67 was studied, applying all available optical modalities of the MOSAIC platform. For the drug-delivery system MIL-88A, we correlated the extrinsic property of light absorption with the crystal morphology. For the water harvesting material MOF-801, we applied a combination of four different modalities (Raman, FWM, CARS, and 2PE) to reveal the nature of the defect sites responsible for localized water clusters. The results were published in the following work:

Fuchs, A., Mannhardt, P., Hirschle, P., Wang, H., Zaytseva, I., Ji, Z., Yaghi, O., Wuttke, S.*, Ploetz, E.*, **Single Crystals Heterogeneity Impacts the Intrinsic and Extrinsic Properties of Metal–Organic Frameworks.**, *Adv. Mater.* 2022, 34, 2104530.

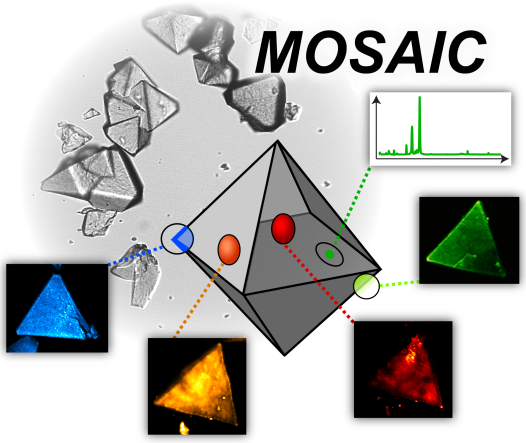

Figure 4.1.: Overview over the methods applied for single-particle analysis of MOFs combined on the MOSAIC analysis platform. Figure adapted from [81].

Motivation and key results

To highlight the feasibility of the developed microscopy platform for MOF systems, a multimodal study of UiO-67 was performed. UiO-67 consists of $Zr_6O_4(OH)_4$ clusters connected with biphenyl-4,4'-dicar-boxylate (BPDC) linkers. The single crystals are colorless and have an octahedral shape with pronounced triangular faces. They can be labelled with RBITC for fluorescence imaging [62], but exhibit also a small amount of auto-fluorescence themselves. Additionally, they only show minor absorption in the VIS to NIR range, making them well suited as a sample system for proof-of-concept experiments with multimodal imaging.

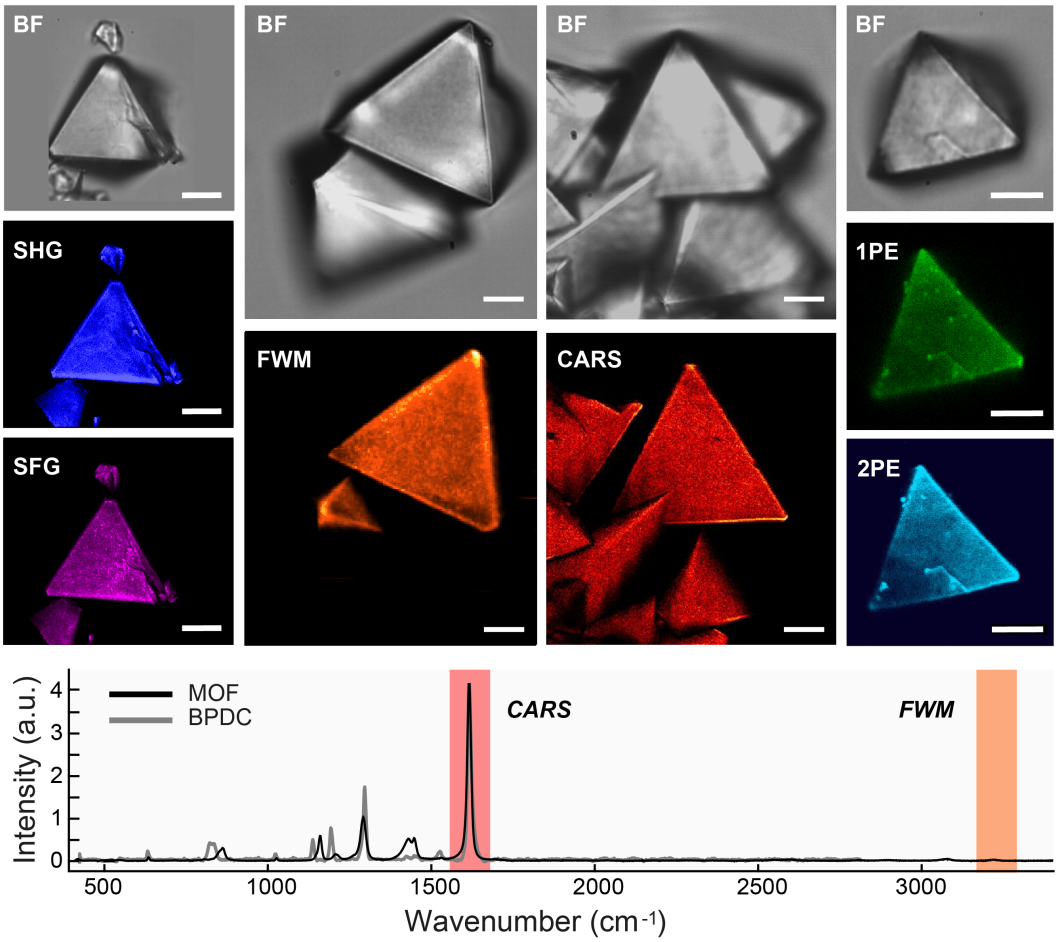

Figure 4.2.: Multimodal analysis of UiO-67 particles. Unlabeled UiO-67 particles imaged by bright field (upper panels, grey) and nonlinear microscopy (middle panels), including SHG and SFG, FWM at 3300 cm^{-1} (616 nm), and CARS at 1615 cm^{-1} (688.2 nm). The right panels show BF (grey) and fluorescence images of RBITC-labeled particles after 1PE and 2PE excited at 532 nm and 774 nm, respectively. Scale bars: 10 μm. Spontaneous Raman signature of UiO-67 particles and their linker molecule biphenyl-4,4'-dicarboxylate (BPDC) in the solid state phase (bottom panel). The spectral regions chosen for FWM and CARS imaging are marked in red and orange, respectively. Figure adapted from [81].

Figure 4.2 displays UiO-67 crystals investigated with the implemented imaging modalities and Raman spectroscopy. The spectral regions selected for FWM and CARS are highlighted in the Raman spectrum. The spatial resolution, relative signal strength, and spectroscopic signatures of the modalities corresponded very well with what was expected. All crystals emit uniform signal intensities over the particle areas indicating a high crystallinity. Cracks and defect sites are visible especially in the surface specific images created with the modalities SHG, SFG, 1PE, and 2PE.
After we demonstrated the general suitability of the MOSAIC approach for MOF sys-

tems exemplary on UiO-67 crystals (see chapter 3), we studied the effect of heterogeneity on selected extrinsic and intrinsic properties of MOFs. Extrinsic properties are defined by particle topology and morphology, physical attributes of surface structure, shape, and size. The chemical properties of the framework constituents define the intrinsic properties. Variety in the intrinsic properties can be caused by defect sites or changes in crystallinity, or by design such as in multivariant MOF systems.

MIL-88A particles are frequently employed for sensing [130] and drug delivery [123–125], due to their excellent biocompatibility. The iron metal centers of MIL-88A are known to quench fluorescent markers making label-free imaging of the particles a necessity for tracking them in biological systems. For this, the interaction with strong, pulsed laser sources needs to be investigated. For live-cell 2PE imaging and tracking NIR laser sources are typically applied. MIL-88A crystals showed no absorption in the NIR wavelength regime. As they are dielectric materials, no strong plasmonic interaction can occur. Therefore, the absorption of the particles is dictated by Mie interaction [131–133]. Mie absorption occurs when a particle is similar in size to the wavelength of the light field. While imaging crystalline microparticles of MIL-88A with FWM we observed that absorbing particles degraded and emitted a strong chemiluminescence (CL). The multimodal images allowed us to correlate the shape and size of the crystals to their absorption behaviour. Surprisingly, when studying the heterogeneous crystals, we found a clear correlation between CL after adsorption and the crystal shape, but no significant correlation to the actual size. Employing the fact, we showed that one can tune the absorption threshold of micrometer MIL-88A crystals based on their shape alone, which enables potential sorting of heterogeneous particle batches.

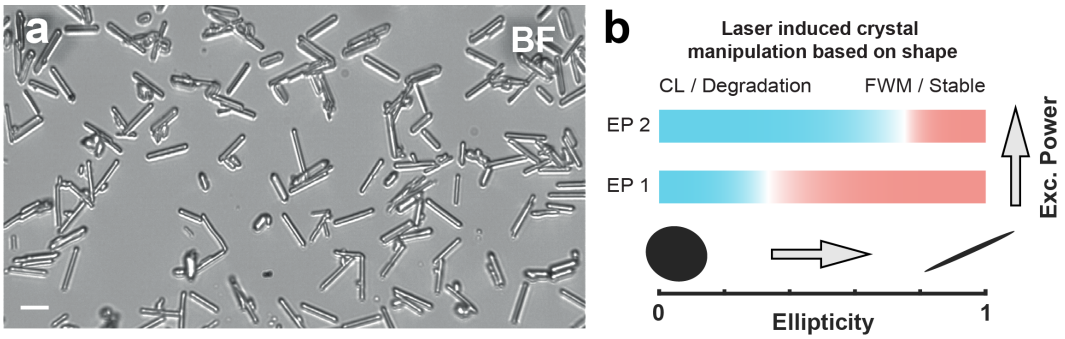

Figure 4.3.: Optical behavior of MIL-88A crystals for different morphologies. **a)** A BF image of MIL-88A crystals shows a wide distribution in ellipticity and size. **b)** Schematic of the observed correlation between CL and ellipticity depending on the excitation power at EP1 = 1.9 mW. An increase in excitation power (EP2 = 3.0 mW) shifts the absorption threshold to higher ellipticities, resulting in increased CL also for needle-like particles. Figure adapted from [81].

The third MOF particle-property relation study that was presented in the publication, was the influence of defect sites on MOF-801 water adsorption. MOF-801 is a promising

material for atmospheric water harvesting. The shortage of clean water sources is an impending problem and is becoming more threatening year by year with the increase in world population [134]. Possible solutions, such as large-scale desalination or deep water reservoirs, are cost expensive to set up and maintain, limiting their wide spread application especially in regions with low infrastructure. A possible alternative is provided by harvesting water out of the air [134]. Large quantities of clean water can potentially be gained directly from the atmosphere [135], bypassing the need of setting up large infrastructure for clean water extraction and distribution. The efficiency of these atmospheric water harvesting (AWH) devices is strongly dependent on the water harvesting material in combination with the surrounding climatic conditions, especially temperature and relative humidity (RH). MOF-801 is one of the most applied materials for this task [126–128]. The development of MOF based AWH materials is based on understanding the water uptake and release mechanism and the tuning the composure of the material on the crystal structure level [136]. Heterogeneities caused by defect sites can drastically alter the uptake behaviour, jeopardizing the desired performance [137]. By applying correlated FWM and CARS imaging, we found an uneven distribution of water over a cluster of MOF-801 single crystals. With fluorescence and FWM imaging, we could exclude missing linker defects as the sole source of the uneven distribution. By recording Raman spectra of the water cluster sites and comparing them to the regular single crystal spectra, we found clear indication for missing metal cluster defects in the difference spectra. This correlation could only be accessed by a multimodal approach demonstrating the power of MOSAIC microscopy for the MOF community.

Outlook

The study of particle diversity-property relations with the presented correlated multimodal analysis platform can be extended to a wide variety of MOF systems. It proved especially beneficial for the study of sorption processes, where guest molecules are interacting with the metal-organic framework, and to investigate the interaction of MOF crystals with light. Due to the high active surface area per volume in combination with the high flexibility in functionalization, MOF systems are prominent in many applications with guest-host interactions, most notably CO_2 capturing and storage [11]. Regarding light-matter interaction studies, a current research direction is the development of MOF up-conversion nanoparticles [138]. Based on the presented results from this publication, MOSAIC analysis can be a powerful tool in characterizing materials from these fields of research and unveil the influence of heterogeneity on these materials.

4.2. Project 2: "*Water harvesting at the single crystal level*"

While defect sites in MOF-801 crystals could be localized and identified in the previous publication, their the influence on the performance of the water harvesting process could not be quantified for this sub-micrometer regime. To this end, we expanded the available toolbox in combination with the MOSAIC in this follow-up project. It presents a novel methodology based on Raman spectroscopy that enables us to acquire single-particle water adsorption isotherms and kinetic curves with sub-micrometer resolution. With this technique, the influence of intra- and inter-particle effects on the water harvesting performance of MOF-801 could be unveiled. We found a significantly faster kinetic on the single-crystal level, compared to the bulk material. FWM and CARS imaging revealed inter-particle condensation as the main source for this difference. The upper limit of a MOF-801 crystal performance could produce around 91.9 $L/kg_{MOF}/day$, which is more then 360 times higher then previously reported water harvesting prototypes in literature [127, 128]. The results are summarized in a manuscript, which is currently under review:

Fuchs, A., Wang, H., Ji, Z., Knechtel, F., Wuttke, S., Yaghi, O.*, Ploetz, E.*, et al., **Water harvesting at the single crystal level.**, *submitted manuscript* 2022.

Motivation and key results

In the previously presented publication (project 1, section 4.1), we visualized and qualitatively studied the effect of heterogeneity on water uptake. The quantitative influence on the performance of the material could not be determined simply because there is currently no method available for quantitative water sorption characterization with sub-micrometer resolution. The water harvesting performance of a material is determined in bulk. Differentiating between the material performance and alterations induced by intra-particle effects, like defect sites and multi-crystalline areas, and inter-particle effects, like condensation between particles, is therefore not possible. Raman spectroscopy enables substance specific analysis with sub-micrometer resolution as well as quantitative analysis, since Raman scattering scales linearly with the concentration. Based on this premise, we developed a Raman-based methodology to quantitatively extract the uptake of water in single crystals as volume per mass MOF. MOF-801 single crystals were characterized, extracting isotherms and kinetic curves and compared them to defect-rich crystals and bulk measurements. While intra-particle effects had relatively little influence isotherms and kinetic curves, the bulk material showed an at least 20 times decrease in kinetic rate compared to a regular single crystal. Multimodal imaging revealed the formation of inter-particle layers of liquid water in the bulk during a ad- and desorption cycle. The liquid water not only hinders the efficient exchange of humid and dry air of the nearby crystals, but can also not be recovered on the same fast time scale as the gaseous water molecules absorbed in the crystal pores. To quantify the influence of the effects, we performed adsorption / desorption cycles in a single crystal of MOF-801 at the upper limit of the materials performance capability (160 s cycling time). The measurement

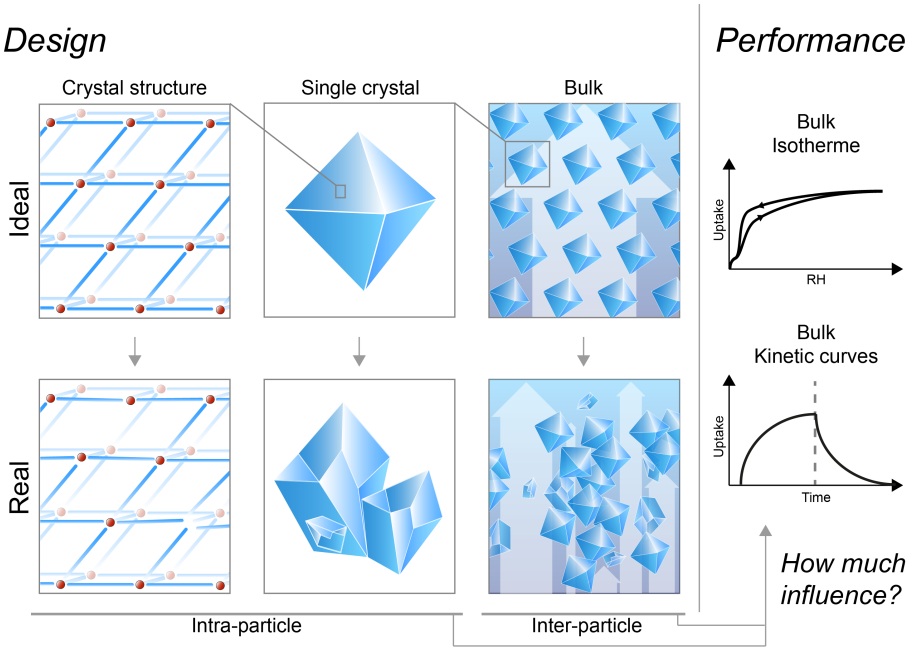

Figure 4.4.: Design and performance evaluation of atmospheric water harvesting MOF materials. A schematic representation of intra- and inter-particle effects in MOF materials that can influence the performance of the bulk material regarding uptake at a certain temperature (isotherm) as well as ad- and desorption kinetics. To quantify the influence of these effects one would need to directly compare the performance of a regular single crystal (middle, top panel) to the (real) bulk material (lower,right panel).

revealed a potential maximum harvest of 91.9 L/kg$_{MOF}$/day instead of the previously reported 0.1 and 0.25 L/kg$_{MOF}$/day in published prototypes [127, 128].

Methods

For investigating water uptake in single MOF-801 crystals as $\frac{V_{H_2O}}{m_{MOF}}$, it was needed to control the relative humidity (RH) around the sample and then to develop a methodology for the quantification of the number of water molecules per MOF unit. The former was achieved by a home-built gas mixer, the later by a ratiometric analysis of spatially resolved Raman spectra. Figure 4.5a shows the implementation of a unit to control the relative humidity around the MOF-801 crystals on the MOSAIC platform. Raman spectra were acquired after excitation with the 532 nm cw laser. Direct integration over the Raman peak corresponding to the OH-stretch vibration results in an unexpected heterogeneity over a regular single crystal (figure 4.5b). The reason for this heterogeneity is a difference in scattering properties at the crystal interfaces, altering the peak intensities (see figure 4.5c). The ratio of the OH-stretch peak strength (A_{OH}) of water to the CH-stretch of the framework (A_{CH}) is independent from the scattering and uniform throughout the crystal (figure 4.5e). It is only dependent on the amount of water molecules per unit cell MOF-801, $N_{H_2O}(RH)$.

The ratio $\frac{A_{OH}}{A_{CH}}$ is connected to the volume water uptake $\frac{V_{H_2O}}{m_{MOF}}$ by the density of the dry

MOF material ρ_{MOF}, and a constant scaling factor, specific for the material Γ:

$$\frac{V_{H_2O}}{m_{MOF}} = \frac{A_{OH}}{A_{CH}} \cdot \frac{1}{\rho_{MOF}} \cdot \Gamma \tag{4.1}$$

The density of MOF-801 is known from literature [128]. To determine the scaling factor Γ, a fit function for $N_{H_2O}(RH)$ was derived using literature values [128]. The conversion factor between the fit function and the volume water uptake, $\frac{V_{H_2O}}{m_{MOF}}$, was determined to be 8.22:

$$\frac{V_{H_2O}}{m_{MOF}} = N_{H_2O}(RH) \cdot 8.22 \tag{4.2}$$

Since the ratio $\frac{A_{OH}}{A_{CH}}$ is also only dependent on $N_{H_2O}(RH)$, Raman spectra of MOF-801 crystals were recorded for a variety of different RH values and the curve was fitted to determine the conversion factor f_{fit} (figure 4.5f):

$$\frac{A_{OH}}{A_{CH}} = N_{H_2O}(RH) \cdot f_{fit} \tag{4.3}$$

The general conversion factor Γ could be determined by combining equations 4.1 to 4.3:

$$\Gamma = \frac{8.22 \cdot \rho_{MOF}}{f_{fit}} = 0.0938 \pm 0.0041 \tag{4.4}$$

The standard deviation of the fit was found to be in the range of the intrinsic noise of the measured Raman spectra. By applying equation 4.1 to measured Raman spectra, we are able to obtain the single-crystal water sorption performance of MOF-801 (figure 4.5g).

Outlook

The presented methodology can be easily applied for quantitative monitoring of similar guest-host interactions in MOF systems other than water uptake, for example the characterization of heterogeneity in CO_2 or H_2 storage in MOF materials [12, 139]. In combination with localization and identification of defect sites in materials, the developed microscope enables the qualitative and quantitative characterization of the influence of defects in the sorption processes.

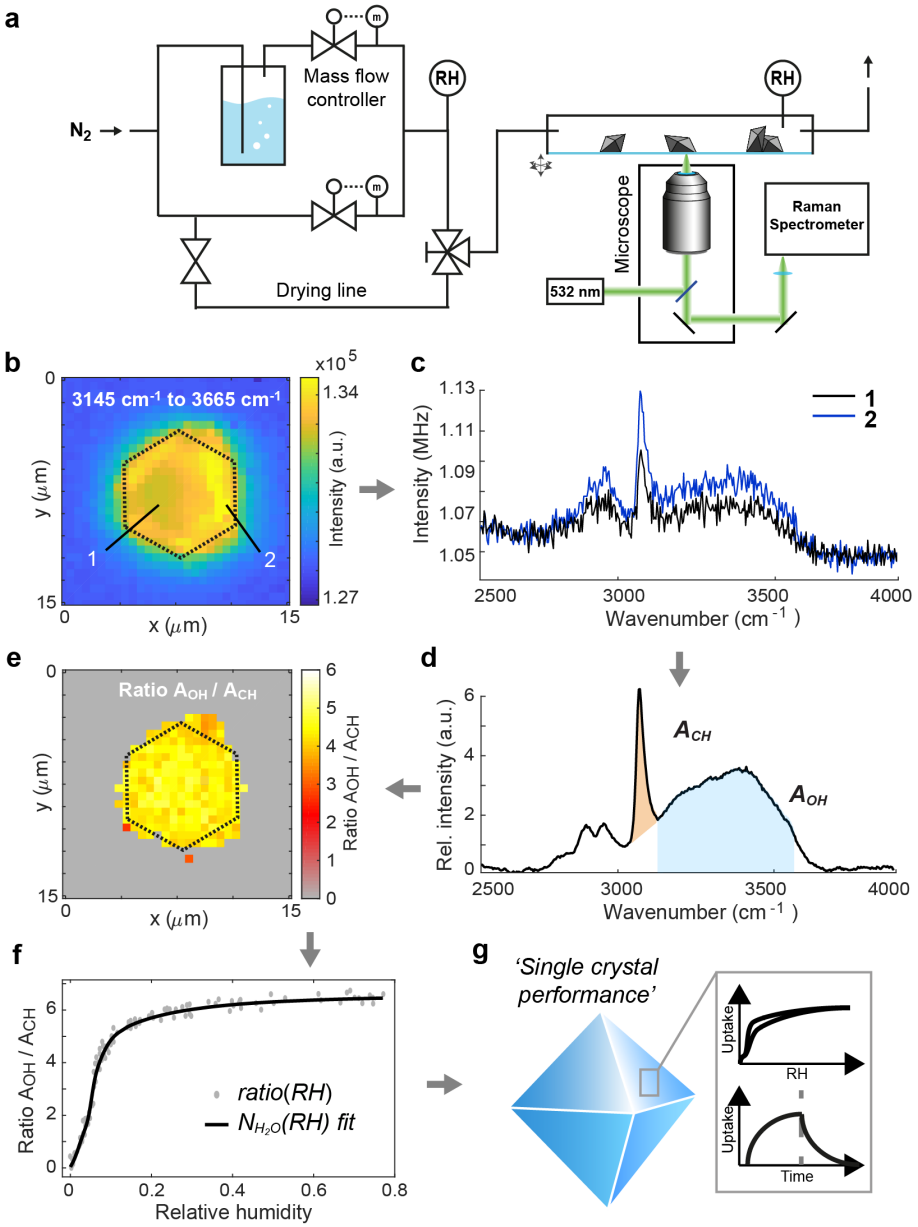

Figure 4.5.: Quantification of water uptake in MOF-801 at the single crystal level by Raman spectroscopy. **a)** A schematic of the micro-spectroscopy setup with a unit for controlling the relative humidity over the sample. RH: relative humidity measuring stations. **b)** Univariate analysis of a hyperspectral Raman data set in the water OH—stretch region reveals an irregular water distribution in a regular single crystal of MOF-801. the crystal border in the measurement plane is indicated as a dotted line. Raman mapping was carried out using 5 s integration time. The scanning range was 20 x 20 μm with 40 pixels per line. **c)** Raman spectra of selected pixels marked in (b). **d)** the background corrected, mean spectrum over all pixels inside the crystal border is shown. The strength of the CH- (orange) and the OH-stretch vibration (blue) are indicated as the area under the graph. **e)** The ratiometric representation A_{OH} / A_{CH} calculated per pixel for the Raman data set in (b) shows a uniform water distribution. **f)** The ratio A_{OH} / A_{CH} at varying relative humidities between 0 and 77 %RH recorded for 7 regular single crystals (grey points) is shown. By fitting the data set, it becomes possible to determine the number of water molecules per unit cell, i.e. N_{H_2O} (RH). This allows us to get the quantitative water uptake with sub-micrometer resolution. **g)** A schematic summary of the single crystal performance analysis.

Chapter 5.

Localization and Identification of Uptaken Material in Biological Systems

The selected modalities combined in the MOSAIC analysis are equally suited to study uptake processes *in vivo*. The microscopy platform allows for the simultaneous fluorescent and label-free characterization of biological systems. In addition, it provides the sensitivity to study uptaken material, for example small molecules like water (as discussed in the previous chapter), inorganic particles, but also dinucleotides or proteins (as we will present in this chapter). To demonstrate the suitability of the developed microscopy platform for the study of biological systems, we pursued three different projects. The sample systems range from large tissue sections over cell spheroids to single cells and show the sensitivity and capability of the implemented imaging modalities.
First, unlabeled sponge samples from the Indonesian Sea were examined for microparticulate pollutants. 3D, label-free, 2PE induced autofluorescence imaging of large tissue sections was performed to determine the location of uptaken, inorganic particles. It was combined with Raman spectroscopy to distinguish between naturally occurring particles and anthropogenic microparticluate pollutants. Next, the role of YAP in the cancerous growth of cell spheroids was studied with multiplexed fluorescence imaging. Simultaneous 1PE and 2PE imaging of large HeLa cell spheroids in the millimeter range, revealed that the translocation of YAP to the nucleus causes cancerous growth. In the third project, we investigated the synthetic dinucleotide cthGAMP on the single-cell level. cthGAMP, a fluorescent analogue of the important innate immune response messenger cGAMP, was localized with a combination of 2PE imaging and Phasor-FLIM in THP1 cells. These projects demonstrated the feasibility of MOSAIC also for advanced fluorescence imaging methods.

5.1. Project 3: *"Sponges as bioindicators for microparticulate pollutants?"*

Quantifying the extent of oceanic microparticluate pollutant stress is challenging due to the small particle size. In this work, sponges were studied for their suitability as unbiased microparticle filters. 2PE imaging combined with Raman spectroscopy was applied to localize and identify microparticluate pollutants in sponge tissue collected in the Indonesian Sea. The results indicate the high potential of sponges as bioindicators for microparticulate pollutants around the world and are presented in the following publications:

Girard, E., Fuchs, A., Kaliwoda, M., Lasut, M., Ploetz, E., Schmal, W., Wörheide, G.*, **Sponges as bioindicators for microparticulate pollutants?**, *Environmental Pollution* 2020, 268, 115851.

The results were also summarized in German for the journal *Laborpraxis* in 2021 under the title: **Schwamm drüber? Schwämme als Bioindikatoren für Mikroplastikverschmutzung in Gewässern.**

Motivation and key results

Man-made pollution of the world's oceans is bearing an increasing threat to our planet. Current countermeasures against oceanic waste pollution mainly target macro-sized pollutants (plastic waste, such as bags and wrappings). The micron seized pollutant particles, however, are more challenging to address since they are difficult to detect due to their small size. To map the distribution of microparticulate pollutants one would need a set of microparticle filters distributed worldwide. Despite the fact that it would be technically challenging and very expensive, there is already a possible alternative: *Phylum Porifera*, the common sponge is geographically widely spread and can be found near almost any coast [141]. All sponges incorporate micrometer seized particles to stiffen their structure [142]. Assuming the uptake is only based on particle size, a sample of sponge tissue could reveal the microparticle composition of the surrounding environment and provide insight into the local microparticulate pollutant stress level.

In collaboration with the group of Prof. Wöhrheide we investigated whether sponges are suited as bioindicators for man-made microparticulate pollutants. 15 sponge samples, belonging to three different sponge species, were collected around Bangka Island (North Sulawesi, Indonesia, figure 5.1(1)). Thin slices (around 170 μm) were prepared (2) and histologically analysed to identify the sponge species (3). BF and 2PE induced autofluorescence imaging were used to localize inorganic particles in the sponge tissue (4). For fast, high statistical analysis the organic components of the collected samples were dissolved and the remaining inorganic particles identified and quantified using Raman

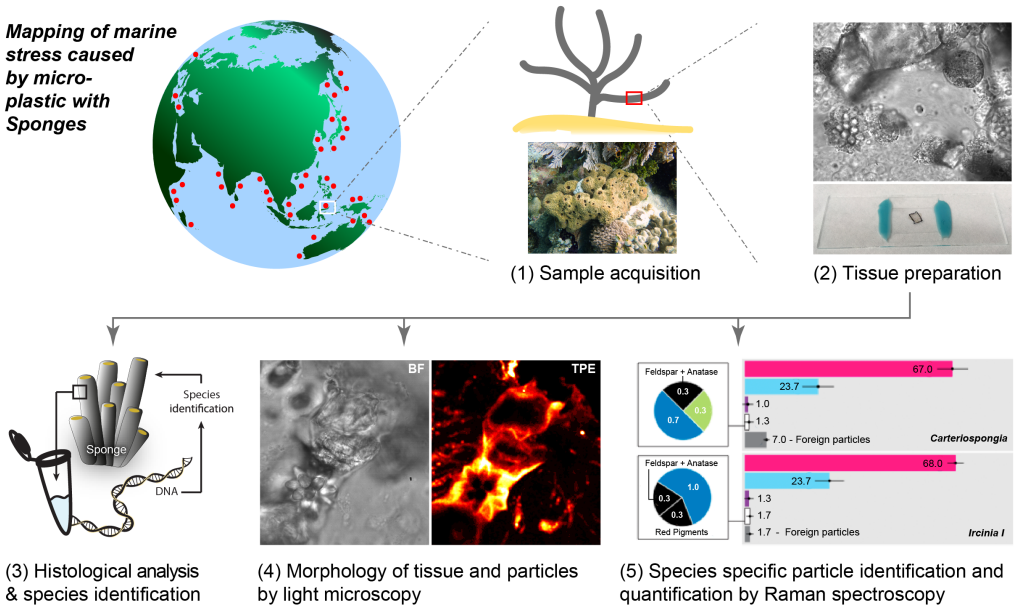

Figure 5.1.: Work flow for characterizing the local microplastic pollution with sponges. On-site acquiesce of local sponge tissue (1) and preparation for further analysis (2). First, the sample is classified according to its morphology, species and histology (3). Inorganic particles in the tissue are localized using light microscopy (BF and 2PE) (4). Finally, the inorganic particles are separated from the biological tissue and identified by Raman spectroscopy. The results are then correlated to calculate the microparticulate pollutant induced stress on the original sample collection site (5). The work flow shows exemplary the results from the analysis of two of the three collected species. The work flow could enable a worldwide mapping of microparticulate pollutant distribution. Figures adapted from [140].

spectroscopy (5). Sponges are reported to integrate micro-particles into their structure to enhance their rigidity. Some species posses small fibers where particles can be stored (e.g. keratose sponges), while others directly integrate the particles unspecific into their cell tissues, the mesohyl. Sponges feed on micron-sized plankton particles which they can digest in so-called chanozyte chambers. So far, no method for a specific identification and localization of inorganic particles inside of sponge tissue sections has been reported. Since the samples were collected and prepared for imaging analysis on-site, fluorescent labeling was no longer possible. To distinguish between the organic tissue and the inorganic particles we exploited a difference in interaction after 2PE. The prepared samples displayed a strong auto-fluorescence of the organic sponge tissue while the inorganic foreign particles showed no emission. This allowed us to image and characterize the sponge tissue label-free and identify incorporated micro-particles with respect to the type of surrounding tissue. The imaging analysis revealed the highest particle density in the spongin fibers of keratose sponges (figure 5.2a,d), enhancing the structural integrity of the sponge. In the mesohyl less particles of smaller size were found (figure 5.2b,e). While the tissue surrounding chanocyte chambers contained particles, none were found inside of a chamber (figure 5.2c,f). A total of 1686 incorporated particles were chemically identified by Raman spectroscopy, revealing 34 different materials. A comparison of the

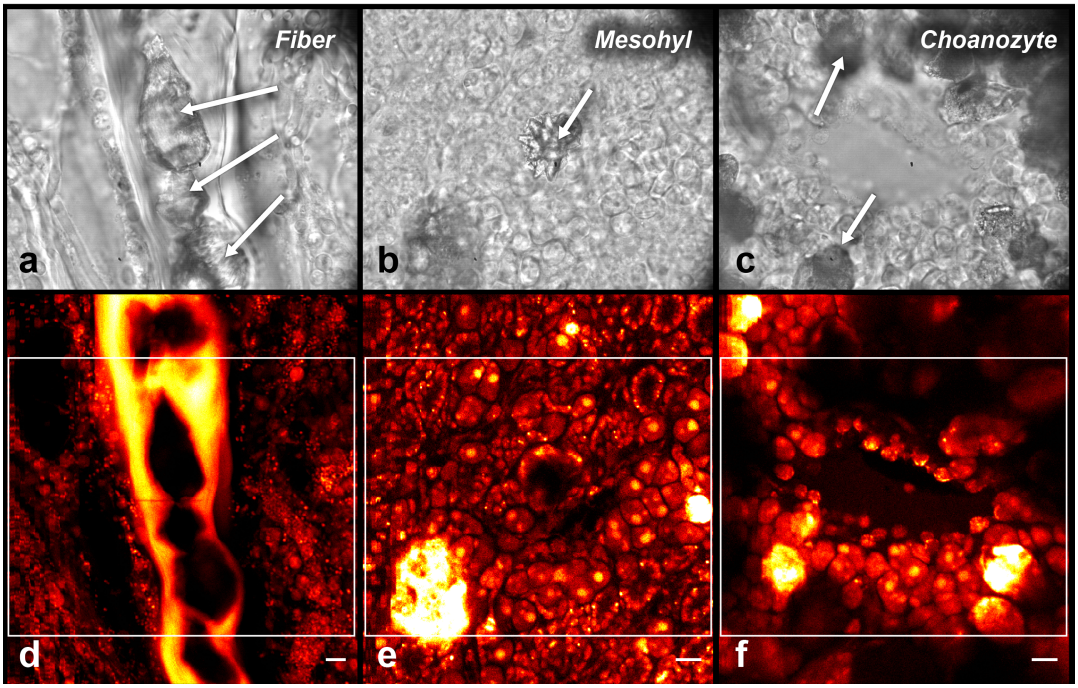

Figure 5.2.: Localization of inorganic particles embedded in sponge tissue. By combining BF (a-c) and 2PE (d-f) imaging, we could identify inorganic particles of varying sizes (examples marked by white arrows in the BF images) in different parts of the tissue: **a,d** fiber channels, **b,e** mesohyl sections, and **c,f** chanozyte chambers. Scale bars 10 μm. Figures adapted from [143].

chemical composition of the inorganic particles from the sponge tissue to the composition of a sample from the surrounding beach sand, unveiled no material bias in the uptake of micro-particles. Even in the small sample size of our experiment we could identify multiple man-made pollutant particles including car paint and polystyrene. The results strongly suggest that sponges are a potent bioindicators for monitoring microparticulate pollutants. By exploiting the difference in the 2PE adsorption behaviour of biological and inorganic materials, the MOSAIC platform could be applied for inorganic particle localization in biological samples. The 3D imaging capabilities for large tissue sections on the microscope could be demonstrated in the scope of this project.

Outlook

The methodology employed here can be applied to all sponge species, enabling a potential worldwide mapping of the local micro-pollution. A further optimization of the method would be to exploit the fact that anthropogenic polymer materials, in contrast to natural inorganic microparticles, typically possess Raman bands around 2700 to 4000 cm^{-1}. Enhanced Raman methods, especially quantitative SRS imaging, would therefore be ideal for specific high-throughput screening of the microplastic pollution.

5.2. Project 4: *"Spatio-selective activation of nuclear translocation of YAP with light directs invasion of cancer cell spheroids"*

After the label-free 3D imaging of sponge tissue sections, MOSAIC imaging was applied to multiplexed 3D imaging of labeled HeLa cell spheroids. The combination of 1PE and 2PE fluorescence imaging could elucidate the role of the Yes-associated protein (YAP) in the cancerous growth of cell spheroids. A YAP mutant (optoYAP) allowed us to trigger the translocation of YAP into the cell nucleus at a specific point in time. We found that this translocation temporary triggers cancerous growth of cells. After four days, YAP is completely relocated back to the cytosol. The opto-YAP system in combination with fluorescent imaging enabled direct observation of the influence of YAP on cellular processes for the first time. These findings are summarized in the following publication:

Illes, B., Fuchs, A., Gegenfurter, F., Ploetz, E., Zahler, S., Vollmer, A., Engelke, H.*, **Spatio-selective activation of nuclear translocation of YAP with light directs invasion of cancer cell spheroids**, *iScience* 2021, 24, 102185.

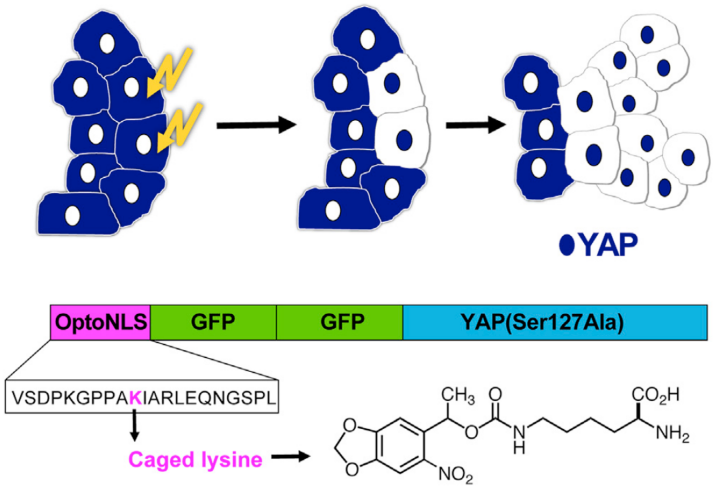

Figure 5.3.: Schematics of the opto-genetic experiment and the optoYAP construct. Using photoactivation, the localization of the opto-YAP construct can be switched from the cytosol to the nucleus (upper panel) . OptoYAP is composed of the optoNLS with a caged lysine and two GFP prepended to YAP Ser127Ala (lower panel). The optoNLS is activated by uncaging the lysine with light leading to nuclear localization of optoYAP followed by enhanced proliferation in the photo-activated area. Figures adapted from [144].

Motivation and key results

Cancer is a leading cause of death worldwide, resulting in almost ten million deaths in 2020.[1] Cancer originates from a spontaneous growth of abnormal cells (tumor), which can spread consecutively over other parts of the body (metastasis), causing bodily harm and can result in death. Uncovering the underlying process of tumor progression and invasion is of utmost importance in developing potent cancer treatment drugs. The Yes-associated protein (YAP) was identified as an important player in tumor progression. While being cytoplasmic in non-invasive cells, it was found in the nucleus during cell elongation and invasion [145, 146]. In collaboration with the group of Prof. Engelke, we set out to answer the question of whether translocation of YAP into the nucleus alone is sufficient to cause directed cancerous growth.

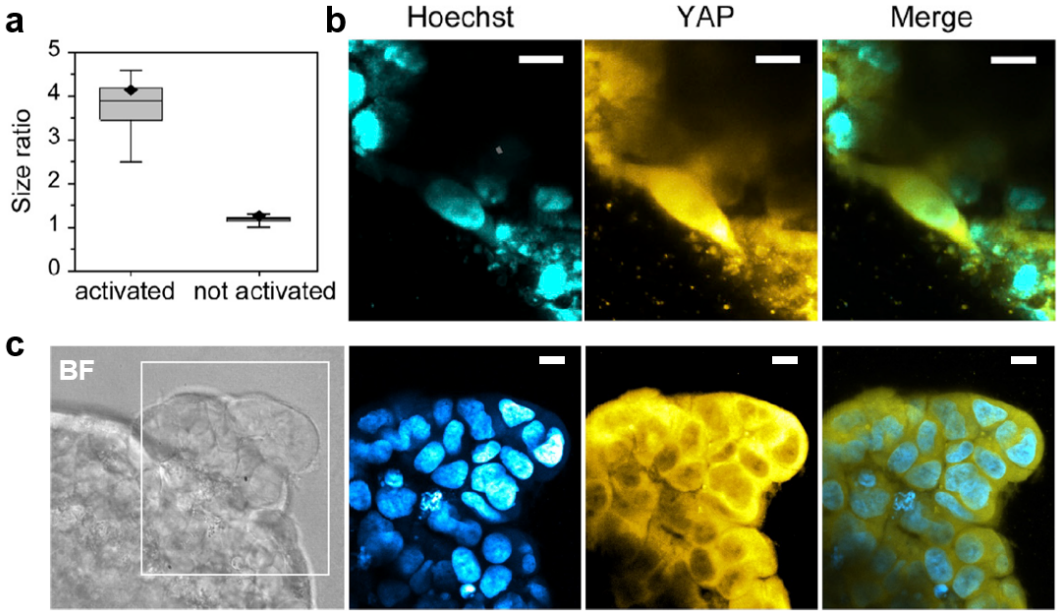

Figure 5.4.: High resolution confocal microscopy imaging of the inside of a fixed HeLa spheroid transfected with optoYAP. **a)** Quantification of the change in average spheroid size over three days. Activated samples (light gray) show nearly a fourfold increase in their size (measured from the area in the central image plane) after three days while non-activated samples (dark gray) grew only by a factor of 1.2. **b)** A fluorescence image of activated YAP in a cell spheroid 24 h after activation. The spheroid is embedded in a collagen gel and was completely illuminated for activation. **c)** BF and fluorescent images of a spheroid fixed four days after activation. YAP appears concentrated in the cytosol. Scale bars: 5 μm. Figure adapted from [144].

[1] Numbers from the website of the World Health Organisation, 3rd February 2022

As a readout, a photo-activatable YAP mutant (figure 5.3) called optoYAP was developed, where a genetically induced side-group with a caged lysine (OptoNLS) completely inhibits nuclear import. Exposure with UV-light cleaves the OptoNLS group of optoYAP in the irradiated cells, triggering the import of YAP into the nucleus. If YAP was directly responsible for the cancerous growths, this would lead to a localized burst in cell proliferation (figure 5.4a). The position of YAP can be localized by GFPs, also genetically inserted into the optoYAP construct, while the cell nuclei were located using Hoechst dye. To simulate the conditions of tumorous cell clusters in the surrounding tissue, spheroids of HeLa cancer cells containing optoYAP were cultivated and embedded in a collagen gel matrix. The imaging method of choice (1) requires a high spatial resolution in 3D to follow the import of YAP into the nucleus, and (2) needs to be robust against scattering to image cells hundreds of μm above the slide surface. Our microscopy platform is designed for fluorescent, 3D, multi-color imaging of tissue and is well suited to tackle the required tasks. 2PE was applied to localize the Hoechst-stained nuclei with high spatial resolution, and an additionally applied antibody staining with Alexa Fluor 546 against GFP further enhanced our detection sensitivity for YAP. The later was excited via 1PE by the 561 nm laser line while the Hoechst dye was imaged with 2PE at 774 nm, correlating information from linear and nonlinear fluorescent imaging on our setup. YAP was localized in the nucleus of photo-activated cells in a cell spheroid, resulting in directed growth into the surrounding matrix from the activated spot (figure 5.4b,c). The same photo-activation of cells without opto-YAP did not result in a change of growth rate. The results confirmed the theory that YAP can directly trigger cancerous growth.
However, contrary to expectations, we found the translocation of YAP into the nucleus to be not permanent. When imaging cells four days after activation, YAP was completely relocated into the cytoplasm (figure 5.4c). This relocation corresponds with a decrease in growth rate back to the level measured before activation. This work demonstrates the high suitability of the setup for state of the art, 3D fluorescence cell (spheroid) imaging.

Outlook
The developed opto-YAP system provides a novel route for studying the impact of YAP on cellular processes. While the presented research focuses on cell clusters, the system has the potential for investigations *in organello* and even in living animals, similar to studies with artificial amino acids performed in zebrafish [147] and mice [148].

5.3. Project 5: *"Chemical synthesis of the fluorescent, cyclic dinucleotides cthGAMP"*

To further push the MOSAIC detection sensitivity, 2PE imaging was complemented with the Phasor-FLIM analysis. The following publications employs the new modality to verify that synthetically manufactured 2'3'-cthGAMP can be applied for *in cellular* applications:

Veth, S., Fuchs, A., Özdemir, D., Dialer, C., Drexler, J.D., Knechtel, F., Witte, G., Hopfner, K., Carell, T.*, Ploetz, E.* **Chemical synthesis of the fluorescent, cyclic dinucleotides cthGAMP.**, *ChemBioChem* 2022, 23, e202200005.

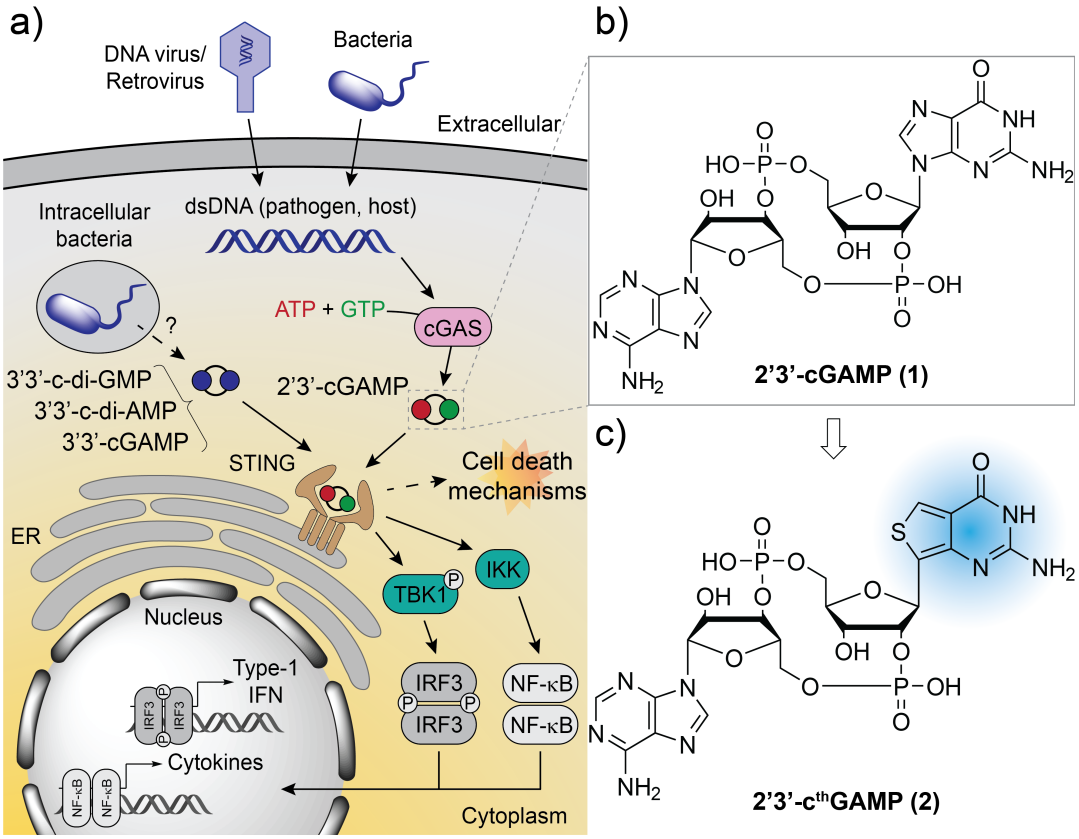

Figure 5.5.: The biological role of CDNs. **a)** Molecular activation and regulation of the cGAS-cGAMP-STING pathway leading to interferon activation, inflammatory response and potential cell death. **b)** Chemical structure of CDN 2'3'-cGAMP. **c)** Chemical structure of the fluorescent analogue 2'3'-cthGAMP. Figure taken from [149].

Motivation and key results

Double-stranded DNA (dsDNA) in the cellular cytosol indicates danger for the cell, usually caused by an infection or by tumorigenesis [150, 151]. The sensing of dsDNA

in healthy cells triggers an innate immune response via the cyclic GMP-AMP synthase (cGAS)-stimulator of interferon genes (STING) pathway (figure 5.5a). Even small deviations in the pathway can lead to severe changes in the immune response [152]. Hence, a detailed understanding of the cGAS-STING pathway is of high therapeutic potential. It is known that the dinucleotide cyclic guanosine monophosphate-adenosine (cGAMP) acts as the secondary messenger between cGAS and the STING receptor. Unfortunately, *in vivo* studies of cGAMP with fluorescence microscopy have been hindered by the small size of the dinucleotide: even small labels inhibit its biological functionality.

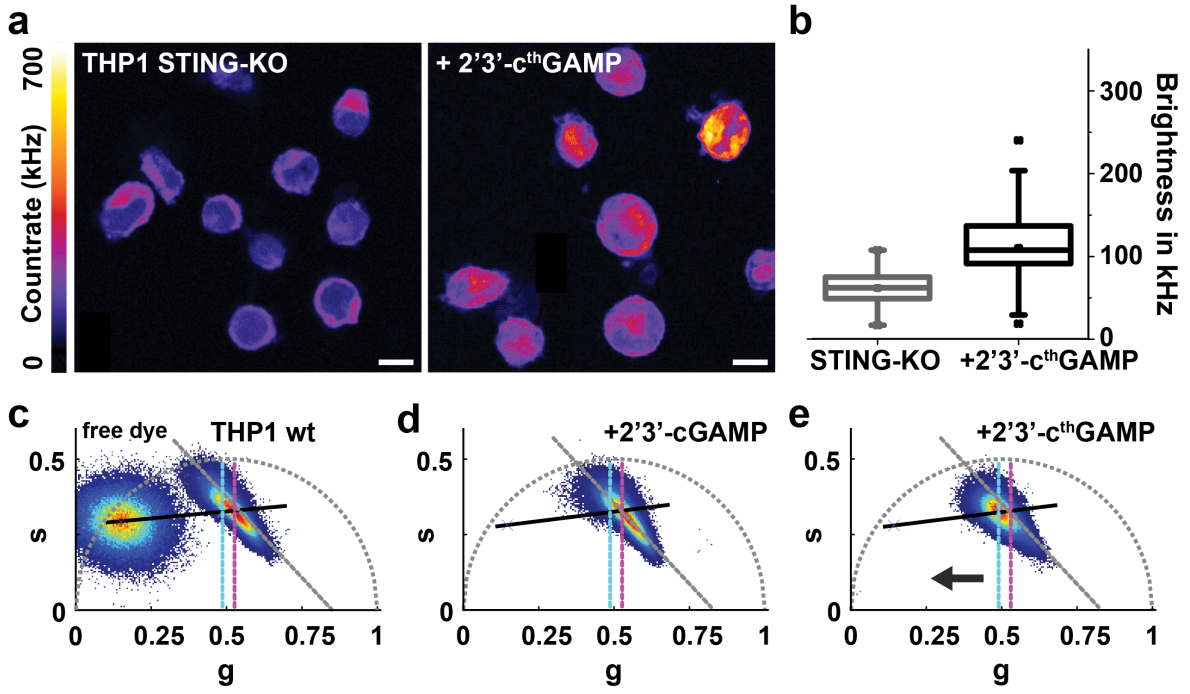

Figure 5.6.: Fluorescence microscopy investigation of the cellular uptake of 2'3'-cthGAMP in THP-1 cells. **a,b)** 2PE images (a) and average cell brightness (b) of THP-1 STING-KO cells in the absence and presence of 2'3'-cthGAMP. Uptake of 2'3'-cthGAMP in STING knockout cells leads to a fluorescence increase. The fluorescence emission was recorded between 417-477 nm and evaluated for 70-130 cells per condition. **c)** The Phasor representation of the fluorescence signature of THP-1 wt cells and free 2'3'-cthGAMP in cell medium. The angled dotted line (grey) marks the multicomponent autofluorescent background in THP-1 wt cells. The center positions of the populations before (pink) and after (cyan) addition of 2'3'-cthGAMP (e) are marked with dotted lines. **d)** The addition of the nonfluorescent compound cGAMP triggers a shift in cellular autofluorescence towards shorter lifetimes and reduces the brightness. **e)** The addition of 2'3'-cthGAMP leads to an off-axis shift towards free 2'3'-cthGAMP (along the black line), confirming the successful uptake of 2'3'-cthGAMP. Figure adapted from [149].

Recently the group of Yitzak Tor synthesized a fluorescent analogue of cGAMP by replacing the guanosine with an emissive thieno[3,4-d]pyrimidine-based thG derivative (figure 5.5b,c, [153]). However, even so the proof-of-concept measurement of the fluorescent base thG alone were promising (possessing excellent structural isomorphicity, good quantum yield and long lifetime), the developed enzymatic syntheses route of this cthGAMP was not able to produce the necessary amount of material for *in vivo* applications. In the presented publication together with the group of Prof. Carell, the successful, efficient organic synthesis of cthGAMP is described. Both compounds, 2'3'-cthGAMP and 3'3'-cthGAMP are co-synthesized with good yields. The binding affinities to the STING receptor and the biological functionality of both cthGAMP could be evaluated. 3'3'-cthGAMP showed no favourable binding affinity neither to human nor murine STING. 2'3'-cthGAMP, on the other hand, while possessing a lower binding affinity than natural cGAMP, retained its biological functionality. This enabled us to study its uptake in THP-1 monocyte cells.
Using two-photon excited fluorescence lifetime imaging, we first characterized the spectral and temporal properties of the designed fluorophore. We found that the spectroscopic properties of the compound change significantly in the cellular environment. The lifetime decreases from 16.8 ns in water to 4.3 ns in THP-1 cell medium. In addition, the 2PE induced an auto-fluorescent background in the THP-1 cells which spectrally overlaps with the 2'3'-cthGAMP emission. Although, an increase in average fluorescence intensity of STING knock-out (STING-KO) cells after addition of the compound was observed (figure 5.6a,b), it could not be directly linked to the compound due to the unknown background contribution. By applying Phasor-FLIM (see chapter 2.2.1), it was possible to distinguish between the cellular auto-fluorescence and the 2'3'-cthGAMP emission (figure 5.6c,d). The shift of the lifetime population towards that of pure dye strongly indicates the successful import of 2'3'-cthGAMP into THP1 cells (figure 5.6e). MOSAIC enabled the spectroscopic characterization of a novel compound. To address the challenging project, the platform was combined with the optical modality of Phasor-FLIM, demonstrating the suitability of the microscope for state of the art fluorescent analysis methods.

Outlook
Due to its fluorescence properties in combination with biological activity, 2'3'-cthGAMP has high potential as a fluorescent analogue for studies of the innate immune response. However, the low binding affinity and the short lifetime are significant challenges, which need to be overcome in future applications.

Chapter 6.

Summary and Conclusion

In this thesis, a multimodal analysis platform, combining fluorescence techniques with non-linear imaging and spectroscopy, was developed. It can correlate information from a suite of different modalities, including 1PE fluorescence imaging, fluorescence lifetime analysis, Raman spectroscopy, SFG, SHG, 2PE, FWM, and CARS, which were combined on a single confocal microscopy platform referred to as MOSAIC. The design and the technical realization of the platform were presented in detail (chapter 3). The multimodal approach enabled the investigations a variety of different sample system, ranging from the *in situ* investigation of reticular framework crystals (chapter 4), over tissue sections and cell spheroids, to single cell studies (chapter 5).

The feasibility and advantage of this approach for the field of synthetic materials was investigated by studying the influence of heterogeneity on reticular metal-organic framework particles *in situ* (section 4.1). Firstly, all modalities were applied to UiO-67, highlighting the accessible spectral characteristics of MOF crystals. The general benefits of a particle and heterogeneity sensitive method for MOF systems were demonstrated for the extrinsic property of optical absorption in MIL-88A crystals. In particular, the influence of morphology, regarding shape and size, on the microcrystal light absorption properties was elucidated. We found that in the micrometer regime the shape alone dictates the optical absorption. Surprisingly, no correlation between crystal size and light absorption was found. This could potentially enable shape-specific sorting of MOF crystals.
For the intrinsic property of water adsorption in MOF-801 frameworks, an uneven water adsorption behaviour at low relative humidities was found. Small clusters of water were observed using CARS imaging, which are known to decrease the performance of the material [137]. With a combination of multimodal imaging and Raman spectroscopy we determined that missing metal-cluster defects were the reason for the water droplet formation. After the qualitative analysis of the influence of heterogeneity on water adsorption in MOF-801 we wanted to extend the investigation to quantitative studies. However, there was currently no method available to compare the uptake and release performance of a material in the sub-micrometer regime directly to the respective performance in bulk. Therefore, the MOSAIC toolbox was extended with a Raman-based method to determine the quantitative water uptake of single crystals as a function of the RH (isotherm) and the time (kinetic curves) (section 4.2). By comparing regular single crystals of MOF-801 to the bulk material it was possible to determine the quantitative influence of inter-and intra-particle effects on the performance. It was found that

current water harvesting devices based on MOF-801 perform significantly lower than the observed performance of single MOF-801 crystals. Multimodal imaging revealed inter-particle condensation of water as the most likely cause for the difference in bulk performance, in agreement with literature [127]. Our results highlights the importance of single-particle analysis in general and the characterization of heterogeneity and defects in particular. The developed methodologies can potentially be applied to study a wide variety of guest-host interactions, such as CO_2 [11] and H_2 storage [12] or to quantify the impact of particle morphology and especially defect sites on heterogeneous catalysis [154]. The recent development of multivariant MOF systems [155] is a next step in the evolution of MOF materials, but demands even more awareness about the influence of heterogeneity on the material properties [156]. Here, a multimodal characterization will be of great value. Moreover, the potential sample systems are not limited to MOFs. Similar analysis can be performed in other important reticular systems, such as covalent-organic frameworks (COFs) [157], zeolites [46], or mesoporous silica [46].

MOSAIC was also applied to the study of uptaken material in biological systems. In cooperation with the group of Prof. Wörheide, sponge samples collected in the Indonesian Sea were investigated for their potential as bioindicators (section 5.1). 2PE induced auto-fluorescence imaging localized inorganic particles inside the tissue sections and Raman spectroscopy was applied for identification of the inorganic particles. Several mircoparticulant pollutants were found including microplastic, demonstrating the possibility of using sponges to map the oceanic pollutant stress. Fluorescence 3D imaging of HeLa cell spheroids revealed the influence of YAP on the cancerous growth of cells (section 5.2). A photoswitchable YAP-mutant (opto-YAP), developed by the team of Prof. Engelke, enabled site-specific activation of enhanced growth by triggering the transport of YAP into the nucleus. However, we found that the translocation was only temporary. After four days, opto-YAP relocated into the cytosol and the growth rate decreased to the pre-activation level. Opto-YAP can be applied as a tool to monitor and understand the role of YAP in cellular processes. The potential of another synthetic mimic of a biomolecule was investigated: 2'3'-cthGAMP and its import in THP-1 cells (section 5.3). This fluorescent analogue of the important messenger 2'3'-cGAMP in the innate immune response was reported to be biologically active as well as fluorescent [153]. However, the reported enzymatic synthesis did not allow for high enough yields to enable cellular measurements. The group of Prof. Carell developed an organic synthesis route with a high yield, such that the import of 2'3'-cthGAMP in THP-1 cells could be studied. Combining 2PE with Phasor-FLIM, MOSAIC could verify the import and characterize the performance of the synthetic messenger analogue. Investigation on uptaken synthetic materials in biological systems demonstrated the feasibility of the microscope for state-of-the-art fluorescent techniques.

The presented projects highlight the flexibility of the platform regarding sample requirements, and the general benefit of a multimodal characterization. The platform is capable of *in situ* and *in vivo* techniques and equally suited for inorganic material characterization and cell imaging. Therefore, the MOSAIC microscope has high po-

tential to investigate the interaction of synthetic particles with surrounding biological environment, e.g. in theranostic applications [45]. Especially unveiling the complex cell chemistry response on the MOF particle degradation *in situ* [32] requires a correlated investigation, which is now accessible with the selected modalities of the developed MOSAIC analysis platform.

Bibliography

[1] Ziv, Y.; Burns, L. D.; Cocker, E. D.; Hamel, E. O.; Ghosh, K. K.; Kitch, L. J.; Gamal, A. E.; Schnitzer, M. J. *Nature Neuroscience* **2013**, *16*, 264–266.

[2] Skala Melissa, C.; Riching Kristin, M.; Gendron-Fitzpatrick, A.; Eickhoff, J.; Eliceiri Kevin, W.; White John, G.; Ramanujam, N. *Proceedings of the National Academy of Sciences* **2007**, *104*, 19494–19499.

[3] Provenzano, P. P.; Eliceiri, K. W.; Keely, P. J. *Clinical and Experimental Metastasis* **2009**, *26*, 357–370.

[4] Jones, J. D.; Ramser, H. E.; Woessner, A. E.; Quinn, K. P. *Communications Biology* **2018**, *1*, 198.

[5] Gitanjal, D.; Wei-Wen, W.; Fu-Jen, K. *Journal of Biomedical Optics* **2012**, *18*, 1–9.

[6] Deka, G.; Okano, K.; Wu, W.-W.; Kao, F.-J. In *Multiphoton Microscopy in the Biomedical Sciences XIV*; International Society for Optics and Photonics; SPIE; pp 200 – 206. `https://doi.org/10.1117/12.2038472`.

[7] Mazumder, N.; Balla, N. K.; Zhuo, G.-Y.; Kistenev, Y. V.; Kumar, R.; Kao, F.-J.; Brasselet, S.; Nikolaev, V. V.; Krivova, N. A. *Frontiers in Physics* **2019**, *7*.

[8] Jayachandrababu, K. C.; Verploegh, R. J.; Leisen, J.; Nieuwendaal, R. C.; Sholl, D. S.; Nair, S. *Journal of the American Chemical Society* **2016**, *138*, 7325–7336.

[9] Ameloot, R.; Vermoortele, F.; Hofkens, J.; De Schryver, F. C.; De Vos, D. E.; Roeffaers, M. B. *Angew Chem Int Ed Engl* **2013**, *52*, 401–5.

[10] Slepkov, A. D.; Ridsdale, A.; Pegoraro, A. F.; Moffatt, D. J.; Stolow, A. *Biomed. Opt. Express* **2010**, *1*, 1347–1357.

[11] Ding, M.; Flaig, R. W.; Jiang, H.-L.; Yaghi, O. M. *Chem. Soc. Rev.* **2019**, *48*, 2783–2828.

[12] Ahmed, A.; Seth, S.; Purewal, J.; Wong-Foy, A. G.; Veenstra, M.; Matzger, A. J.; Siegel, D. J. *Nature Communications* **2019**, *10*, 1568.

[13] He, S.; Wu, L.; Li, X.; Sun, H.; Xiong, T.; Liu, J.; Huang, C.; Xu, H.; Sun, H.; Chen, W.; Gref, R.; Zhang, J. *Acta Pharmaceutica Sinica B* **2021**, *11*, 2362–2395; Hot Topic Reviews in Drug Delivery.

[14] Wollman, A. J. M.; Nudd, R.; Hedlund, E. G.; Leake, M. C. *Open biology* **2015**, *5*, 150019–150019.

[15] Gest, H. *Notes and Records of the Royal Society of London* **2004**, *58*, 187–201.

[16] Landecker, H. *Critical Inquiry* **2005**, *31*, 903–937.

[17] Marvin, M. *Patent* **1961**.

[18] Schulte, E. K. W. *Histochemistry* **1991**, *95*, 319–328.

[19] Zubairy, M. S. *A Very Brief History of Light*; Springer, Cham, 2016.

[20] Stokes, G. G. *Philosophical Transactions of the Royal Society of London* **1852**, *142*, 463–562.

[21] Digman, M. A.; Caiolfa, V. R.; Zamai, M.; Gratton, E. *Biophysical journal* **2008**, *94*, L14–L16.

[22] Hendrix, J.; Dekens, T.; Schrimpf, W.; Lamb, D. C. *Biophysical Journal* **2016**, *111*, 1785–1796.

[23] Magde, D.; Elson, E.; Webb, W. W. *Physical Review Letters* **1972**, *29*, 705–708.

[24] Hendrix, J.; Schrimpf, W.; Höller, M.; Lamb, D. C. *Biophysical journal* **2013**, *105*, 848–861.

[25] Chen, H.; Wang, H.; Slipchenko, M. N.; Jung, Y.; Shi, Y.; Zhu, J.; Buhman, K. K.; Cheng, J.-X. *Opt. Express* **2009**, *17*, 1282–1290.

[26] Göppert-Mayer, M. *Annalen der Physik* **1931**, *401*, 273–294.

[27] Kaiser, W.; Garrett, C. *Physical review letters* **1961**, *7*, 229.

[28] Franken, P. A.; Hill, A. E.; Peters, C. W.; Weinreich, G. *Phys. Rev. Lett.* **1961**, *7*, 118–119.

[29] Bush, P. G.; Wokosin, D. L.; Hall, A. C. *Frontiers in bioscience : a journal and virtual library* **2007**, *12*, 2646–2657.

[30] Baker, J. *Newtons Farbtheorie*; Spektrum Akademischer Verlag: Heidelberg, 2009; pp 56–59.

[31] Raman, C. V.; Krishnan, K. S. *Nature* **1928**, *121*, 711–711.

[32] Ploetz, E.; Zimpel, A.; Cauda, V.; Bauer, D.; Lamb, D. C.; Haisch, C.; Zahler, S.; Vollmar, A. M.; Wuttke, S.; Engelke, H. *Advanced Materials* **2020**, *32*, 1907267.

[33] Käppler, A.; Windrich, F.; Löder, M. G. J.; Malanin, M.; Fischer, D.; Labrenz, M.; Eichhorn, K.-J.; Voit, B. *Analytical and Bioanalytical Chemistry* **2015**, *407*, 6791–6801.

[34] Jones, R. R.; Hooper, D. C.; Zhang, L.; Wolverson, D.; Valev, V. K. *Nanoscale Research Letters* **2019**, *14*, 231.

[35] Duncan, M. D.; Reintjes, J.; Manuccia, T. J. *Optics Letters* **1982**, *7*, 350–352.

[36] Zumbusch, A.; Holtom, G. R.; Xie, X. S. *Physical Review Letters* **1999**, *82*, 4142–4145.

[37] Freudiger, C. W.; Min W Fau Saar, B. G.; Saar Bg Fau Lu, S.; Lu S Fau Holtom, G. R.; Holtom Gr Fau He, C.; He C Fau Tsai, J. C.; Tsai Jc Fau Kang, J. X.; Kang Jx Fau Xie, X. S.; Xie, X. S. *Science* **2008**, *322(5909)*.

[38] Ploetz, E.; Laimgruber, S.; Berner, S.; Zinth, W.; Gilch, P. *Applied Physics B* **2007**, *87*, 389–393.

[39] Schie, I.; Stiebing, C.; Popp, J. *J Biomed Opt* **2021**, *26*.

[40] Kong, K.; Rowlands Christopher, J.; Varma, S.; Perkins, W.; Leach Iain, H.; Koloydenko Alexey, A.; Williams Hywel, C.; Notingher, I. *Proceedings of the National Academy of Sciences* **2013**, *110*, 15189–15194.

[41] Shipp, D. W.; Rakha, E. A.; Koloydenko, A. A.; Macmillan, R. D.; Ellis, I. O.; Notingher, I. *Breast Cancer Research* **2018**, *20*, 69.

[42] Lin, D.; Qiu, S.; Huang, W.; Pan, J.; Xu, Z.; Chen, R.; Feng, S.; Chen, G.; Li, Y.; Short, M.; Zhao, J.; Fawzy, Y.; Zeng, H. *Journal of Biophotonics* **2018**, *11*, e201700251.

[43] Muller, K.; Vankova, N.; Schottner, L.; Heine, T.; Heinke, L. *Chem Sci* **2019**, *10*, 153–160.

[44] Illes, B.; Hirschle, P.; Barnert, S.; Cauda, V.; Wuttke, S.; Engelke, H. *Chemistry of Materials* **2017**, *29*, 8042–8046.

[45] Shrivastava, S.; Jain, S.; Kumar, D.; Soni, S.; Sharma, M. *Asian Journal of Pharmaceutical Research and Development* **2019**, *7*, 63–69.

[46] Liang, J.; Liang, Z.; Zou, R.; Zhao, Y. *Adv Mater* **2017**, *29*.

[47] Graziano, G. *Nature Reviews Chemistry* **2017**, *1*, 0037.

[48] Haase, F.; Hirschle, P.; Freund, R.; Furukawa, S.; Ji, Z.; Wuttke, S. *Angewandte Chemie International Edition* **2020**, *59*, 22350–22370.

[49] Yaghi, O. M.; Li, H. *Journal of the American Chemical Society* **1995**, *117*, 10401–10402.

[50] Eddaoudi, M.; Kim J Fau Rosi, N.; Rosi N Fau Vodak, D.; Vodak D Fau Wachter, J.; Wachter J Fau O'Keeffe, M.; O'Keeffe M Fau Yaghi, O. M.; Yaghi, O. M. **2002**.

[51] Gropp, C.; Canossa, S.; Wuttke, S.; Gandara, F.; Li, Q.; Gagliardi, L.; Yaghi, O. M. *ACS Cent Sci* **2020**, *6*, 1255–1273.

[52] Farha, O. K.; Eryazici, I.; Jeong, N. C.; Hauser, B. G.; Wilmer, C. E.; Sarjeant, A. A.; Snurr, R. Q.; Nguyen, S. T.; Yazaydın, A. z.; Hupp, J. T. *Journal of the American Chemical Society* **2012**, *134*, 15016–15021.

[53] Lee, J.; Farha, O. K.; Roberts, J.; Scheidt, K. A.; Nguyen, S. T.; Hupp, J. T. *Chemical Society Reviews* **2009**, *38*, 1450–1459.

[54] Bavykina, A.; Kolobov, N.; Khan, I. S.; Bau, J. A.-O.; Ramirez, A. A.-O.; Gascon, J. A.-O. *Chemical Reviews* **2019**.

[55] Wang, Q.; Astruc, D. *Chemical Reviews* **2020**, *120*, 1438–1511.

[56] Freund, R.; Lächelt, U.; Gruber, T.; Rühle, B.; Wuttke, S. *ACS Nano* **2018**, *12*, 2094–2105.

[57] Lismont, M.; Dreesen, L.; Wuttke, S. *Advanced Functional Materials* **2017**, *27*, 1606314.

[58] Ploetz, E.; Engelke, H.; Lächelt, U.; Wuttke, S. *Advanced Functional Materials* **2020**, *30*, 1909062.

[59] Fuchs, A.; Mannhardt, P.; Hirschle, P.; Wang, H.; Zaytseva, I.; Ji, Z.; Yaghi, O.; Wuttke, S.; Ploetz, E. *Advanced Materials* **2022**, *34*, 2104530.

[60] Katzenmeyer, A. M.; Canivet, J.; Holland, G.; Farrusseng, D.; Centrone, A. *Angew Chem Int Ed Engl* **2014**, *53*, 2852–6.

[61] Mandemaker, L. D. B.; Rivera-Torrente, M.; Geitner, R.; Vis, B. M., C. M. and *Angew Chem Int Ed Engl* **2020**, *59*, 19545–19552.

[62] Schrimpf, W.; Jiang, J.; Ji, Z.; Hirschle, P.; Lamb, D. C.; Yaghi, O. M.; Wuttke, S. *Nat Commun* **2018**, *9*, 1647.

[63] Wolf, M.; Hirai, K.; Toyouchi, S.; Fron, E.; Peeters, W.; De Feyter, S.; Uji, I. H. *Chem Commun (Camb)* **2020**, *56*, 13331–13334.

[64] Strauss, I.; Mundstock, A.; Hinrichs, D.; Himstedt, R.; Knebel, A.; Reinhardt, C.; Dorfs, D.; Caro, J. *Angew Chem Int Ed Engl* **2018**, *57*, 7434–7439.

[65] Strauss, I.; Mundstock, A.; Treger, M.; Lange, K.; Hwang, S.; Chmelik, C.; Rusch, P.; Bigall, N. C.; Pichler, T.; Shiozawa, H.; Caro, J. *ACS Appl Mater Interfaces* **2019**, *11*, 14175–14181.

[66] Version, R. A. S. *The Holy Bible*; Providence Press LLC, 2022.

[67] Al-Amri, M. D. *Optics in our time*; Springer, Cham, 2016.

[68] Maxwell, J. C. *Philosophical Transactions of the Royal Society of London* **1865**, *155*, 459–512.

[69] Hertz, H. *Annalen der Physik* **1888**, *270*, 551–569.

[70] Newton, I. *Opticks*; Dover Press, 1704.

[71] Einstein, A. *Annalen der Physik* **1905**, *322*, 132–148.

[72] Planck, M. *Annalen der Physik* **1901**, *309*, 553–563.

[73] Orfanidis, S. J. *Electromagnetic Waves and Antennas [Online]*, 2016.

[74] Boyd, R. W. *Chapter 1 - The Nonlinear Optical Susceptibility*; Academic Press: Burlington, 2008; pp 1–67.

[75] Einstein, A. *Deutsche Physikalische Gesellschaft* **1916**, *18*, 318–323.

[76] Planck, M. *Annalen der Physik* **1901**, *309*, 553–563.

[77] Maxwell, J. C. *Philosophical Transactions of the Royal Society of London* **1865**, *155*, 459–512.

[78] Maiman, T. H. *Nature* **1960**, *187*, 493–494.

[79] Lewis, G. N.; Lipkin, D.; Magel, T. T. *Journal of the American Chemical Society* **1941**, *63*, 3005–3018.

[80] Cheng, J.-X.; Xie, X. *Coherent Raman Scattering Microscopy*, 1st ed.; CRC Press, 2012.

[81] Fuchs, A.; Mannhardt, P.; Hirschle, P.; Wang, H.; Zaytseva, I.; Ji, Z.; Yaghi, O.; Wuttke, S.; Ploetz, E. *Advanced Materials* **2022**, *34*, 2104530.

[82] Jablonski, A. *Nature* **1933**, *131*, 839–840.

[83] Shimomura, O.; Johnson, F. H.; Saiga, Y. *Journal of Cellular and Comparative Physiology* **1962**, *59*, 223–239.

[84] Gärtner, W.; Gröbler, B.; Schubert, D.; Wabnitz, H.; Wilhelmi, B. *Experimental Techniques in Physics* **1988**, *36*, 443–451.

[85] Veth, S.; Fuchs, A.; Özdemir, D.; Dialer, C.; Drexler, D. J.; Knechtel, F.; Witte, G.; Hopfner, K.-P.; Carell, T.; Ploetz, E. *ChemBioChem* **2022**, *23*, e202200005.

[86] Weber, G. *The Journal of Physical Chemistry* **1981**, *85*, 949–953.

[87] Skala, M. C.; Riching, K. M.; Gendron-Fitzpatrick, A.; Eickhoff, J.; Eliceiri, K. W.; White, J. G.; Ramanujam, N. *Proceedings of the National Academy of Sciences* **2007**, *104*, 19494–19499.

[88] Brasselet, S. *Adv. Opt. Photon.* **2011**, *3*, 205.

[89] Kumar, R.; Grønhaug, K. M.; Romijn, E. I.; Finnøy, A.; Davies, C. L.; Drogset, J. O.; Lilledahl, M. B. *Journal of Biophotonics* **2014**, *8*, 730–739.

[90] Engelbrecht, R. *Nichtlineare Faseroptik*, 1st ed.; Springer Vieweg Berlin, Heidelberg, 2014.

[91] Dudley, J. M.; Genty, G.; Coen, S. *Rev. Mod. Phys.* **2006**, *78*, 1135–1184.

[92] Smith, A. M.; Mancini, M. C.; Nie, S. *Nature Nanotechnology* **2009**, *4*, 710–711.

[93] Kneipp, J.; Kneipp, H.; Kneipp, K. *Proceedings of the National Academy of Sciences of the United States of America* **2006**, *103*, 17149–17153.

[94] Smekal, A. *Naturwissenschaften* **1923**, *11*, 873–875.

[95] Boltzmann, L. *Studien über das Gleichgewicht der lebendigen Kraft zwischen bewegten materiellen Punkten*; Hasenöhrl, F., Ed.; Cambridge Library Collection - Physical Sciences, Vol. 1; Cambridge University Press, 2012; p 49–96.

[96] Osawa, M.; Matsuda, N.; Yoshii, K.; Uchida, I. *The Journal of Physical Chemistry* **1994**, *98*, 12702–12707.

[97] Stöckle, R. M.; Suh, Y. D.; Deckert, V.; Zenobi, R. *Chemical Physics Letters* **2000**, *318*, 131–136.

[98] Aroca, R. *Surface-Enhanced Vibrational Spectroscopy* **2006**, 73–106.

[99] Szaniawska, A.; Kudelski, A. *Front Chem* **2021**, *9*, 664134.

[100] Shanmukh, S.; Jones, L.; Driskell, J.; Zhao, Y.; Dluhy, R.; Tripp, R. A. *Nano Letters* **2006**, *6*, 2630–2636.

[101] Fu, Y.; Kuppe, C.; Valev, V. K.; Fu, H.; Zhang, L.; Chen, J. *Environmental Science & Technology* **2017**, *51*, 6260–6267.

[102] Xu, L.-J.; Lei, Z.-C.; Li, J.; Zong, C.; Yang, C. J.; Ren, B. *Journal of the American Chemical Society* **2015**, *137*, 5149–5154.

[103] Ji, M.; Orringer Daniel, A.; Freudiger Christian, W.; Ramkissoon, S.; Liu, X.; Lau, D.; Golby Alexandra, J.; Norton, I.; Hayashi, M.; Agar Nathalie, Y. R.; Young Geoffrey, S.; Spino, C.; Santagata, S.; Camelo-Piragua, S.; Ligon Keith, L.; Sagher, O.; Xie, X. S. *Science Translational Medicine* **2013**, *5*, 201ra119–201ra119.

[104] Moura, C. C.; Tare, R. S.; Oreffo, R. O. C.; Mahajan, S. *Journal of The Royal Society Interface* **2016**, *13*, 20160182.

[105] Nan, X.; Potma, E. O.; Xie, X. S. *Biophysical Journal* **2006**, *91*, 728–735.

[106] Volkmer, A.; Cheng, J.-X.; Sunney Xie, X. *Physical Review Letters* **2001**, *87*.

[107] Peiponen, K.-E.; Lucarini, V.; Saarinen, J. J.; Vartiainen, E. *Applied Spectroscopy* **2004**, *58*, 499–509; PMID: 15165324.

[108] Liu, Y.; Lee, Y. J.; Cicerone, M. T. *Opt. Lett.* **2009**, *34*, 1363–1365.

[109] Oudar, J.; Smith, R. W.; Shen, Y. R. *Applied Physics Letters* **1979**, *34*, 758–760.

[110] Cheng, J.-X.; Book, L. D.; Xie, X. S. *Opt. Lett.* **2001**, *26*, 1341–1343.

[111] Li, X.; Jiang, M.; Lam, J. W. Y.; Tang, B. Z.; Qu, J. Y. *Journal of the American Chemical Society* **2017**, *139*, 17022–17030.

[112] Brewster, D. *Die Fortschritte der Physik* **1852**, *4. 1848*, 979.

[113] SEEGER, R. J. In *Men of Physics: Galileo Galilei, his Life and his Works*; SEEGER, R. J., Ed.; Pergamon, 1966; pp 16–25.

[114] Placzek, G. *Rayleigh-Streuung und Raman-Effekt*; Akademische Verlagsgesellschaft: Leipzig, 1934.

[115] Latychevskaia, T. *Appl. Opt.* **2019**, *58*, 3597–3603.

[116] El-Azazy, M. In *Infrared Spectroscopy*; El-Azazy, M., Ed.; IntechOpen: Rijeka, 2019; Chapter 1.

[117] Czerny, M.; Turner, A. F. *Zeitschrift für Physik* **1930**, *61*, 792–797.

[118] Hecht, E. *Frontmatter*; De Gruyter, 2018.

[119] Hanesch, M. *Geophysical Journal International* **2009**, *177*, 941–948.

[120] Hellerer, T.; Enejder, A. M.; Zumbusch, A. *Applied Physics Letters* **2004**, *85*, 25–27.

[121] Schrimpf, W.; Barth, A.; Hendrix, J.; Lamb, D. C. *Biophysical Journal* **2018**, *114*, 1518–1528.

[122] Schindelin, J.; Arganda-Carreras, I.; Frise, E.; Kaynig, V.; Longair, M.; Pietzsch, T.; Preibisch, S.; Rueden, C.; Saalfeld, S.; Schmid, B.; Tinevez, J.-Y.; White, D. J.; Hartenstein, V.; Eliceiri, K.; Tomancak, P.; Cardona, A. *Nature methods* **2012**, *9*, 676–682.

[123] Rojas, S.; Arenas-Vivo, A.; Horcajada, P. *Coordination Chemistry Reviews* **2019**, *388*, 202–226.

[124] Guo, A.; Durymanov, M.; Permyakova, A.; Sene, S.; Serre, C.; Reineke, J. *Pharmaceutical Research* **2019**, *36*, 53.

[125] Horcajada, P.; Chalati, T.; Serre, C.; Gillet, B.; Sebrie, C.; Baati, T.; Eubank, J. F.; Heurtaux, D.; Clayette, P.; Kreuz, C.; Chang, J.-S.; Hwang, Y. K.; Marsaud, V.; Bories, P.-N.; Cynober, L.; Gil, S.; Férey, G.; Couvreur, P.; Gref, R. *Nature Materials* **2010**, *9*, 172–178.

[126] Furukawa, H.; Gandara, F.; Zhang, Y. B.; Jiang, J.; Queen, W. L.; Hudson, M. R.; Yaghi, O. M. *J Am Chem Soc* **2014**, *136*, 4369–81.

[127] Kim, H.; Rao, S. R.; Kapustin, E. A.; Zhao, L.; Yang, S.; Yaghi, O. M.; Wang, E. N. *Nat Commun* **2018**, *9*, 1191.

[128] Fathieh, F.; Kalmutzki, M. J.; Kapustin, E. A.; Waller, P. J.; Yang, J.; Yaghi, O. M. *Science Advances* **2018**, *4*, eaat3198.

[129] Pascanu, V.; González Miera, G.; Inge, A. K.; Martín-Matute, B. *Journal of the American Chemical Society* **2019**, *141*, 7223–7234.

[130] Zhang, J.; Cheng, F.; Li, J.; Zhu, J.-J.; Lu, Y. *Nano today* **2016**, *11*, 309–329.

[131] F.R.S., L. R. *The London, Edinburgh, and Dublin Philosophical Magazine and Journal of Science* **1899**, *47*, 375–384.

[132] Mie, G. *Annalen der Physik* **1908**, *330*, 377–445.

[133] Bohren, N. *Absorption and Scattering by an Arbitrary Particle*; John Wiley & Sons, Ltd, 1998; Chapter 3, pp 57–81.

[134] Hanikel, N.; Prevot, M. S.; Yaghi, O. M. *Nat Nanotechnol* **2020**, *15*, 348–355.

[135] Xu, W.; Yaghi, O. M. *ACS Cent Sci* **2020**, *6*, 1348–1354.

[136] Hanikel, N.; Pei, X.; Chheda, S.; Lyu, H.; Jeong, W.; Sauer, J.; Gagliardi, L.; Yaghi, O. M. *Science* **2021**, *374*, 454–459.

[137] Delen, G.; Monai, M.; Meirer, F.; Weckhuysen, B. M. *Angew Chem Int Ed Engl* **2021**, *60*, 1620–1624.

[138] Chen, G.; Qiu, H.; Prasad, P. N.; Chen, X. *Chemical Reviews* **2014**, *114*, 5161–5214; PMID: 24605868.

[139] Ding, M.; Flaig, R. W.; Jiang, H.-L.; Yaghi, O. M. *Chem. Soc. Rev.* **2019**, *48*, 2783–2828.

[140] Fuchs, A.; Girard, E. B.; Ploetz, E.; Wörheide, G. *Laborpraxis* **2021**, *45*, 14.

[141] Bell, J. J. *Estuarine, Coastal and Shelf Science* **2008**, *79*, 341–353.

[142] Teragawa, C. *Duke University* **1985**, 252–258.

[143] Girard, E. B.; Fuchs, A.; Kaliwoda, M.; Lasut, M.; Ploetz, E.; Schmahl, W. W.; Wörheide, G. *Environmental Pollution* **2021**, *268*, 115851.

[144] Illes, B.; Fuchs, A.; Gegenfurtner, F.; Ploetz, E.; Zahler, S.; Vollmar, A. M.; Engelke, H. *iScience* **2021**, *24*.

[145] Zanconato, F.; Cordenonsi, M.; Piccolo, S. *Cancer Cell* **2016**, *29*, 783–803.

[146] Lin, C.-H.; Pelissier, F. A.; Zhang, H.; Lakins, J.; Weaver, V. M.; Park, C.; LaBarge, M. A. *Molecular biology of the cell* **2015**, *26*, 3946–3953.

[147] Liu, J.; Hemphill, J.; Samanta, S.; Tsang, M.; Deiters, A. *Journal of the American Chemical Society* **2017**, *139*, 9100–9103; PMID: 28657738.

[148] Ernst, R. J.; Krogager, T. P.; Maywood, E. S.; Zanchi, R.; Beránek, V.; Elliott, T. S.; Barry, N. P.; Hastings, M. H.; Chin, J. W. *Nature Chemical Biology* **2016**, *12*, 776–778.

[149] Veth, S.; Fuchs, A.; Özdemir, D.; Dialer, C.; Drexler, D. J.; Knechtel, F.; Witte, G.; Hopfner, K.-P.; Carell, T.; Ploetz, E. *ChemBioChem* **2022**, *23*, e202200005.

[150] Medzhitov, R.; Janeway, J., Charles A. *Cell* **1997**, *91*, 295–298.

[151] Gordon, S. *Cell* **2002**, *111*, 927–930.

[152] Decout, A.; Katz, J. D.; Venkatraman, S.; Ablasser, A. *Nature Reviews Immunology* **2021**, *21*, 548–569.

[153] Shin, D.; Sinkeldam, R. W.; Tor, Y. *Journal of the American Chemical Society* **2011**, *133*, 14912–14915.

[154] Bavykina, A.; Kolobov, N.; Khan, I. S.; Bau, J. A.; Ramirez, A.; Gascon, J. *Chemical Reviews* **2020**, *120*, 8468–8535.

[155] Deng, H.; Doonan, C. J.; Furukawa, H.; Ferreira, R. B.; Towne, J.; Knobler, C. B.; Wang, B.; Yaghi, O. M. *Science* **2010**, *327*, 846–850.

[156] Viciano-Chumillas, M.; Liu, X.; Leyva-Pérez, A.; Armentano, D.; Ferrando-Soria, J.; Pardo, E. *Coordination Chemistry Reviews* **2022**, *451*, 214273.

[157] Côté, A. P.; Benin, A. I.; Ockwig, N. W.; O'Keeffe, M.; Matzger, A. J.; Yaghi, O. M. *Science* **2005**, *310*, 1166–1170.

Acknowledgement

There are a great many people, I owe gratitude to.
First and foremost:

This work is dedicated to J.S.F.
– for everything and every day (especially 24.07.2021 & 13.08.2022).

I'd like to thank Don, for giving me the opportunity to work in his group. The combination of optical engineering, physic, and biology in his research never ceased to amaze me and the developed techniques in his lab are even more fascinating when one finally understands them. It was a pleasure working with you and I am especially grateful for the joined evening meetings and the sport sessions over the years. I hope you enjoyed seeing me cheering and suffering with my team as much as the other way round (although given our home team records over the last years I think the FCN and me had the worse deal).

The next people I'd like to thank are the wonderful groups I had the pleasure to cooperate and work side-by-side with over the last years: Philip and his Tinnefeld group for the constant support and the (life-saving) coffee supply. Stefan and his Wuttke group, who was a constant companion and aide over the years and always there to provide motivation and help when the research got tough again. The group of Prof. Hartschuh for all the interesting conversations, usually late in the evening. Tino and his Hoch group, which were my last remaining connection to proper chemistry in Munich. Prof. Yaghi and his students, especially Haoze, Zhe, and Nikita, who taught me all I know about water harvesting and quite a lot about scientific work-flow.

This work would not have been possible, without the support of my fellow colleagues during my time. It is impossible to mention everyone, but I would like to use this opportunity, to at least mentioned a few, loosely in order of appearance during my PhD: Wehne, who got me addicted to optical laser microscopy. Bässem, Philipp, and Waldi, for the countless support in the lab and the adventuring together. Vanessa, Nader, Chen, Ganesh, and Ivo for scientific discussions - and the fun evenings to counter balance all the science. It is also a pleasure, seeing the next generation with Pooyeh, Irene, Ecenaz, and Virgile, taking over the lab. Rock on!

A special mentioning is necessary for all those wonderful people, I had the pleasure of working side by side in the lab. My students: Timo, the very organized one, the first I'd supervised – I got better at it, I swear. Max, the very smart one and Ludwig, the

very competent one, please back me up on that claim. To my collaborators, Elsa, Simon, and Bernhard, I immensely enjoyed our conversations in the dark, while your samples slowly burned on the microscope. A special thank you for Patrick, you're a true friend and a wonderful person. Looking forward to sharing stories about the married life in the very near future. And to Irina, a friend for a long time, even if the collaboration period was short. And of course the brave colleagues, brothers and sisters in arms, sharing the caprice of the Raman setup with me: Simon, the first (and to date last) person, who got the Raman setup to produce a nice FCS curve. Petra, who helped me to at least double my knowledge about optics and setups – and there was so much more I could not learn before her time with us was over. Her influence on our labs progress cannot be overstated. And working together was great! And Fabian, who, despite my warnings had taken over the Raman setup. It couldn't be in better hands. Thank you for the darts, the official office dog, and the company! I wish you a fun marriage and a wonderful honeymoon.

Frank, we shared more beers, coffees, lab times, football (the real deal), football (the falsely labeled), dart games, Schafkopf sessions, conversations, interesting booze, parties, offices and work problems than I can count. When I find the correct words, I will thank you properly for everything. Until then, I let the list speak for itself.

A fresh PhD student can only hope to get at least a few of the following things during his PhD duration: a good project plan, competent scientific guidance, good working environment, a supervisor with superior people skills and a good eye for new projects, and good chemistry with the closest colleague. In that regard, I was incredibly lucky, since I got everything combined in one person:

Never had the statement of *last but not least* been more true: the biggest thank you is reserved for Professor Evelyn Plötz. Evelyn, you are an outstanding scientist and person. I truly enjoyed the work with you in the Ploetz Lab and I'm proud of our papers (which is a very rare thing to me). I cannot thank you enough. Raman heroes forever!

Appendix A.

Appended publications

Contents

A.1. Single Crystals Heterogeneity Impacts the Intrinsic and Extrinsic Properties of Metal-Organic Frameworks.

Check for updates

ADVANCED MATERIALS
www.advmat.de

Single Crystals Heterogeneity Impacts the Intrinsic and Extrinsic Properties of Metal–Organic Frameworks

Adrian Fuchs, Petra Mannhardt, Patrick Hirschle, Haoze Wang, Irina Zaytseva, Zhe Ji, Omar Yaghi, Stefan Wuttke, and Evelyn Ploetz**

At present, an enormous characterization gap exists between the study of the crystal structure of a material and its bulk properties. Individual particles falling within this gap cannot be fully characterized in a correlative manner by current methods. The authors address this problem by exploiting the noninvasive nature of optical microscopy and spectroscopy for the correlative analysis of metal-organic framework particles in situ. They probe the intrinsic as well as extrinsic properties in a correlated manner. The authors show that the crystal shape of MIL-88A strongly impacts its optical absorption. Furthermore, the question of how homogeneously water is distributed and adsorbed within one of the most promising materials for harvesting water from humid air, MOF-801, is addressed. The results demonstrate the considerable importance of the particle level and how it can affect the property of the material.

1. Introduction

An ongoing challenge in material science is to determine whether the bulk properties are represented by the individual particles. The difficulty arises because most common characterization methods measure statistical averages over an entire sample to achieve an enhanced signal-to-noise ratio. While high-resolution imaging or diffraction techniques can access the single-particle level, they are unsuited for multiple-particle screening and often probe only one aspect of a sample.[1] Moreover, they are often invasive,[2] require high vacuum,[3] or preclude real-space information,[4] thus preventing in situ studies of materials. These two characterization levels are also reflected in current research efforts, for instance, on metal–organic frameworks (MOFs) that mainly focus on two distinct aspects: molecular structures being tuned and bulk properties being measured.[5] MOF chemists often vary the molecular building units (e.g., installation of a functional group) and examine the corresponding change in the performance of a bulk sample (e.g., gas adsorption isotherm). Alteration of MOF particle properties can be caused twofold: (1) by differences in "extrinsic properties", that is, physical parameters like their particle size, shape, and surface structure, or (2) by variations in "intrinsic properties" ruled by chemical attributes of the framework. These include casual differences in the composition of building blocks,[6] crystallinity,[7] functionalization,[8] and defects,[2] but also designed variations as in multivariate MOFs. The interplay of both kinds of properties determines the overall performance for any application; the mutual impact of intrinsic and extrinsic variations correlated to any change in individual particle properties in situ is challenging to explore in a correlative manner.

A. Fuchs, P. Mannhardt, P. Hirschle, I. Zaytseva, S. Wuttke, E. Ploetz
Department of Chemistry and Center for NanoScience (CeNS)
LMU Munich
81377 Munich, Germany
E-mail: stefan.wuttke@bcmaterials.net; evelyn.ploetz@lmu.de

H. Wang, Z. Ji, O. Yaghi
Department of Chemistry
University of California–Berkeley
Materials Sciences Division
Lawrence Berkeley National Laboratory
Kavli Energy NanoSciences Institute at Berkeley
and Berkeley Global Science Institute
Berkeley, CA 94720, USA

The ORCID identification number(s) for the author(s) of this article can be found under https://doi.org/10.1002/adma.202104530.

© 2021 The Authors. Advanced Materials published by Wiley-VCH GmbH. This is an open access article under the terms of the Creative Commons Attribution License, which permits use, distribution and reproduction in any medium, provided the original work is properly cited.

DOI: 10.1002/adma.202104530

Z. Ji
Department of Chemistry, Stanford University
Stanford, CA 94305, USA

O. Yaghi
UC Berkeley-KACST Joint Center of Excellence for Nanomaterials for Clean Energy Applications
King Abdulaziz City for Science and Technology
Riyadh 11442, Saudi Arabia

S. Wuttke
BCMaterials
Basque Center for Materials
UPV/EHU Science Park
Leioa 48940, Spain

S. Wuttke
Ikerbasque
Basque Foundation for Science
Bilbao 48013, Spain

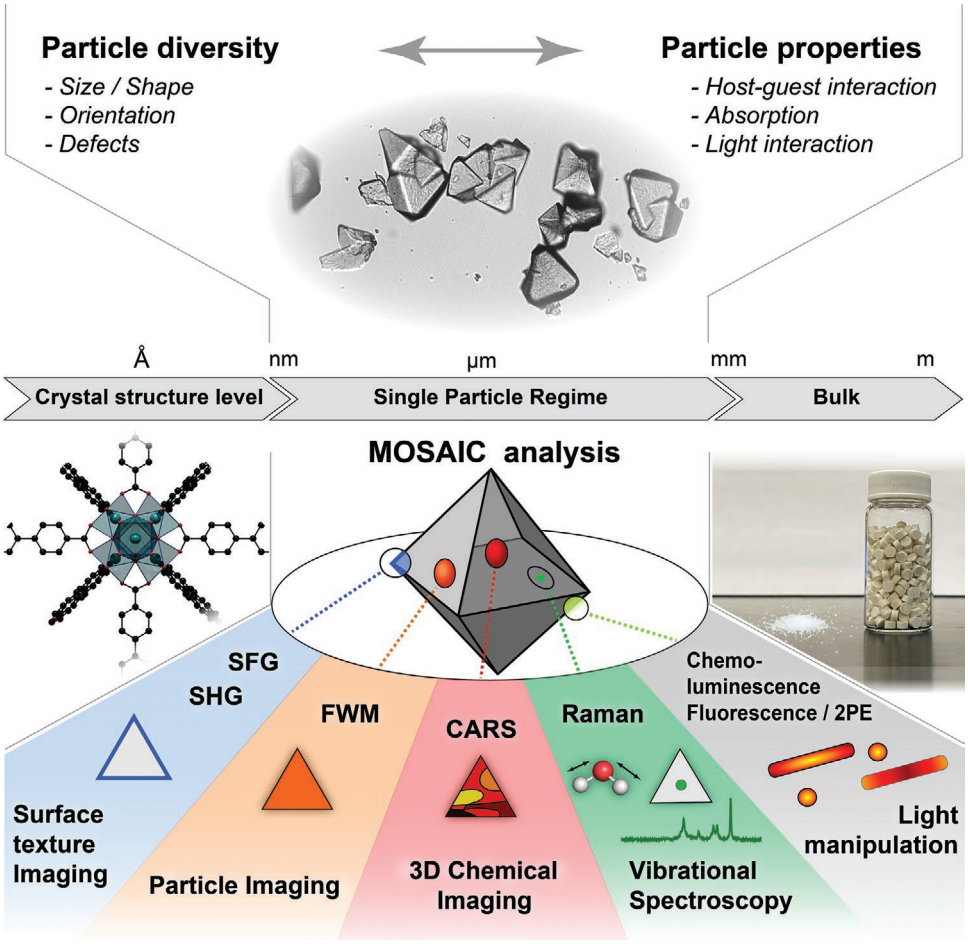

Figure 1. Graphic illustration of the MOSAIC analysis for the single-particle level characterization. The lower colored panels provide an overview of available MOSAIC methods, the observed particle characteristics, and the general modality behind the method. Images from left to right: crystal structure, brightfield image, and crystalline powder of MOF UiO-67. Abbreviations: SFG: sum-frequency generation; SHG: second harmonic generation; FWM: four-wave-mixing; CARS: coherent anti-Stokes Raman scattering; 2PE: two-photon excitation.

Optical microscopy has proven to be a reliable approach for the characterization of MOF particles, beyond bulk experiments.[9–11] Fluorescence microscopy, which relies on light-emitting functional groups or molecules as readout, could reveal key properties and parameters of MOFs by studying the location, distribution, and interplay of luminescent probes with the hosting MOF scaffold.[9] Even the level of defects and heterogeneity within MOFs could be probed at the nano level with advanced fluorescence lifetime methods.[10,12] Label-free methods, including nonlinear microscopy,[13,14] and vibrational, microspectroscopic tools[15] based on Raman scattering or IR absorption, have demonstrated their strength by following guest molecules in MOFs across micrometer-sized crystals while probing the surrounding environment and defect distributions.

Here, we report the development of a dedicated multifunctional imaging system to monitor in situ how spatial variations and particle diversity influence the material properties of MOFs without the need to consecutively use separate methodologies. We combined space-resolved fluorescence and Raman spectroscopy with a suite of optical confocal imaging techniques, which we abbreviate as multimodal optical spectroscopy and in situ imaging correlating (MOSAIC) approach (**Figure 1**). The designed MOSAIC platform combines five modalities for correlative material characterization: (1) second harmonic generation (SHG) and sum-frequency generation (SFG) to visualize the surface texture of MOF crystals; (2) the electronic response generated by four-wave-mixing (FWM) to investigate particle morphology and heterogeneity; (3) polarization-sensitive coherent anti-Stokes Raman scattering (pCARS) for mapping the 3D distribution of chemical compounds within the reticular frameworks; (4) space-resolved vibrational spectroscopy, that is, spontaneous Raman scattering, to identify and quantify any changes within the modified host material; (5) two-photon-induced chemiluminescence as a reporter signal for direct targeting light-sensitive materials. All five modalities for imaging and spectroscopy are complementary to each other and extendable by modalities that provide, for example, higher spatial resolution or faster data acquisition.[16]

The power of the label-free MOSAIC platform was demonstrated first on the multimodal characterization of single crystals of UiO-67, an archetypical MOF, as a proof-of-concept. Next, we turned our attention toward probing MOFs' extrinsic properties (i.e., particle-dependent interactions with light).

© 2021 The Authors. Advanced Materials published by Wiley-VCH GmbH

Specifically, we investigated the photochemical behaviors of the MOF, MIL-88A, which can serve as nano-antennas and exhibit morphology-dependent responses. The micron-sized crystals resonate shape-dependently with incident laser irradiation, allowing for a selective, optically triggered manipulation of crystals. Finally, we examined the intrinsic property (guest–framework interaction) of water adsorption in MOF-801 and found that water adsorbs in clusters within the material, which is characterized by missing cluster defects. Thus, the label-free, multimodal platform developed here enables us to reveal the impact of crystal heterogeneities in MOFs.

2. Results and Discussion

2.1. Development of Multimodal Imaging and Spectroscopy

The developed multimodal setup is shown in **Figure 2**a (Experimental Section, Note S1, Supporting Information) and based on a confocal laser-scanning microscope (CLSM) with two types of laser sources: (1) we implemented continuous wave (CW) lasers in the visible for fluorescence and spontaneous Raman scattering-based imaging and spectroscopy; and (2) we incorporated an all-fiber-based, jitter-free, dual-color femtosecond-laser in the near-infrared (NIR) for nonlinear imaging. The excitation laser at 774 nm was implemented as the pump laser, while the laser excitation at 1053 nm served for super-continuum generation between 770 and 1100 nm in a photonic crystal fiber (Note S1, Supporting Information). Both NIR light sources (and their combinations) are dedicated to probing nonlinear optical responses in MOF crystals at the confocal volume. The nonlinear responses are detected by avalanched photodiodes (APD) and recorded via a dual-channel time-correlated single-photon counting (TCSPC) card. Spectral information originating from the confocal volume is collected in epi-direction by a spectrograph equipped with an emCCD camera. The sCMOS camera is implemented as the third detection alternative in epi-direction and used for bright-field imaging to position the sample on the confocal microscope.

The spectroscopic signatures of the imaging modalities are designed to occur between 390 and 750 nm (Figure 2b). They are orthogonally combinable and, hence, allow for probing different material properties simultaneously. Here, label-free processes are based on nonlinear interactions of the pulsed laser fields with the investigated material and are described by their higher-order, nonlinear susceptibility $\chi^{(n)}$. The expected power dependencies for each spectroscopic signature were experimentally confirmed (Note S2 and Figure S1, Supporting Information). A detailed overview of each method is given in Table S1, Supporting Information.

To characterize metal–organic framework particles spectroscopically in a label-free manner, we incorporated SHG and SFG (Figure 2c) using the fundamental laser lines at 774 and 1053 nm of the dual-color fs-laser. The observed signals (Figure 2b) were generated at $\omega_{SHG} = 2 \cdot \omega_{pump}$ and $\omega_{SFG} = \omega_{pump} + \omega_{probe}$ and observed at 387 and 457.8 nm, respectively. To probe the inner structure and chemical composition of MOF particles, we incorporated FWM and CARS imaging in the red to NIR spectral range. FWM occurs at $\omega_{FWM} = 2\,\omega_{pump} - \omega_{probe}$ (Figure 2c), that is, its spectral signature is blue-shifted with respect to the pump pulse at 774 nm. In this paper, we mainly use FWM at 612 nm, if not stated otherwise. To provide chemical sensitivity, we chose the wavelength of the probe pulse ω_{probe}, such that the energy difference between both light fields $\omega_{pump} - \omega_{probe}$ coincides with a specific vibrational transition ω_i of the material; in Figure 2b, it is illustrated for the C—C stretch vibration in UiO-67 at 688 nm, that is, at 1614 cm^{-1}. This resonantly enhanced FWM process is referred to as CARS (Figure 2c). To suppress any additional, non-resonant, electronic background, we exploited the polarization-dependence of the signal and implemented polarization-sensitive CARS (pCARS; Experimental Section).[17] In combination with spectral focusing, [18] we established pCARS as a fast 3D chemical imaging tool that selectively maps characteristic Raman resonances of MOFs. As the last imaging contrast, we incorporated one photon (1PE) and two-photon excitation (2PE) induced fluorescence imaging at 532 and 774 nm (Figure 2c). These allowed mainly for addressing fluorescent probes or MOF materials emitting in the blue/green spectral range (Figure 2b) if combined with other modalities probed by our MOSAIC approach.

Next, we demonstrated the strength of the MOSAIC platform to correlatively image and spectrally characterize reticular materials, in particular, MOF at the single-particle level. In a proof-of-concept experiment, we studied the electronic and vibrational properties of UiO-67 particles (Note S4, Supporting Information) in a space-resolved manner. To probe the surface properties of unlabeled UiO-67 particles, we used both spectroscopic signatures: SHG and SFG. SHG allows for the mapping of surfaces or non-centrosymmetric materials and polarization information in crystalline structures (Table S1, Supporting Information). SFG as a second-order nonlinear optical response is equally sensitive to non-centrosymmetric species as it is usually the case for symmetry-breaking interfaces. As seen in both panels of Figure 2d, both types of imaging clearly show the surface roughness of UiO-67 and reveal cracks and substructures of the particle surface, which are barely visible in bright-field images. Next, we tested two label-free imaging modalities to access the 3D structure of UiO-67, namely FWM and pCARS (Figure 2e,f). The spectral regions addressed for FWM (no spectral resonance) and pCARS (resonant to the strong peak at 1615 cm^{-1}) are marked in Figure 2g. The particles show a very homogeneous signature and regular shape identical to the bright-field image, as it is expected from the crystalline, solid material with little to no defects. FWM and pCARS offer strong 2D sectioning capabilities that restrict the detected signal to single cross-sections through the UiO-67 assembly. Consecutively, it can reconstruct the inner structure of MOF crystals in 3D (Figure S2, Supporting Information). To control the homogenous chemical composition of UiO-67, we further employed spontaneous Raman spectroscopy within the particle volume as well as at air–particle interfaces of the same particle in addition to CARS microscopy. (Figure S3, Supporting Information). A detailed assignment of vibrations in the solid-state Raman spectra of linker and UiO-67 (Figure 2g) is given in Table S2, Supporting Information. In line with space-resolved Raman mapping of the sample (Figure S4, Supporting Information), both measurements yielded no spectral differences in the recorded Raman signatures but concomitantly confirmed the crystallinity of the sample (Figure S5, Supporting Information).

© 2021 The Authors. Advanced Materials published by Wiley-VCH GmbH

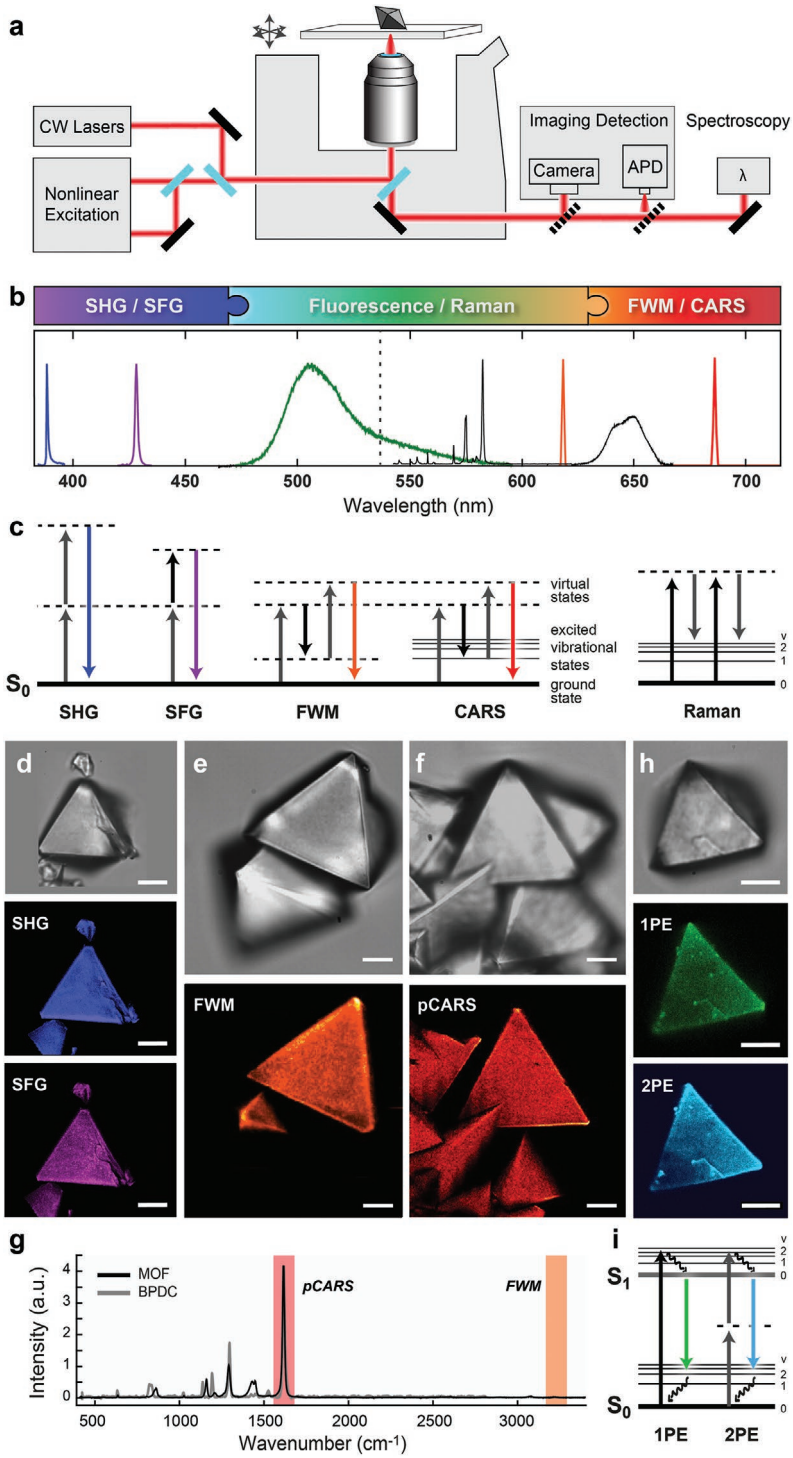

Figure 2. MOSAIC analysis: physical background, technical realization, and characterization of UiO-67 crystals. a) Schematic of the multimodal, scanning microscope. b) Incorporated imaging modalities are spectrally complementary: SHG and SFG occurs at 387 and 458 nm as shown on a silica wafer; 2PE induced emission of RBITC is centered around 510 nm; Raman scattering in UiO-67 and water after 532 nm excitation can be detected between 550 and 650 nm and FWM and pCARS in UiO-67 for example, at 612 and 688 nm. c) Energy diagrams of the implemented nonlinear processes, including SHG, SFG, FWM, CARS, and Stokes Raman scattering. d–f) Unlabeled UiO-67 particles imaged by bright field and nonlinear microscopy, including SHG and SFG (d), FWM at 3300 cm^{-1} (616 nm; e), and pCARS at 1615 cm^{-1} (688.2 nm; f), g) Spontaneous Raman signature of UiO-67 particles and their linker molecule BPDC in solid state phase. The spectral regions chosen for FWM and pCARS imaging in panel (e,f) are marked in red and orange, respectively. h) Brightfield and fluorescence images of RBITC-labeled particles after 1PE and 2PE induced emission at 532 and 774 nm. i) Corresponding energy diagrams for 1PE and 2PE induced fluorescence in panel (h). Scale bars: 10 µm. Arrows indicate the electric fields of exciting light sources and resulting signatures.

© 2021 The Authors. Advanced Materials published by Wiley-VCH GmbH

To highlight the flexibility of the developed system, we further incorporated luminescence-based imaging with a high signal-to-noise ratio. Figure 2h shows fluorescently labeled UiO-67 particles after one-photon excitation (1PE, green; Figure 2i) at 532 nm and two-photon excitation (2PE, cyan; Figure 2i) at 774 nm. These particles were labeled with 2-RhodamineB-isothiocyanate (RBITC) at the particle surface based on a linker-exchange reaction,[10] while particles in Figure 2d–f were completely unlabeled. Due to the 1.6-fold better axial resolution as well as the centrosymmetric sensitivity of 2PE imaging, small cracks and defects at the surface are more visible. Nevertheless, intrinsic labeling of 3D structures is challenging and interferes with the original particle structure. Labeling alters the material under investigation. Moreover, the fluorescence emission is inherently spectrally broad (Figure 2b), which significantly limits the multiplexing capabilities. Overall, the one- and two-photon excitation images in Figure 2h highlight the resolution enhancement of nonlinear optical microscopy compared to one-photon CLSM. The developed multimodal microscope system can combine these modalities orthogonally, as demonstrated for simultaneous 2PE, SHG, and FWM imaging (Figure S6, Supporting Information).

2.2. Correlating MIL-88A Crystal Morphologies with Their Optical Properties

To illustrate the influence of extrinsic properties of MOF crystals, we investigate the correlation between the optical properties and different morphologies of MIL-88A via our MOSAIC platform. We draw our attention to MIL-88A since it is frequently employed for applications including drug delivery,[19] sensing,[20] and photocatalysis,[21] but also synthesized in a large variety of different morphologies.[22] We exploited the label-free modalities of our microscope in combination with spatially resolved spectroscopy since the quenching behavior of the iron centers in MIL-88A renders fluorescence-based single-particle studies challenging.

MIL-88A crystals can be synthesized in four different distinct morphologies:[22] as needle-like and bipyramidal microparticles with sizes of ≈1–4 µm, bipyramidal nanoparticles with diameters ≈300–500 nm, and spherical nanoparticles of 50 nm in size (Note S4, Supporting Information). Independent of their morphology, all particle types show an identical unit cell as seen from the XRD.[22] Similar findings were made using Raman spectroscopy (Figure S7, Supporting Information). While the Raman signature of linker molecules strongly differs from MIL-88A particles, it is remarkably similar for particles with different morphologies (Table S3, Supporting Information). No additional enhancement effects or shifts in Raman resonances due to varying particle geometries were observed. To study the influence of extrinsic properties on the optical properties of MOF crystals, we chose crystalline microparticles, which differ in morphology but share similar dimensions. **Figure 3**a,b shows the SEM images of both microparticle morphologies. We first determined the length and width distribution for both morphologies by label-free FWM imaging at ≈3400 cm^{-1} (i.e., at 612.7 nm; Figure 3c; Figure S8, Supporting Information). The elongated needle-shaped particles have a length of 3.29 (±1.12) µm and a width of 0.79 (± 0.34) µm. The broad length distribution with an FWHM of 2.52 µm can be explained by the unsynchronized stochastic growth during synthesis.

In contrast, the approximately spherical, bipyramidal microparticles show a narrow distribution 1.47 (± 0.23) µm in length and 1.26 (± 0.18) µm in width. Next, we imaged a mixture of both morphologies with FWM microscopy to study how this spatial variance of the MIL-88A morphologies influences their electronic response. While both types of particles are sensitive to FWM (Figure 3d, upper panels), the observed FWM intensity of MIL-88A needles depends on two parameters: the volume of individual particles and the alignment with respect to the *p*-polarization of the excitation laser field. Horizontally aligned particles are maximally susceptible to FWM. Their observed intensity decreases with an increasing angle toward the horizontal orientation. It almost vanishes for particles with a vertical alignment as seen in the upper panels of Figure 3d. In contrast, bipyramids are strongly susceptible to FWM without any preferred orientation. In addition to FWM, they surprisingly exhibit chemiluminescence (CL; Figure 3d, blue, lower right panel) with a spectrally broad emission spectrum, easily distinguishable from the FWM response (Figure S9, Supporting Information). This property is not observed for needle-shaped MIL-88A particles at an identical excitation power (i.e., below 1.9 and 0.1 mW for the pump and probe laser pulses). The observed luminescence is accompanied by a strongly progressing degradation and consecutive splitting of particles (Figure 3d, left lower panel, marked particle). The degradation products are visible in the bright-field channel. They co-localize with the bipyramidal particles before the scanning and the detected CL signature during the imaging process.

Degradation and resulting chemiluminescence of the MIL-88A microcrystals can occur, when the absorbed energy provided by the pulsed, incident laser radiation is higher than the activation energy for the oxidation reaction with surrounding oxygen (Figure S9c, Supporting Information). Here, the optical absorption of (sub-)micron-sized particles is not only dependent on the absorption coefficient of the material itself, but also on morphology-dependent resonances, so-called Mie modes.[23] Their contribution to absorption and scattering of light by small particles becomes most dominant when the light-induced electromagnetic field inside the particle boundaries becomes resonant with the incident light fields. As predicted for elongated particles,[24] the absorption of micron-sized particles is dictated by their chemical composition, the incident laser field, the surrounding medium as well as their size and shape. Since the first conditions are identical for the different types of MIL-88A microcrystals, differences in absorption behavior are thought to only depend on the shape or size of the crystals (or both). As shown in Figure 3b, which highlights the major axis (length) and the minor axis (width) for needle and bipyramidal crystals, the overall shapes of the particles mainly differ in the width over length ratio. We, hence, introduced the ellipticity per particle as a ratiometric parameter to describe their morphology. It is given as 1 minus the width to length ratio and varies between 0 and 1 for spherical and elongated particles, respectively. The advisability of the ellipticity parameter is illustrated when comparing the volumes of needle-like and bipyramidal particles, which can be approximately

© 2021 The Authors. Advanced Materials published by Wiley-VCH GmbH

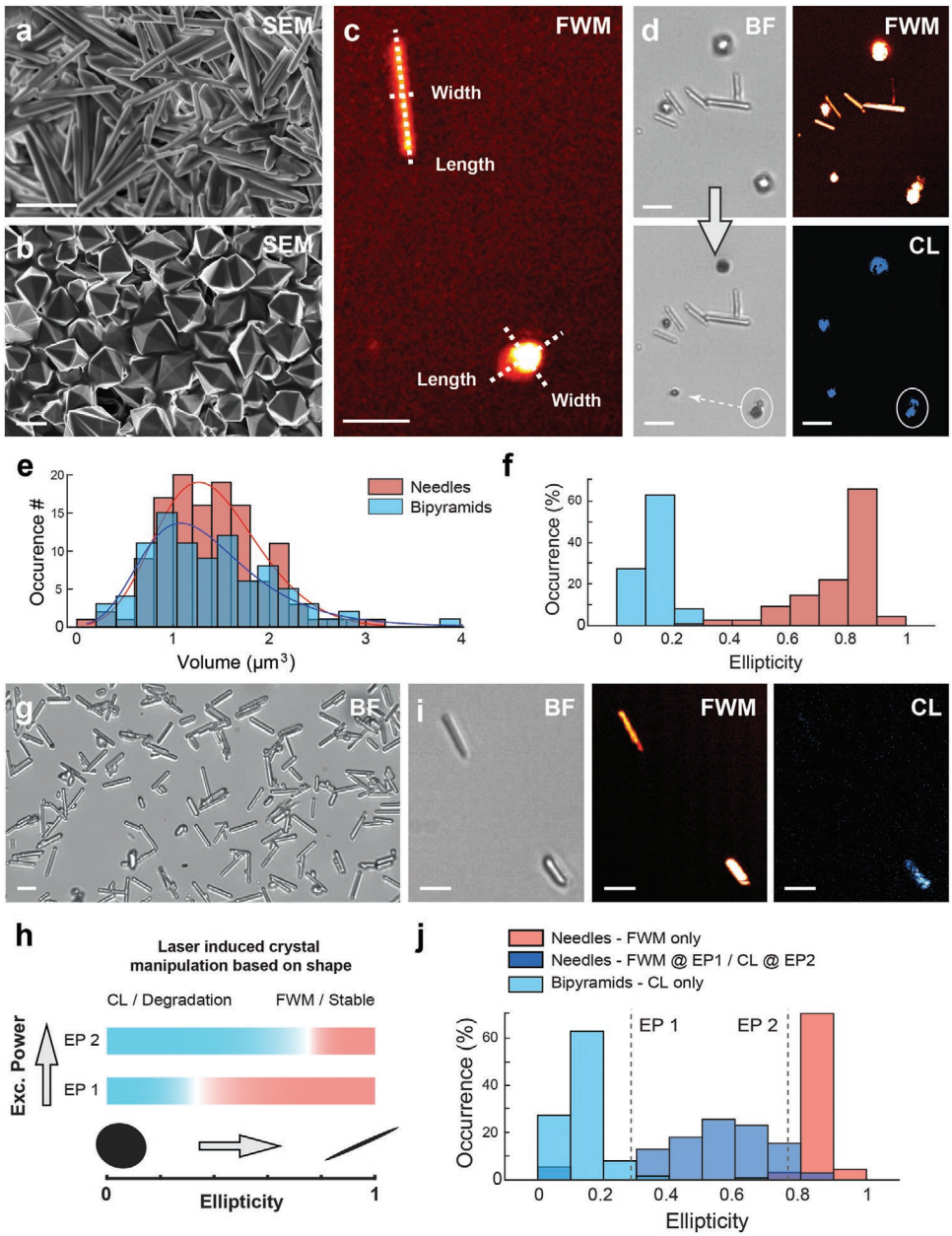

Figure 3. Optical behavior of MIL-88A crystals for different morphologies. a,b) SEM images of particles in needle (a) and bipyramidal morphology (b). c) Label-free FWM imaging at 3400 cm^{-1} can determine length and width for every particle. d) Correlative imaging by brightfield, chemiluminescence (CL), and four-wave-mixing FWM. e) The volume and f) ellipticity distributions for each morphology clarify the difference in optical behavior. While both morphologies are comparable in volume (Needles: $V = 1.08 \pm 0.52$ μm^3; $N = 246$. Bipyramids: $V = 1.18 \pm 0.49$ μm^3; $N = 115$), they are distinguishable by their ellipticity (Needles: $E = 0.81 \pm 0.09$; $N = 246$ / Bipyramids: $E = 0.13 \pm 0.04$; N = 115). g) The wide distribution in ellipticity represents the variance in particle length of needle-like MIL-88A, also observed in brightfield. h) Schematic of the observed correlation between CL occurrence and ellipticity depending on the excitation power from panel (f) at $EP_1 = 1.9$ mW. An increased excitation power ($EP_2 = 3.0$ mW) is expected to shift the absorption threshold to higher ellipticities, resulting in increased CL for needle-like particles. i) BF, FWM, and CL images of needle-shaped crystals at EP_2. Only the bipyramidal particle shows CL. Scale bars: 1 μm. j) Ellipticity distribution of needles showing only FWM (red, $N = 75$), needles showing CL at EP_2 (lilac, $N = 40$), and bipyramidal particles (light blue, $N = 115$). The dashed lines indicate roughly the threshold for the respective excitation powers. Scale bar (except panel (i)): 2 μm.

described as ellipsoidal and spherical volume. Their distribution is depicted in Figure 3e,f (Note S5, Supporting Information). While the needle-like particles feature a slightly larger volume of 1.08 (± 0.52) μm^3 than bipyramids (1.18 ± 0.49 μm^3) on average, they still share a similar distribution (Figure S8 and Table S4, Supporting Infomation). The overlap of both distributions is very high, dissuading the idea that size is the dominant factor for intrinsic particle absorption. It is further supported by the fact that bipyramidal crystals of varying sizes show chemiluminescence due to degradation, while needles of similar

© 2021 The Authors. Advanced Materials published by Wiley-VCH GmbH

volume stay intact (Figure S10, Supporting Information). The ellipticity, on the other hand, clearly differentiates between the morphologies and varies between 0.81 (±0.09) for needles and 0.13 (±0.04) in the case of bipyramids. Notably, the ellipticity distribution of the bipyramids is narrow, while the distribution of needle-like particles features a sharp peak around 0.85 and a broad width between 0.3 and 0.8.

Overall, needle-like particles show a wide distribution in size and shape (Figure 3g). As indicated by the additional chemiluminescence (Figure 3d), there might be a strong correlation between the reduced ellipticity of particles and the enhanced interaction of the exciting laser field. Our results predict that more sphere-like particles with small ellipticity foster the coupling of the exciting laser field to the particle and consecutively, the emission of chemiluminescence by single MIL-88A crystals (Figure 3h). This implies we could generate chemiluminescence in needle-like particles by adjusting the incident excitation power and target MIL-88A crystals below a certain ellipticity threshold specifically. The observed FWM signature of MIL-88A results from a nonlinear interaction with two pulses laser sources: a spectrally broad but chirped probe beam at low intensity and a spectrally narrow pump beam at high intensities. While we used an excitation power of I_{probe} = 0.1 mW and I_{pump} = 1.9 mW at first (Figure 3c–f; which we referred to as excitation power EP_1), we increased the excitation power of the pump beam to 3.0 mW (EP_2) to test our hypothesis in the following. When measuring particles with needle morphology at higher excitation power, we, indeed, found the same variance in absorption behavior for the particles as in the artificial mixture of needle and bipyramidal morphologies depicted in Figure 3c. One fraction was susceptible to FWM only, while other particles showed additional chemiluminescence (Figure 3i). To exclude the possibility that the luminescent particles have a different chemical composition, we additionally used single-particle-based spontaneous Raman spectroscopy (Figure S11, Supporting Information). The spectrum clearly identified the luminescent particle as MIL-88A. When sorting the ellipticities of individual needle particles according to their absorption behavior, we could directly distinguish between the "FWM only" fraction and the luminescent fraction (Figure 3j). The group of particles only featuring an FWM signal as the optical response was characterized by a narrow distribution (FWHM = 0.07) of elongated needles centered with an ellipticity of ≈0.86 (± 0.015). The degraded particles (CL, lilac) featured a much broader distribution (FWHM = 0.33), centered around 0.63 (± 0.07). They comprise a mixture of particles with varying degrees of the needle and the bipyramidal morphology. The dashed grey lines in Figure 3j indicate the ellipticity threshold for the optical absorption at the two different excitation power levels. Of additional interest in ellipticity is the overlap of both fractions between 0.7 and 0.9. The existence of this group of particles can be explained by two scenarios, in which the intrinsic optoelectronic properties of well-defined needle particles are altered: (1) it depends on a coupling of magnetic fields by neighboring particles, similar to the reported behavior of dielectric silica rods.[25] This is dependent on the proximity and concentration of particles and should vanish for not-stationary particles in solution. Indeed, we found such enhanced light-induced degradation of MOF needles for overlapping MIL-88A particles (Figure S12a, Supporting Information). (2) The absorption is caused by an increase in the morphologic complexity as suggested by Kulachenkov et al.[26] Our findings indicate that the observed absorption might be the result of defects within the MOF structure (Figure S12b, Supporting Information). Hence, MOSAIC enabled us to unveil the relationship between the extrinsic property of particle morphology with their absorption behavior. To further highlight the impact of local variances on intrinsic properties, we investigated the water distribution in MOF-801 crystals.

2.3. Particle-Dependent Host–Guest Interactions of MOF-801

MOF-801 is an auspicious material for harvesting water from humid air.[27] It was reported that MOF-801 single crystals with lower volume have a higher affinity to water than larger-sized particles.[28] This difference, however, could not be explained by the crystal size alone nor correlated with the local morphology and intrinsic properties of the material. We, hence, investigated the position-dependent performance of water adsorption in MOF-801 particles in situ.

MOF-801 crystals feature an octahedral shape with sizes up to tenths of micrometers with triangular faces. They consist of zirconium oxide clusters and fumaric acid linkers arranged in a cubic framework (Note S4, Supporting Information).[28] Per unit cell, three water binding sites are reported: two tetrahedral and one octahedral binding site. Starting from the dry MOF material, water molecules attach first to primary binding sites, that is, the zirconium oxide clusters in the tetrahedral cavities. Consecutively, water molecules bridge the primarily bound molecules in the tetrahedral cavities before filling up the octahedral cavities until saturation is reached.[28] To elucidate the distribution of water in MOF-801, we employed Raman spectroscopy and hyperspectral imaging in combination with pCARS imaging, next. **Figure 4**a depicts the Raman spectrum of the evacuated MOF-801 (black curve). The MOF scaffold is characterized by its dominant bands at ≈1440 cm^{-1} (symmetric O-C-O stretching mode), ≈1666 cm^{-1} (C-C stretching mode), and ≈3150 cm^{-1} (C-H stretch vibration) and is in excellent agreement with the literature (Table S5, Supporting Information). The stretch mode of μ_3—OH in Zr cluster is present as a sharp resonance at 3680 cm^{-1} (Figure 4b). Upon exposure to humid air, additional water molecules diffuse into the material and adsorb within the pores. This process alters the Raman spectrum, most dominantly between 3100 and 3700 cm^{-1} (Figure 4a,b): the signature of the hydroxyl groups in the crystal lattice around 3680 cm^{-1} vanishes due to hydrogen bonding with adsorbed water molecules while a broad Raman resonance between 3200 and 3600 cm^{-1} appears due to the O-H stretch vibration of bridging water molecules (spectra at ≈33%RH). This broad peak is characteristic for liquid water and served to visualize the water adsorption in the framework via Raman based imaging.

We, therefore, addressed the question of how homogeneously water is distributed and adsorbed within MOF-801. To map the water distribution over a region of interest and

© 2021 The Authors. Advanced Materials published by Wiley-VCH GmbH

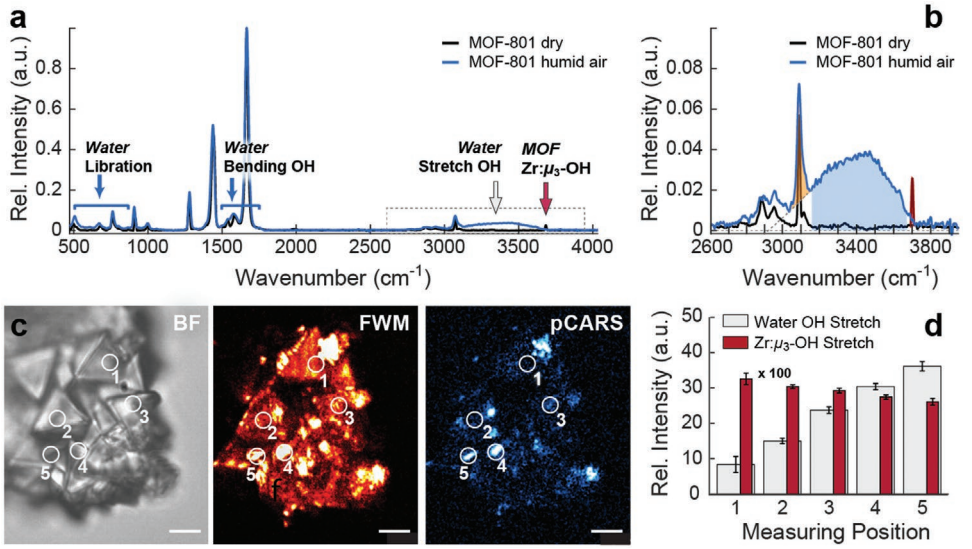

Figure 4. Water adsorption in MOF-801. a) Raman spectrum of MOF-801 in dry (black) and humid environment (blue; 32%RH). Characteristic spectral contributions due to adsorbed water and the hydroxyl vibration within the Zr cluster are marked with arrows. b) Zoom-in of (a). The integrated bands serve to determine the relative amount of water and hydrogen bonding compared to MOF-801. c) Water distribution in MOF-801 crystals visualized by brightfield, FWM, and pCARS imaging at 10%RH. Numbered circles indicate measurement points in (d). Scale bar: 2 µm. d) Relative amount of adsorbed water observed by Raman spectroscopy at selected areas in panel (b).

quantify the absolute amount of water at 3%RH, we employed spatially-resolved pCARS imaging in addition to brightfield and FWM imaging. Figure 4c displays an example area of clustered crystals at 22.1 °C and 3%RH. While brightfield and FWM imaging showed a random clustering of crystals, the pCARS modality revealed an additional, surprisingly uneven distribution of water molecules over the field of view. Most areas showed a similar level of uptaken water as observed by hyperspectral Raman imaging on homogeneously grown crystals (Figure S13, Supporting Information), but small, localized spots exhibited a significantly higher water content. We performed in situ Raman spectroscopy at selected points in the region of interest to exclude the possibility that this distribution could be an artifact introduced by the imaging modality or a potential nonlinear FWM background hampering a quantitative determination of uptaken water. Using the linear concentration dependence of spontaneous Raman scattering, we determined the relative amount of water compared to MOF-801 (Figure 4c; Note S6, Supporting Information) and found a correlation between an increased level of adsorbed water and the increase in pCARS intensity (Figure 4d). Concomitantly, we observe a reduction in signal strength of the μ_3-OH stretch in Zr cluster around 3680 cm^{-1}, which can be ascribed to the formation of hydrogen bonds between adsorbed water molecules and the μ_3-H residue. Although less prominent, we equally observe localized water accumulations in samples exposed to higher humidity (Figure S14, Supporting Information). Water molecules tend to accumulate in small, confined areas (e.g., at measuring position 5, Figure 4c). When comparing the results from brightfield and pCARS imaging of various particles in 3D, we could indeed identify locally confined volumes with enhanced, incorporated water (Figure S15, Supporting Information) that co-localized with deformed crystals visible in the brightfield channel.

Structural defects are ubiquitous and occur at various levels in MOFs,[29] starting at missing linkers and/or metal sites, substitutional defects over to crystal mismatches or amorphous particles, to name a few. In particular, extended defects in MOF, that is, at a grain boundary of two crystals or within polycrystalline areas, could contribute to the enhanced water uptake. To decipher the underlying mechanism of water collection and the chemical nature of the observed defects, we set out for various correlative approaches. We combined pCARS imaging for fast chemical identification, spontaneous Raman spectroscopy to probe the local chemical fingerprint of the material and/or the defects, fluorescence imaging for monitoring local cluster defects and FWM imaging, which allows to visualize structural defects[14] by probing the electronic response of the material.

Enhanced water incorporation is spatially confined in 3D as observed by pCARS (**Figure 5**a). FWM imaging can identify spatial inhomogeneities (as seen at locations 1–3), which frequently (but not conclusively) coincide with areas localized by pCARS. Confined water uptake below the dew point can only occur if additional space due to missing linker or metal sites is available. To answer the question, if enhanced FWM signals were due to unsaturated metal sites, we made use of the liquid-phase, acid-catalyzed self-condensation reaction[30] of furfuryl alcohol (FA). Oligomerization of the colorless FA takes place at accessible Brønsted acid sites leading to fluorescent products (see Note S7, Supporting Information). We employed two-photon excited fluorescence microscopy in correlation with FWM imaging to probe the spatial distribution of the FA condensation mediated by MOF-801 via fluorescence imaging and the material's response by FWM (Figure 5b,c). As expected, we observed pronounced emission in the green channel (520–600 nm), at uneven surfaces and cracks (white area), as

© 2021 The Authors. Advanced Materials published by Wiley-VCH GmbH

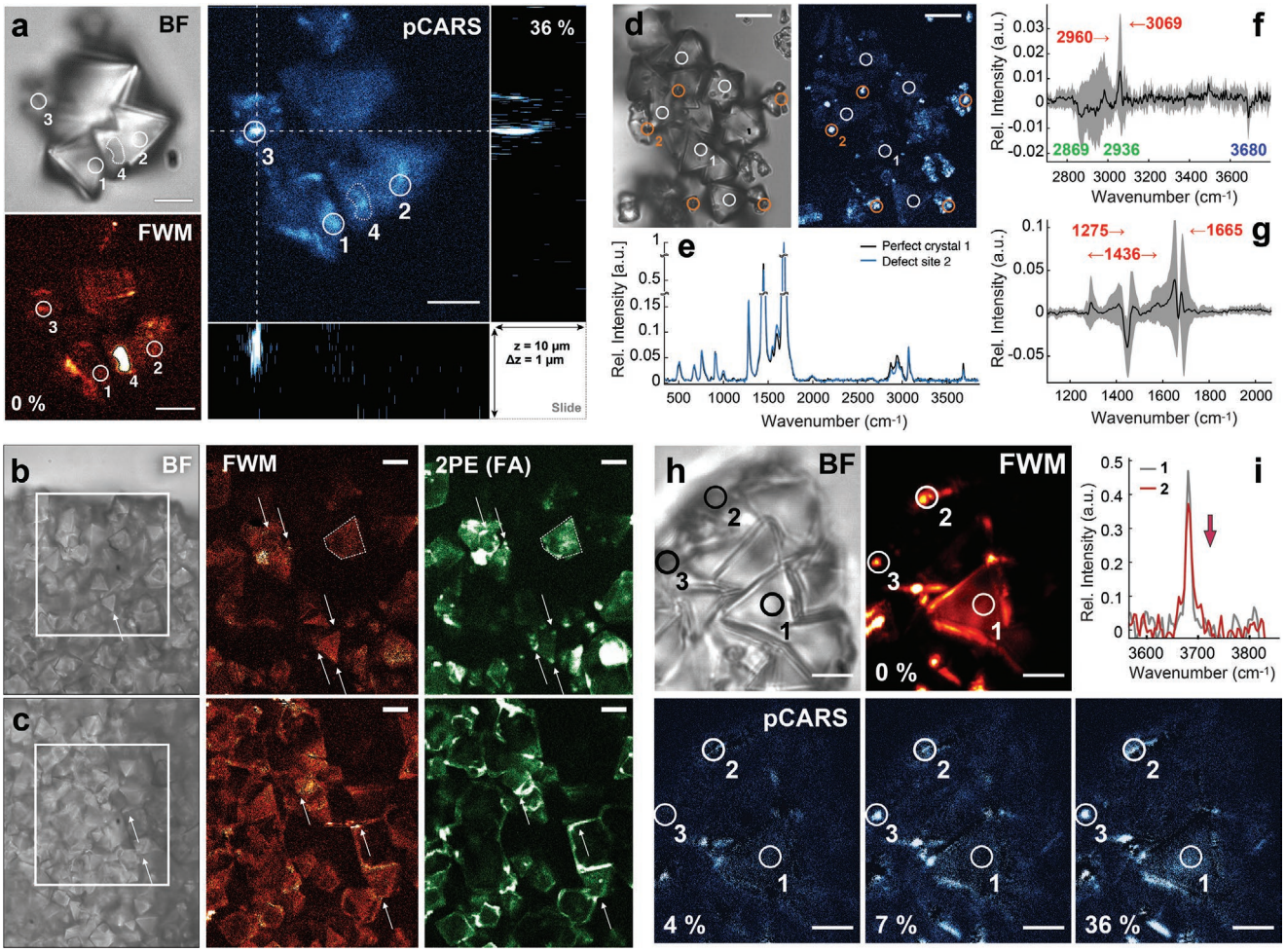

Figure 5. Chemical characterization of water clustering sites in MOF-801. a) 3D localization of a confined water cluster in MOF-801 by pCARS at 35.6%RH in comparison to FWM at 0%RH. b,c) Detection of open metal clusters by acid-site assisted polymerization of furfuryl alcohol (FA) in MOF-801 crystals using BF, FWM, and 2PE imaging. Enhanced polymerization is observed at b) edges and tips and c) areas of inter-crystal growth. d–f) Correlative characterization of the chemical environment at areas with enhanced water incorporation by d) pCARS imaging and e–g) spontaneous Raman spectroscopy. Water cluster sites and regular crystals were identified by pCARS imaging at 38.5 %RH (d). e) Raman spectra at positions 1 and 2 that are marked in (d). f–g) Difference spectra between the Raman signature at defect sides and sites of normal crystal growth in the fingerprint region (f) and C-H stretch to water region (g). The mean values (line) and standard deviations (shaded area) represent the average over five locations each. Differences due to missing clusters (blue) and concomitant reduction in residual DMF (green) and uncaging of fumaric acid (red) are marked for the corresponding resonances. Arrows indicate the direction of spectral shift. h) Water distribution at different relative humidities mapped by pCARS imaging in correlation with FWM microscopy at 0%RH and Raman spectroscopy. i) For 0 %RH, the Raman signature at confined water clusters also shows a reduction of the Zr: μ_3—OH stretch vibration, indicating a smaller degree of metal clusters in MOF-801. Scale bars: 5 µm. Abbreviations: bright-field (BF), four-wave mixing (FWM), two-photon excited fluorescence (2PE), polarization-sensitive coherent anti-Stokes Raman scattering (pCARS).

well as at sharp edges of MOF-801 crystals (Figure 5b; arrows). Here, unsaturated metal sites at the interface of three surfaces were freely accessible and featured strong catalytic activity. Enhanced polymerization was further observed at the interface of grain boundaries (Figure 5c; arrows), where different crystals were growing into each other. While the fluorescence assay successfully reported extended defect sites due to missing linkers, the collected material response by FWM imaging hardly co-localized with the signature of polymerized FA molecules, indicating that open metal sites are not the key element responsible for enhanced water incorporation.

Next, we combined pCARS imaging with in situ Raman spectroscopy to directly probe the local chemical environment around water clusters (Figure 5d–g). First, confined water clusters in MOF-801 were identified via pCARS imaging at 38.5 %RH (marked by orange circles in Figure 5d). Afterward, the sample was dried for half an hour by a nitrogen flow to study the chemical differences without the influence of guest molecules. The chemical composition of MOF-801 in dry state was probed by spontaneous Raman spectroscopy. A comparison (Figure 5d,e) between the spectral signature of a defect site (Position 2) and regular crystal (Position 1) reveals large chemical similarities of the MOF material probed within the confocal volume. Nevertheless, subtle changes in amplitude, that is, in the concentration of different species are apparent. Distinct changes in the fingerprint and water region become

© 2021 The Authors. Advanced Materials published by Wiley-VCH GmbH

visible in the difference spectrum (between defect sites to crystals; Figure 5f,g). Negative signatures report on species that are more abundant in the regular crystalline material. Figure 5f reveals a decrease in Zr: μ_3-OH stretch vibration intensity at 3680 cm^{-1} and a reduction of the aliphatic C-H stretch vibration between 2830 and 2950 cm^{-1} due to fewer residual DMF molecules. Both findings hint toward missing metal sites that are complexed with residual organic solvent molecules in the regular material. As the vibrational signature of free fumaric acid significantly differs from complexed linker molecules in MOF-801 (Tables S3 and S5, Supporting Information), missing metal sites should cause shifts of the linker-associated resonances. Indeed, we observe a broadening and shift of linker-associated Raman resonances toward the signature of the free fumaric di-anion,[31] respectively linker molecule in the fingerprint region (Figure 5g). In particular, the broadening of the symmetric carboxyl stretch vibration at 1436 cm^{-1} showcases the coexistence of fully-coordinated and partially-coordinated linkers in the studied volume. Our findings indicate that missing clusters defects are majorly responsible for the macropore formation and enhanced water incorporation, which is in line with a missing co-localization with FA polymers that form at metal clusters (Figure 5b,c).

On the other hand, it is unintuitive, as one might expect less binding events of water at missing cluster defects due to its higher affinity for hydrogen bonding to cluster than to carboxylate residues of the linker. As different kinds of defects might contribute at early and later stages of water uptake, we next probed the onset and progression of water adsorption in macropores by pCARS at different humidities. In combination with Raman spectroscopy to identify missing cluster defects and FWM to visualize the material response, the MOSAIC platform can correlate the results and enables in-depth studies of the influences of defect types on water uptake (Figure 5h,i). As expected, FWM shows a heterogeneous material response with strong signals at interfaces and edges (Figure 5h) and highly located defect sites. pCARS reveals already at 3.9 %RH, an overall broad uniform increase of water uptake mixed with confined areas that show an enhanced amount of water. While spontaneous Raman spectroscopy could confirm a reduced availability of metal centers at these sites (Figure 5i), pCARS imaging clearly shows a heterogeneous uptake of water with increasing exposure to humid air: we observed a gradual increase of water uptake, for example, at position 2, while water uptake at position 3 shows an almost stepwise response – which underlines, again, the heterogeneous chemical surrounding of each water cluster.

Overall, our findings give strong evidence that primarily missing metal clusters are responsible for extended defects, which provide additional bindings sites for water. Water can accumulate in the macro-pores created by the initial defects, which consecutively act as seeds for droplet formation and, hence, locally restricted compartments with high water content. Moreover, this example highlights the capability of the developed approach: while each of the applied spectroscopic techniques provides selective insights, MOSAIC allows for combining them in a full picture, in which macropores can be localized, chemically characterized, and water uptake monitored in situ in a spatially resolved manner.

3. Conclusion

We presented a dedicated, correlative optical imaging approach combining nonlinear microscopy and spectroscopy to resolve hitherto unexplored property relations of MOF crystals at the single-particle level. Our method addresses the gap of material characterization between the bulk and the unit-cell regime, allowing for studying heterogeneity in properties and their interplay across crystals and within a single crystal. The developed MOSAIC approach allows to study the physical and chemical variance of MOF particles in a label-free manner as shown for UiO-67, to answer how particle composition and morphology affect material properties. To demonstrate this fundamental connection, we explored the orthogonal nature of FWM and degradation-induced chemiluminescence in MIL-88A crystals and could reveal an unexpected correlation between optical properties of the material and their morphology. In a second example, we investigated the chemical nature of extended defects in MOF-801 and showed by a correlative study in situ that heterogeneities in intrinsic properties such as defects in MOF-801 affect the host–guest interaction of the material. These two examples highlight the large versatility of the developed multimodal system, which is easily applicable to study further MOF systems and their heterogeneity with respect to host–guest interaction, multivariance in composition or defects combining information of separate methodologies in situ. Since the interplay of intrinsic and extrinsic properties determines the final performance of the synthesized material, we anticipate that the MOSAIC analysis giving direct access will turn into an important tool for material characterization.

4. Experimental Section

Sample Preparation: Unlabeled UiO-67 crystals were synthesized from Zirconium(IV) chloride, biphenyl-4,4'-dicarboxylic acid, and benzoic acid following the procedure by Ko et al.[32] Labeling of UiO-67 crystals with RBITC by linker exchange followed the protocol by Schrimpf et al.[10] Both particle types were evacuated after synthesis and stored in powder form. Crystalline MIL-88A particles as differently sized needles and pyramidal particles were synthesized from Iron(III) chloride hexahydrate and fumaric acid following the optimized procedures described in Hirschle et al.[22] They were stored in ethanol or DMF. A detailed description of the synthesis and sample preparation is given in Note S2, Supporting Information.

Multimodal Nonlinear Scanning Microscope: Images and spectra were taken on a home-built, confocal laser scanning microscope (Note S1, Supporting Information) equipped with three light sources: two CW lasers at 532 and 633 nm as well as a fiber-based, dual-color femtosecond laser system (FemtoFiber dichro bioMP, Toptica Photonics, Germany) with two synchronized pulse trains at 80 MHz. It provides laser pulses with ≈180 fs pulse duration and 1 W output power at 774 nm. The second fs-laser has a central wavelength of 1053 nm, an output power of 1.5 W, and a transform-limited pulse duration of ≈135 fs. The unmodified laser pulses at 774 and 1053 nm serve for 2PE, SHG, and SFG imaging. For FWM and CARS microscopy, laser pulses at 774 nm are chosen as pump pulses. To coherently excite molecular vibrations in MOFs, the authors employed the 1053 nm excitation to derive a spectrally broad probe beam by super-continuum generation within a photonic crystal fiber (PCF, NL-1050-Zero-2, NKT Photonics; Note S1, Supporting Information) with spectral components between 770 and 1100 nm. The available supercontinuum was temporally stretched afterward using an SF6 glass rod for spectral focusing. The spectral resolution could be tuned between 15 and 25 cm^{-1} depending on the added chirp. To address the full spectrum of MOF particles, the temporal delay between both laser pulses

© 2021 The Authors. Advanced Materials published by Wiley-VCH GmbH

was adjusted. The excitation power as well as the linear polarization at 774 nm (tuned for pCARS) were controlled by a half-wave plate in combination with a linear polarizer. The diameter of all exciting lasers was fourfold expanded to overfill the objective of the confocal microscope.

The CW laser lines were superimposed with the designed NIR laser pulses and coupled into the inverted scanning microscope by dichroic mirrors before focusing onto the sample with a water immersion objective (Plan APO VC 60×, 1.2 NA; Nikon). For widefield imaging, the authors used a mercury lamp in combination with an sCMOS camera. Surface scans were performed by using an XYZ-piezo stage with a 200 × 200 × 200 µm travel range. Excitation and detection paths were decoupled via dichroic beam splitters depending on the chosen imaging modalities. The induced signals based on SHG, SFG, FWM, pCARS, and fluorescence in the sample were collected by the same objective, focused onto a 50 µm pinhole and spectrally separated. The authors used an additional notch filter to block the pump wavelength during nonlinear imaging. After suited filtering, the detected light was focused on APDs (Count Blue / Count Red; LaserComponents) for the blue (<620 nm) and red-shifted spectral region, respectively. The detector signal was registered by a dual-channel TCSPC card. The data was recorded using custom software written in Labview 2018 (National Instruments) and C# (VisualStudio 2010, Microsoft). The software employs an FPGA to synchronize the recording, the XYZ scanning via analog output signal, and the TCSPC card via digital TTL trigger. The pulsed signal of the laser (80 MHz) serves as a master clock and is used to trigger the TCSPC card detection intervals. Confocal data was extracted for further analysis using the software framework PAM.[33] It was further processed using Fiji[34] and Matlab 2018b (The MathWorks, Inc; Natick, MA, USA).

Nonlinear Imaging: The excitation power for SHF and SFG imaging amounted up to 20 mW for both channels. FWM and pCARS images of UiO-67 and MOF-801 were recorded with 11.2 mW for the probe pulses and 22.8 mW for the pump pulse, if not stated otherwise. FWM imaging of MIL-88A was performed with I_{probe} = 0.1 mW and I_{pump} = 1.9 mW or I_{pump} = 3.0 mW. For labeled samples, the excitation power was set to 9.9 µW for one-photon excitation at 532 nm, and 2.7 mW for two-photon excitation at 774 nm at the microscope backport. For a good SNR, count rates were always kept between 150 and 400 kHz at an acquisition time per pixel of 180 µs. All images were averaged over three to four frames. For MIL-88A needles, 60 × 60 µm^2 areas with 120 nm pixel-size were chosen as standard parameters (if not specified otherwise). UiO-67 particles were recorded with a pixel size of 160 nm over an area of 500 by 500 pixels (80 µm total image size). MOF-801 crystal clusters were imaged over 50 × 50 µm^2 areas with a pixel size of 100 nm. Single MOF-801 crystals were imaged over 20 × 20 µm^2 areas with a pixel size of 40 nm and averaged over ten frames in z with a step size of 0.5 µm if not stated otherwise.

Supporting Information

Supporting Information is available from the Wiley Online Library or from the author.

Acknowledgements

Funding by the Center for NanoScience Munich (CeNS), the Center for Integrated Protein Science Munich (CiPSM), Nanosystems Initiative Munich (NIM), and the Deutsche Forschungsgemeinschaft (PL 696/4-1; WU 622/4-1; Project-ID 201269156 - SFB1032, B03) is gratefully acknowledged. The authors thank Don C. Lamb and Constantin Hoch for support and access to laboratory facilities.

Open access funding enabled and organized by Projekt DEAL.

Conflict of Interest

The authors declare no conflict of interest.

Author Contributions

E.P. and S.W. conceived the research. E.P. supervised the project. A.F., P.H., O.Y., S.W., and E.P. designed the experiments. Synthesis and characterization of MOF particles was carried out by P.H., H.W., and Z.J under the supervision of S.W. and O.Y., respectively. P.H. carried out SEM and XRD experiments. A.F. set up and developed the multimodal system for spectroscopy and imaging with the support from P.M. and carried out the correlative imaging and spectroscopy measurements under the supervision from E.P. A.F., P.H., P.M., and I.Z. performed experiments. A.F., P.H., P.M., S.W., and E.P. analyzed the data. E.P. and A.F. conducted the statistical analysis. E.P. and A.F. designed the figures. A.F., Z.J, S.W., and E.P. wrote the manuscript. All authors approved the final version of the manuscript.

Data Availability Statement

The data that support the findings of this study are available from the corresponding author upon reasonable request.

Keywords

heterogeneity, metal–organic framework crystals, nonlinear imaging, particle level, spectroscopy

Received: June 13, 2021
Revised: September 3, 2021
Published online: November 21, 2021

[1] a) M. Rivera-Torrente, L. D. B. Mandemaker, M. Filez, G. Delen, B. Seoane, F. Meirer, B. M. Weckhuysen, *Chem. Soc. Rev.* **2020**, *49*, 6694; b) V. Bon, E. Brunner, A. Pöppl, S. Kaskel, *Adv. Funct. Mater.* **2020**, *30*, 1907847.
[2] L. Liu, D. Zhang, Y. Zhu, Y. Han, *Commun. Chem.* **2020**, *3*, 99.
[3] a) C. Wiktor, M. Meledina, S. Turner, O. I. Lebedev, R. A. Fischer, *J. Mater. Chem. A* **2017**, *5*, 14969; b) X. Gong, K. Gnanasekaran, Z. Chen, L. Robison, M. C. Wasson, K. C. Bentz, S. M. Cohen, O. K. Farha, N. C. Gianneschi, *J. Am. Chem. Soc.* **2020**, *142*, 17224.
[4] a) J. Hafizovic, M. Bjørgen, U. Olsbye, P. D. C. Dietzel, S. Bordiga, C. Prestipino, C. Lamberti, K. P. Lillerud, *J. Am. Chem. Soc.* **2007**, *129*, 3612; b) E. Brunner, M. Rauche, *Chem. Sci.* **2020**, *11*, 4297.
[5] C. Gropp, S. Canossa, S. Wuttke, F. Gándara, Q. Li, L. Gagliardi, O. M. Yaghi, *ACS Cent. Sci.* **2020**, *6*, 1255.
[6] a) H. Furukawa, K. E. Cordova, M. O'Keeffe, O. M. Yaghi, *Science* **2013**, *341*, 1230444; b) L. J. Wang, H. Deng, H. Furukawa, F. Gándara, K. E. Cordova, D. Peri, O. M. Yaghi, *Inorg. Chem.* **2014**, *53*, 5881; c) P. Li, N. A. Vermeulen, C. D. Malliakas, D. A. Gómez-Gualdrón, A. J. Howarth, B. L. Mehdi, A. Dohnalkova, N. D. Browning, M. O'Keeffe, O. K. Farha, *Science* **2017**, *356*, 624; d) L. Feng, J.-L. Li, G. S. Day, X.-L. Lv, H.-C. Zhou, *Chem* **2019**, *5*, 1265; e) M. J. Kalmutzki, N. Hanikel, O. M. Yaghi, *Sci. Adv.* **2018**, *4*, eaat9180; f) E. Ploetz, A. Zimpel, V. Cauda, D. Bauer, D. C. Lamb, C. Haisch, S. Zahler, A. M. Vollmar, S. Wuttke, H. Engelke, *Adv. Mater.* **2020**, *32*, 1907267.
[7] J. Fonseca, T. Gong, L. Jiao, H.-L. Jiang, *J. Mater. Chem. A* **2021**, *9*, 10562.
[8] E. Ploetz, H. Engelke, U. Lächelt, S. Wuttke, *Adv. Funct. Mater.* **2020**, *30*, 1909062.
[9] a) R. Ameloot, F. Vermoortele, J. Hofkens, F. C. De Schryver, D. E. De Vos, M. B. J. Roeffaers, *Angew. Chem., Int. Ed.* **2013**, *52*, 401; b) K. C. Jayachandrababu, D. S. Sholl, S. Nair, *J. Am. Chem. Soc.* **2017**, *139*, 5906.

© 2021 The Authors. Advanced Materials published by Wiley-VCH GmbH

[10] W. Schrimpf, J. Jiang, Z. Ji, P. Hirschle, D. C. Lamb, O. M. Yaghi, S. Wuttke, *Nat. Commun.* **2018**, *9*, 1647.

[11] a) Q. Zhang, X. Tian, H. Zhou, J. Wu, Y. Tian, *Materials* **2017**, *10*, 223; b) J. Langer, D. Jimenez de Aberasturi, J. Aizpurua, R. A. Alvarez-Puebla, B. Auguié, J. J. Baumberg, G. C. Bazan, S. E. J. Bell, A. Boisen, A. G. Brolo, J. Choo, D. Cialla-May, V. Deckert, L. Fabris, K. Faulds, F. J. García de Abajo, R. Goodacre, D. Graham, A. J. Haes, C. L. Haynes, C. Huck, T. Itoh, M. Käll, J. Kneipp, N. A. Kotov, H. Kuang, E. C. Le Ru, H. K. Lee, J.-F. Li, X. Y. Ling, et al., *ACS Nano* **2020**, *14*, 28; c) J. R. Zhou, G. Tian, L. J. Zeng, X. E. Song, X. W. Bian, *Adv. Healthcare Mater.* **2018**, *7*, 1800022; d) A. C. McKinlay, R. E. Morris, P. Horcajada, G. Ferey, R. Gref, P. Couvreur, C. Serre, *Angew. Chem., Int. Ed.* **2010**, *49*, 6260; e) S. Beg, M. Rahman, A. Jain, S. Saini, P. Midoux, C. Pichon, F. J. Ahmad, S. Akhter, *Drug Discovery Today* **2017**, *22*, 625; f) M. B. J. Roeffaers, R. Ameloot, M. Baruah, H. Uji-i, M. Bulut, G. De Cremer, U. Müller, P. A. Jacobs, J. Hofkens, B. F. Sels, D. E. De Vos, *J. Am. Chem. Soc.* **2008**, *130*, 5763; g) A. Kubarev, E. Plessers, M. Roeffaers, in *Nanotechnology in Catalysis: Applications in the Chemical Industry, Energy Development, and Environment Protection*, (Eds: M. V. de Voorde, B. Sels), Wiley-VCH, Weinheim, Germany **2017**, p. 979; h) C. Sprung, B. M. Weckhuysen, *J. Am. Chem. Soc.* **2015**, *137*, 1916.

[12] N. Al Danaf, W. Schrimpf, P. Hirschle, D. C. Lamb, Z. Ji, S. Wuttke, *J. Am. Chem. Soc.* **2021**, *143*, 10541.

[13] a) X. Cheng, J. Yao, H. Zhang, X. Wang, J. Bai, *J. Alloys Compd.* **2021**, *855*, 157433; b) L. R. Mingabudinova, V. V. Vinogradov, V. A. Milichko, E. Hey-Hawkins, A. V. Vinogradov, *Chem. Soc. Rev.* **2016**, *45*, 5408; c) R. Medishetty, L. Nemec, V. Nalla, S. Henke, M. Samoć, K. Reuter, R. A. Fischer, *Angew. Chem., Int. Ed.* **2017**, *56*, 14743; d) R. Medishetty, J. K. Zaręba, D. Mayer, M. Samoć, R. A. Fischer, *Chem. Soc. Rev.* **2017**, *46*, 4976; e) R.-J. Niu, W.-F. Zhou, Y. Liu, J.-Y. Yang, W.-H. Zhang, J.-P. Lang, D. J. Young, *Chem. Commun.* **2019**, *55*, 4873; f) S. Van Cleuvenbergen, I. Stassen, E. Gobechiya, Y. Zhang, K. Markey, D. E. De Vos, C. Kirschhock, B. Champagne, T. Verbiest, M. A. van der Veen, *Chem. Mater.* **2016**, *28*, 3203.

[14] M. Wolf, K. Hirai, S. Toyouchi, E. Fron, W. Peeters, S. De Feyter, H. Uji-i, *Chem. Commun.* **2020**, *56*, 13331.

[15] a) B. M. Weckhuysen, *Angew. Chem., Int. Ed.* **2009**, *48*, 4910; b) S. Bordiga, C. Lamberti, F. Bonino, A. Travert, F. Thibault-Starzyk, *Chem. Soc. Rev.* **2015**, *44*, 7262; c) D. Tzoulaki, L. Heinke, H. Lim, J. Li, D. Olson, J. Caro, R. Krishna, C. Chmelik, J. Kärger, *Angew. Chem., Int. Ed.* **2009**, *48*, 3525; d) F. Hibbe, C. Chmelik, L. Heinke, S. Pramanik, J. Li, D. M. Ruthven, D. Tzoulaki, J. Kärger, *J. Am. Chem. Soc.* **2011**, *133*, 2804; e) A. Ghosh, P. Mukherjee, S. Deb, R. Bhargava, *J. Phys. Chem. Lett.* **2017**, *8*, 5325; f) M. Rivera-Torrente, M. Filez, C. Schneider, E. C. van der Feltz, K. Wolkersdörfer, D. H. Taffa, M. Wark, R. A. Fischer, B. M. Weckhuysen, *Phys. Chem. Chem. Phys.* **2019**, *21*, 25678; g) K.-L. Liu, A. V. Kubarev, J. Van Loon, H. Uji-i, D. E. De Vos, J. Hofkens, M. B. J. Roeffaers, *ACS Nano* **2014**, *8*, 12650; h) K. F. Domke, T. A. Riemer, G. Rago, A. N. Parvulescu, P. C. A. Bruijnincx, A. Enejder, B. M. Weckhuysen, M. Bonn, *J. Am. Chem. Soc.* **2012**, *134*, 1124; i) C. Hess, *Chem. Soc. Rev.* **2021**, *50*, 3519; j) I. Strauss, A. Mundstock, M. Treger, K. Lange, S. Hwang, C. Chmelik, P. Rusch, N. C. Bigall, T. Pichler, H. Shiozawa, J. Caro, *ACS Appl. Mater. Interfaces* **2019**, *11*, 14175; k) A. M. Katzenmeyer, J. Canivet, G. Holland, D. Farrusseng, A. Centrone, *Angew. Chem., Int. Ed.* **2014**, *53*, 2852; l) A. M. Katzenmeyer, V. Aksyuk, A. Centrone, *Anal. Chem.* **2013**, *85*, 1972; m) G. Delen, M. Monai, F. Meirer, B. M. Weckhuysen, *Angew. Chem., Int. Ed.* **2021**, *60*, 1620.

[16] a) C. E. Harvey, E. M. van Schrojenstein Lantman, A. J. G. Mank, B. M. Weckhuysen, *Chem. Commun.* **2012**, *48*, 1742; b) A. I. Gómez-Varela, D. R. Stamov, A. Miranda, R. Alves, C. Barata-Antunes, D. Dambournet, D. G. Drubin, S. Paiva, P. A. A. De Beule, *Sci. Rep.* **2020**, *10*, 1122; c) P. Bondia, S. Casado, C. Flors, *Methods Mol. Biol.* **2017**, *1663*, 105; d) H. Abramczyk, A. Imiela, B. Brozek-Pluska, M. Kopec, *Nanomedicine* **2019**, *14*, 1873; e) W. R. Adams, B. Mehl, E. Lieser, M. Wang, S. Patton, G. A. Throckmorton, J. L. Jenkins, J. B. Ford, R. Gautam, J. Brooker, E. D. Jansen, A. Mahadevan-Jansen, *Sci. Rep.* **2021**, *11*, 8067.

[17] J.-X. Cheng, L. D. Book, X. S. Xie, *Opt. Lett.* **2001**, *26*, 1341.

[18] M. Mohseni, C. Polzer, T. Hellerer, *Opt. Express* **2018**, *26*, 10230.

[19] a) A. Guo, M. Durymanov, A. Permyakova, S. Sene, C. Serre, J. Reineke, *Pharm. Res.* **2019**, *36*, 53; b) P. Horcajada, T. Chalati, C. Serre, B. Gillet, C. Sebrie, T. Baati, J. F. Eubank, D. Heurtaux, P. Clayette, C. Kreuz, J. S. Chang, Y. K. Hwang, V. Marsaud, P. N. Bories, L. Cynober, S. Gil, G. Ferey, P. Couvreur, R. Gref, *Nat. Mater.* **2010**, *9*, 172; c) S. Rojas, A. Arenas-Vivo, P. Horcajada, *Coord. Chem. Rev.* **2019**, *388*, 202.

[20] H. Tan, G. Tang, Z. Wang, Q. Li, J. Gao, S. Wu, *Anal. Chim. Acta* **2016**, *940*, 136.

[21] S. Gholizadeh Khasevani, M. R. Gholami, *Inorg. Chem. Commun.* **2019**, *102*, 221.

[22] P. Hirschle, C. Hirschle, K. Böll, M. Döblinger, M. Höhn, J. M. Tuffnell, C. W. Ashling, D. A. Keen, T. D. Bennett, J. O. Rädler, E. Wagner, M. Peller, U. Lächelt, S. Wuttke, *Chem. Mater.* **2020**, *32*, 2253.

[23] a) L. Lewin, *J. Inst. Electr. Eng., Part 3* **1947**, *94*, 65; b) X. Fan, W. Zheng, D. J. Singh, *Light Sci. Appl.* **2014**, *3*, e179; c) B. R. Johnson, *J. Opt. Soc. Am. A* **1993**, *10*, 343.

[24] a) L. Rayleigh, *London Edinburgh Dublin Philos. Mag. J. Sci.* **1899**, *47*, 375; b) G. Mie, *Ann. Phys.* **1908**, *330*, 377; c) L. Lorenz, *Eur. Phys. J H* **1890**, *44*, 135; d) C. F. Bohren, D. R. Huffman, *Absorption and Scattering of Light by Small Particles*, Wiley-VCH, Weinheim, Germany **1998**, p. 57.

[25] A. I. Kuznetsov, A. E. Miroshnichenko, M. L. Brongersma, Y. S. Kivshar, B. Luk'yanchuk, *Science* **2016**, *354*, 846.

[26] N. K. Kulachenkov, S. Bruyere, S. A. Sapchenko, Y. A. Mezenov, D. Sun, A. A. Krasilin, A. Nominé, J. Ghanbaja, T. Belmonte, V. P. Fedin, E. A. Pidko, V. A. Milichko, *Adv. Funct. Mater.* **2019**, *30*, 1908292.

[27] a) H. Kim, S. Yang, S. R. Rao, S. Narayanan, E. A. Kapustin, H. Furukawa, A. S. Umans, O. M. Yaghi, E. N. Wang, *Science* **2017**, *356*, 430; b) F. Fathieh, M. J. Kalmutzki, E. A. Kapustin, P. J. Waller, J. Yang, O. M. Yaghi, *Sci. Adv.* **2018**, *4*, eaat3198.

[28] H. Furukawa, F. Gandara, Y. B. Zhang, J. Jiang, W. L. Queen, M. R. Hudson, O. M. Yaghi, *J. Am. Chem. Soc.* **2014**, *136*, 4369.

[29] A. K. Cheetham, T. D. Bennett, F.-X. Coudert, A. L. Goodwin, *Dalton Trans.* **2016**, *45*, 4113.

[30] M. Choura, N. M. Belgacem, A. Gandini, *Macromolecules* **1996**, *29*, 3839.

[31] L. Maury, L. Bardet, R. Brunel, R. Vierne, *J. Raman Spectrosc.* **1981**, *11*, 14.

[32] N. Ko, J. Hong, S. Sung, K. E. Cordova, H. J. Park, J. K. Yang, J. Kim, *Dalton Trans.*. **2015**, *44*, 2047.

[33] W. Schrimpf, A. Barth, J. Hendrix, D. C. Lamb, *Biophys. J.* **2018**, *114*, 1518.

[34] a) J. Schindelin, I. Arganda-Carreras, E. Frise, V. Kaynig, M. Longair, T. Pietzsch, S. Preibisch, C. Rueden, S. Saalfeld, B. Schmid, J.-Y. Tinevez, D. J. White, V. Hartenstein, K. Eliceiri, P. Tomancak, A. Cardona, *Nat. Methods* **2012**, *9*, 676; b) C. T. Rueden, J. Schindelin, M. C. Hiner, B. E. DeZonia, A. E. Walter, E. T. Arena, K. W. Eliceiri, *BMC Bioinformatics* **2017**, *18*, 529.

© 2021 The Authors. Advanced Materials published by Wiley-VCH GmbH

ADVANCED MATERIALS

Supporting Information

for *Adv. Mater.,* DOI: 10.1002/adma.202104530

Single Crystals Heterogeneity Impacts the Intrinsic and Extrinsic Properties of Metal–Organic Frameworks

Adrian Fuchs, Petra Mannhardt, Patrick Hirschle, Haoze Wang, Irina Zaytseva, Zhe Ji, Omar Yaghi, Stefan Wuttke, and Evelyn Ploetz**

Supporting Information

Single crystals heterogeneity impacts the intrinsic and extrinsic properties of metal-organic frameworks

Adrian Fuchs[a], Petra Mannhardt[a], Patrick Hirschle[a], Haoze Wang[b], Irina Zaytseva[a], Zhe Ji[b,c], Omar Yaghi[b,d], Stefan Wuttke[a,e,f,*], and Evelyn Ploetz[a,*]

[a] *Department of Chemistry and Center for NanoScience (CeNS), Ludwig-Maximilians-Universität München, Butenandtstraße 5-13, 81377 Munich, Germany*

[b] *Department of Chemistry, University of California–Berkeley; Materials Sciences Division, Lawrence Berkeley National Laboratory; Kavli Energy NanoSciences Institute at Berkeley; and Berkeley Global Science Institute, Berkeley, CA 94720, USA*

[c] *now: Department of Chemistry Stanford University, Stanford, CA 94305, USA*

[d] *UC Berkeley-KACST Joint Center of Excellence for Nanomaterials for Clean Energy Applications, King Abdulaziz City for Science and Technology, Riyadh 11442, Saudi Arabia*

[e] *BCMaterials, Basque Center for Materials, UPV/EHU Science Park, 48940 Leioa, Spain*

[f] *Ikerbasque, Basque Foundation for Science, 48013, Bilbao, Spain*

Corresponding author: stefan.wuttke@bcmaterials.net and evelyn.ploetz@lmu.de

Table of Content

Supplementary Note 1. Multimodal spectroscopic imaging system

1.1. Multimodal nonlinear scanning microscope

The multi-modal imaging system is based on a home-built, confocal scanning microscope (**Figure S1.1)** equipped with two light sources: a dual-color, fs-laser in the NIR for nonlinear, label-free imaging in combination with CW excitation for single-molecule fluorescence and spontaneous Raman scattering spectroscopy and microscopy. Here, two CW lasers at 532 nm (Samba™100 04-01 Series; Cobolt) and 633 nm (HeNe laser; Coherent) serve as the excitation source.

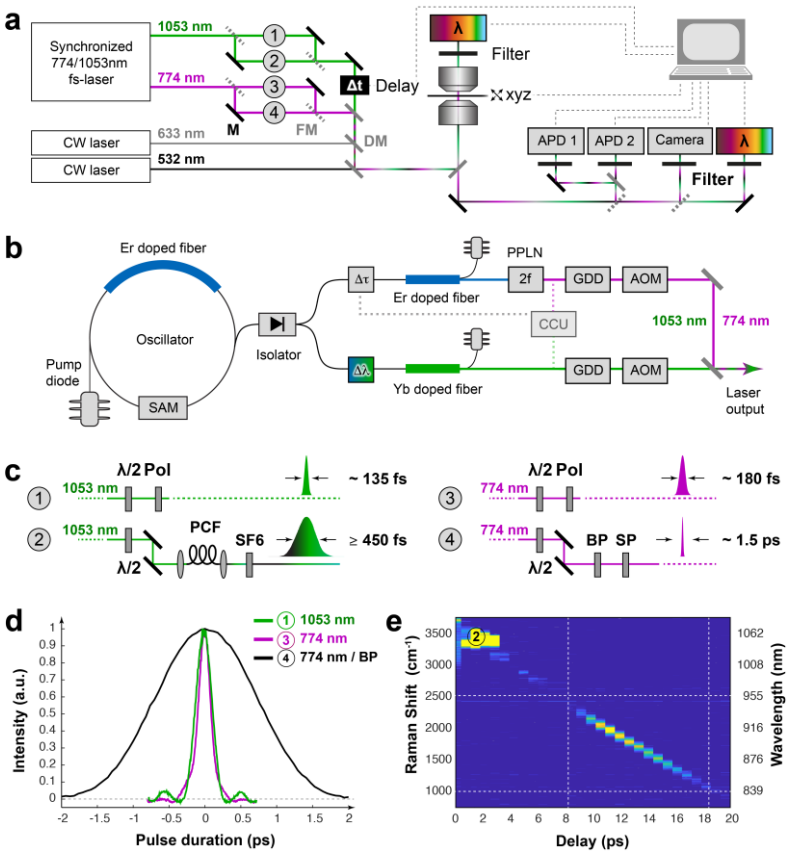

Figure S1.1. MOSAIC imaging system. a) *The setup consists of three parts: scanning confocal microscope, detection unit and laser excitation. The latter comprises two types of light sources: CW excitation and a synchronized, dual-output fs-laser for nonlinear-imaging that are coupled into an inverted scanning microscope.* ***b)*** *Schematic of the fiber-based fs-laser source based on a SESAM mode-locked ring oscillator as a master-oscillator that seeds two polarization-maintaining, high-power fiber amplifier.* ***c)*** *Schematics of the available excitation sources. The direct excitation (Path 1 and 3) is used for SHG, SFG and 2PE imaging. Super-Continuum generation at 1053 nm is achieved in a PCF (Path 2) and serves as probe pulse for FWM/pCARS applications. The white light is chirped in an SF6 glass rod for spectral focusing. The pump pulse for pCARS imaging is derived after spectral clean-up at 774 nm (Path 4).* ***d)*** *Autocorrelation of laser pulses designed for nonlinear imaging.* ***e)*** *Temporal behavior of the super continuum derived at 1053 nm after a 20 cm SF6 glass rod.* ***Legend:*** *APD: avalanched photodiode; λ: Spectrometer; xyz: piezo-stage; Δt: temporal delay unit; DM: dichroic mirror; FM: flipping mirror; CW: continuous wave; PCF: photonic crystal fiber; λ/2: half-wave plate; BP: band pass filter; SP: short pass filter.*

The main light source for nonlinear imaging is a jitter-free, fiber-based, dual-color femtosecond laser system (FemtoFiber dichro bioMP, Toptica Photonics, Germany) with two synchronized pulse trains at

80 MHz (**Figure S1.1b**). In this custom-built light source, a SESAM mode-locked ring fiber oscillator seeds two polarization-maintaining, high-power fiber amplifier based on erbium and ytterbium. Laser pulses with a central wavelength at 774 nm are generated by frequency doubling in a PPLN crystal of the laser output of an erbium-based fiber amplifier. The resulting light sources has a power of ~ 1W and a transform-limited pulse duration of ~180 fs (**Figure S1.1c-d**). The second laser line is derived in an ytterbium-based fiber amplifier after soliton-based frequency shifting. It has a fixed central wavelength at 1053 nm, an output power of 1.5 W, and a transform-limited pulse duration of about 135 fs (**Figure S1.1c-d**). The precise pulse duration and temporal shape of both laser beams can be adjusted by chirped mirrors (free-space inside the laser) as part of motorized dispersion units (GDD; range – 20000 to 0 fs^2). These compressor units are employed to pre-compensate for the chirp of the optical system, *e.g.* the microscope objective and are used to optimize the SHG, SFG, and 2PE signal at the scanning microscope. The output power of each laser beam is adjusted by acousto-optic modulators. For nonlinear imaging based on SFG, FWM and pCARS, the temporal overlap between the designed laser pulses is controlled by a linear stage in the 774-nm associated path (**Figure S1.1a**). In addition, a cross-correlation unit (CCU; **Figure S1.1b**) in the laser system itself locks the temporal overlap between both laser pulses reducing the temporal and spectral jitter and shift. Here, SFG between a small fraction of the amplified laser radiation at 774 nm and 1053 nm is monitored on a photodiode. The temporal overlap between both pulses is optimized in an active feedback loop by adjusting the delay stage in the laser such that the SFG intensity between 774 and 1053 nm excitation remains maximal.

Laser pulses for nonlinear excitation are derived by manipulating the fs-laser output. Both lines are separated after the laser and recombined later via dichroic beam splitters (HR1064HT806; LaserComponents, Germany/ RT 785 rdc; AHF). The unmodified output at 1053 nm is e.g. used for 2PE, SHG and SFG generation (**Figure S1.1c;** Path 1). Its excitation power and linear polarization are controlled by a half-wave plate (WPH10M-1053; Thorlabs) in combination with a linear polarizer (WP25M-UB, Thorlabs). For FWM and CARS microscopy we used two interacting, synchronized laser pulses, termed pump and probe pulses. In our realization, we use 1053 nm excitation to derive the probe beam by super-continuum generation within a photonic crystal fiber (PCF, **Figure S1.1c**, Path 2) with spectral components between 770-1100 nm. These allow us to coherently excite molecular vibrations in the spectral region between 0-3800 cm^{-1}. Pump pulses are derived at 774 nm. To obtain the spectrally broad probe pulse, 500 mW of the laser output at 1053 nm (66% BS1064 nm, LaserComponents, Germany) is coupled into a photonic crystal fiber (NL-1050-Zero-2, NKT Photonics). A quarter-wave plate (WPQ10M-1053, Thorlabs) in combination with a half-wave plate (WPH10M-1053; Thorlabs) in front of the fiber ensure a maximum coupling efficiency. After re-collimation and spectral clean-up (LP 775nm #80-689; SP 1150 #89-573; Edmund Optics), the available supercontinuum is temporally stretched using an SF6 glass rod for spectral focusing. Linear polarization of the continuum is ensured via a linear polarizer after the fiber (WP25M-UB, Thorlabs). The white light intensity is adjusted using

an additional, achromatic half-wave plate (AHWP10M-980; Thorlabs). The direct output at 774 nm serves either for 2PE, SHG, and SFG, or as pump pulse in CARS and FWM (**Figure S1.1c;** Path 3). For the later, two approaches were frequently employed to shape the excitation at 774 nm: (1) laser pulses were either spectrally narrowed to ~ 16.5 cm^{-1} FWHM, *i.e.*, 1.5 ps (780/1, OD6; Alluxa; **Figure S1.1c-d;** Path 4) in combination with broadband probe pulses, or (2) they are temporally confined to select spectral components within a temporally stretched supercontinuum during temporal overlap. Since this approach requires acquisition times in the millisecond range per pixel, we implemented the spectral focusing strategy to increase the imaging speed to ~ 5 µs per pixel using a point detector. We therefore chirped the super-continuum in SF6 glass rods (**Figure S1.1c-d**, Path 3) and address single Raman resonances within the chirped spectrum using this temporally narrow unmodified pump pulse with 185 fs pulse duration. The spectral resolution can be tuned between 15-25 cm^{-1} depending on the added chirp (**Figure S1.1e**). To address the full spectrum of MOF particles, the temporal delay between both laser pulses is adjusted. The excitation power as well as the linear polarization at 774 nm (tuned for pCARS; **Figure S1.1c;** Path 3) are controlled by a half-wave plate (WPH10M-780, Thorlabs) in combination with a linear polarizer (WP25M-UB, Thorlabs). The diameter of the laser excitation is 4-fold expanded to overfill the objective of the confocal microscope before recombination with the Raman probe pulses or laser pulses derived from 1053 nm radiation.

Both CW laser lines are superimposed with the designed NIR laser pulses and coupled into the inverted microscope (TE200; Nikon) by dichroic mirrors (zt532/640rpc; Chroma/ #69-219, EdmundOptics/ zt532/633/NIRrpc; Chroma) before focusing onto the sample with a water immersion objective (Plan APO VC 60x 1.2 NA; Nikon). Sample positioning is achieved via manual micrometer stage (manmicLP; PiezoConcept). For widefield imaging, we use a mercury lamp (LH-M 100CB-1; Nikon) in combination with a CMOS camera (DCC1545C; Thorlabs). Surface scans are performed by using an XYZ-piezo stage with a 200x200x200 μm^3 travel range (BIO3.200; PiezoConcept). Excitation and detection paths are decoupled via dichroic beam splitters (DC1: zt532/642/NIRrpc, DC2: HC BS 749 SP and DC3: zt532/NIRrpc; AHF, Germany) depending on the chosen imaging modalities. The induced signals based on SHG, SFG, FWM, pCARS and fluorescence in the sample are collected by the same objective, focused onto a 50 µm pinhole and spectrally separated. We use an additional notch (Notch Filter 785 nm, Edmund Optics) filter to block the pump wavelength during nonlinear imaging. After suited filtering (**SHG**: 377/50 BrightLine HC; **SFG**: 417/60 BrightLine HC; **pCARS/FWM**: HQ 685/150 M; **Fluorescence**: 680/42 BrightLine HC (red) / HC 680/SP (blue), AHF, Germany; **CL**: 560/40 ET, AHF, Germany), the detected light is focused on APDs (Count Blue / Count Red; LaserComponents) for the blue (< 620 nm) and red-shifted spectral region, respectively. The detector signal is registered by a dual-channel TCSPC card (TH260 pico dual; PicoQuant). The data is recorded using custom software written in Labview 2018 (National Instruments) and C# (VisualStudio 2010, Microsoft). The software employs an FPGA (cRIO-9063; National Instruments) to synchronize the recording, the XYZ scanning via analog

output signal (NI9263; National Instruments) and the TCSPC card via digital TTL trigger (NI9401; National Instruments). The pulsed signal of the laser (80MHz) serves as a master clock and is used to trigger the TCSPC card detection intervals. Confocal data is extracted for further analysis using the software framework PAM.[1] It is further processed using Fiji [2] and Matlab 2018b (The MathWorks, Inc; Natick, MA, USA).

1.2. Fluorescence spectroscopy

Fluorescence emission was either collected by a water-immersion objective (Plan Apo VC 60x, 1.20 NA; Nikon) in epi-detection or an air-objective (CFI Plan Apo 60x; Nikon) in transmission. It was spectrally separated from the excitation by long-pass edge filters in combination with two notch filters to block the Rayleigh scattering originating from the chosen laser lines. Spectra were taken on a spectrograph (Kymera 328i; Oxford Instruments) with 300 l/mm grating (Blaze 500 nm) using an emCCD camera (iXon 897, Andor; Oxford Instruments). Data were recorded using *Andor Solis for Imaging V4.30* (Oxford Instruments). The acquisition time amounted to 100 s with an excitation power at the sample plane of 46 µW, and 2.15 mW for 532 and 774 nm excitation.

1.3. Spontaneous Raman spectroscopy and Hyperspectral imaging

Spontaneous Raman spectroscopy and hyperspectral Raman imaging were carried out using 532-nm and 633 nm excitation and a 60x 1.2 NA water immersion objective (Plan Apo VC 60x, 1.20 NA, Nikon). Excitation and detection paths are decoupled by a dichroic filter (zt532NIR rpc; AHF Analysentechnik) in combination with two filters to block shorter wavelengths including Rayleigh scattering at 532 nm (RET 537 LP, AHF Analysetechnik; 532nm Notch filter, OD6, Edmund Optics). Raman backscattered radiation was collected through the microscope objective and recorded via a spectrograph (Kymera 328i, Oxford Instruments) with an emCCD camera (iXon 897, Andor). The spectral resolution at 532 nm amounts to 7.2 and 3.4 cm^{-1} per pixel (Grating with 600 and 1200 l/mm and blazed at 500 nm). Data were recorded using *Andor Solis for Imaging V4.30* (Oxford Instruments). For hyperspectral image acquisition, areas with 1 µm step-size were raster-scanned, while full Raman spectra were recorded at each pixel of the image. The acquisition time per pixel was set to 720 ms with an excitation power of 1.2 mW at the sample plane.

The recorded Raman spectra were processed with Matlab 2018b (The MathWorks, Inc; Natick, MA, USA). All presented spectra were corrected for cosmic rays, Rayleigh scattering, and spurious background. If necessary, a linear gradient was additionally removed by spline subtraction. For Raman spectra of MIL-88A, the solvent spectrum of pure ethanol was determined separately and subtracted.

Supplementary Note 2. Setup performance

2.1. Auto-Correlation

We employed an intensity-based autocorrelation analysis to characterize the pulse duration of the individual excitation sources via a commercial autocorrelator (PulseCheck equipped with NIR optics set; APE). After coupling the near-infrared fs-pulses into the autocorrelator, these incoming laser pulses are split into two copies via a 50:50 beam splitter. Afterward, both laser pulses are focused onto a nonlinear crystal in a non-collinear fashion. The resulting second harmonic signal $I(t)$ is recorded as a function of the temporal delay between both pulse copies and yields the intensity autocorrelation function $G_{ACF}(\tau)$ given as [3]

$$G_{ACF}(\tau) = \int I(t)I(t-\tau)\,dt \qquad \text{Eq. (1)}$$

Under the assumption of Gaussian-shaped laser beams, the measured ACF function $G_{ACF}(\tau)$ was approximated by a Gaussian function using Matlab2018b (The MathWorks, Inc; Natick, MA, USA) with a full width half maximum (FWHM) that is related to the pulse duration via:[3]

$$\Delta\,\tau_{pulse}^{FHWM} = \frac{1}{1.41}\,\Delta\,\tau_{ACF}^{FWHM} \qquad \text{Eq. (2)}$$

2.2. Determination of power dependencies

The power dependency of the various spectroscopic signatures (**Supplementary Figure S1**) available on the scanning microscope was verified using two different sample systems: (*i*) Atto532 dissolved in PBS in case of one- and two-photon excitation and (*ii*) silicon waver for all nonlinear effects. The resulting signals were either detected on an APD or the spectrometer with 600 lines/mm grating (see below) as a function of laser power. All determined power series are triplicates.

2.2.1. One-photon fluorescence

The fluorescence of a 5.3 µM Atto532 solution was measured on an APD (Count Blue; LaserComponents) in the spectral region between 545-615 nm (Filter combination: BP 580/70; SP 680; zt 532 NIR rdc) after 532 nm excitation. After a background measurement without excitation, the excitation power was varied between 0 and 70 µW laser power after the objective. The count rate was recorded over a time window of 30 s per point. Matlab 2018b (The MathWorks, Inc; Natick, MA, USA) and PAM [1] were employed afterward to analyze and linearly approximate the count rate as a function of laser power.

2.2.2. Two-photon fluorescence

The fluorescence of a 50 nM Atto532 solution was measured on an APD (Count Blue; LaserComponents) in the spectral region between 545-615 nm (Filter combination: BP 580/70; SP 680; BS 749 SP). Laser pulses centered at 774 nm with 150 fs temporal width served as excitation. The

excitation power was varied from 0 to 12 mW in 1 mW steps, which translates to 19.09 % output power as power after the objective. The count rate was recorded over a time window of 120 s per point, Matlab 2018b (The MathWorks, Inc; Natick, MA, USA) and PAM [1] were employed afterward to analyze and quadratically approximate the count rate as a function of laser power.

2.2.3. Spontaneous Raman scattering

The spontaneous Raman signature of a crystalline silicon wafer was recorded on the spectrometer for CW excitation at 532 nm. After a background measurement without excitation, the excitation power was varied from 0.80 to 2.5 A in 0.1 A steps in the GUI of the laser controller software. This corresponds to a range of 0 to 150 mW output power. The intensity after the objective is 13.85 % of the laser output power. The data was recorded using *Andor Solis for Imaging V4.30* (Oxford Instruments) (EM Gain: 150, 1 x 6 s measurement time) and analyzed using a self-written script in Matlab 2018b (The MathWorks, Inc; Natick, MA, USA). After spectral background correction, the area under the peak at 522 cm^{-1} was integrated as a function of applied laser power and approximated to a line.

2.2.4. Sum-frequency generation

The SFG signal at 450 nm generated in a crystalline silicon wafer was recorded on the spectrometer for excitation at 774 nm (185 fs) and 1053 nm (135 fs). The SFG signal was decoupled from the excitation via a dichroic mirror (BS 749 SP, AHF) and bandpass filter (HC 680/SP, AHF) that was mounted in front of the spectrometer. For the pump dependence, the laser output power was varied from 0 to 100 mW in 10 mW steps, while the probe power remains fixed at 25.6 mW (measured at 1050 nm). Analog, the probe power range was 0 to 9 mW in 1 mW steps with a pump power of 117.5 mW. All powers were determined in the beam path after the telescope systems. The power conversion factor of the laser power at the focus was determined as 19.09 % for both laser lines. The data was recorded using *Andor Solis for Imaging V4.30* (Oxford Instruments) (EM Gain: 200, 5 x 5 s measurement time per spectrum) and analyzed using a self-written script in Matlab 2018b (The MathWorks, Inc; Natick, MA, USA). After spectral background correction, the area under the peak at 450 nm was integrated as a function of applied laser power and linearly approximated.

2.2.5. Second-harmonic generation

The SHG signal at 387 nm generated in a crystalline silicon wafer was recorded on the spectrometer. Laser pulses centered at 774 nm with 185 fs temporal width served as excitation. The SHG signal was decoupled from the excitation via a dichroic mirror (BS 749 SP, AHF) and bandpass filter (HC 680/SP, AHF) that was mounted in front of the spectrometer. The pump laser power was varied from 0 to 30 mW in 10 mW steps and from 30 to 80 mW in 5 mW steps. The power conversion factor of the laser power at the focus was determined as 19.09 %. The measured data was recorded using *Andor Solis for Imaging V4.30* (Oxford Instruments) (EM Gain: 200, 5 x 5 s measurement time per spectrum) and analyzed using

a self-written script in Matlab 2018b (The MathWorks, Inc; Natick, MA, USA). After spectral background correction, the area under the peak at 387 nm was integrated and quadratically approximated.

2.2.6. Four-wave mixing generation

The FWM signal at 612 nm generated in a crystalline silicon wafer was recorded on the spectrometer for excitation at 774 nm (185 fs) and 1053 nm (135 fs). The FWM signal was decoupled from the excitation via a dichroic mirror (BS 749 SP, AHF) and bandpass filter (HC 680/SP, AHF) that was mounted in front of the spectrometer. For the pump dependence, the power at 774 nm was varied from 0 to 50 mW in 5 mW steps and from 50 to90 mW in 10 mW steps, while the probe power remained fixed at 17.4 mW. The probe power at 1053 nm was varied between 0 and 20 mW in 2 mW steps with a pump power of 120.2 mW. The power conversion factor for the laser power at the confocal spot amounted to 19.09 % for both laser lines. The measured data was recorded using *Andor Solis for Imaging V4.30* (Oxford Instruments) (EM Gain: 100, 5 x 5 s measurement time per spectrum) and analyzed using a self-written script in Matlab 2018b (The MathWorks, Inc; Natick, MA, USA). After spectral background correction, the area under the peak at 612 nm was integrated. The FWM signature was approximated linearly and quadratically as a function of the probe and pump power, respectively.

Supplementary Note 3. Characterization

3.1. Scanning electron microscopy (SEM)

SEM images were taken using a Helios G3 UC (Fei). Before the measurement, the particles were dispersed in ethanol and dried overnight on a carbon grid placed on an aluminum sample holder. The samples were then additionally sputtered with carbon. The electron microscope was operated at 3 kV using a through lens detector. Sample evaluation was performed using the software Fiji.[2]

3.2. X-ray diffraction (XRD)

X-ray diffraction was performed on an STOE Transmission-Diffractometer System STADI P using a Ge(111) primary monochromator. The setup was working with Cu K$\alpha 1$ radiation in transmission geometry in which the sample is fixed on a rotary disc between two polymer foils. For data evaluation, the software WINXPOW (v.3.0.2.1) was used.

Supplementary Note 4. MOF synthesis and sample preparation

4.1. Chemicals

Unless stated otherwise, reagents of luminescence grade were used as received. We ordered iron (III) chloride hexahydrate (Grüssing GmbH), anhydrous N,N-dimethylformamide (DMF), formic acid (purity ≥ 99.0 %), and anhydrous methanol from EMD Millipore Chemicals. Anhydrous acetone was obtained from Acros Organics. In addition we purchased acetone, benzoic acid (≥ 99,5%, ACS Reagent), biphenyl-4,4'-dicarboxylic acid (BPDC; 97%), dimethyl biphenyl-4,4'-dicarboxylate (99%), fluorescein-5(6)-isothiocyanate (FITC; ≥ 90%), ethanol (≥ 99.5%, ACS Reagent), ethyl acetate (99.9%, HPLC Plus), fumaric acid (≥ 99.0%), hydrochloric acid (37%, ACS Reagent), 2-(Hydroxymethyl)furan (Furfuryl alcohol; 98%), isopropyl alcohol (≥ 99.5%, BioReagent), nitric acid (70%, ACS Reagent), palladium on carbon (Pd/C, 10 wt.% loading), potassium hydroxide (90%), 2-Rhodamine-B-isothiocyanate (RBITC; mixed), sodium bicarbonate (BioReagent), sodium sulfate (≥ 99.0, ACS Reagent), sulfuric acid (95.0–98.0%, ACS Reagent), tetrahydrofuran (THF, ≥ 99.9%, for high-performance liquid chromatography (HPLC)), zirconium(IV) chloride (≥ 99.5%, trace metal basis), zirconium oxychloride octahydrate ($ZrOCl_2 \cdot 8H_2O$, purity ≥ 99.5%), fumaric acid, and Sigmacote® siliconizing reagent from Sigma-Aldrich.

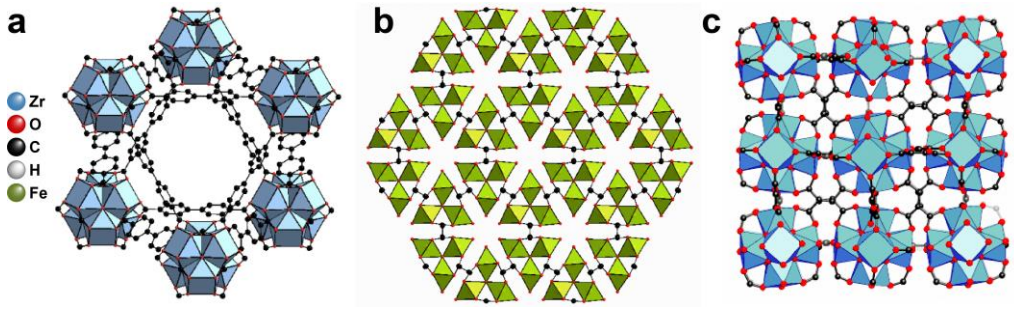

Figure S4.1. Synthesized MOF crystals. *The schematic depicts the structure of (**a**) UiO-67, (**b**) MIL-88A(Fe) and (**c**) MOF-801(Zr).*

4.2. Preparation of UiO-67 particles

UiO-67 crystals were synthesized following the protocol described in Ko *et al.*[4] Zirconium(IV) chloride (82 mg, 0.35 mmol), biphenyl-4,4'-dicarboxylic acid (85 mg, 0.35 mmol) and benzoic acid (1.28 g, 10.5 mmol) were dissolved in 20 mL dimethylformamide (DMF) in a glass reactor vessel (20 mL). After 20 min of sonication, the reaction mixture was kept at 120 °C for 48 h. After cooling down to room temperature, the resulting product was washed first with DMF and then in acetone – 3×/day for 3 days long per solvent. The sample was evacuated afterward (120 °C to 30 mTorr) and stored in powder form.

4.3. Dye-H_2BPDC Synthesis

The synthesis of Dye-H_2BPDC followed the procedure described in the literature.[5] It comprises a five-steps synthesis generating dye-functionalized linkers (**Figure S4.2**). In brief, dimethyl 2-nitrobiphenyl-

4,4'-dicarboxylate (**II**) was synthesized from dimethyl biphenyl-4,4'-dicarboxylate (**I**) in presence of concentrated sulfuric acid and 58% nitric acid. In the second reaction step, dimethyl 2-aminobiphenyl-4,4'-dicarboxylate (**III**) was formed at room temperature from compound (**II**) in acetic acid and 10% Pd/C within a high-pressure reactor under 10-50 atm of hydrogen pressure. The mixture was filtered afterwards, and the crude product was recrystallized from ethanol. Next, compound (**III**) was dissolved in THF and methanol and then mixed with a solution of KOH and water to retrieve 2-Aminobiphenyl-4,4'-dicarboxylic acid (NH_2-H_2BPDC, **IV**). In the last step, dye-H_2BPDC was derived from 2-NH_2-BPDC that has been covalently coupled to either FITC or RBITC via EDC mediated amide-coupling reaction.[6] The obtained dye-labeled H_2BPDC molecules were employed after filtration and purification via HPLC.

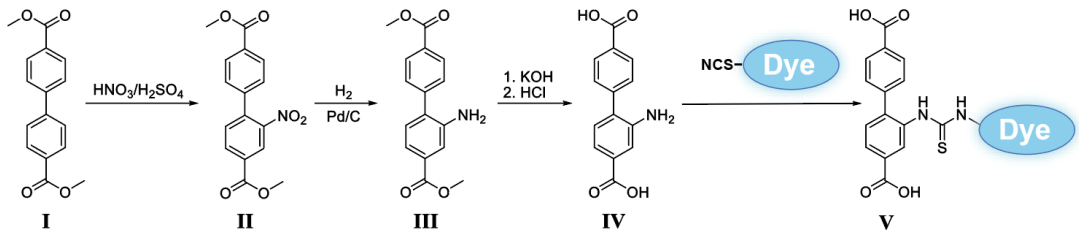

Figure S4.2. Dye-H2BPDC Labeling. *The schematic depicts a 5-step synthesis route to generate a dye-functionalized BPDC linker. FITC and RBITC served as dyes.*

4.4. Labeling of UiO-67 particles for fluorescence imaging

Labeled UiO-67 crystals were prepared following the procedure described in Schrimpf *et al.*[5] In brief, the *de novo* synthesis of UiO-67 was modified and carried out by replacing a fraction of BPDC linker molecules by dye-labeled BPDC (dye-H_2BPDC). It was either replaced by 0.1 % FITC- or 2% RBITC-labeled BPDC.

4.5. Preparation of crystalline MIL-88A(Fe) particles

Crystalline MIL-88A particles, *i.e.*, differently sized needles and bipyramids were prepared following the optimized procedures described in Hirschle *et al.*[7] A short description is given below.

4.5.1. MIL-88A(Fe) needles

Iron(III) chloride hexahydrate (1084 mg, 4.010 mmol) was dissolved in water (MilliQ, 20 mL). The solution was then transferred into a glass reactor (50 mL Volume) and fumaric acid powder (485 mg, 4.179 mmol) was added under stirring. The reaction mixture was heated in an oven for 24 h at 80 °C. After cooling the reaction mixture down to room temperature, the resulting product was washed 3x via centrifugation (7184 rpm, 15 min) and re-dispersed and stored in ethanol (20 mL).

4.5.2. MIL-88A(Fe) bipyramids

Iron(III) chloride hexahydrate (1626 mg, 6.0155 mmol) and fumaric acid powder (727.5 mg, 6.268 mmol) were dissolved in DMF (30 mL). To obtain micron-sized particles, a fraction (10 mL) of the reaction mixture was aliquoted 10x in 1.5 mL Eppendorf tubes and heated in an oven at 120 °C for 30 min. The resulting particles were washed 3x via centrifugation (16873 rpm, 10 min) and re-dispersed and stored in DMF. To generate nanoparticles, a fraction (20 mL) of the reaction mixture was given into an 80 mL Teflon tube and placed in a microwave reactor (Synthos 3000, Anton Paar) in presence of 20 mL water in the chamber. The sample was heated up to 120 °C within 30 s and afterward constantly heated at 120 °C for 5 min. The reaction was quenched afterward by mixing the sample with DMF (50 mL) at room temperature. The resulting product was washed 3x via centrifugation (7197 rpm, 20 min), re-dispersed and stored in DMF (20 mL).

4.6. Preparation of single crystal sample of MOF-801 [$Zr_6O_4(OH)_4(fumarate)_6$]

Fumaric acid (0.027 g, 0.23 mmol) and $ZrOCl_2 \cdot 8H_2O$ (0.075 g, 0.23 mmol) were dissolved in DMF (11.67 ml). Formic acid (1.76 ml) was added afterwards to the solution. The solvent mixture was placed in a 20-ml vial and heated at 120 °C for two days. Octahedral colourless crystals were collected and washed with DMF three times per day for three days. The crystals were subsequently washed with methanol for three days, three times per day. The solid was then dried under dynamic vacuum at 120 °C for 24 hours to yield activated sample. The activated MOF crystals were transferred into a Schlenk vessel under Argon flow and evacuated down to 2 µbar multiple times to ensure a water-free environment. They were stored under Argon atmosphere [$c(O_2) < 0.1$ ppm, $c(H_2O) < 1$ ppm]. To reduce the nucleation in the growth of MOF-801 single-crystals, the inner surface of the 20-ml vial was rinsed with siliconizing reagent Sigmacote®, washed with acetone and dried in oven before use.

4.7. Sample preparation for multi-modal imaging and spectroscopy

The UiO-67 powder was suspended into 1 mL of double distilled water at ~ 1-10 mg mL^{-1} and vortexed for one minute. 200 µL of this suspension was added into a chamber of an 8-well slide (Thermofisher; Nunc LabTek I) and sealed with parafilm before imaging or recording of spectra. MIL-88A particles were diluted 1:10 in ethanol from the stock and mixed by pipetting the sample up and down 10x to ensure even distribution. After adding the dispersion (50 µL) to the 8-well slide, the sample was kept at room temperature for ~ 10-20 min until the solvent evaporated. The sample was closed with parafilm afterward and investigated on the microscope within 3-4 hours after sample preparation. MIL-88A particles showed first signs of degradation after 4-5 hours.

For measuring the water distribution in MOF-801, particle powder was transferred into an eight-well microscopy slide (X-well cell culture chamber, 8 Well auf Slide II, Sarstedt). The slide was sealed and stored under Argon until the measurement. Dry particles were measured in Argon atmosphere. For equilibrium measurements at defined relative humidity, MOF-801 was transferred into a microscopy

channel slide (µ-Slide I Luer Glass Bottom, Ibidi). A continuous nitrogen flow with a specific relative humidity was applied (one norm liter per minute). To dry the MOF crystals, the sample was flushed with pure nitrogen for at least 20 minutes.

Supplementary Note 5. Particle analysis of MIL-88A(Fe)

Size distribution analysis of MIL-88A(Fe) particles

To provide a morphological description of individual MIL-88A particles with needle-like morphology with high signal-to-noise ratio, each field of view was scanned four times and an averaged image was generated using Fiji.[2] In the next step, averaged images from consecutive measurements were combined as TIFF stack and converted to binary images. Using the 'Analyze Particles' tool of Fiji for shape identification and particle size distribution,[8] the needle-like shape of each non-overlapping MOF particle was approximated to an ellipse. The major axis a and minor axis b were particle-wise extracted to describe the particle's length l and width w:

$$l = 2 \cdot a \text{ and } w = 2 \cdot b \qquad \text{Eq. (3)}$$

Next, the length and width of each particle was sorted into histograms with a bin width of 0.344 µm in Matlab 2018b (The MathWorks, Inc; Natick, MA, USA. The histograms were fitted with a normal distribution to calculate the mean and standard deviation. With this information at hand, we introduce the ellipticity *E* as a ratiometric parameter to describe the shape of the particles. It is defined as the ratio of width w over length l:

$$E = 1 - \frac{w}{l} \qquad \text{Eq. (4)}$$

The ellipticity per fraction was also sorted into histograms and fitted with a normal distribution.

To additionally compare and correlate the particle volumes of MOFs with their associated optical properties, the needle particles were approximated as cylinders with the radius w / 2 and the height l leading to a volume V_N of:

$$V_N = \pi \cdot \left(\frac{w}{2}\right)^2 \cdot l \qquad \text{Eq. (5.1)}$$

The volume of the bipyramidal particles V_P was approximated as a perfect sphere, with the medium diameter between length and width:

$$V_P = \pi \cdot \left(\frac{w + l}{4}\right)^3 \cdot \frac{4}{3} \qquad \text{Eq. (5.2)}$$

Supplementary Figure S7 shows an overview of the histograms and their corresponding fitting curves. Fitting results are provided in **Supplementary Table S3**.

Supplementary Note 6. Water quantification in MOF-801

Upon exposure to humidity, water molecules diffuse into the framework of MOF-801. To quantify the amount of adsorbed water within the framework, we need to relate the integrated signal strength of the appearing OH-stretch vibration to the Raman spectrum of water and dry MOF material. Hence, all background-corrected Raman spectra of the wet MOF-801 need to be referenced to the Raman spectrum of the dry MOF material. The amount of adsorbed water is quantified by comparing the signal strength of the liquid water OH-stretch vibration to the one of adsorbed water. For water quantification, we determined the Raman spectrum of dry MOF-801 and liquid water first before measuring the water content in MOF-801 afterward.

The Raman spectrum of MOF-801 between ~2500 and 4200 cm^{-1} shows distinct peaks from the fumaric di-anion linker and (potentially) water (see **Figure 4**). To quantify the amount of adsorbed water, a calibration, a background correction and reference to the dry material is essential. Regions without Raman resonances (*i.e.,* between 2595-2620 cm^{-1} and 3760- 4190 cm^{-1}) allowed for determining the spectral background without prior knowledge of potentially adsorbed water to the MOF framework. The background was approximated by a 2nd order polynomial function and subtracted afterward from the recorded Raman spectra. To quantify the adsorbed water, we calculate the area under the OH-stretch signature, *i.e.*, we integrated over the water peak (3145-3665 cm^{-1}).

$$A_{Raman\ Peak} = \int_{\lambda_1}^{\lambda_2} I_{Raman\ Peak}(\lambda)\ d\lambda \qquad \text{Eq. (1)}$$

The amount of MOF material can vary in the confocal volume (and hence the adsorbed water), therefore, we need to weight the determined area of water with the concentration of MOF-801 in the confocal volume. The strength of the C-H stretch vibration can act as a reporter. It gives us the relative amount of water per MOF-801 material $I_{rel,H2O}$ which reads as following:

$$I_{rel,H2O} = \frac{A_{OH}}{A_{CH}} \qquad \text{Eq. (2)}$$

Supplementary Note 7. Probing macropores by furfuryl alcohol condensation

To elucidate the nature of the macroscale defect sites in MOF-801, we employed the liquid-phase acid-catalyzed self-condensation reaction[9, 10] of furfuryl alcohol (FA). Oligomerization between two single FA moieties (**A**) takes place at Brønsted acid sites. FA (**A**) and bisfurylmethyl units (**B**) formed after linear self-condensation are colorless. A consecutive loss of hydride ions (**C**) to neighboring carbenium ions formed from FA or growing ends, however, results in the local formation of resonance-stabilized bisfuryl carbenium ions. With reoccurring H- exchange, this reaction cycle leads to an enhanced degree of conjugation (**D**) and progressing coloration. With progressing conjugation and parallel branching[9] of the oligomers, extended π-conjugated systems are formed leading to a spectral red-shift in absorption and emission over time.

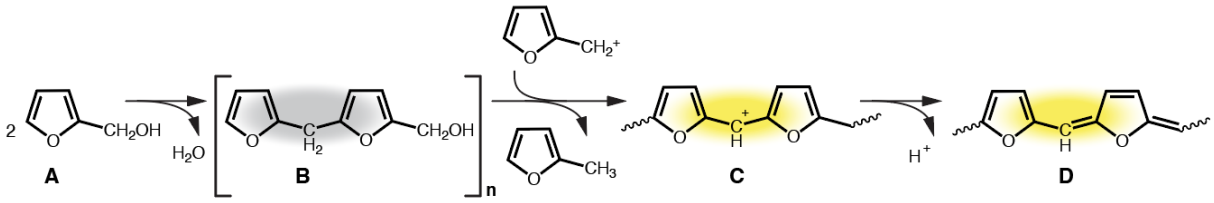

Figure 7.1. Self-condensation of furfuryl alcohol and mechanism of color formation. *After linear self-condensation, a H- exchange with protonated chain ends of FA or growing species results in the formation of a resonance-stabilized bisfuryl carbenium ion and a progressing formation of a π-conjugated system.*

To image the distribution of free metal clusters in MOF-801, we incubated MOF-801 with furfuryl alcohol for 12h at room temperature.[11]. Non-polymerized FA molecules were removed afterwards by washing with MQ water, before drying the particles by nitrogen. To visualize defects and FA condensation simultaneously, we employed FWM and fluorescence imaging in parallel. Two-photon excitation at 780 nm and 1053 nm simultaneously led to pronounced fluorescence in the visible range. We detected the emission of the polymerized FA in the green channel between 520-600 nm. The FWM signature of the MOF-801 crystals at 612 nm (3423 cm^{-1}) was recorded in the red channel (590-650 nm). Additional fluorescent background by long-chained FA polymers in the red channel was separated from the recorded FWM signature in the temporal domain. For this, we introduced a delay of 12 ps between the pump and probe beam and recorded the off-resonant background. The resulting FWM image was obtained by subtracting the signature in the resonant and off-resonant case. The applied laser power amounted to 0.7 mW and 3.5 mw for the probe and pump beam, respectively.

`

2. *Supplementary Figures*

Supplementary Figure S1

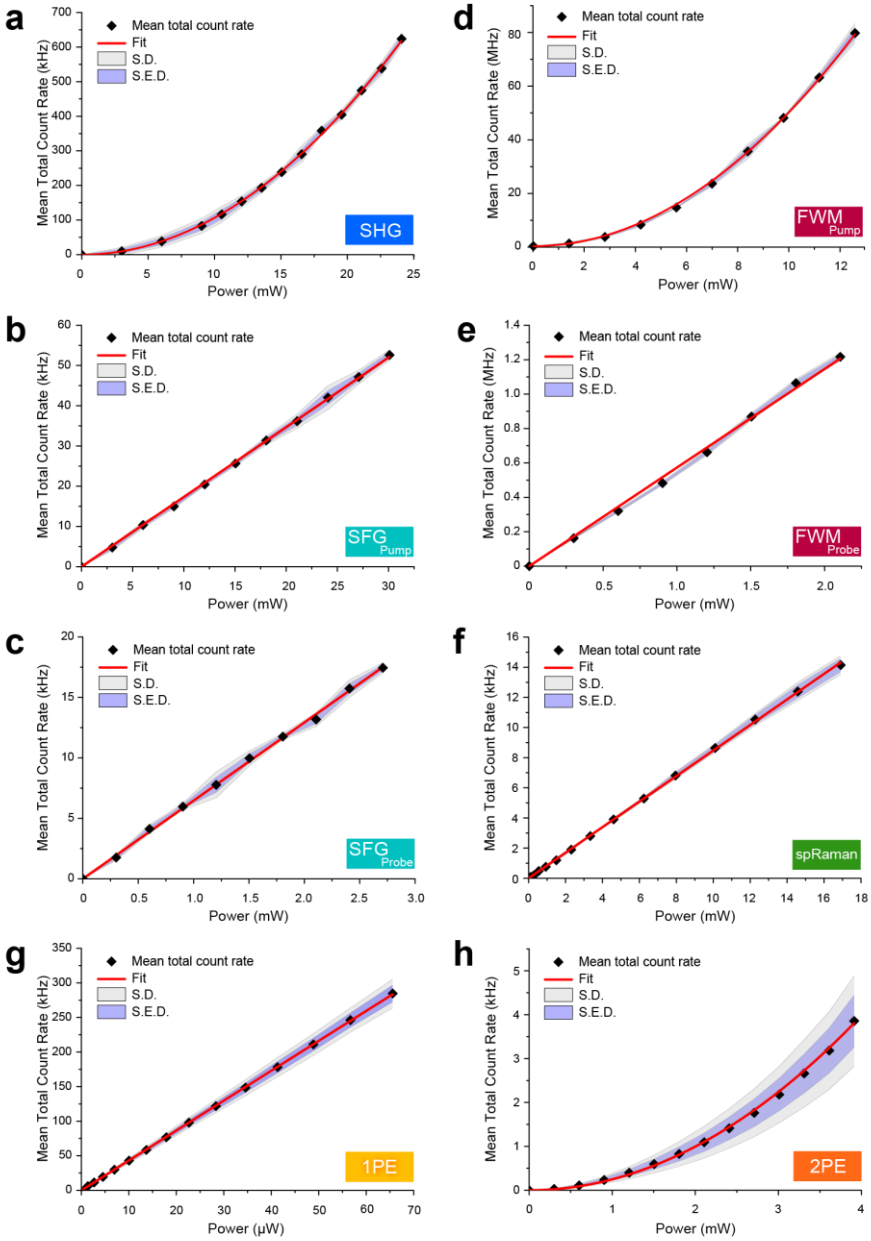

***Figure S1. Power dependencies of spectral signatures**. **a-f)** Nonlinear signatures of crystalline silicon (c-Si). **a)** Quadratic dependence of SHG intensity at 774 nm excitation, **b-c)** Linear dependence of SFG intensity on the pump and probe power **b)** with fixed probe power of 25.6 mW at 1050 nm and **c)** with a fixed pump power of 117.5 mW at 774 nm at the sample, **d-e)** Quadratic and linear dependence of FWM intensity on the pump and probe power **d)** with fixed probe power of 17.4 mW at 1050 nm and **e)** fixed pump power of 120.2 mW at 774 nm at the sample. **f)** Linear dependence of spontaneous Raman scattering at 520 cm^{-1} determined at 532 nm excitation. **g-h)** Fluorescence emission of 5 µM Atto532 in PBS under **g)** direct excitation at 532 nm and **h)** two-photon excitation at 774 nm. Mean values and standard deviations and standard error of the mean represent the average of triplicates.*

Supplementary Figure S2

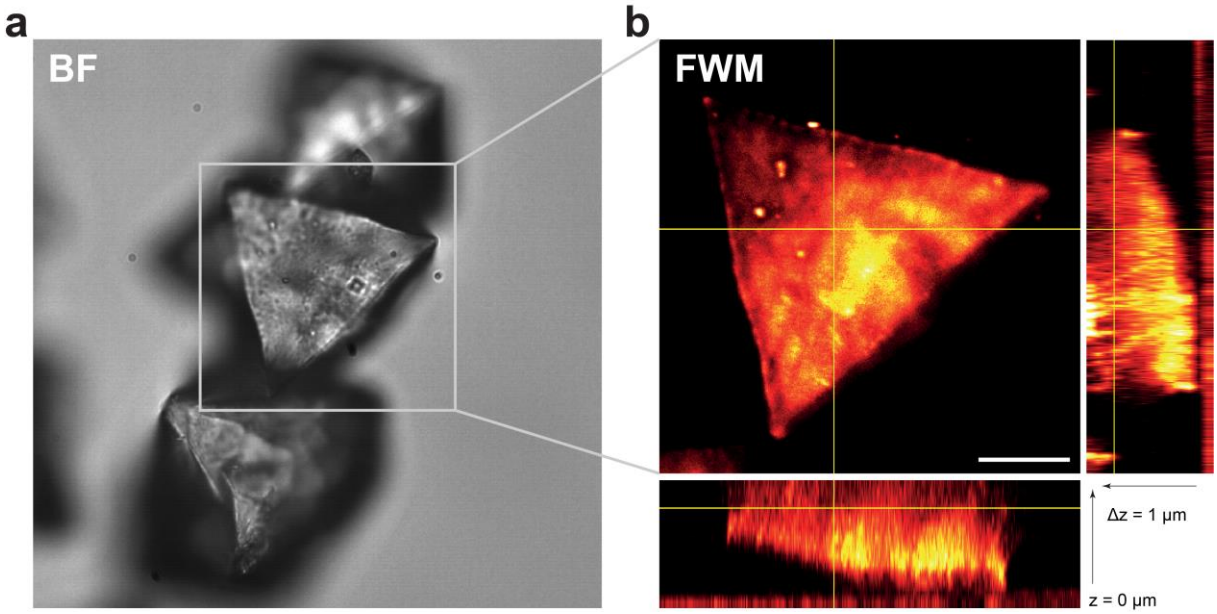

Figure S2. 3D image of UiO-67 based on FWM. a) *Brightfield image and* ***b) 3D FWM*** *dataset of a UiO-67 crystal on a glass coverslide surface. The main panel shows the 2D xy projection averaged over all 14 scans along the vertical axis in step sizes of 1 µm. The lower panel visualizes a horizontal xz cut through the crystal along the horizontal yellow line. The right panel shows the vertical xy cut through the crystal along the vertical yellow line. FWM imaging allows to visualize the inner structure of the crystal, without a significant decrease of the FWM signal in the crystal. The narrow layer at z = 0 µm visualizes the glass slide surface. Scale bar: 10 µm.*

Supplementary Figure S3

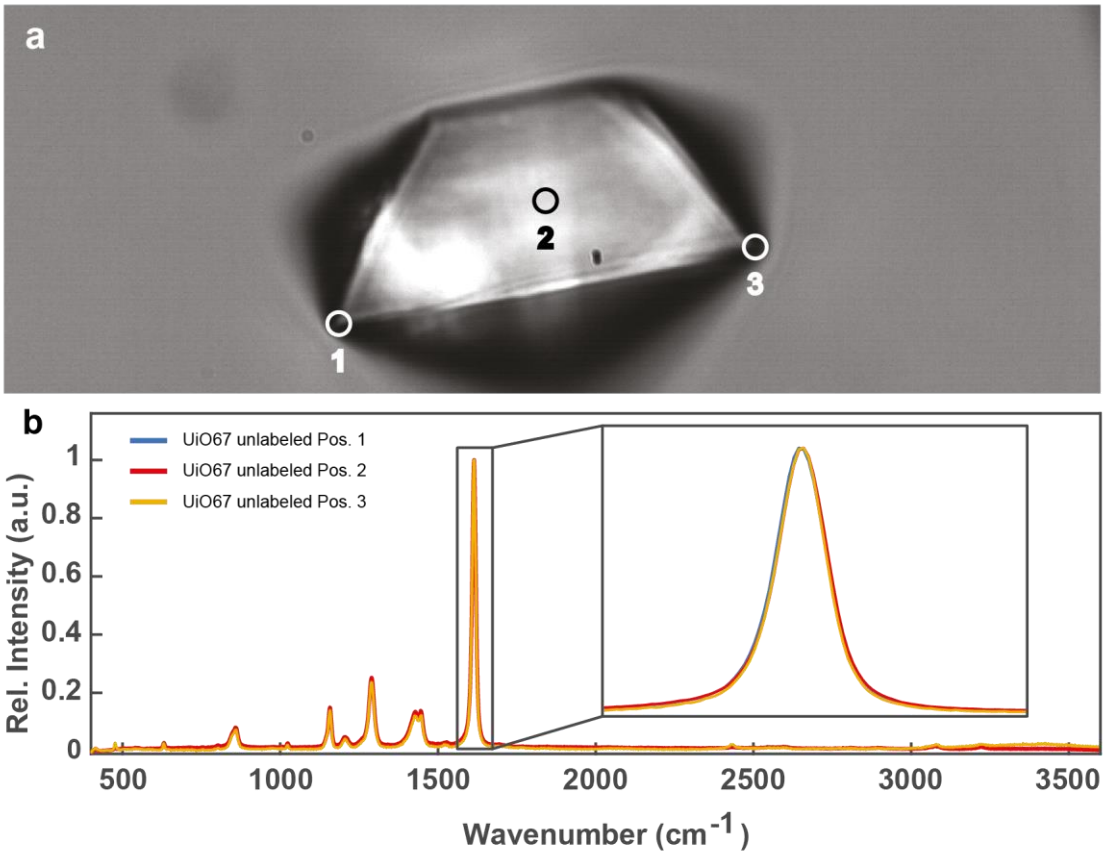

Figure S3. Raman signature of a UiO-67 MOF within the particle and at particle/air interfaces*. **a)** Bright-field image of the MOF particle. Circles indicate the measurement position at which spontaneous Raman spectra were recorded. **b)** Corresponding spontaneous Raman spectra. Spectrometer settings: EM gain 130, integration time 5 s, 10 repeats, grating 600 lines / mm. Excitation power 21 mW at 632.8 nm.*

Supplementary Figure S4

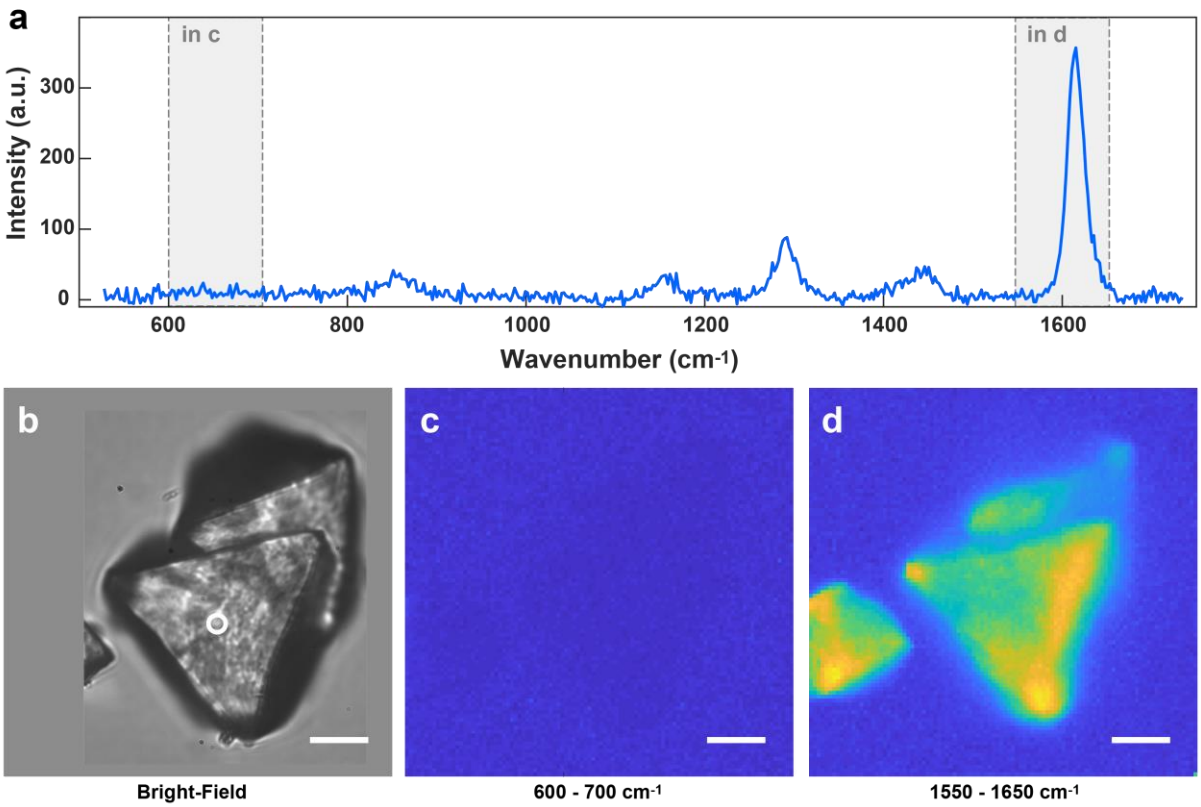

Figure S4. Hyperspectral imaging of UiO-67. ***a)*** *Raman spectrum at the position marked in the bright-field imaging in (b). Grey areas indicate the selected spectral regions for the univariate images in (c) and (d). The spectrum was recorded with 700 ms integration time using a grating with 600 lines / mm. The excitation power amounted to 21 mW at 632.8 nm.* ***b)*** *Bright-field image of UiO-67 particles.* ***c)*** *Univariate image based on the spectral components between 600 and 700 cm^{-1}.* ***d)*** *Univariate image plot based on the spectral components between 1550 and 1650 cm^{-1}. The color scale for both images is the same. The scanning range was 100 x 100 µm with 100 pixels per line. Scale bar: 15 µm.*

Supplementary Figure S5

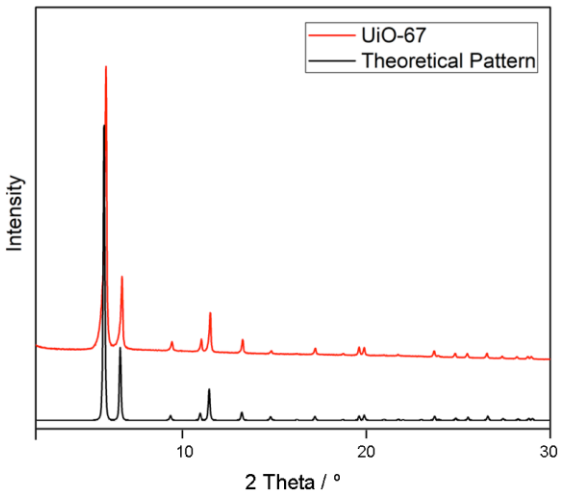

Figure S5. XRD characterization of UiO-67*. X-ray diffraction pattern of UiO-67 powder in comparison to literature data.[4] All reflections are in agreement with the theoretical pattern.*

Supplementary Figure S6

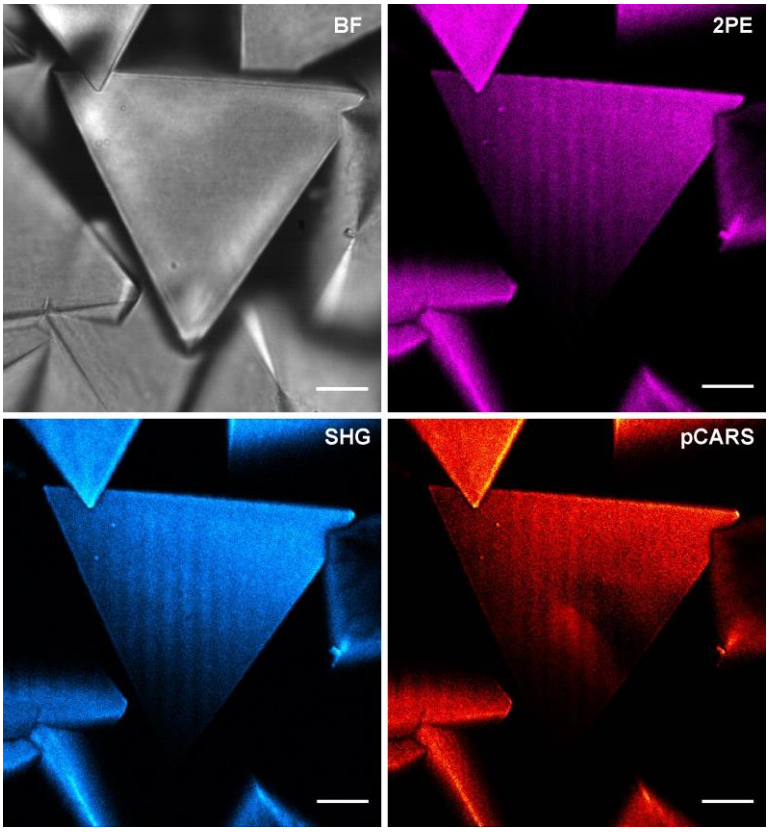

Figure S6. Multi-modal, nonlinear imaging on unlabeled UiO-67-MOFs*. Bright-field, 2PE induced autofluorescence and SHG show a smooth surface and well-defined edges of the particles. Together with pCARS imaging, spectral information on MOFs can be obtained over the full spectral range between 395 and 775 nm simultaneously. The chemical response is very even as expected. The scale bar amounts to 10 µm, Excitation power after the objective: pump: 3.8 mW, probe 4.2 mW (measured at 1050 nm). All images are summed up over triplets with an integration time of 720 ns/pixel. 2PE emission was detected using a 685/150 bandpass filter in combination with 750 SP and 785/10 Notch filter to block the laser excitation. SHG was detected at 387 nm using a 377/50 bandpass filter in combination with 680 SP to block the laser excitation. pCARS at 1615 cm-1 (688.2 nm) was measured consecutively to 2PE and with identical detection settings. All scale bars are 10 µm.*

Supplementary Figure S7

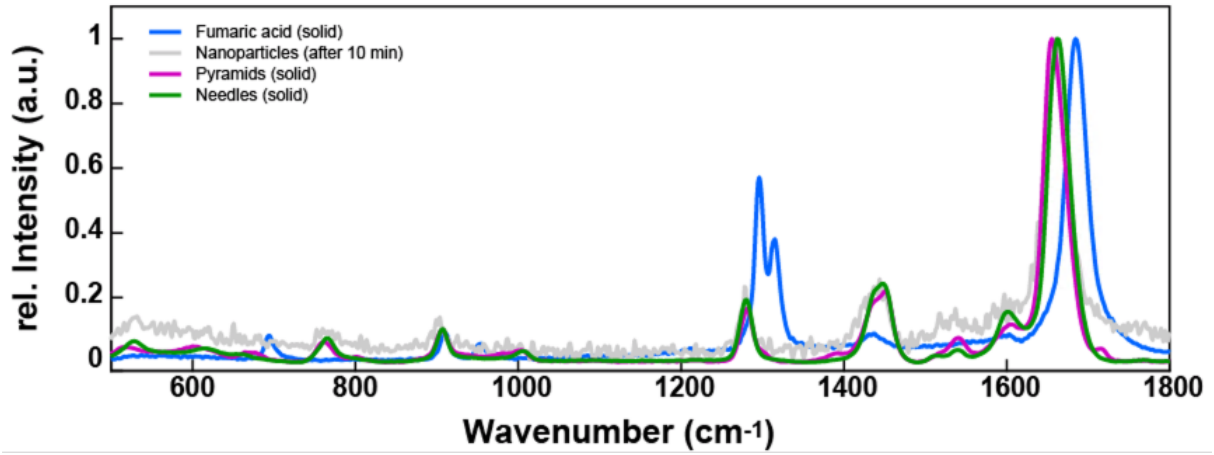

Figure S7. Raman signature of MIL-88A particles with different morphologies*. MIL-88A in the shape of needles, bipyramids, and crystalline nanoparticles were recorded in comparison to the fumaric acid linker. The MIL88-A nanoparticles were measured during the first 10 minutes after synthesis from their aqueous educts solutions. Excitation power was 15.1 mW at 532 nm. EM Gain was 200, with 10 s integration time and 10 repeats.*

Supplementary Figure S8

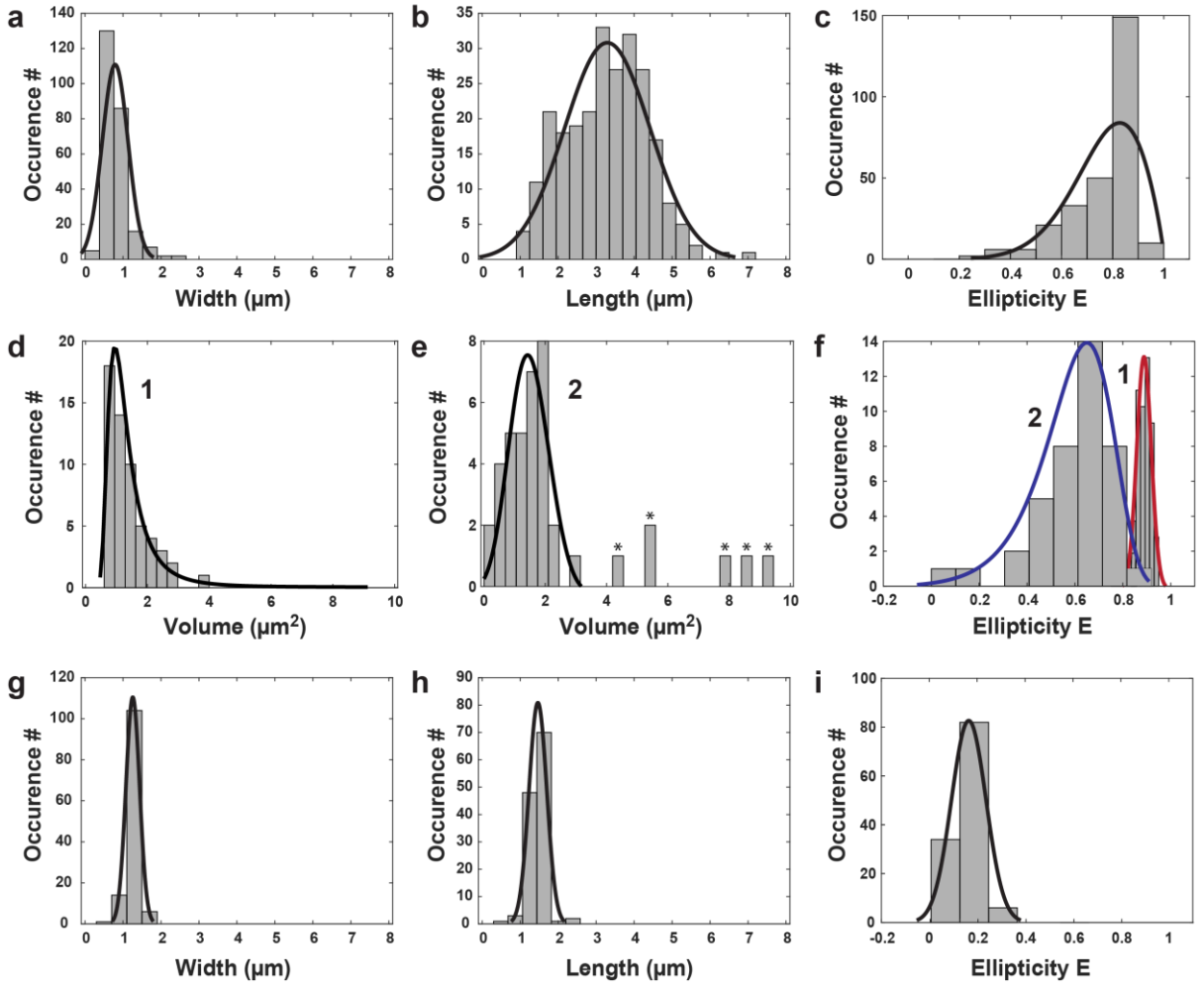

Figure S8. Histograms and fit curves for the particle-wise size distribution of MIL88-A microparticles depicted in Figure 6. a-e) *Size-distribution and volume of needle-shaped MIL88-A microparticles.* ***a)*** *Width and* ***b)*** *length for single particles are binned into a histogram and fitted to a normal distribution (N = 248). Their width and length amount to 0.79 ± 0.34 µm and 3.29 ± 1.12 µm, respectively.* ***c)*** *The ellipticity E for needles.* ***d)*** *Volume of the particles that show only FWM (N = 75). Fitted with a generalized extreme value model* ***e)*** *Volume of the particles that show CL under degradation (N = 40, star tagged values are excluded from the fit). Fitted with a generalized extreme value model.* ***f)*** *The ellipticity E distinguishes between particles that show (1; d) only FWM (N = 75, red) or (2; e) 2PE under degradation (N = 40, blue). Fitted with a generalized extreme value model.* ***g-h)*** *Size-distribution of bipyramidal MIL88-A microparticles:* ***g)*** *Width and* ***h)*** *length for single particles are binned into a histogram and fitted with a normal distribution. Their width and length amount to 1.25 ± 0.18 µm and 1.47 ± 0.23 µm, respectively.* ***i)*** *The ellipticity reveals a homogenous distribution for the particles (N = 125). Fitted with a normal distribution. Fit values for the mean (µ), the standard deviation (σ), and the full width at half maximum (FWHM) can be found in Supplementary* ***Table S4****.*

Supplementary Figure S9

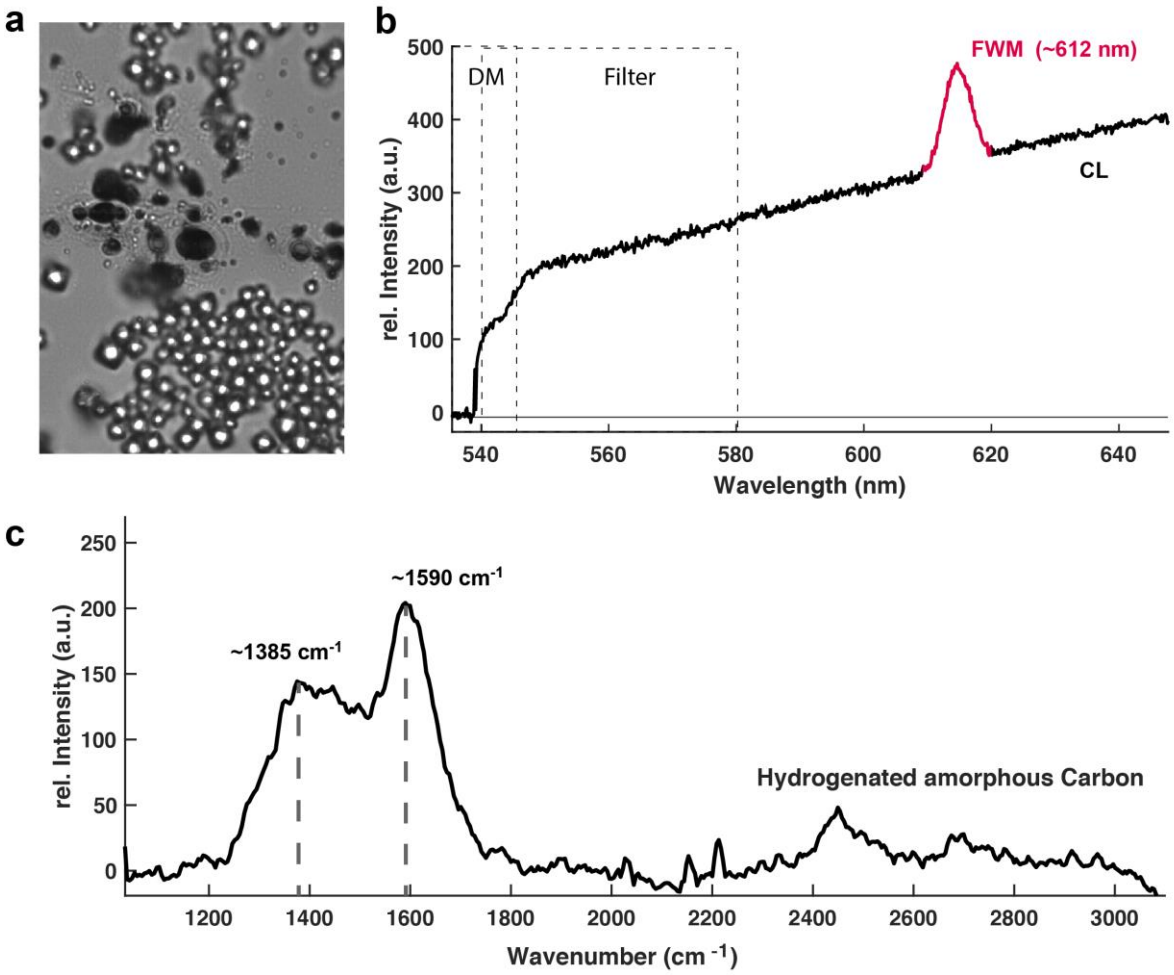

Figure S9. Chemiluminescence and degradation of pyramidal MIL-88A particles. a) *Brightfield image of intact bipyramidal particles (e.g. within the lower half, bright particles) and particles after degradation (e.g. center, black).* ***b)*** *Chemiluminescence (CL) spectrum between 540 and 650 nm. The edge of the dichroic mirror (DM) is marked on the left with dashed line. The FWM mixing signal around 612 nm is marked in red. The chosen spectral region for CL detection is highlighted in dashed lines and labeled with "Filter".* ***c)*** *Raman spectrum of the degraded particle in the center of panel a). The substance could be identified as hydrogenated amorphous carbon,[12] showing the complete oxidation of the linker with surrounding oxygen while emitting CL.*

Supplementary Figure S10

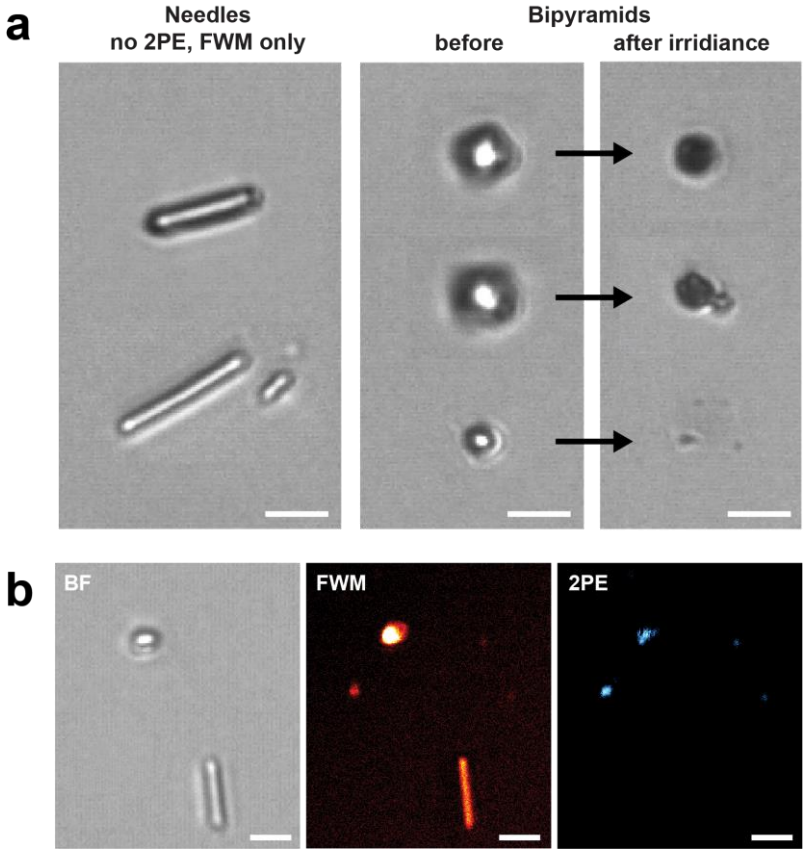

Figure S10. Correlation between particle volume and absorption-induced particle degradation during nonlinear excitation in the near-infrared (in Figure 6). a) *MIL88-A microparticles show a variable size distribution as seen by bright-field microscopy. Left: examples for needles-shaped particles. They only exhibit FWM, no 2PE; Middle panel: Bipyramidal particles of various diameters absorb and degrade as seen in the right panel. Scale bar is 2 µm.* ***b)*** *Example of two needle-shaped particles with comparable volume in the BF, FWM and 2PE channel. The elongated particle is showing only FWM, while the rounder particle is degrading and splintering into two fractions while emitting 2PE induced emission.* P_{pump} *= 3 mW and* P_{probe} *= 0.1 mW. Scale bar is 2 µm.*

Supplementary Figure S11

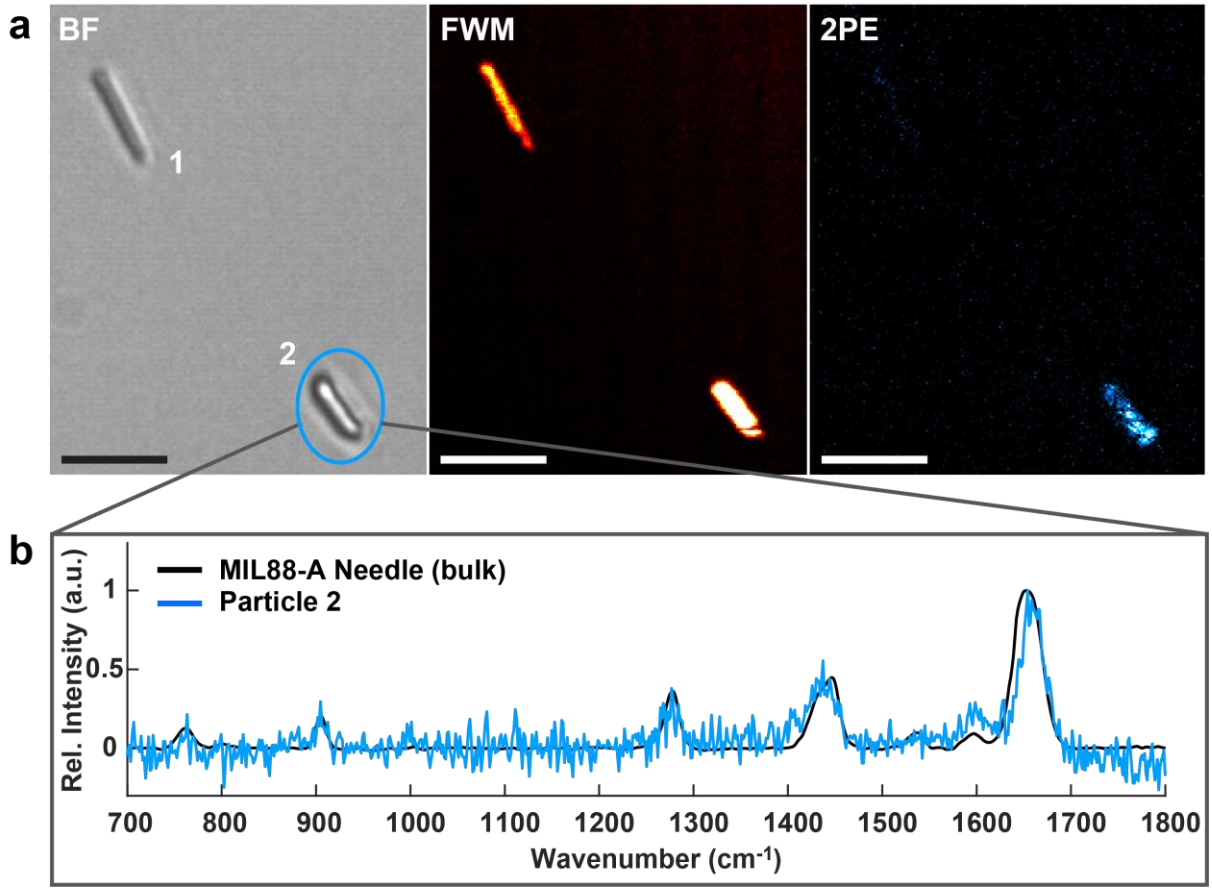

Figure S11. Raman signature of a MIL88-A needle-shaped particles displaying 2PE induced emission. a) *MIL88-A needle-shaped particles recorded by BF, FWM and 2PE imaging. While particle 1 shows FWM exclusively, particle 2 features both effects: FWM and 2PE. While 2PE can discriminate between them, BF and FWM cannot distinguish the particles according to their optical properties. Scale Bar is 5 µm.* ***b)*** *Raman spectroscopy on the single particle 2 and MIL88-A particles in bulk as comparison demonstrate that particle 2 clearly shows the identical chemical composition to MIL-88A. The spectra were recorded using a grating with 600 lines/mm, an integration time of 20 s, and 15 repeats. The excitation power amounted to 20 mW at 632.8 nm.*

Supplementary Figure S12

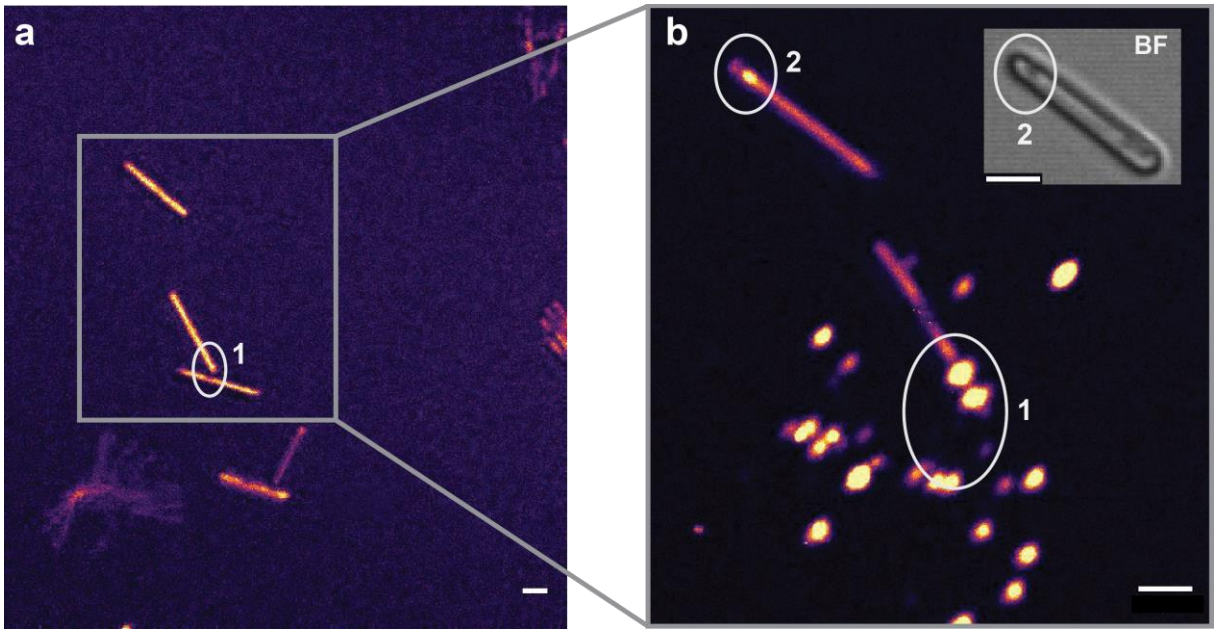

Figure S12. Degradation of elongated needle-shaped MIL-88A particles. a) *FWM image of MIL-88A needle-shaped particles in contact. Marker 1 indicates the contact area between the two lower particles. Single scan image, Scale bar 2 µm.* ***b)*** *Zoom onto selected particles. The overlaid FWM/2PE image shows the sum over 10 consecutive frames. Constant exposure to near-infrared laser excitation can lead to particle degradation. This occurs primarily in contact areas with higher electric fields, as indicated by Marker 1 (former contact site). The lowest particle has already completely degraded, while the middle particle is at the onset of degradation starting from the former contact site. A second possibility that triggers degradation are defects. These are observed as increasing 2PE signal with laser exposure. Marker 2 indicates an area with beginning degradation in the upper particle as seen by the intensity increase. (Inset) This hypothesis is supported by bright-field microscopy showing the same particle (BF, scale bar 2 µm). The darker spot indicating a defect area in the crystalline structure, overlapping with the brighter signal in the nonlinear channels. Scale bar: 2 µm.*

Supplementary Figure S13

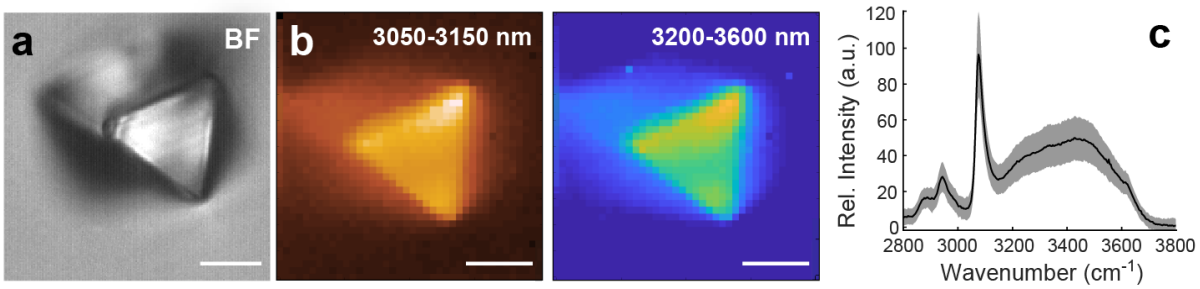

Figure S13. Water distribution in homogeneously grown MOF-801 crystals. a) *Brightfield (BF) image taken at saturated humid air (RH: 39.2 %). Scale bar: 5 µm.* ***b)*** *Hyper-spectral Raman images show the distribution of the water-corrected C-H stretch vibration around 3100 cm^{-1} (MOF linker) and the O-H stretch resonance (uptaken water) centered around 3200 and 3600 cm^{-1}. Water is homogeneously distributed and scales with the concentration of available MOF material. Raman mapping was carried out at 5 s integration time using a grating with 300 lines / mm. The excitation power was set to 4.5 mW at 532 nm. The scanning range was 20 x 20 µm with 40 pixels per line. Scale bar: 5 µm.* ***c)*** *Mean Raman spectrum of the hyper-spectral data set recorded in b) including standard deviation per spectral window.*

Supplementary Figure S14

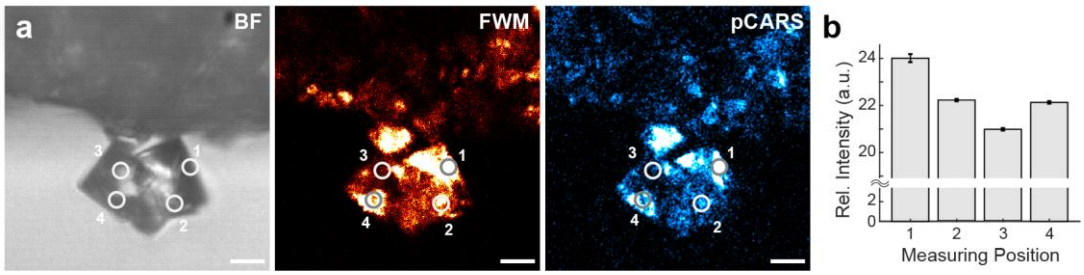

Figure S14. Water distribution over a cluster of MOF-801 crystals. a) *Brightfield (BF, left panel), Four-wave mixing (FWM, middle panel) and polarization-sensitive Coherent Anti-Stokes Scattering (pCARS, right panel) images of MOF-801 crystals saturated with humid air (RH: 33.1 %). Grey circles and numbers mark the positions for the Raman measurements underlying panel B. Scale bar: 5 µm.* ***b)*** *The relative intensity of the Raman signal of liquid water (scaled to the C-H stretch vibration of the MOF linker) varies with the position in the MOF.*

Supplementary Figure S15

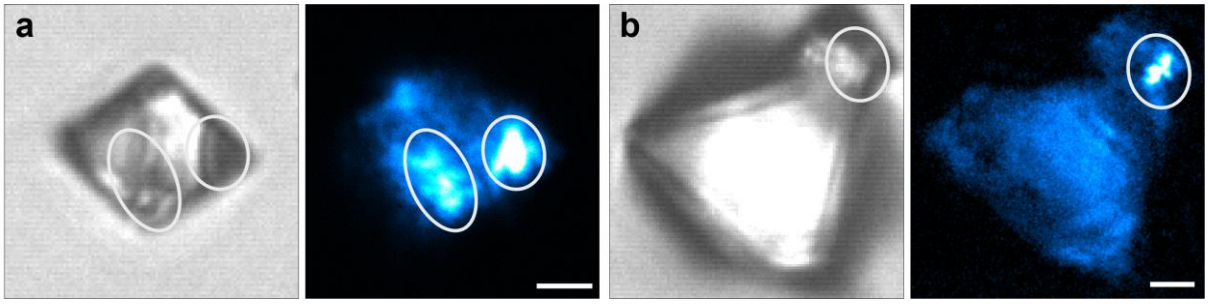

Figure S15. Brightfield and pCARS image depicting the water distribution in isolated MOF-801 crystals. a, b) *Two examples of single crystals. Marked are areas with higher water content and the respective region in the brightfield image. Scale bars are 2 µm. Measured at RH of 39.7 % and T = 22.1 °C.*

3. Supplementary Tables

Supplementary Table S1

Technique	Method	Properties			Strength	Limitation	
		Order	Electronic / Vibrational	Surface / Volume			
SHG	NLO microscopy using a single fs laser	$\chi(2)$	e / -	Volume Surfaces	Sensitive to areas made of non-centrosymmetric species, label-free, monolayer sensitivity	No sensitivity for molecular species with inversion symmetry	
SFG	NLO microscopy using two different fs lasers, probing an electronic transition at surfaces	$\chi(2)$	e / (v)	Volume Surfaces	Sensitive to areas made of non-centrosymmetric species, label-free, monolayer sensitivity	No sensitivity for molecular species with inversion symmetry	
FWM	NLO microscopy using two different fs lasers	$\chi(3)$	e / -	Volume	Label-free 3D imaging	No vibrational information High laser power	
pCARS	NLO microscopy using two different fs lasers, probing a vibrational transition.	$\chi(3)$	e / v	Volume	Vibrational imaging, label-free, spectroscopic identification possible	Non-resonant background, no linear correlation to the concentration	
Raman	Linear technique using a strong CW laser	$\chi(3)$	- / v	Volume	Full vibrational spectroscopy	Weak signal, long acquisition time	
1PE	Linear technique using a weak CW laser	$\chi(1)$	e / -	Volume	Linear proportional to concentration of dyes	Incoherent process, label required	
2PE	NLO microscopy using a single fs laser	$\chi(1)$	e / -	Volume	Less photodamage, deeper penetration depth	Incoherent process, label required	

Table S1. Overview and important aspects of NLO imaging and spectroscopy techniques employed in this work. *Colors encode the different techniques employed through-out the manuscript.*

Supplementary Table S2

BPDC			UiO-67		
Exp. [cm^{-1}]	**Lit. [cm^{-1}]**	**Assignment**	**Exp. [cm^{-1}]**	**Lit. [cm^{-1}]**	**Assignment**
628	628	Ring deformation	631	620	Zr-(OC) asymmetric stretching
			741	730	Zr-μ3-O stretching
				787	OH bending + CH bending (in-phase)
819	818	C-H out-of-plane			
830			856		Ring breathing
1022	1020	Ring deformation	1023		
1135	1134	C_{ring}-C in-plane	1157		
1190	1189	C-H in plane			
			1206	1209	Collective mode of the BPDC linker
1294	1293	Inter-ring C-C stretching	1290		
				1350	CC ring
1423			1428	1425	OCO asymmetric stretching (in)
1445			1445	1436	OCO asymmetric stretching (out)
1524	1522	C-C ring	1527	1540	CC ring
1613	1611	ν_s(C-C)	1615	1634	ν_s(C-C)

Table S2. Experimental Raman shifts (cm^{-1}) in comparison to literature for the linker 4,4'-biphenyl dicarboxylic acid (BPDC) and UiO-67.[13, 14] *Nomenclature: ν: stretching / δ: rocking mode / ρ: bending-in plane / ω: bending out-of plane / Def: deformation mode.*

Supplementary Table S3

Fumaric Acid			MIL-88A (Needle Morphology)		
Exp. [cm^{-1}]	**Lit. [cm^{-1}]**	**Assignment**	**Exp. [cm^{-1}]**	**Lit. [cm^{-1}]**	**Assignment**
695	694	ω(–CH); ω(–OH); ω(O–C=O)	648	650	ω(–CH); ω(–OH); ω(O–C=O)
			759	762	Rocking mode δ(O–C=O)
912	913	Bending vibration ω(–CH)	905	905	Bending vibration ω(–CH)
954	954	Bending vibration ω(–CH)		953	Bending vibration ω(–CH)
	971	Bending vibration δ (–CH); ω(–CH)		970	Bending vibration δ (–CH); ω(–CH)
1296	1299	ν(C–O); δ(–CH); ρ(–OH)	1278	1297	ν(C–O)
1315	1315	δ(C–O–H); ρ(–OH) / wide shoulder			
1437	1435	δ(–CH); ρ(–OH) / weak peak	1448	1430	ν_s(O–C=O)
1598	1605	ν(C=C)	1589	1580	ν_{as}(O–C=O)
1685	1685	ν(C=O), ν(C=C)	1653	1687	ν_s(C=C)
	2958	ν(-C-H)	2975	2980	ν(-C-H)
			3071	3070	ν_s(=C-H)

Table S3. Experimental Raman shifts (cm^{-1}) in comparison to literature for the linker fumaric acid and MIL-88A.[14, 15, 16] *Nomenclature: ν: stretching / δ: rocking mode / ρ: bending-in plane / ω: bending out-of plane / Def: deformation mode*

Supplementary Table S4

	Width [µm]		Length [µm]		Ellipticity				Volume [µm^3]		
	N_{EP1}	P	N_{EP1}	P	N_{EP1}	N_{EP2} FWM	N_{EP2} CL	P	N_{EP2} FWM	N_{EP2} CL	P
µ	0.7929	1.2569	3.2949	1.4655	0.8061	0.8587	0.6276	0.1250	1.0077	1.1638	1.1826
σ	0.3392	0.1805	1.1236	0.2343	0.0868	0.0304	0.1353	0.0441	0.3901	0.6194	0.4899
FWHM	0.7606	0.4048	2.5195	0.5255	0.1765	0.0682	0.3293	0.0988	0.6898	1.5058	1.2172

Table S4. Fit parameters from the Fit curves in Supplementary Figure S8. *µ is the mean value of the histogram, σ the corresponding standard deviation, and FWHM the full width at half maximum of the fit curve. N stands for needle morphology, P for the bipyramidal morphology. While the latter is always measured with a constant excitation power (EP1, see* ***Figure 4****), the needle morphology excitation power level is added in subscript (EP1 or 2). FWM stands for the fraction of needle particles at EP2 that show only stable FWM, while CL is representing the fraction of particles that additionally emit chemiluminescence.*

Supplementary Table S5

Fumaric Acid			MOF-801		
Exp. [cm^{-1}]	**Lit. [cm^{-1}]**	**Assignment**	**Exp. [cm^{-1}]**	**Lit. [cm^{-1}]**	**Assignment**
695	694	ω(–CH); ω(–OH); ω(O–C=O)	679	650	ω(–CH); ω(–OH); ω(O–C=O)
			760	762	Rocking mode δ(O–C=O)
			876	*866*	*DMF*
912	913	Bending vibration ω(–CH)	911	910	Bending vibration ω(–CH)
954	954	Bending vibration ω(–CH)		953	Bending vibration ω(–CH)
			998	980	Stretching vibration C-C(OO)
1296	1299	ν(C–O); δ(–CH); ρ(–OH)	1277	1297	ν(C–O), δ(–CH)
1315	1315	δ(C–O–H); ρ(–OH) / wide shoulder			
1437	1435	δ(–CH); ρ(–OH) / weak peak	1436/1447	1430	ν_s(O–C=O)
				1443	*DMF*
			1537	1542	δ(O–C=O) overtone
1598	1605	ν(C=C)	1582	1582	ν_{as}(O–C=O)
1685	1685	ν(C=O), ν(C=C)	1665	1667	ν_s(C=C)
				1676	*DMF*
			2869	*2867*	*DMF*
			2936	*2939*	*DMF*
	2958	ν(-C-H)			
			3069		ν(=C-H)
			3682		Zr μ_3-OH stretching

Table S5. Experimental Raman shifts (cm^{-1}) in comparison to literature for the linker fumaric acid and MOF-801.[14, 15, 17] *Nomenclature: ν: stretching / δ: rocking mode / ρ: bending-in plane / ω: bending out-of plane / Def: deformation mode. DMF: remaining contributions by DMF in MOF-801.*

4. Supplementary References

[1] W. Schrimpf, A. Barth, J. Hendrix, D. C. Lamb, Biophys. J. 2018, 114, 1518.

[2] J. Schindelin, I. Arganda-Carreras, E. Frise, V. Kaynig, M. Longair, T. Pietzsch, S. Preibisch, C. Rueden, S. Saalfeld, B. Schmid, J.-Y. Tinevez, D. J. White, V. Hartenstein, K. Eliceiri, P. Tomancak, A. Cardona, Nat. Methods 2012, 9, 676; C. T. Rueden, J. Schindelin, M. C. Hiner, B. E. DeZonia, A. E. Walter, E. T. Arena, K. W. Eliceiri, BMC Bioinformatics 2017, 18, 529.

[3] A. Laubereau, in *Ultrashort Laser Pulses: Generation and Applications*, (Ed: W. Kaiser), Springer Berlin Heidelberg, Berlin, Heidelberg 1993, 35.

[4] N. Ko, J. Hong, S. Sung, K. E. Cordova, H. J. Park, J. K. Yang, J. Kim, Dalton Trans. 2015, 44, 2047.

[5] W. Schrimpf, J. Jiang, Z. Ji, P. Hirschle, D. C. Lamb, O. M. Yaghi, S. Wuttke, Nat. Commun. 2018, 9, 1647.

[6] A. Zimpel, T. Preiß, R. Röder, H. Engelke, M. Ingrisch, M. Peller, J. O. Rädler, E. Wagner, T. Bein, U. Lächelt, S. Wuttke, Chemistry of Materials 2016, 28, 3318.

[7] P. Hirschle, C. Hirschle, K. Böll, M. Döblinger, M. Höhn, J. M. Tuffnell, C. W. Ashling, D. A. Keen, T. D. Bennett, J. O. Rädler, E. Wagner, M. Peller, U. Lächelt, S. Wuttke, Chem. Mater. 2020.

[8] C. Igathinathane, L. O. Pordesimo, E. P. Columbus, W. D. Batchelor, S. R. Methuku, Comput. Electron. Agric. 2008, 63, 168.

[9] M. Choura, N. M. Belgacem, A. Gandini, Macromolecules 1996, 29, 3839.

[10] M. B. J. Roeffaers, B. F. Sels, H. Uji-i, B. Blanpain, P. L'hoest, P. A. Jacobs, F. C. De Schryver, J. Hofkens, D. E. De Vos, Angew. Chem. Int. Ed. 2007, 46, 1706.

[11] R. Ameloot, F. Vermoortele, J. Hofkens, F. C. De Schryver, D. E. De Vos, M. B. J. Roeffaers, Angew. Chem. Int. Ed. 2013, 52, 401.

[12] S.-H. Hong, J. Winter, J. Appl. Phys. 2005, 98, 124304.

[13] S. Chavan, J. G. Vitillo, D. Gianolio, O. Zavorotynska, B. Civalleri, S. Jakobsen, M. H. Nilsen, L. Valenzano, C. Lamberti, K. P. Lillerud, S. Bordiga, PCCP 2012, 14, 1614; Y. R. Lee, S. Y. Eom, H. L. Kim, C. H. Kwon, J. Mol. Struct. 2013, 1050, 128; M. R. Lohe, M. Rose, S. Kaskel, Chem. Commun. 2009, 6056.

[14] A. Benítez, J. Amaro-Gahete, D. Esquivel, F. J. Romero-Salguero, J. Morales, Á. Caballero, Nanomaterials 2020, 10.

[15] Y. Du, H. X. Fang, Q. Zhang, H. L. Zhang, Z. Hong, Spectrochimica Acta Part A: Molecular and Biomolecular Spectroscopy 2016, 153, 580; Q. Cai, J. Xue, Q. Wang, Y. Du, Spectrochimica Acta Part A: Molecular and Biomolecular Spectroscopy 2017, 186, 29; K. I. Hadjiivanov, D. A. Panayotov, M. Y. Mihaylov, E. Z. Ivanova, K. K. Chakarova, S. M. Andonova, N. L. Drenchev, Chem. Rev. 2020.

[16] J. Amaro-Gahete, R. Klee, D. Esquivel, J. R. Ruiz, C. Jiménez-Sanchidrián, F. J. Romero-Salguero, Ultrasonics Sonochemistry 2019, 50, 59.

[17] L. Maury, L. Bardet, R. Brunel, R. Vierne, Journal of Raman Spectroscopy 1981, 11, 14; T. Matemb Ma Ntep, H. Breitzke, L. Schmolke, C. Schlüsener, B. Moll, S. Millan, N. Tannert, I. El Aita, G. Buntkowsky, C. Janiak, Chem. Mater. 2019, 31, 8629.

A.2. Water harvesting at the single crystal level.

Water harvesting at the single crystal level

Adrian Fuchs, Haoze Wang, Zhe Ji, Stefan Wuttke, Omar M. Yaghi* and Evelyn Ploetz*

Adrian Fuchs, Evelyn Ploetz
Department of Chemistry and Center for NanoScience (CeNS), LMU Munich, 81377 Munich, Germany
Email: evelyn.ploetz@lmu.de

Haoze Wang, Zhe Ji, Omar M. Yaghi,
Department of Chemistry, University of California–Berkeley; Materials Sciences Division, Lawrence Berkeley National Laboratory; Kavli Energy NanoSciences Institute at Berkeley; and Berkeley Global Science Institute, Berkeley, CA 94720, USA
Email: yaghi@berkeley.edu

Zhe Ji
Current address: Department of Chemistry Stanford University, Stanford, CA 94305, USA

Omar M. Yaghi
UC Berkeley-KACST Joint Center of Excellence for Nanomaterials for Clean Energy Applications, King Abdulaziz City for Science and Technology, Riyadh 11442, Saudi Arabia

Stefan Wuttke
BCMaterials, Basque Center for Materials, UPV/EHU Science Park, 48940 Leioa, Spain

Stefan Wuttke
Ikerbasque, Basque Foundation for Science, 48013, Bilbao, Spain

Knowing the upper limit of an intrinsic property for a material is critically important in realizing its full potential. For example, determination of all the adsorptive sites in metal-organic frameworks (MOFs) has led to the design of structures with exceptionally high surface areas[1]. Recently, MOFs have been shown to be useful in harvesting water from desert air[2-10], where the water productivity depends on how fast water can move in and out of the pores.[4,11-14] While such cycling kinetics of water sorption could be measured experimentally in bulk[2-4,6,10,15-19], this has yet to be done on the single crystal level, leaving unanswered the question of what is the upper limit of how much water can be harvested in a given time. Herein, we present a general strategy to quantitatively determine the water sorption isotherm and the kinetics of uptake and release within a single crystal by Raman spectroscopy. We found that for a MOF-801 crystal, water moves ~20 times faster than in the bulk[11]. This represents the upper limit for MOF-801, and indicates that water harvesting devices could produce up to 3.8 L of water per hour per kilogram of MOF, a vast improvement over the previously reported 2.8 L per day[4,11].

Main

Motivation

The uptake performance of porous materials is usually determined by measuring bulk properties using mass gravimetric methods[3,8], and described by the total uptake, the uptake mechanism (hence isotherm type), and the kinetic behavior. However, metal-organic framework (MOF) materials feature – like all crystalline materials – diverse defect sites (**Figure 1**), resulting in the disruption of their crystallinity due to macropores, mechanical deformations, or inter-crystal growth. The latter leads to particles with multiple crystalline zones or amorphous areas. In addition to defects (even if ideally grown), single crystals interfere with each other's uptake behavior in

multiple ways, such as (i) shielding neighboring particles from adsorbing guest molecules in the surrounding airflow and, hence, reducing the accessibility to pores or (ii) by creating condensation pockets between them[20]. Measuring the performance of the sorbent material alone, without the interference of intra- and inter-particle effects, would require a spatially resolved, quantitative method for monitoring the uptake.

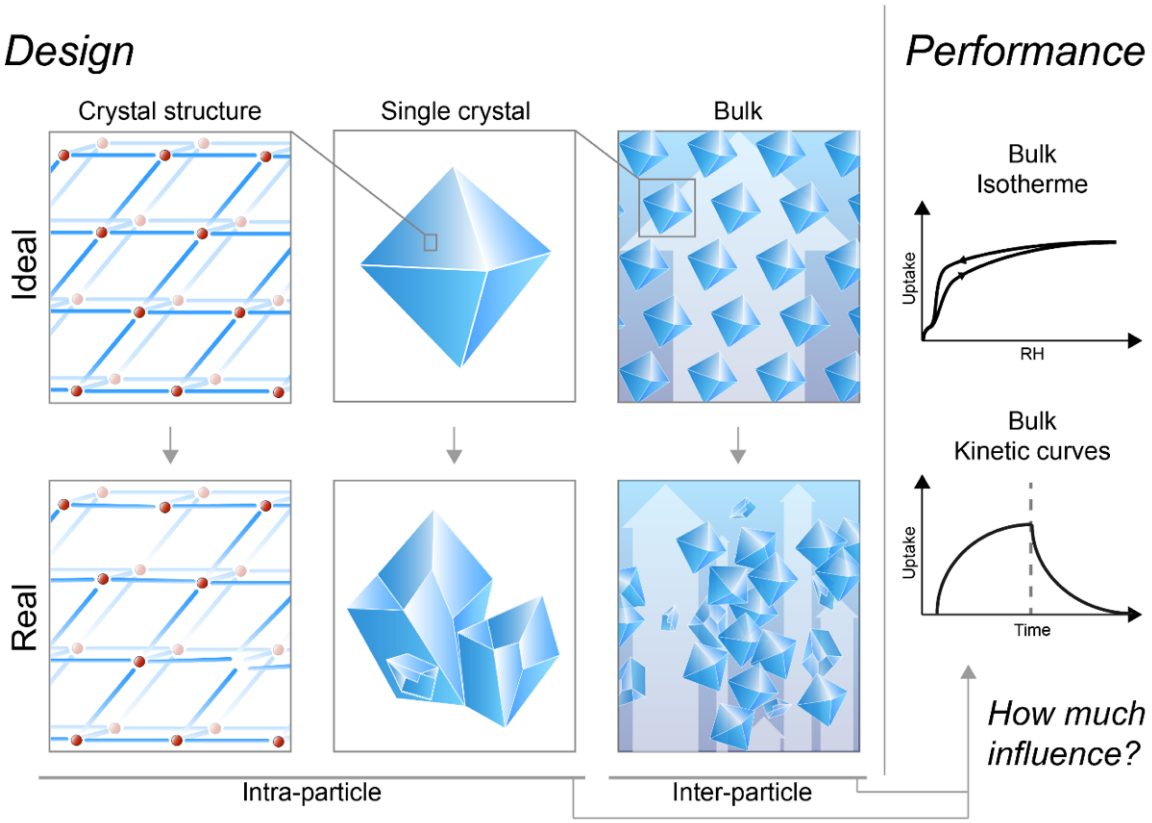

Figure 1: Design and performance evaluation of atmospheric water harvesting MOF materials. *Comparing the influence of intra- and inter-particle effects on the bulk performance of sorbent systems for an ideal (single crystal) and real (bulk) material.*

Monitoring the water uptake in MOF-801 crystals via Raman spectroscopy

We report an optical methodology based on Raman spectroscopy (**Methods Section 1-2**) to quantitatively determine isotherm and kinetic curves with sub-micron spatial resolutions, thereby effectively probing the water uptake performance (total uptake, isotherm, and kinetics) of single crystals (SC). We chose MOF-801 in this study, an

important and well-studied MOF for atmospheric water harvesting (AWH).[2] The MOF-801 structure is made by linking zirconium-oxide / -hydroxide clusters linked with fumarate dianions, typically synthesized as octagonal-shaped crystals with triangular faces (**Figure 2a**) and sizes of up 10 µm. We implemented Raman spectroscopy for a label-free, 3D characterization of the chemical composition and background-free detection of water inside MOF-801. The water signature (characterized by the broad OH-stretch vibration around 3300 cm^{-1}) and MOF-801 are spectrally well resolved (**Figure 2b**). We employed this spectral orthogonality in combination with the linear dependence of the intensity on the amount of water to monitor water uptake *in situ* with a spatial resolution of ~ 270 nm provided by the confocal microscope. Therefore, the probed volume is significantly lower than the average MOF-801 crystal size.

Firstly, we employed Raman spectroscopy to confirm the known mechanism of water uptake originally derived from single-crystal X-ray diffraction.[2] A detailed description of the model is given in **Supplementary Note 1.2**. We monitored the Raman signature of water in MOF-801 in terms of position and shape of the OH-stretch vibration, with increasing relative humidity (RH). MOF-801 features a multi-step mechanism for water uptake with binding sites in tetrahedral and octahedral cages within the asymmetric unit cell of MOF-801 (**Figure 2c**). In the dry state with no water molecules bound, only the Zr: μ_3-OH stretch vibration of the metal-bound hydroxyl ligand at 3682 cm^{-1} was detectable (**Figure 2c**). This sharp, defined resonance gives clear evidence of the crystalline nature of this Zr(μ_3-OH) hydroxyl group and the absence of guest molecules. The binding of water molecules is expected to occur first in the tetrahedral binding pocket to Zr(μ_3-O) units (purple water molecules). Indeed, we observed already at 2% RH a rising contribution of the OH-stretch resonance of water molecules between 3400 to 3700 cm^{-1} due to the incorporation of guest water molecules. As predicted, the Zr(μ_3-

OH) sites were unaffected and showed an identical Raman intensity as in the dry state (**Figure 2c**). Between 2 to 6% RH, water also adsorbs at the Zr(μ_3-OH) sites (turquoise water molecules), altering and diminishing the free vibration of the hydroxyl OH stretch Raman band at 3682 cm^{-1}, until it vanished. At 8% RH, the hydroxyl Raman peak was no longer detectable, while the uptaken water led to a further intensity increase in the OH-stretch Raman signal between 3400 to 3700 cm^{-1}.

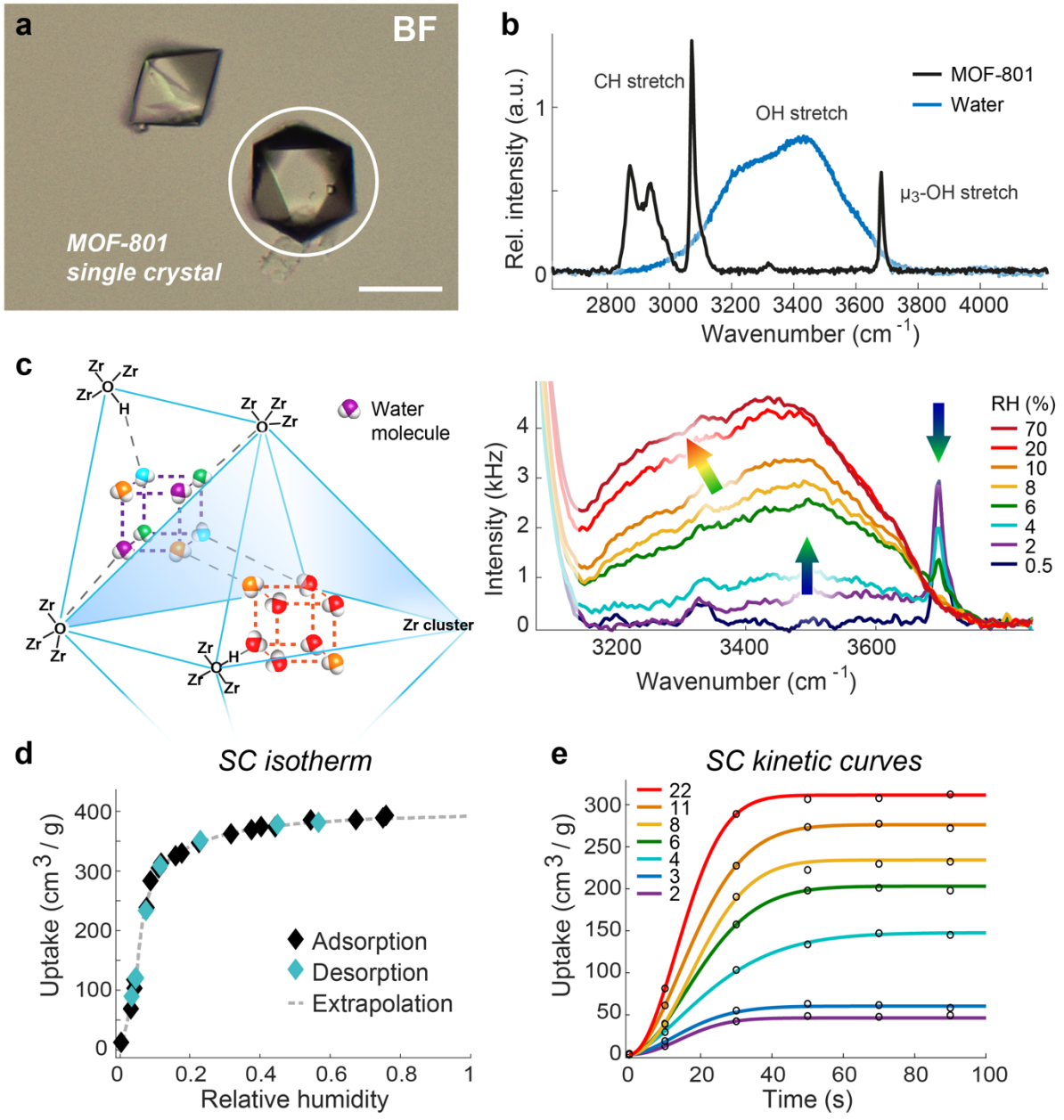

Figure 2: Water uptake in single, isolated MOF-801 crystals monitored by Raman spectroscopy. ***a)*** *The bright-field image of MOF-801 shows isolated single crystals. Scale bar 50 µm.* ***b)*** *Raman spectra of dry MOF-801 and liquid, double-distilled water.* ***c)*** *Raman spectroscopy of MOF-801 at increasing*

relative humidity (RH) confirms consecutive binding of water molecules in the tetrahedral (purple dotted cube) and octahedral (red dotted cube) binding sites of the crystal structure. Coloring of water molecules (starting from blue, purple, cyan, green, and orange to red) indicates the binding order according to the reported uptake mechanism[2] for MOF-801. Arrows indicate spectral changes between corresponding humidities. Abbreviations: Zr: zirconium; O: oxygen; H: hydrogen atoms ***d)*** *Absolute water uptake of single crystal (SC) MOF-801 derived from the ratiometric Raman analysis at varying humidity. Adsorption (black) and desorption (cyan) are reversible. The dotted line indicates the underlying isotherm, extrapolated to 100 %RH.* ***e)*** *Kinetic of water uptake within the same crystal after exposure to selected relative humidities. The uptake saturates in ca. 50 s. Colored lines represent single-step Avrami fits, black dots show the data points.*

In addition to the rise in intensity, the OH peak maximum also shifted to lower wavenumbers, indicating increased damping due to consecutive hydrogen bond formation to neighboring water molecules (green and orange water molecules). After saturation of the tetrahedral binding sites, the octahedral binding pockets are occupied until saturation is reached (red water molecules). Saturation starts above 20% RH with only a small amplitude increase still up to 70% RH. With increasing relative humidity, every new water molecule is further away from the metal clusters and shielded from the host framework. The spectral shape of the OH-stretch water peak in MOF-801 starts resembling the Raman signature of liquid water (**Figure 2c; Extended data Figure 1a**), as water guest molecules fill up the pores of MOF-801 gradually. Humidity-dependent Raman spectra clearly support the published uptake mechanism in MOF-801.

Given the observed good agreement between the spectroscopic data and model, we next derived a theory-supported method to quantify the adsorbed water at the single crystal level (**Methods Section 2** and **Supplementary Note 2**). The volume of water uptake $\frac{V_{H2O}}{m_{MOF}}$ (in cm^3/g of MOF) can be expressed via the density of the water-free host

material ρ_{MOF} and the ratiometric expression $\frac{A_{OH}}{A_{CH}}$ linking the Raman intensity of the OH-stretch vibration of water to the CH-stretch vibration of MOF-801.

$$\frac{V_{H2O}}{m_{MOF}} = \frac{A_{OH}}{A_{CH}} \cdot \frac{1}{\rho_{MOF}} \cdot \Gamma \qquad \text{Eq. (1)}$$

The scaling factor Γ (cf. Materials and Methods and **Supplementary Note 1.2**) can be experimentally calibrated or theoretically modeled from the predicted number of water molecules $N_{H2O}(RH)$ in the asymmetric unit cell of MOF-801 at a given relative humidity. With this, we can quantify the water uptake at the SC level by converting the ratiometric ratio of measured OH to CH stretch Raman intensity.

We subsequently evaluated the inherent material performance of MOF-801 for taking up water without the interference of intra- or inter-particle effects using a series of Raman spectra inside of homogeneous, single crystals (SC). These were recorded as a function of relative humidity (*i.e.,* as isotherm curves) or as a function of the time after exposure to a given humidity (*i.e.*, kinetic curves). **Figure 2d** displays the SC isotherm for MOF-801 at 23.3 °C with a sub-micron resolution. The isotherm is characterized by a three-step behavior: after a steep uptake increase below ~8% RH, it features a second phase with slower adsorption behavior until 20% RH and slow saturation as the last phase above 20% RH. In contrast to bulk experiments[2], no hysteresis could be observed, as expected for regular single crystals with uniform pore size. Monitoring the temporal behavior of water uptake by MOF-801 at different relative humidities between 2 and 20% RH (**Figure 2e**) shows a nearly instantaneous uptake within the first tenth of seconds and the built-up of a constant plateau identical to the total amount of water observed in the SC isotherm. By modeling the kinetics using an Avrami model[21,22], we found a saturation time around ~ 50 s (**Supplementary Note 1.1)**.

Influence of defects and inter-particle effects at the SC level

For water harvesting applications, MOF-801 is usually grown in monocrystalline, regular single crystals (Type 1).[2] For about 10 % of the particles, however, we found

MOF-801 particles without crystalline faces (Type 2); see SEM images in **Extended Data Figure 1b**). While regular crystals possess strongly reflecting surfaces with defined triangular shapes, Type 2 crystals display a complex inner structure as seen already by bright-field microscopy (**Extended Data Figure 1c-d)**. We verified the associated, higher level of defects by four-wave mixing (FWM) imaging, which is susceptible to defect sites and irregularities[23]. In contrast to the regularly formed, homogenous MOF-801 crystals**,** we found inhomogeneous substructures in defect-rich particles (**Extended Data Figure 1d)** with localized, enhanced FWM signals indicating open metal sites inside the material[23]. SC X-ray diffraction on Type 1 and 2 crystals further confirmed the monocrystalline or amorphous, polycrystalline nature of the material (**Supplementary Note 3**), respectively. While Type 1 crystals possessed the expected cubic unit cell[2] with space group Pn-3, Type 2 particles were composed of multiple MOF-801 unit cell patterns with different orientations in the same crystal, hence representing defect-rich crystals with sub-crystallization zones.

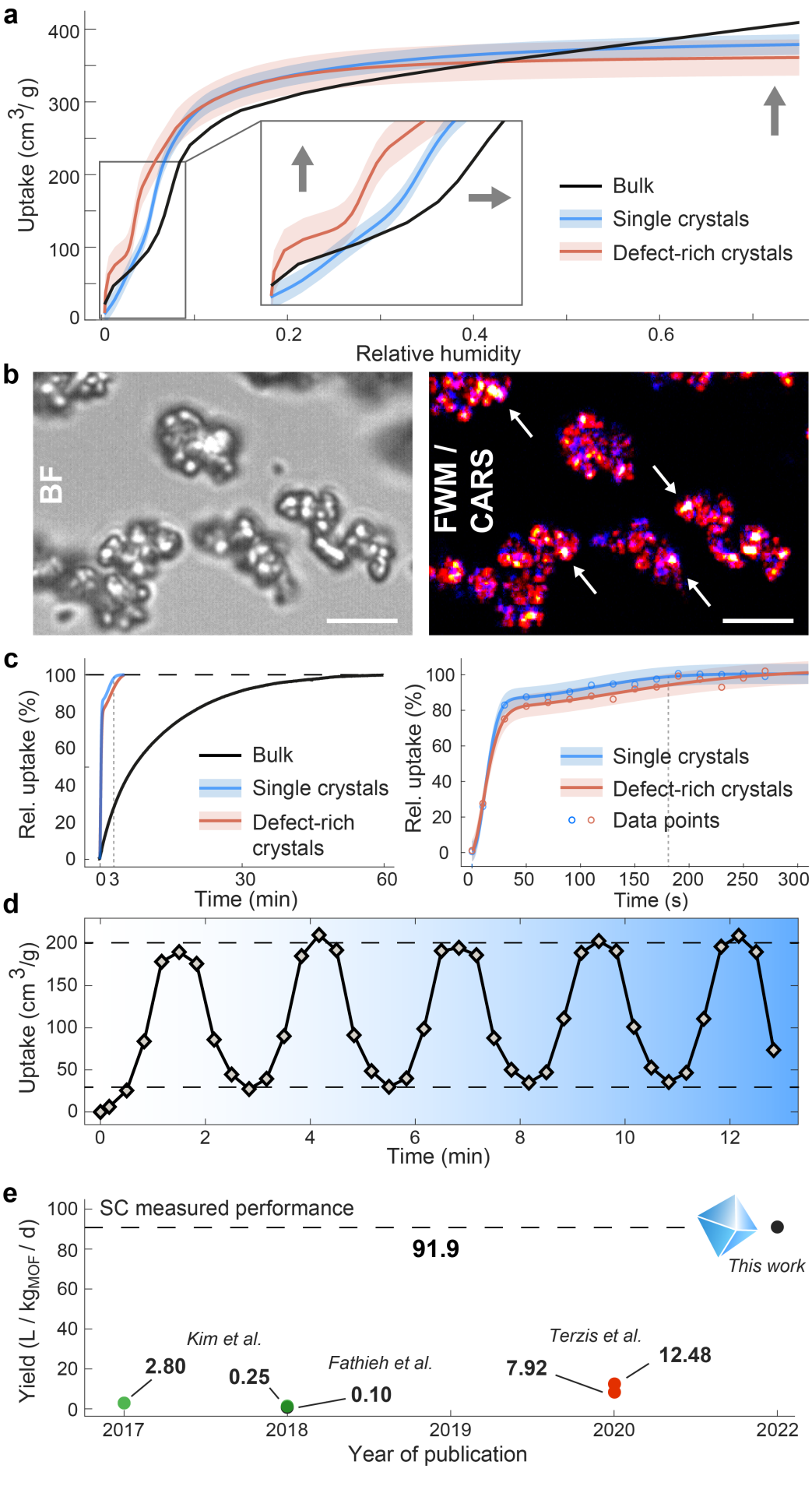
a
Uptake (cm3/ g)
Relative humidity
Bulk
Single crystals
Defect-rich crystals
b
BF
FWM / CARS
c
Rel. uptake (%)
Time (min)
Bulk
Single crystals
Defect-rich crystals
Rel. uptake (%)
Time (s)
Single crystals
Defect-rich crystals
Data points
d
Uptake (cm3/g)
Time (min)
e
SC measured performance
91.9
This work
Yield (L / kgMOF / d)
Kim et al.
2.80
0.25
Fathieh et al.
0.10
Terzis et al.
7.92
12.48
Year of publication

176

Figure 3: Influence of intra- and inter-particle effects in MOF-801 on SC isotherms and water kinetics. a) *Isotherms of the bulk, the regular, single, and defect-rich MOF-801 crystals. The colored lines represent the mean fit curve of SC (N = 7) and defect-rich (N = 5) particles. The shaded areas represent the corresponding standard deviation.* ***b)*** *Bright-field (BF, left panel) and label-free imaging based on FWM (red hot) and CARS (blue) microscopy to monitor the morphology and position of particle clusters with respect to uptaken water at 30% RH after saturation at ~70% RH for 5 minutes. CARS imaging based on the Raman resonance around 3400 cm^{-1}, i.e. 612 nm, shows the distribution of water within the material. While, some defect sites coincide with enhanced uptake (white spots, marked by arrows), we found a dominating contribution of inter-particle adsorption of water. Scale bar 2 µm.* ***c)*** *Bulk and average SC adsorption kinetic of dry MOF-801 (N = 5) after exposure to nitrogen with 8 %RH, described by a customized Avrami fit function. While even a thin layer of bulk material needs about 1 h until saturation, single crystals saturate in 3-4 minutes (left panel). Dotted lines mark the 3 min time point. Even defect-rich particles take up >80 % of the total amount in less than 60 s (right panel). Circles mark the center of the 20 s long detection window per point. The standard deviation (shaded area) was derived per data point.* ***d)*** *Relative SC uptake when switching the RH that surrounds the sample between 0 and 8 %RH every 80 s.* ***e)*** *Overview of published water yields in MOF-801 in bulk compared to the relative SC uptake in (d) (91.91 ± 1.44 L/kg_{MOF}/d, dotted line): Kim et al. (Ref. [4,11]; green) reported a potential yield for a solar powered device at 20% RH of 2.8 L/kg_{MOF}/d in 2017 and a prototype in 2018, that could produce 0.25 L/kg_{MOF}/d at 10-40% RH. At the same time, Fathieh et al. (Ref. [24]; black) reported a prototype with a capacity of 0.1 L/kg_{MOF}/d tested in the desert with no additional cooling and only ambient sunlight. Terzis et al. (Ref. [25]; red) applied active heating and cooling to a fluidized MOF-801 powder to enable fast cycling times with 7.92 (at 18% RH) and 12.48 L/kg_{MOF}/d (at 39% RH).*

Next, we set out to investigate how intra-particle effects in defect-rich particles influence the SC performance compared to monocrystalline MOF-801. **Figure 3a** depicts the mean SC isotherm of regular single crystals (blue; standard deviation as blue shade; cf. **Supplementary Figure S12**) at 23.3 °C. We found a type IV isotherm with a clear step around 7% RH, a fast saturation below 20% RH, and maximum uptake of about 379 cm^3/g (±16.5 cm^3/g) at ~77% RH.

While the mean isotherm of defect-rich particles (orange) resembled the overall performance of regular crystal isotherms, it displayed three major differences: (i) Firstly, the standard deviation was significantly higher, reflecting the high variance of the underlying defects in the selected particles. (ii) Secondly, a faster uptake at low relative humidity was seen for isotherms in type 2 particles. The accompanying shift of the isotherm step towards lower RH confirms a higher amount of primary water molecules in the structure, as well as macropores created by missing cluster defects as observed by FWM imaging (**Figure 3b**). (iii) Thirdly, the average maximum uptake is decreased compared to regular crystals, meaning the inner surface per volume of defect-rich particles was found to be lower.

The bulk isotherm showed a higher uptake compared to the regular SC isotherm at very low RH, indicating open metal sites as observed for defect-rich particles. Below 10% RH, the bulk isotherm rises less steeply than the SC isotherm, causing a shift of the infliction point toward higher RH. Above 10% RH, the SC and the defect-rich isotherm both show a strong and distinct saturation, while it still increases linearly in bulk. At RH over ~60%, this results in more water per bulk material than in single crystals alone. However, water adsorbed in this regime is not accessible for harvesting applications at low humidity.

Next, we approached the question of what effects are responsible for the different uptake behavior in bulk and at the SC level. In bulk, water molecules can condense in the inter-particle space between crystals leading to an additional uptake. As defects like cracks or macropores can equally contribute to water incorporation and hysteresis, we employed a combination of FWM and Coherent Anti-Stokes Raman Scattering (CARS) imaging to visualize the morphology and position of MOF-801 in comparison to the distribution of uptaken water. FWM monitors the distribution of MOF-801 material

and especially open metal sites[23], while CARS localizes and quantifies uptaken water. **Figure 3b** displays the overlay of an FWM (red) and a CARS (blue) image over the same region at 20.8% RH, measured after saturating the system at 70% RH for about 5 min. Areas, where local water clusters are caused by defect sites, appear white in the image (examples marked with arrows). We found that the water signal was mostly anti-correlated to the FWM signal, indicating liquid water between and around the crystals. This explains the larger amount of uptaken water and the missing hysteresis in SC isotherms of regular single crystals compared to bulk (**Extended Data Figure 1e, f**).

Due to interparticle adsorption, the bulk kinetics differs significantly from the SC kinetic behavior (**Figure 3c)**. While the SC isotherms of MOF-801 were saturated within less than 3 min after a change in RH around the sample, the uptake in bulk saturated after 1h. The kinetic response of dry, regular MOF-801 crystals (8% RH) revealed a fast uptake, reaching > 85 % within the first 60 s. The datasets were approximated by a dual-step Avrami model (**Supplementary Note 1.1; Supplementary Figure S13**). It revealed a second uptake step between 100 and 200 s, probably due to subsequent filling of the octahedral binding sites in MOF-801. The kinetic behavior of Type 2 particles (**Figure 3c**; orange curve) followed the Type 1 curve very closely. When modeling the condensation of water within MOF-801 by a dual-step Avrami fit, more than 80 % uptake was found to occur within the first minute, while the successive filling process was observed around 100 to 200 s. Overall, water uptake by Type 2 particles was found to happen slower than by regular crystals. This might be caused by the complex inner structure, hindering the fast transport to the inside of the particles. It could also be that defect sites on the peripheral regions of the particle spawn fast water clusters, which are blocking the diffusion of water molecules further inside[26].

Since the desorption time of single crystals are in the same regime as the adsorption (**Extended Data Figure 1g**), the inherent cycle time for MOF-801 itself is significantly faster than currently possible in water harvesting devices due to inter-particle contributions. To demonstrate the maximum capabilities of the undisturbed MOF-801 framework, we selected a regular single crystal and cycled the RH between 0 and 8% with a cycle time of 160 s (**Figure 3d**). The sample was first completely dried with nitrogen (**Methods Section 3)**. Next, the RH of the gas stream over the sample was changed from 0 to 8% RH (or back) every 80 s while the uptake was monitored. The first desorption is not returning to the ground level at t = 0 s, which could be caused by primary bound water molecules that are not desorbing on the selected time scale. During the recorded cycle, we found a total difference in relative uptake (maximum – minimum per cycle) of 851 ± 13.3 cm^3 / g MOF over five cycles, i.e., a possible harvest of ~170 cm^3 / g MOF every 160 s or 91.91 ± 1.44 $L/kg_{MOF}/d$ (**Figure 3e**). In comparison, MOF-801 was implemented into a water harvesting device to test practical water harvesting cycling (WHC).[24] It produced 100 g of water per kg of material, however requiring a day-and-night cycle. Similarly, Kim et al. reported a theoretical harvest of ~250 g per kg MOF per day.[4,11] Faster WHC (36 and 26 minutes) were achieved by fluidization of the MOF particles, but requiring active heating and cooling,[25] in contrast to the experiments in this work. The remarkable time difference of WHC on the single crystal level to literature values indicates the vast potential of achieving the upper limit of the material. This corresponds to harvest between 360 – 920 times more water compared to currently available devices without active heating.

Conclusion

We have demonstrated a methodology based on *in situ* Raman spectroscopy for measuring qualitative and quantitative water sorption with sub-micron resolution. By monitoring and understanding the intra- and inter-particle contribution of water uptake via adsorption-desorption isotherm and kinetic curves in MOF-801 at the single-crystal level, we found a striking difference in sorption behavior between single crystals and the bulk material. Before this work, it was assumed that the measured bulk sample was representative for each crystal when applying sorption isotherms, although crystals were not created equally nor possessed identical characteristics, such as size, morphology, or defect level. By measuring cyclic water sorption at the single-crystal level, which is the most intrinsic state of solid material, we determined the upper limit for MOF-801 with a minimum cycle time below 3 minutes. This surprisingly fast cycle time enables a potential harvest of ~3.8 L water per hour per kilogram of MOF, a significant improvement over the previously estimated 2.8 L per day[4,11]. Therefore, our approach could help to reveal the upper limit of a material's inherent property to push technology advancement.

Materials

1. Hyperspectral Raman imaging at a controlled relative humidity

Static and dynamic Raman spectroscopy measurements were carried out on a home-built, confocal, multi-modal microscope[23] using a 532 nm CW laser source (Samba 100 04-01, Cobolt GmbH). The excitation power was 21 mW (measured at the entrance of the microscope backport) for all measurements. Spectra were recorded between 2300 and 4215 cm^{-1} probing the CH-stretch region of the MOF-801 material, and the OH-stretch vibrations of adsorbed water molecules, if not mentioned otherwise. The spatial resolution of the Raman mapping experiment was 0.27 µm in the lateral and 0.74 µm in the axial direction for a 60x water-immersion objective lens (1.2 NA). The scattered light at the sample was collected in epi-detection using a spectrometer (Kymera 328i, Andor Solis) equipped with a 300 lines/mm grating and a 512x512 pixel emCCD camera (iXon 897, Andor Solis). This instrumental configuration enables a spectral resolution of ~15 cm^{-1}. The spectral acquisition was controlled by *Andor Solis for Imaging V4.30* (Oxford Instruments). For image acquisition, areas with 500 nm step-size were raster-scanned while full Raman spectra were recorded at each pixel of the image. The acquisition time per pixel was set to 5 s.

For monitoring adsorbed water molecules in MOF-801 *in situ*, we installed a relative humidity control unit (**Figure 4a**) on the confocal setup. The MOF sample is located in a channel slide (µ-Slide I Luer Glass Bottom, Ibidi) on top of the XYZ scanning stage of the microscope and connected to the flow system. Dry nitrogen serves as the reference and carrier gas for extracting water molecules from the MOF materials through constant flow. A three-way vault can switch between this drying line and the 'wet line' containing nitrogen with a specific relative humidity. The latter can be adjusted

by the flow ratio regulated by two mass flow controllers (MFC, D-6311-FGD-33-AV-99-0-S-DR, Wagner Mess- und Regeltechnik GmbH): the nitrogen in the ‘wet line’ is enriched with water vapor by diffusing through a double-distilled, water-filled vessel. The relative humidity is controlled directly after mixing and at the sample chamber, as marked by RH in **Figure 4a**. The laboratory temperature was set to 23.3 °C, and the total mass flow was held constant at 1 standard liter nitrogen per minute for all experiments.

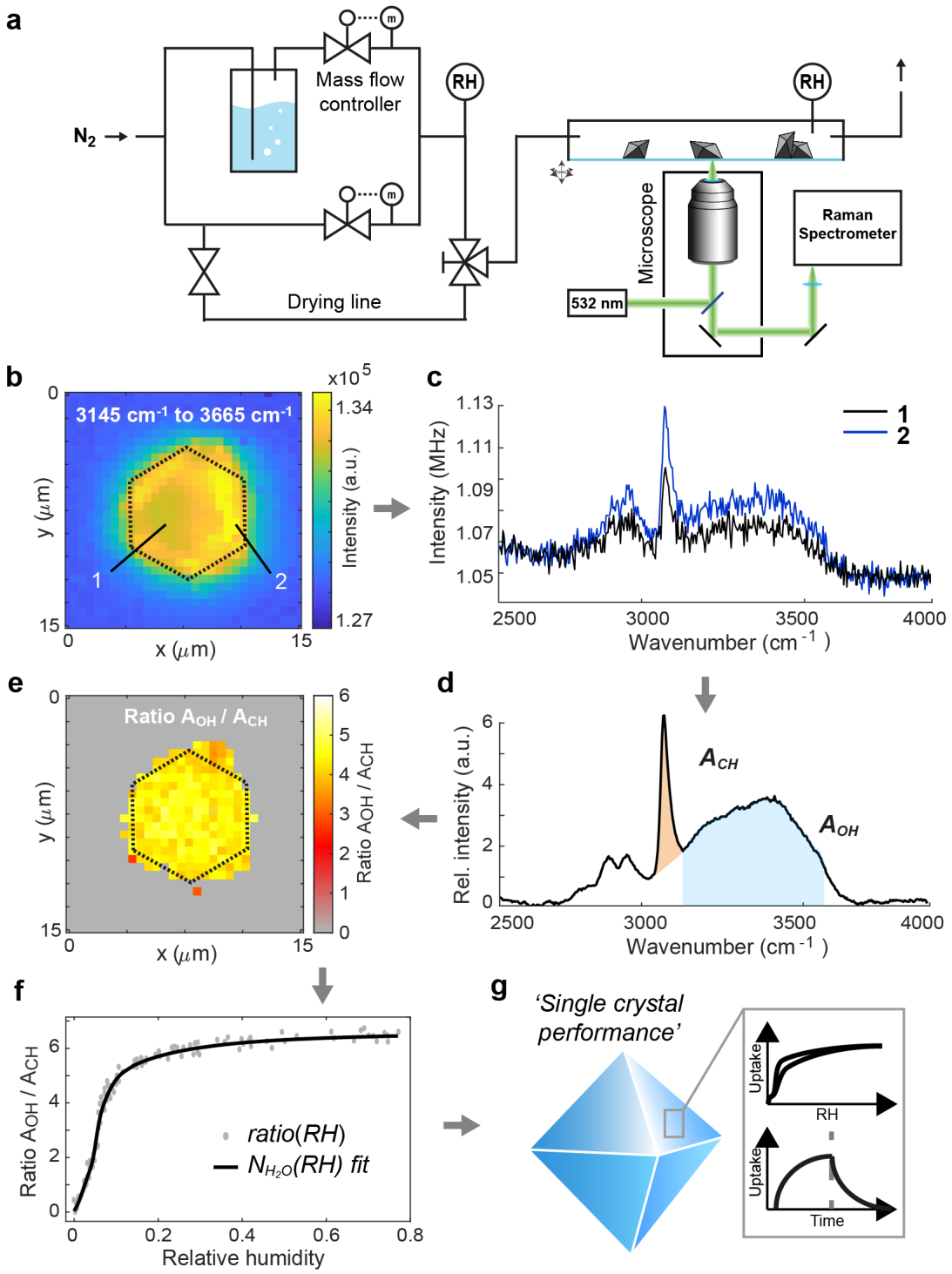

Figure 4: Quantification of water uptake in MOF-801 at the single crystal level by Raman spectroscopy. a) *Schematics of the micro-spectroscopy setup with the unit for controlling the relative humidity over the sample. RH: relative humidity measuring stations.* ***b)*** *Univariate analysis of a hyperspectral Raman data set in the water OH—stretch region reveals an irregular water distribution in a regular single crystal of MOF-801. Crystal border at measurement plane is indicated as dotted line. Raman mapping was carried out at 5 s integration time. The scanning range was 20 x 20 µm with 40 pixels per line.* ***c)*** *Raman spectra of selected pixels marked in (a).* ***d)*** *Background corrected, mean*

spectrum over all pixels inside the crystal border. The strength of the CH- (orange) and the OH-stretch vibration (blue) is indicated as area under the graph. ***e)*** *The ratiometric representation* A_{OH} / A_{CH} *of the HRI data set in (a) shows a uniform water distribution.* ***f)*** *Ratio* A_{OH} / A_{CH} *at varying relative humidities between 0 and 77 %RH recorded for 7 regular single crystals (grey points) allows for determining number of water molecules per unit cell, i.e.* $N_{H2O}(RH)$. ***g)*** *Schematic of the single crystal performance methodology.*

2. Quantification of water uptake

The local uptake and distribution of water were quantified based on the linear dependence of Raman scattering on the number of scattering molecules in the confocal volume (**Supplementary Note 2.31**). To ensure that water is evenly distributed in uniformly grown MOF-801 crystals, we first used hyperspectral Raman imaging (HRI) within a region of interest and recorded Raman spectra at each pixel. We visualized the water content in MOF-801 crystals first by univariate data analysis and derived the Raman intensity A_{OH} of the OH stretch vibration of water between 3145 and 3665 cm^{-1} as a function of the position within the crystal

$$A_{OH}(x,y) = \int_{3145\ cm^{-1}}^{3665\ cm^{-1}} I_{Raman}(\tilde{\nu},x,y)\ d\tilde{\nu} \qquad \text{Eq. (1)}$$

Figure 4b depicts an exemplary water distribution at ~38 %RH (**Figure 4b**). The apparent hexagonal shape of the crystal clearly confirms the sectioning capabilities of HRI and the correct positioning for imaging the particle: the image plane was successfully selected at around 50% height of the octahedral crystal (**Supplementary Figure S15**) for monitoring the water content inside the crystal center. The HRI image shows a continuous water distribution throughout the whole crystal with apparently increased water content at the surface boundaries, in addition to an intensity gradient from left to right. This apparent increase at the edges would indicate that saturation inside the crystal would not have been reached yet, even after 1 h of equilibration at ~38 %RH. For a regularly shaped crystal, we would expect an even distribution of adsorbed water per MOF material within minutes due to fast intra-crystalline diffusion[20], contrary to the experimental findings.

Deviations in apparent water uptake are caused by a combination of light scattering at the edges and a varying amount of MOF material inside of the detection volume due to defects and the 3D nature of the particles. Both effects lead to a variation in local

excitation power and detection efficiency, an incomplete filling of the confocal volume, and concomitantly to a change in absolute amplitude of the recorded Raman spectra, as for example seen for areas within the interior (Position 1) and at the edge (Position 2) in MOF-801 (**Figure 4c**).

To prevent any influence of these effects on the quantification of the water uptake in MOF-801, we introduced a ratiometric approach that quantifies the amount of detected, water-associated OH-stretch intensity in comparison to the observed CH-stretch signal reporting on MOF-801 and hence the amount of surrounding host material present. Here, the water uptake relates not to A_{OH} alone but to the ratio of A_{OH} / A_{CH}.[27] **Figure 4d** shows the background-corrected, mean spectrum over all pixels inside the crystal. The strength of the OH-stretch band A_{OH} is marked in blue, the CH-stretch A_{CH} is in orange. To correct against the spectral overlap between the water-based OH-stretch and MOF-801-associated CH-stretch resonance below 3150 cm^{-1}, modeling and deconvolution of the water peak from the MOF-signature (**Supplementary Note 2.2**) was employed, resulting in the area marked in orange. Using the ratiometric representation, i.e., when plotting the peak ratio A_{OH} / A_{CH} as a function of position, the interior displays an even signal (**Figure 4e**), representing the expected uniform, saturated uptake of water inside the crystal.

To convert the ratiometric Raman ratio into a quantitative measure, i.e., into water volume per mass of MOF-801, three interrelations need to be considered (please confer to **Supplementary Note 2** for a detailed description):

(1) The uptake can be related to the density of water ρ_{H2O}, the respective molecular weight M_x, as well as the amount of material n_x in the confocal volume and hence the Raman intensity of the OH and CH stretch vibration

$$\frac{V_{H2O}}{m_{MOF}} = \frac{n_{H2O} \cdot \frac{M_{H2O}}{\rho_{H2O}}}{n_{MOF} \cdot M_{MOF}} = \frac{A_{OH}}{A_{CH}} \cdot \frac{cf_{OH}}{cf_{CH}} \cdot \frac{M_{H2O}}{\rho_{H2O} \cdot M_{MOF}} \quad \text{Eq. (2)}$$

393 The latter formula takes into account that the detected intensities of both Raman
394 resonances A_x are proportional to the quantity of guest and host species

$$n_{H2O} = cf_{OH} \cdot A_{OH} \,/\, N_A \quad \text{and} \quad n_{MOF} = cf_{CH} \cdot A_{CH} \,/\, N_A \quad \text{Eq. (3)}$$

395 (2) The conversion factors can be determined either experimentally or theoretically.
396 Experimental calibration was carried out in pure water and dry MOF-801 material.
397 Knowing the density of the host and guest material allows for calculating the number
398 of Raman active species in the confocal volume in the first step, irrespective of the
399 absolute Raman intensities. The conversion factors of dry MOF-801 and water under
400 excitation intensity would amount to

$$cf_{OH} = \frac{n_{H2O,cal}}{A_{OH,cal}} = \frac{\rho_{H2O} \cdot V_{confocal}}{A_{OH,cal} \cdot M_{H2O}} \quad \text{Eq. (4a)}$$

$$cf_{CH} = \frac{n_{MOF,cal}}{A_{CH,cal}} = \frac{\rho_{MOF} \cdot V_{confocal}}{A_{CH,cal} \cdot M_{MOF}} \quad \text{Eq. (4b)}$$

401 with $A_{x,cal}$ referring to the peak strength of the OH- or CH-stretch vibration for the host
402 and guest material. When combining eq. 4-5, the expression for water uptake shortens
403 to

$$\frac{V_{H2O}}{m_{MOF}} = \frac{A_{OH}}{A_{CH}} \cdot \frac{A_{CH,cal}}{A_{OH,cal}} \cdot \frac{1}{\rho_{MOF}} \quad \text{Eq. (5)}$$

404 For identical measurement conditions of the calibration measurements, the ratio
405 $\frac{A_{CH,cal}}{A_{OH,cal}} := \Gamma$ of calibrated Raman intensities remains constant and can be treated as a
406 scaling factor

$$\frac{V_{H2O}}{m_{MOF}} = \frac{A_{OH}}{A_{CH}} \cdot \Gamma \cdot \frac{1}{\rho_{MOF}} \qquad \text{Eq. (6)}$$

As laid out in **Supplementary Note 2,** the measurement conditions for calibrations of host and guest molecules-associated scaling factors differ due to variations in excitation intensity induced by scattering in the detection volume. While no polarization dependency in MOF-801 was found for the CH and the OH-stretch Raman peak (**Supplementary Figure S6**), we need to incorporate the reduction in excitation power and hence linearly decreased Raman signature of the detected CH stretch vibration and adopt the experimental scaling factor to

$$\Gamma_{exp} = \frac{A_{CH,cal}}{A_{OH,cal} \cdot L_{scatter}} \qquad \text{Eq. (7)}$$

We estimated the average scattering loss $L_{scatter}$ on MOF-801 compared to transparent water alone by determining the integrated transmission intensity of broadband white-light via brightfield microscopy (**Supplementary Figure S7**). We experimentally obtained the loss parameter for MOF-801 to be 0.5651 ± 0.0884 and the experimental scaling factor Γ_{exp} as 0.0837 ± 0.0131.

(3) Since the experimental determination of Γ is challenging, we further modeled the number of water molecules in the asymmetric unit cell of MOF-801 as a function of the relative humidity $N_{H2O}(RH)$ based on the water uptake mechanism[2] in MOF-801. Modeling by an adapted Klotz model reveals that the volume water uptake in (cm^3 / g MOF) and relative humidity N_{H2O} are related by a linear scaling factor of 8.22 (**Supplementary Note 1.2**).

$$\frac{V_{H2O}}{m_{MOF}} = N_{H2O}(RH) \cdot 8.22 \qquad \text{Eq. (8)}$$

Knowing that the ratio A_{OH} / A_{CH} describes the uptake as a function of relative humidity while being proportional to the number of water molecules $N_{H2O}(RH)$ by a constant factor f_{fit}

$$\frac{A_{OH}}{A_{CH}} = N_{H2O}(RH) \cdot f_{fit} \qquad \text{Eq. (9)}$$

we can theoretically derive an expression for the scaling factor Γ_{th} (insert eq. 9-10 in eq. 7), that is independent of the calibration procedure

$$\Gamma_{th} = \frac{8.22 \cdot \rho_{MOF}}{f_{fit}} \qquad \text{Eq. (10)}$$

With the theoretical model (**Supplementary Note 2.3**) and eq. 10 at hand, we employ the SC isotherm data itself expressed as ratio A_{OH} / A_{CH} as a function of relative humidity and fit its course to the model function $N_{H2O}(RH)$ to determine the scaling factor Γ_{th}. **Figure 4f** depicts the ratio A_{OH} / A_{CH} at relative humidities between 0 and ~77 %RH and the model fit function $N_{H2O}(RH)$ that determines the number of adsorbed water molecules per asymmetric unit cell. We found a model-supported scaling factor $\Gamma_{th} = 0.0938 \pm 0.0041$ with uncertainty that only depends on the intrinsic noise of the underlying Raman spectrum (**Supplementary Figure S8**). It is in good agreement with the calibration-based scaling factor of $\Gamma_{exp} = 0.0837 \pm 0.0131$ (**Supplementary Figure S9**) within the range of error (cf. **Supplementary Note 2.4**).

442 **3. Raman-based single-crystal isotherms and sorption kinetics**

443 MOF-801 powder was placed in a channel slide (µ-Slide I Luer Glass Bottom, Ibidi) on
444 the microscope and dried under nitrogen flow until the RH reached 0.0 %RH (for at
445 least 1h). In the following, adsorption isotherm / kinetic curves refer to measurements
446 with a prior increase in relative humidity, while desorption experiments refer to a prior
447 decrease in RH. Crystals were selected in the bright field channel and measured in the
448 midplane of the selected particles. The corresponding measurement parameters are
449 summarized in **Table T1**. The laser power was 25 mW (measured in front of the
450 microscope body) for all experiments.
451
452 For SC isotherms, we waited for equilibration of the system after a change in RH (at
453 least 3 min) before starting the measurement of each data point. For SC
454 adsorption/desorption isotherms, we waited at least 10 minutes after the adsorption
455 measurement before reducing the RH again to ensure full saturation with humid air at
456 the upper turning point between adsorption and desorption isotherm.
457 For monitoring the SC adsorption kinetics, we dried the sample as described above
458 and adjusted the RH in the disconnected wet line meanwhile to 8 %RH. At t := 0 s, a
459 kinetic series in the Andor Solis software was started, and the three-way vault was
460 applied to switch from the dry to the humid flow. The tube length between vault and
461 channel slide was ca. 80 cm with an inner tube diameter of 2 mm, resulting in ca.
462 2,5 cm^3 volume. The channel slide has an inner volume of 60 µL. The constant flow of
463 1 standard liter/minute (ca. 18 mL / s, i.e. 1080 mL/min for nitrogen at 23.3 °C) ensures
464 a complete air exchange over the sample in less than 1 s. For the designed system
465 and settings, we found, that the adsorption kinetics is not dominated by the flow rate
466 (**Supplementary Figure S15**).

For monitoring the SC desorption kinetics, the sample system was held at a fixed relative humidity, e.g., at 8 %RH until t := 0 s. Then, the mass flow controllers were set to 1 and 0 standard liter per minute, effectively exposing the sample with dry nitrogen only under a controlled flow at 1 standard liter per minute.

For cycling kinetic experiments, the ratio of the mass flow controllers was alternated every 80 s between only dry air and predefined values (e.g., 0.9 (dry) to 0.1 (humid) standard liter per minute for 8 %RH).

Table T1: *Measurement setting for monitoring the sorption isotherms, kinetics, and spatial distribution of water by Raman spectroscopy.*

	Integration time (s)	Accumulation	EM Gain
Sc isotherm	50	5	0
Sc kinetic	20	1	100
Hyperspectral scan	5	1	100

4. MOF-801 synthesis and material characterization

4.1 MOF-801 synthesis

4.1.1. Chemicals

Zirconium oxychloride octahydrate ($ZrOCl_2 \cdot 8H_2O$, purity ≥ 99.5%), fumaric acid, Sigmacote® siliconizing reagent were obtained from Sigma-Aldrich Co. *N*,*N*-Dimethylformamide (DMF), formic acid (purity ≥ 99.0 %), and anhydrous methanol were obtained from EMD Millipore Chemicals. Anhydrous acetone was obtained from Acros Organics.

4.1.2. Preparation of single MOF-801 crystals

For synthesizing monocrystalline SC-MOF-801 [$Zr_6O_4(OH)_4(fumarate)_6$], fumaric acid (0.027 g, 0.23 mmol) and $ZrOCl_2 \cdot 8H_2O$ (0.075 g, 0.23 mmol) were dissolved in DMF

(11.67 ml) before adding formic acid (1.76 ml) to the solution. The solvent mixture was placed in a 20-ml vial, which was heated at 120 °C for two days. Octahedral colorless crystals were collected and washed with fresh DMF three times per day for three days. The crystals were subsequently washed with fresh methanol for three days, three times per day. The solid was then dried under dynamic vacuum at room temperature for 2 hours and at 120 °C for 24 hours to yield an activated sample.

4.1.3. Preparation of MOF-801 as microcrystalline powder.

For synthesizing microcrystalline powder of MOF-801 [$Zr_6O_4(OH)_4(fumarate)_6$], fumaric acid (0.290 g, 2.50 mmol) and $ZrOCl_2 \cdot 8H_2O$ (0.805 g, 2.50 mmol) were dissolved in DMF (10.0 ml) before adding formic acid (3.50 ml) to the solution. The solvent mixture was placed in a 20-ml vial and heated at 130 °C for 6 hours. As-synthesized microcrystalline powder was collected and washed with fresh DMF three times per day for three days. The sample was then washed with fresh methanol three times per day for three days. The solid was afterward dried under dynamic vacuum at room temperature for 2 hours and at 120 °C for 24 hours to yield an activated sample.
To reduce the nucleation in the growth of MOF-801 samples, the inner surface of the 20-ml vial was rinsed with siliconizing reagent Sigmacote®, washed with acetone, and dried in the oven before use.

4.2 MOF-801 characterization

4.2.1 Single-crystal X-ray diffraction (SC-XRD)

Single-crystal X-ray diffraction (SC-XRD) datasets were collected at the beamline 12.2.1 at the Advanced Light Source (Lawrence Berkeley National Laboratory, USA) using a radiation wavelength of λ = 0.7288 Å. Beamline 12.2.1 is equipped with a

PHOTON-II CMOS detector operating in shutterless mode and a Si(111) monochromator. For the measurement, the crystalline sample was mounted on a Kapton® MiTeGen MicroMount™ in a minimal amount of Paratone® N oil and submerged in a cold gas stream generated by an Oxford Cryosystems 800 Series Cryostream.

4.2.2 Scanning electron-microscopy (SEM)

SEM measurements were carried out on an FEI Quanta 3D FEG scanning electron microscope using an accelerating voltage of 10 kV and a working distance of 10.4 mm. Prior to experiments, crystalline MOF-801 powder was thoroughly washed with DMF and methanol, activated under dynamic vacuum and afterward dispersed on a silicon wafer.

4.2.3 Sorption measurements for determining isotherms and kinetic curves in bulk

Low-pressure N_2 adsorption measurements were carried out on a Micromeritics ASAP 2420 surface area analyzer. Ultrahigh-purity-grade N_2 and He (99.999% purity) were used throughout adsorption experiments. MOF-801 samples were dried under dynamic vacuum at 120 °C for 12 hours prior to the analyses.

Kinetic water adsorption curves were conducted on 1.029 mg of MOF-801, uniformly distributed on a 6.35-mm diameter pan with the help of a thermogravimetric analyzer (TGA) under constant humidified nitrogen flow (200 mL min^{-1}). The water sorption dynamics measurements were conducted with a TA Instruments SDT Q600 series thermal gravimetric analyzer (TGA). The primary gas inlet was directly connected to a nitrogen tank (Praxair, ultrahigh purity, 99.999%). The secondary gas inlet was used to supply a humidified nitrogen feed by regulating the gas flow using a mass flow

controller (Sierra SmartTrak 100) and passing the stream through a gas washing bottle (2 L). The temperature and RH were monitored using high-accuracy thermocouples and humidity sensors downstream of the TGA chamber. For the measurements in thin-layer geometry, ~1 mg of the microcrystalline powder sample of MOF-801 was loaded in the TGA pan. Prior to the adsorption measurement in the TGA, microcrystalline MOF-801 sample was activated under dry nitrogen flow (176 mL min^{-1}) at 150 °C, respectively, until the weights of MOFs do not have noticeable changes. After activation, the samples were cooled down to 30 °C under dry nitrogen flow (176 mL min^{-1}). Immediately after 30 °C was reached, the adsorption measurement was started. The temperature during the adsorption was kept constant at 30 °C, and the RH was kept at 8 %.

5. Correlative FWM and CARS imaging for probing water inside MOF-801

The water distribution between MOF-801 crystals was visualized by multimodal imaging using two microscopy techniques: four-wave mixing (FWM) and coherent anti-Stokes Raman scattering (CARS). For this, we previously coupled a pulsed near-infrared light source in a home-built scanning Raman microscope[23]. Briefly, two synchronized femtosecond laser pulse trains at ω_1 = 774 nm and ω_2 = 1053 nm serve to derive the pump and Stokes beams as third-order nonlinear excitation. The pump beam at 774 nm has a pulse duration of about 150 fs. The spectrally broadened Stokes beam was derived by super-continuum generation in a PCF at 1053 nm. Both pulse trains were recombined and coupled into the scanning microscope collinearly with the CW laser. The details on optical elements controlling the chirp, polarization, intensity, and beam shape have been outlined previously[23]. At given temporal and spatial overlap between both excitation sources within the MOF-801 sample, a nonlinear resonance at $2\omega_1 - \omega_2$ can be detected in epi-direction by decoupling the signal from

565 the excitation via a dichroic mirror (zt532/NIRrpc; AHF, Germany) and spectral filtering
566 via a bandpass filter (HQ 620/60 M; AHF, Germany) before avalanche photodiodes
567 (Count Red; LaserComponents). Scanning of the sample is achieved using an XYZ
568 piezo stage (BIO3.200; PiezoConcept).
569 FWM is a third-order nonlinear process that occurs independently of molecular
570 transitions present in the sample. In presence of a vibrational or electronic resonance,
571 the FWM signal is strongly enhanced and dominated by either coherent Raman
572 scattering (CARS) or stimulated parametric emission, respectively. We employed
573 polarization-dependent CARS (pCARS), to separate the vibrational response of the
574 material from the unspecific FWM background by tuning the relative polarization angle
575 between the linearly polarized exaction beams. An additional polarizer in front of the
576 detector allows for selecting between CARS and FWM signal. To address the OH
577 stretch band around 3400 cm^{-1}, we made use of spectral focusing[23] by chirping the
578 Stokes beam within an 20 cm SF6 glass rod and temporally overlapping the pump
579 beam with corresponding spectral components of the Stokes beam. FWM microscopy
580 at ~ 612 nm used the temporal overlap with non-resonant components around 1050
581 nm.
582 Scan times per image were 180 s with an average beam power of 24 and 20 mW in
583 front of the objective for pump and Stokes pulses respectively. CARS, as well as FWM
584 images were scanned with 500 x 500 pixels, a step size of 180 µm and accumulated
585 over 3 repeats.
586
587 **Data availability**
588 The data that support the findings of this study are available from the corresponding
589 authors upon reasonable request.
590

Code availability

The codes used for quantifying water uptake by Raman spectroscopy are available from the corresponding authors upon reasonable request.

References

1 Chae, H. K. *et al.* A route to high surface area, porosity and inclusion of large molecules in crystals. *Nature* **427**, 523-527, doi:10.1038/nature02311 (2004).

2 Furukawa, H. *et al.* Water adsorption in porous metal-organic frameworks and related materials. *J. Am. Chem. Soc.* **136**, 4369-4381, doi:10.1021/ja500330a (2014).

3 Hanikel, N. *et al.* Evolution of water structures in metal-organic frameworks for improved atmospheric water harvesting. *Science* **374**, 454-459, doi:10.1126/science.abj0890 (2021).

4 Kim, H. *et al.* Adsorption-based atmospheric water harvesting device for arid climates. *Nat. Commun.* **9**, 1191, doi:10.1038/s41467-018-03162-7 (2018).

5 LaPotin, A. *et al.* Dual-Stage Atmospheric Water Harvesting Device for Scalable Solar-Driven Water Production. *Joule* **5**, 166-182, doi:10.1016/j.joule.2020.09.008 (2021).

6 Logan, M. W., Langevin, S. & Xia, Z. Reversible Atmospheric Water Harvesting Using Metal-Organic Frameworks. *Sci Rep* **10**, 1492, doi:10.1038/s41598-020-58405-9 (2020).

7 Wang, W. *et al.* Air-cooled adsorption-based device for harvesting water from island air. *Renewable and Sustainable Energy Reviews* **141**, doi:10.1016/j.rser.2021.110802 (2021).

8 Xu, W. & Yaghi, O. M. Metal-Organic Frameworks for Water Harvesting from Air, Anywhere, Anytime. *ACS Cent. Sci.* **6**, 1348-1354, doi:10.1021/acscentsci.0c00678 (2020).

9 Zhang, L. *et al.* Porous frameworks for effective water adsorption: from 3D bulk to 2D nanosheets. *Inorg. Chem. Front.* **8**, 898-913, doi:10.1039/d0qi01362e (2021).

10 Zhou, X., Lu, H., Zhao, F. & Yu, G. Atmospheric Water Harvesting: A Review of Material and Structural Designs. *ACS Mater. Lett.* **2**, 671-684, doi:10.1021/acsmaterialslett.0c00130 (2020).

11 Kim, H. *et al.* Water harvesting from air with metal-organic frameworks powered by natural sunlight. *Science* **356**, 430, doi:10.1126/science.aam8743 (2017).

12 Hanikel, N. *et al.* Rapid Cycling and Exceptional Yield in a Metal-Organic Framework Water Harvester. *ACS Cent. Sci.* **5**, 1699-1706, doi:10.1021/acscentsci.9b00745 (2019).

13 Hossain, M. I. & Glover, T. G. Kinetics of Water Adsorption in UiO-66 MOF. *Industrial & Engineering Chemistry Research* **58**, 10550-10558, doi:10.1021/acs.iecr.9b00976 (2019).

14 Solovyeva, M. V., Gordeeva, L. G., Krieger, T. A. & Aristov, Y. I. MOF-801 as a promising material for adsorption cooling: Equilibrium and dynamics of water adsorption. *Energy Convers. Manage.* **174**, 356-363, doi:10.1016/j.enconman.2018.08.032 (2018).

15 Liu, X., Wang, X. & Kapteijn, F. Water and Metal–Organic Frameworks: From Interaction toward Utilization. *Chem. Rev.* **120**, 8303-8377, doi:10.1021/acs.chemrev.9b00746 (2020).

16 Bagi, S., Wright, A. M., Oppenheim, J., Dincă, M. & Román-Leshkov, Y. Accelerated Synthesis of a Ni2Cl2(BTDD) Metal–Organic Framework in a Continuous Flow Reactor for Atmospheric Water Capture. *ACS Sustain. Chem. Eng.* **9**, 3996-4003, doi:10.1021/acssuschemeng.0c07055 (2021).
17 Bagi, S., Yuan, S., Rojas-Buzo, S., Shao-Horn, Y. & Román-Leshkov, Y. A continuous flow chemistry approach for the ultrafast and low-cost synthesis of MOF-808. *Green Chemistry* **23**, 9982-9991, doi:10.1039/D1GC02824C (2021).
18 Bon, V. *et al.* Insights into the water adsorption mechanism in the chemically stable zirconium-based MOF DUT-67 – a prospective material for adsorption-driven heat transformations. *J. Mater. Chem. A* **7**, 12681-12690, doi:10.1039/C9TA00825J (2019).
19 Towsif Abtab, S. M. *et al.* Reticular Chemistry in Action: A Hydrolytically Stable MOF Capturing Twice Its Weight in Adsorbed Water. *Chem* **4**, 94-105, doi:10.1016/j.chempr.2017.11.005 (2018).
20 LaPotin, A., Kim, H., Rao, S. R. & Wang, E. N. Adsorption-Based Atmospheric Water Harvesting: Impact of Material and Component Properties on System-Level Performance. *Acc. Chem. Res.* **52**, 1588-1597, doi:10.1021/acs.accounts.9b00062 (2019).
21 Avrami, M. Kinetics of Phase Change. II Transformation-Time Relations for Random Distribution of Nuclei. *The Journal of Chemical Physics* **8**, 212-224, doi:10.1063/1.1750631 (1940).
22 Guo, B. *et al.* Study on CO(2) Capture Characteristics and Kinetics of Modified Potassium-Based Adsorbents. *Materials (Basel, Switzerland)* **13**, 877, doi:10.3390/ma13040877 (2020).
23 Fuchs, A. *et al.* Single Crystals Heterogeneity Impacts the Intrinsic and Extrinsic Properties of Metal-Organic Frameworks. *Adv. Mater.*, 2104530, doi:10.1002/adma.202104530 (2022).
24 Fathieh, F. *et al.* Practical water production from desert air. *Sci. Adv.* **4**, eaat3198, doi:10.1126/sciadv.aat3198 (2018).
25 Terzis, A. *et al.* High-Frequency Water Vapor Sorption Cycling Using Fluidization of Metal-Organic Frameworks. *Cell Reports Physical Science* **1**, 100057, doi:10.1016/j.xcrp.2020.100057 (2020).
26 Müller, K., Vankova, N., Schöttner, L., Heine, T. & Heinke, L. Dissolving uptake-hindering surface defects in metal–organic frameworks. *Chem. Sci.* **10**, 153-160, doi:10.1039/C8SC03735C (2019).
27 Delen, G., Monai, M., Meirer, F. & Weckhuysen, B. M. In situ Nanoscale Infrared Spectroscopy of Water Adsorption on Nanoislands of Surface-Anchored Metal-Organic Frameworks. *Angew Chem Int Ed Engl* **60**, 1620-1624, doi:10.1002/anie.202011564 (2021).

Acknowledgements

Funding by the Center for NanoScience Munich (CeNS), the Center for Integrated Protein Science Munich (CiPSM), Nanosystems Initiative Munich (NIM), the Deutsche Forschungsgemeinschaft (PL 696/4-1; Project-ID 201269156-SFB1032, B03) is gratefully acknowledged. We thank Don C. Lamb for support and access to laboratory facilities. This sorption experiments on bulk material are based on work supported by the Defense Advanced Research Projects Agency (DARPA) under contract HR001-21-C0020. Any opinions, findings, and conclusions or recommendations expressed in this material are those of the author(s) and do not necessarily reflect the views of DARPA. Experimental support by Ludwig Steidl, who helped in setting up measurements under controlled relative humidity, and Nikita Hanikel, who carried out the sorption experiments in bulk, are greatly acknowledged.

Author contribution

E.P. and O.M.Y conceived the research. E.P. supervised the project. A.F., Z.J., O.Y., S.W. and E.P. designed the experiments. Synthesis and characterization of MOF particles was carried out by H.W. under the supervision of Z.J. and O.Y. H.W. carried out SEM and XRD experiments. A.F. setup and developed the Raman-based methodology and performed correlative imaging and spectroscopy on single particle MOF-801 under the supervision from E.P. A.F., H.W., O.M.Y. and E.P. analyzed the data. Z.J. derived the fit function for quantitative water uptake. E.P. and A.F. conducted the statistical analysis. E.P. and A.F. designed the figures. A.F., Z.J., S.W., O.M.Y., and E.P. wrote the manuscript. All authors approved the final version of the manuscript.

Competing Interests

The authors declare no conflict of interest.

Additional Information

1. Extended Data

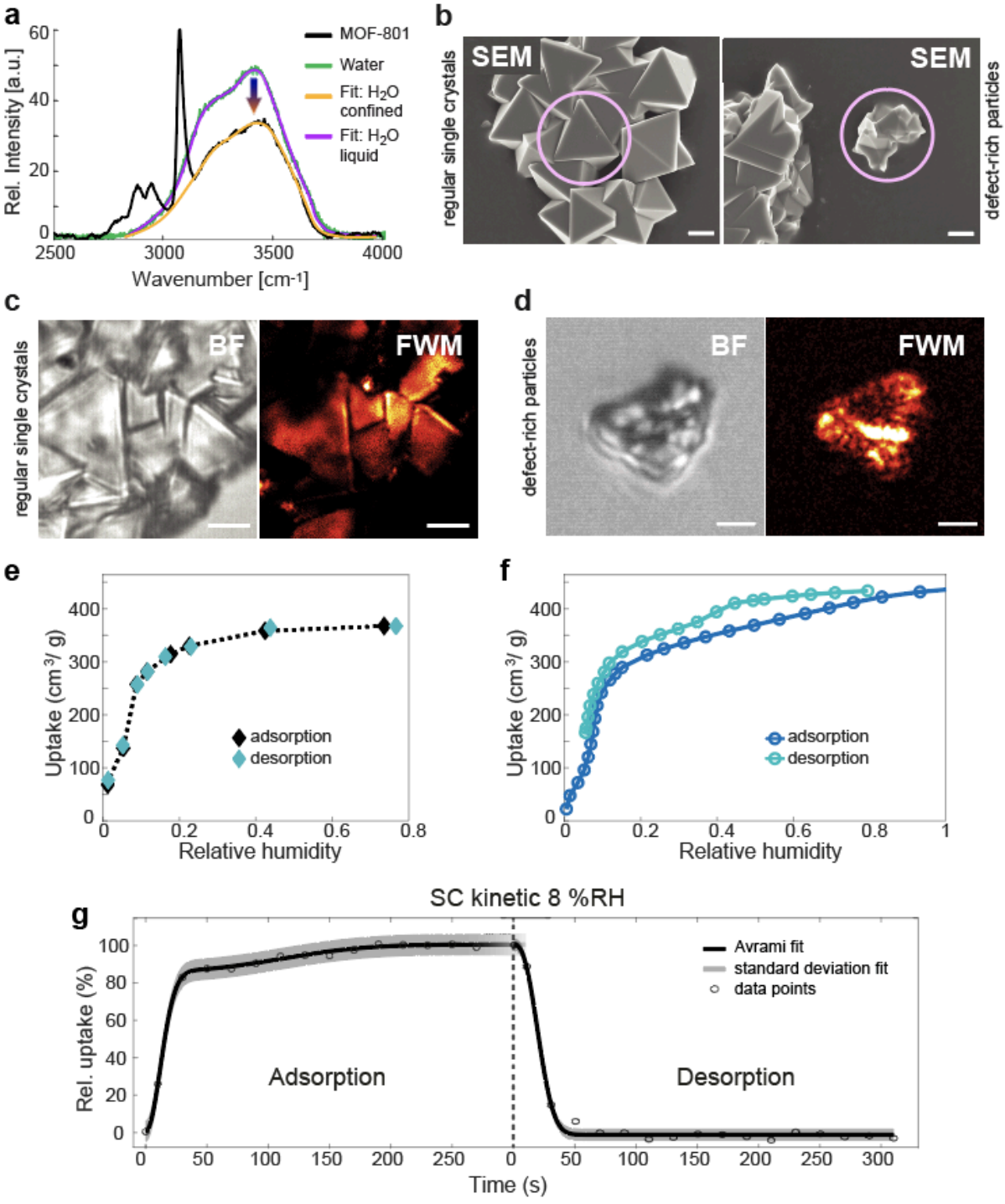

Extended Data Figure 1. a) *Raman spectra of water and MOF-801 under saturating humidity. At high relative humidity the adsorbed water molecule do not sense the surrounding host material. Their Raman signature equals the one of liquid water.* ***b)*** *Scanning electron microscopy (SEM) of regular crystals and polycrystalline particles. Scale bars 5 µm.* ***c, d)*** *Bright-field (BF) and four-wave mixing (FWM) images of*

(c) regular single crystals and (d) polycrystalline particles. Scale bars 5 µm. Measurement details can be found in ***Material section 5****.* ***e, f****) Adsorption and desorption Isotherms of MOF-801 determined (e) at the SC level and (f) in bulk via TGA. Measurement details can be found in* ***Material section 3 and 4.*** ***g)*** *Time course of water attachment after switching from 0 to 8 %RH or reverse on a time window of 300 sec. Time point 0 represents the exposure to the altered relative humidity. Both data sets represent the mean and standard deviation over 5 crystals.*

2. Supplementary Information

The supplementary text comprises three sections: (1) it presents a summary of the uptake mechanism in MOF-801 and the implemented fit model for monitoring the uptake of water as function of time or humidity. (2) It gives a detailed description and derivation of quantitative monitoring of water uptake by Raman spectroscopy. (3) It details the results on polycrystalline MOF-801 particles characterized by single-crystal X-ray diffraction.

Water harvesting at the single crystal level

Supplementary Information

Table of content

Supplementary Notes

Supplementary Note 1: Uptake mechanism description and fit model

1.1 Kinetic curve fit model

For monitoring the water uptake over time in MOF-801, Raman spectra were taken in the center of single MOF-801 crystals. The kinetic series were recorded within a 20 s acquisition time window, with t = 0 s being the time point, at which the sample chamber is either exposed to humid air or to pure N_2. Since spectra at every frame represent the average over the kinetic process during the acquisition time, the respective time points are chosen as the midpoint between the start and end time point of the frame (**Supplementary Figure S1**), while the first frame lasting from t = - 20 s to 0 s was exceptionally set as data point $t_{kinetic}$ = 0 s. The second frame time from 0-20 s was set as $t_{kinetic}$ = 10 s, the third frame time from t = 20 to 40 s as $t_{kinetic}$ = 30 s, etc., continuing until $t_{kinetic}$ = 250 s usually.

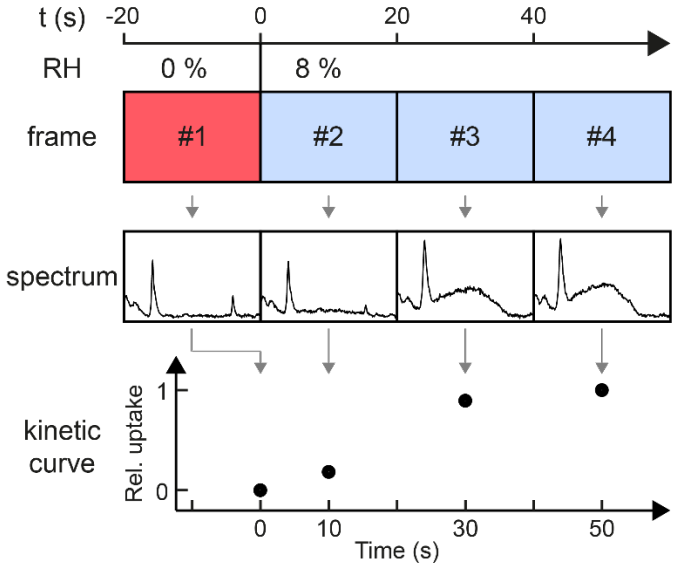

Supplementary Figure S1: Data processing for kinetic series. *Schematics of the data processing for determining the uptake kinetics in MOF-801 from a series of Raman spectra as function of time. The conversion of Raman spectra to quantitative amount of uptaken water is identical as described for the isotherm curves (cf.* ***Supplementary Note 5****).*

The kinetics (**Figure 3c** and **d**) of water uptake in type 1 and type 2 crystals was always determined for 5 single MOF-801 particles of both types each and represented as average increase plus standard deviation. The RH in the humid air flow deviated by 0.5 %RH maximally (e.g.., 8.0 ± 0.5 %RH) during kinetic measurements on different crystals, days, and slightly unbalanced changes in flow rate at the start of the measurement. All kinetic data sets were scaled between the minimum (relative uptake := 0 %) and maximum (relative uptake := 100 %). The average value and standard deviation per relative humidity were calculated for both types. The data were empirically fitted with a dual-step Avrami model [1,2] based on the findings of Martell et al. [3], taking the cooperative binding of water (see **Supplementary Note 1.2**) and transformation from gas to liquid phase into account:

$$\left(\frac{V_{H2O}}{m_{MOF}}\right)(t_{kinetic}) = \left[w_1 \cdot \left(1 - e^{-(k_1 \cdot t_{kinetic})^{n_1}}\right)\right] + \left[w_2 \cdot \left(1 - e^{-(k_2 \cdot t_{kinetic})^{n_2}}\right)\right] \quad \text{Eq. (1.1)}$$

Here, w_i represents the relative amount of adsorbate per single step at pseudo-equilibrium, k_i the temperature-dependent, 'Avrami rate' constant, and n_i the Avrami exponent. The linear combination of Avrami functions allows for empirically modeling the two-step cooperative binding of water. It summarizes individual steps of water binding (that are taking place in parallel; see **Supplementary Note 1.2)** in average rate constants describing the initial binding steps (seed formation for water bridging / first wetting of the dry framework), consecutive pore filling by water molecules (nucleation) and final growth of different nucleation sites into each other.

For the desorption curve, the fit needed to be modified to a one-step Avrami model by fixing $w_2 := 0$ to address the more direct desorption behavior observed (see **Extended Data Figure 5f**). A more detailed study of the desorption mechanism will be the prospect of future research.

1.2 Water adsorption isotherm curve fit model

MOF-801 features a multi-step mechanism for water uptake [4] with binding sites in tetrahedral and octahedral cages(**Supplementary Figure S2**). The following paragraph describes the underlying modeling to quantify the total amount of water molecules N_{H2O} per asymmetric unit cells in MOF-801 in order to explain the observed adsorption isotherms and quantify the total uptake of water at the single-crystal level.

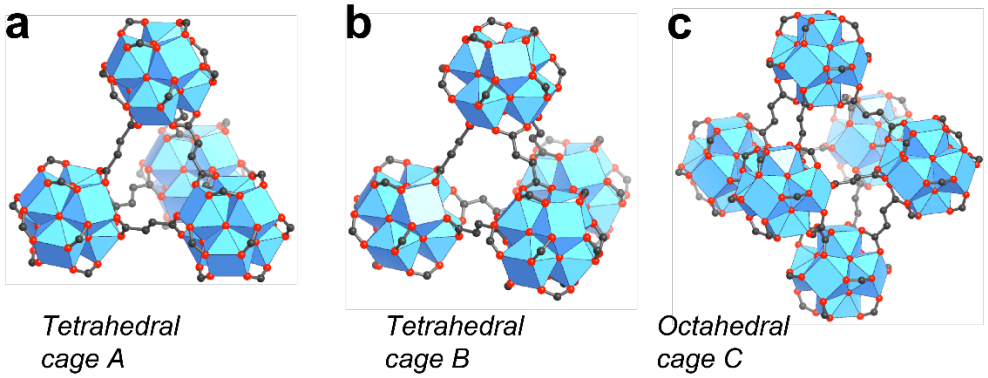

Supplementary Figure S2: *Water binding sites in tetrahedral cages (a, b) and the octahedral cage (c) in an asymmetric unit cell of MOF-801.*

Based on SC-XRD, binding sites of water in an asymmetric unit cell were identified. Overall, the asymmetric unit cell contains two complete $Zr_2O_6(OH)_4$ clusters. Using these clusters as vertices, four tetrahedral cages (3 x Cage A and 1 x B) and two octahedral cages (Cage C) are formed (**Supplementary Figure S3**). In cage B and C, 8 water molecules form a cubic cluster, while in cage A, 7 water molecules form an incomplete cube.

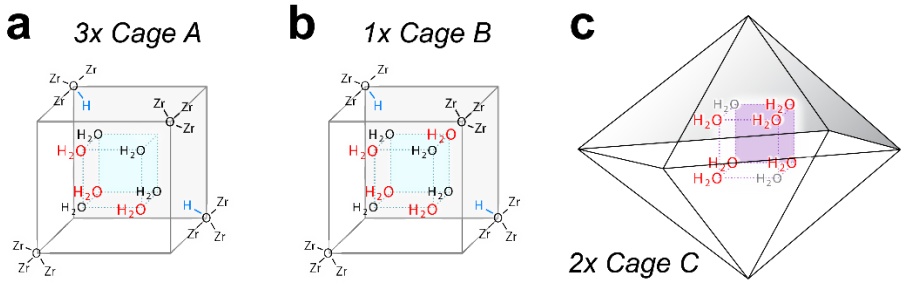

Supplementary Figure S3: *Overview of the water binding sites in the tetrahedral cages (a, b) and the octahedral cage (c) and their multiplicity per asymmetric unit cell.*

Knowing about the number of binding sites as well as about the binding mechanism, we can express the number of adsorbed water molecules N_{H2O} per asymmetric unit cell as a function of the RH using the equilibrium constants. A model based on linear combinations of Klotz equations was created that can be used to fit MOF-801 isotherms. The Klotz equation was originally developed to describe an adsorption process with N binding sites, where only the first binding step is different in binding constant [5]. The model was adapted to describe the binding in one asymmetric unit cell of MOF-801 with 31 distinct binding steps. First, the binding events were divided into the binding sites at cage A (tetrahedral) and the cages B and C (tetrahedral and octahedral). The water binding in cage A is described by 7 equilibrium constants (K_1 to K_7), each corresponding to a water in the incomplete cube. The binding in cage B is coupled with that in the two cage C according to the SC-XRD data, so there are 24

equilibrium constants (K_8 to K_{31}) describing 24 water molecules in the three cubes. The number of bound water in a cage A ($N_{H2O\,cageA}$) and in cage B+2C ($N_{H2O\,cageB,2C}$) can be expressed as:

$$N_{H2O\,cageA}(x) = \frac{K_1 x + 2K_1K_2x^2 + \cdots + 7(K_1K_2 \ldots K_7)x^7}{1 + K_1 x + K_1K_2x^2 + \cdots + (K_1K_2 \ldots K_7)x^7} \qquad \text{Eq. (1.2)}$$

$$N_{H2O\,cageB,2C}(x) = \frac{K_8 x + 2K_8K_9x^2 + \cdots + 24(K_8K_9 \ldots K_{31})x^7}{1 + K_8 x + K_8K_9x^2 + \cdots + (K_8K_9 \ldots K_{31})x^7} \qquad \text{Eq. (1.3)}$$

Here, x is the relative humidity of the surrounding air flow (between 0 and 1). To determine the total amount of water molecules N_{H2O} as a function of the RH, we need to add up all contributions to the four tetrahedral and 2 octahedral cluster. The number of water molecules $N_{H2O}(x)$ within the asymmetric unit cell as a function of the RH reads as

$$N_{H2O}(x) = 3 \cdot N_{H2O\,cageA}(x) + N_{H2O\,cageB,2C}(x) \qquad \text{Eq. (1.4)}$$

However, creating a fit model with 31 open parameters using isotherms will suffer from overfitting issues. In order to simplify the model, we reduce the whole binding mechanism into 5 chemically distinct events (involving multiple binding of water molecules simultaneously), each has a unique value of *K*: The first three events comprise water binding to tetrahedral cage A and B: (1) binding to the metal-oxide cluster at the μ3-O site ($K_{\mu3\text{-}O}$); (2) binding to metal bound hydroxyl groups, μ3-OH($K_{\mu3\text{-}OH}$); and (3) bridging of the previous binding sites into cubes or incomplete cubes in the tetrahedral cages (K_{tc}). The next two events occur in the octahedral cage C: (4) nucleation (K_d) nearby cage B and (5) further growth into cubes (K_{dc}). (cf. **Supplementary Table T1, Supplementary Figure S4**).

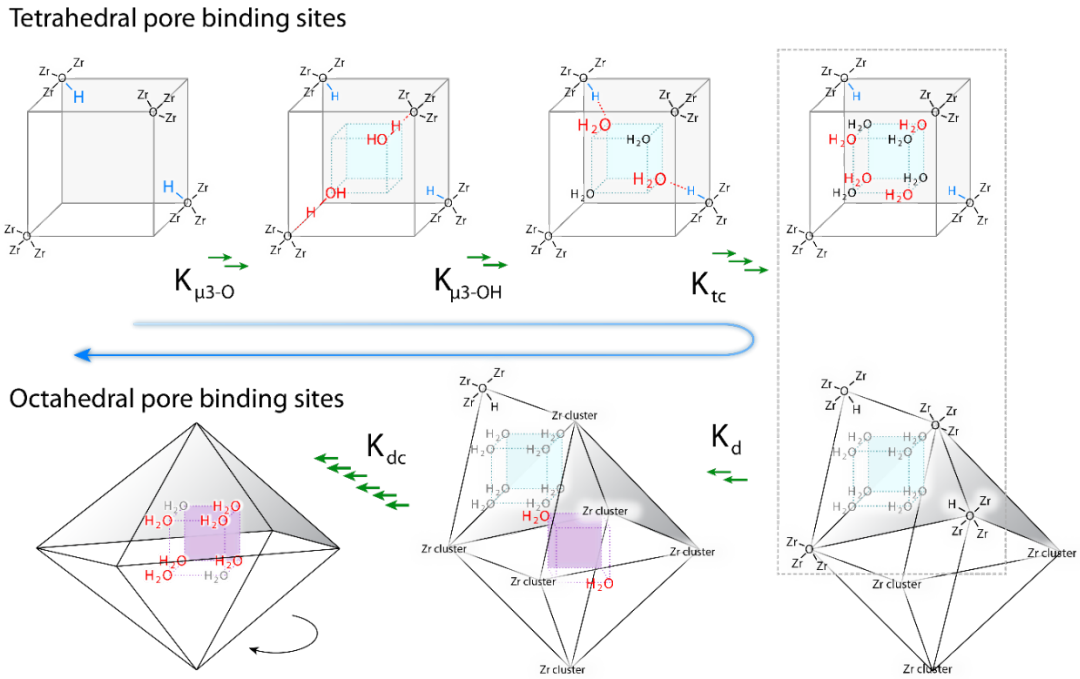

Supplementary Figure S4: *Schematic of the adsorption of water in MOF-801 crystals based Furukawa et al.[4] K_x describes the respective binding constant for the chemically distinct binding events per asymmetric unit cell.*

To convert the number of molecules per asymmetric unit cell into the uptake as volume water (cm^3) per mass MOF-801 (g), a scaling factor is calculated. Given that each asymmetric unit cell contains 2 metal clusters and 12 organic linkers, its chemical formula becomes $Zr_{16}O_{64}C_{48}H_{32}$ and the corresponding molecular weight is 2727.4 g/mol. Combining with the volume of water vapor (2.241×10^4 cm^3/mol), one water molecule bound to an asymmetric unit cell corresponds to a water uptake of 8.22 cm^3/g.

The model describes measured adsorption isotherms of MOF-801 with the five distinct equilibrium constants as fit parameters as Eq. 1.5:

$$\frac{V_{H2O}}{m_{MOF}} = N_{H2O}(RH) \cdot 8.22 \qquad \text{Eq. (1.5)}$$

Supplementary Table T1: *Equilibrium constants of the fit model describing water uptake in MOF-801 per asymmetric unit cell.*

	$K_{\mu 3\text{-}O}$	$K_{\mu 3\text{-}OH}$	K_{tc}	K_d	K_{dc}
K_1	2				
K_2	1/2				
K_3		2			
K_4		1/2			
$K_5 - K_7$			1		
K_8	2				
K_9	1/2				
K_{10}		2			
K_{11}		1/2			
$K_{12} - K_{15}$			1		
K_{16}				4	
K_{17}				3/2	
K_{18}				2/3	
K_{19}				1/4	
$K_{20}/K_{24}/K_{28}$					4
$K_{21}/K_{25}/K_{29}$					3/2
$K_{22}/K_{26}/K_{30}$					2/3
$K_{23}/K_{27}/K_{31}$					1/4

Supplementary Note 2: Quantitative water uptake and kinetics of MOF-801 via Raman spectroscopy

Raman scattering provides detailed spectroscopic fingerprint information of the targeted material, but it is an inherently weak process [6]. Concomitantly, the recorded spectral signature of a Raman scattering process is often dominated by other processes, such as Rayleigh scattering, straight light, and/or autoluminescence by the investigated sample itself. Hence, measured spectra frequently show additional contributions, such as background and unstable baselines. The following paragraph describes the spectral background correction of recorded Raman spectra, the determination of uptaken water compared to MOF-801 within the detection volume, as well as their quantitative analysis. All data analysis was carried out using home-written Matlab scripts (Matlab 2018b, The MathWorks, Inc; Natick, MA, USA).

2.1 Initial Background correction

Mathematical pre-processing was used to eliminate baseline drifts, offset, and background. First of all, recorded Raman spectra were corrected against cosmic rays by *Andor Solis for Imaging V4.30* (Oxford Instruments). Next, Rayleigh scattering and spurious background were removed by polynomial fitting. The background data was automatically approximated by a quadratic function in the region without Raman resonances between 2595 – 2620 cm^{-1} and 3760 – 4190 cm^{-1} and subtracted prior to further analysis (**Supplementary Figure S5a**).

2.2 Determining the intensity of selected Raman resonances

Spontaneous Raman scattering scales linearly with the number of Raman active molecules within the confocal volume [7]. Hence, Raman signatures of two species, such as water and MOF-801, add up linearly. For non-overlapping Raman resonances, the strength of a vibrational transition $A_{Raman\ Peak}$ is directly proportional to the sample concentration. It is given by the area under the background-corrected Raman spectrum and reads as (Eq. 2.1)

$$A_{Raman\ Peak} = \int_{\tilde{\nu}_1}^{\tilde{\nu}_2} I_{Raman}(\tilde{\nu})\ d\tilde{\nu} \qquad \text{Eq. (2.1)}$$

with $\tilde{\nu}_1$ and $\tilde{\nu}_2$ being the lower and upper wavenumber of a selected peak. The uncorrected strength of the CH and OH stretch vibration is given by (**Supplementary Figure S5b**)

$$A_{OH} = \int_{3145\ cm^{-1}}^{3665\ cm^{-1}} I_{Raman}(\tilde{\nu})\ d\tilde{\nu} \qquad \text{Eq. (2.2)}$$

$$A_{CH,raw} = \int_{3130\ cm^{-1}}^{3145\ cm^{-1}} I_{Raman}(\tilde{\nu})\ d\tilde{\nu} \qquad \text{Eq. (2.3)}$$

While the Raman signature of water above 3150 cm^{-1} is well separated from the characteristic peaks of MOF-801, it still overlaps with the CH stretch vibration around 3000 cm^{-1} (**Figure 2b**, leading to an increasing offset of the CH signature with increasing relative humidity (RH). We take this contribution into account by: (i) modeling the shape of the OH stretch vibration of pure water, (ii) approximating the Raman spectrum of humid MOF-801 in the spectral region above 3200 cm^{-1} by the model function, and (iii) determining and subtracting the background contribution of water to the CH stretch vibration of the material.

For modeling the Raman signature of pure water, we first approximated the shape of the OH stretch vibration by a linear combination of two Gaussian functions with a χ^2 of nearly 1 (**Supplementary Figure S5c**).

$$f(\tilde{\nu}) = C \cdot \left(B_1 \cdot \exp\left(-\frac{(\tilde{\nu} - \mu_1)^2}{2w_1^2} \right) + B_2 \cdot \exp\left(-\frac{(\tilde{\nu} - \mu_2)^2}{2w_2^2} \right) \right) \quad \text{Eq. (2.4)}$$

While keeping the model parameter, i.e., the Gaussian amplitudes B_i, center positions μ_i and widths w_i, fixed, we approximated the water content in MOF-801 afterward by linearly scaling the determined model function f with a factor C to the recorded Raman spectrum of the material. From the obtained fit-function $I_{fit,OH\ peak}$ describing the water contribution being present in MOF-801, we deduced its background contribution to the uncorrected CH signature $A_{CH,raw}$

$$A_{OH\ Bg,fit} = \int_{3130\ cm^{-1}}^{3145\ cm^{-1}} I_{fit,OH\ peak}(\tilde{\nu})\ d\tilde{\nu} \quad \text{Eq. (2.5)}$$

$$A_{CH} = A_{CH,raw} - A_{OH\ Bg,fit} \quad \text{Eq. (2.6)}$$

After subtraction, the corrected intensity of the CH stretch vibration A_{CH} can serve as a measure for the amount of the bare MOF material within the confocal volume. (**Supplementary Figure S5d**).

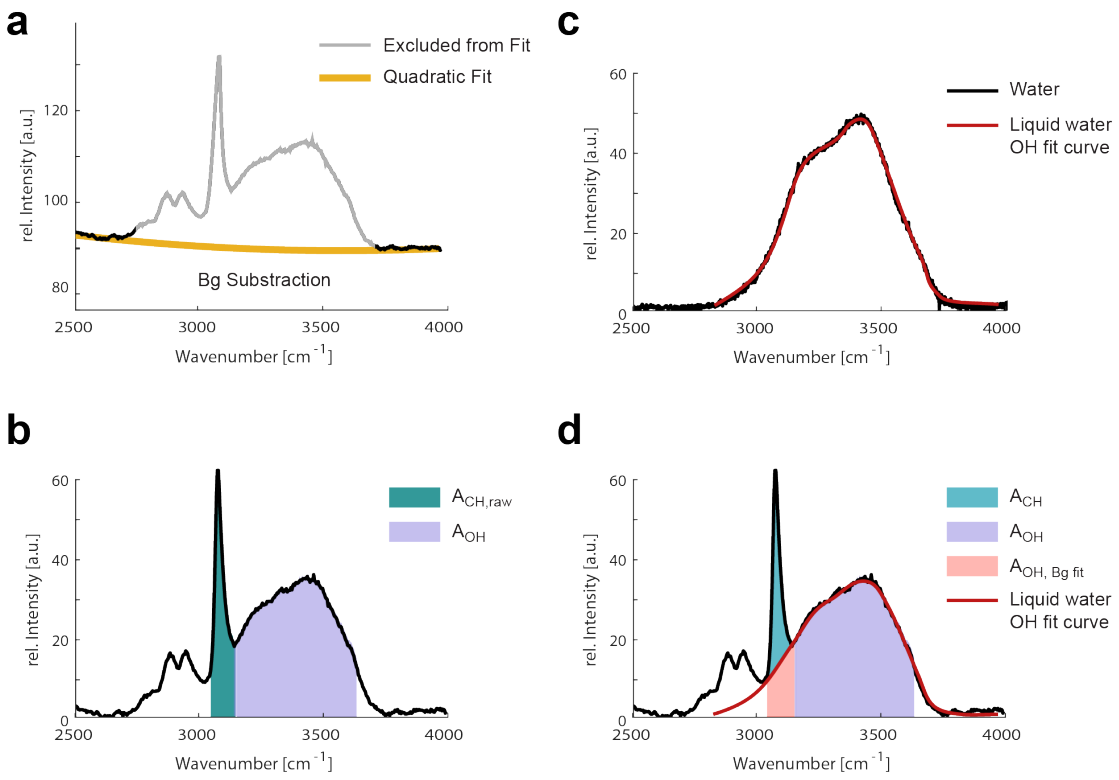

Supplementary Figure S5: Schematic of the background correction and determination of selected Raman intensity a) *The acquired spectra of MOF-801 are background-corrected by subtracting a quadratic background.* ***b)*** *The raw Raman peak strength of the OH stretch and the CH stretch vibration is calculated.* ***c)*** *To correct the CH-stretch vibration, a fit function modeling the liquid water OH-stretch peak is fitted to the spectrum.* ***d)*** *Using the fit function modeling the spectral shape of water, the contribution of the OH peak to the area under the CH peak is determined.*

2.3 Quantification of water uptake in MOF-801 by Raman spectroscopy

2.3.1 Connection between Raman intensities and quantitative water uptake

As Raman scattering scales linearly with the sample concentration, the observed Raman intensity A_{OH} due to OH-stretch resonance of water molecules within MOF-801 should directly relate to the total number of water molecules N_{H2O} inside the confocal volume. In general, the absolute Raman scattering intensity A (at the Stokes-Side)

$$A \propto N \cdot \frac{I_L}{\mu} \cdot \frac{(\nu_L - \nu)^4}{\nu \cdot \left(1 - e^{-\frac{h\nu}{kT}}\right)} \cdot [45\left(\alpha'_a\right)^2 + 7\left(\gamma'_a\right)^2] \qquad \text{Eq. (2.7)}$$

is proportional [7,8] to the number of scattering molecules N, the excitation intensity I_L, the reduced mass μ of vibrating atoms, the wavelength c/ν_L of the exciting light source, and the frequency ν of the observed Raman resonance. Moreover, it depends linearly on the temperature T following a Boltzmann distribution and quadratically on the vibration-induced change in polarizability $\frac{\partial \alpha}{\partial q}$ of the material, that can be related to the mean invariant α'_a and anisotropy invariant γ'_a of the polarizability tensor. It describes the polarization-orientation dependency of the material, which is negligible for freely vibrating water molecules and frequently found to be phase independent [9].

To automatically quantify the water uptake in MOF-801, we need a constant, calibrated conversion factor that relates the measured Raman intensity of the OH stretch vibration to the number of adsorbed water molecules. For constant experimental conditions, i.e., identical observation range, detection and excitation geometry, we can limit the dependencies on the OH-stretch signal according to Eq. 2.7 to 1) the temperature T, 2) the wavelength ν_L, 3) polarization P of the excitation laser / orientation of water molecules in the crystal, 4) the excitation intensity of the laser at the confocal volume I_L, and 5) the number of water molecules in the confocal volume N_{H2O}, which influence our experiment with different strength:

1) The laboratory is equipped with active temperature control, ensuring temperature stability of < 0.2 °C over 24 h. With an average lab temperature of 23.3 °C, the Boltzmann-associated scaling factor varies only on 33 digits after the comma for changes in lab temperature. The heating of the material by the visible, incident laser excitation at 532 nm was further on not observed as expected for the non-absorbing host material [10].

2) The diode-pumped laser at 532 nm serving as excitation laser features a line width of < 1 MHz and wavelength stability of < 1 pm over 8 hours. Changes in excitation laser wavelength can hence be excluded.

3) MOF-801 has a cubic unit cell with space group $P_{n\text{-}3}$. It is highly symmetric, i.e., the effect of polarization of the incident laser light I_L on the linker Raman spectrum is expected to be little. Water molecules adsorbed inside the MOF framework have varying orientations and can rotate. Therefore, no influence of the polarization is expected on the OH-stretch vibration. Indeed, we found no significant shift in the spectrum of humid MOF-801 when the polarization of the excitation beam is rotated by 90° (**Supplementary Figure S6**). Therefore, any influence of the incident laser polarization can be neglected.

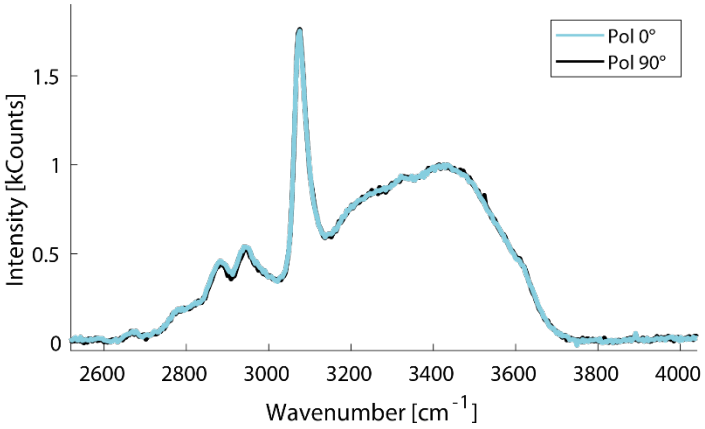

Supplementary Figure S6: Polarization dependency of the OH and CH-stretch vibration in MOF-801. *Raman spectrum of MOF-801 with p-polarization (blue) and s-polarization (black) after rotating the linear polarization of the excitation laser by 90° by a half-wave plate. Including a fixed detection geometry, both spectra are acquired under identical experimental settings otherwise. No polarization dependence for the OH- and CH-stretch vibrations are observed.*

4) The excitation intensity depends on the deposited laser power of the excitation laser within the confocal volume. Since the laser system features a low noise level (<0.25% RMS) and power stability (< 0.3 %), the scattering by the MOF-801 crystal is the major source causing changes in the exciting laser intensity and detection efficiency. At the same time, a decrease in laser intensity also affects the signature height of the CH-stretch vibration, as expected with a linear dependency on the laser power:

$$A_{CH};\ A_{OH} \propto I_L \qquad \text{Eq. (2.8)}$$

We, therefore, introduced a ratiometric approach (see below) to correlate the ratio of the Raman peaks A_{OH}/A_{CH} directly to the number of molecules in the confocal volume and correct for changes in absolute intensity.

5) The ratio of Raman peak strength of OH to CH-stretch vibration can be related to the uptake in cm^3 per gram of MOF-801. For the following, we take the laser intensity for all materials in the confocal volume as constant and will discuss the influence of scattering again for the calibration measurements (**Supplementary Note 2.3.3**). We can relate the amount of a given material in the confocal volume, *i.e.*, the number of scattering molecules N_x to their corresponding Raman peak strength A_x by a conversion factor $\mathrm{c}f_{RamanPeak}$.

$$N_x = \mathrm{c}f_{RamanPeak} \cdot A_x \qquad \text{Eq. (2.9)}$$

For ease of reading, we expressed the number of scattering particles N_x as the substance amount n_x by applying the Avogadro constant N_A in the following paragraph.

$$N_x = n_x \cdot N_A \qquad \text{Eq. (2.10)}$$

For quantifying the water uptake, we describe the uptake as the amount of water volume per mass MOF-801, which again is a function of the substance amount n_x:

$$\frac{V_{H2O}}{m_{MOF}} = \frac{\frac{m_{H2O}}{\rho_{H2O}}}{m_{MOF}} = \frac{n_{H2O} \cdot \frac{M_{H2O}}{\rho_{H2O}}}{n_{MOF} \cdot M_{MOF}} \qquad \text{Eq. (2.11)}$$

Here, M_x is the molecular weight of material x, and ρ_{H2O} is the density of water at the measurement temperature of 23.3 °C. For a given molecular weight and density of water-free MOF-801 ($\rho_{H2O} = 1.592$ mg/mm^3; see Ref. [11]), we can relate the volume per weight of MOF-801 to the Raman signatures of guest and host by combining Eq. 2.09 - 2.11 to

$$\frac{V_{H2O}}{m_{MOF}} = \frac{A_{OH}}{A_{CH}} \cdot \frac{cf_{H2O}}{cf_{MOF}} \cdot \frac{M_{H2O}}{\rho_{H2O} \cdot M_{MOF}} \qquad \text{Eq. (2.12)}$$

Determining the conversion factors is the crucial step in calculating the quantitative water uptake from the Raman spectrum of MOF-801. For Raman spectra of MOF-801 and water that are collected on the same microscope, with the same excitation wavelength, and the same objective (as for all presented spectra), the conversion factors are only dependent on (1) the Raman band of the material and (2) the incident laser power. In a broader sense, the same material irradiated with the same laser power will always result in the same Raman spectrum (with the restrictions from above). The conversion factors cf_{H2O} and cf_{MOF} can be considered as constant for a fixed excitation laser power for water-free MOF-801 and liquid water. These conversion factors cf_{H2O} and cf_{MOF} can be theoretically determined with calibration measurements in dry MOF-801 and liquid water excited with the same laser power, based on Eq. 2.09 and Eq. 2.10:

$$cf_{H2O} = \frac{n_{H2O,cal}}{A_{OH,cal}} = \frac{\rho_{H2O} \cdot V_{confocal} \cdot N_A}{A_{OH,cal} \cdot M_{H2O}} \qquad \text{Eq. (2.13a)}$$

$$cf_{MOF} = \frac{n_{MOF,cal}}{A_{CH,cal}} = \frac{\rho_{MOF} \cdot V_{confocal} \cdot N_A}{A_{CH,cal} \cdot M_{MOF}} \qquad \text{Eq. (2.13b)}$$

Here, $A_{x,cal}$ is the Raman intensity of the peak x according to Eq. 2.2-2.6 from the calibration measurement. When combining Eq. 2.12 and 2.13, the expression shortens to:

$$\frac{V_{H2O}}{m_{MOF}} = \frac{A_{OH}}{A_{CH}} \cdot \frac{A_{CH,cal}}{A_{OH,cal}} \cdot \frac{1}{\rho_{MOF}} \qquad \text{Eq. (2.14)}$$

For an equal excitation intensity, the ratio $\frac{A_{CH,cal}}{A_{OH,cal}}$ is constant between calibration measurements and can be expressed as a simple scaling factor leading to Eq. 2.15:

$$\frac{V_{H2O}}{m_{MOF}} = \frac{A_{OH}}{A_{CH}} \cdot \Gamma \cdot \frac{1}{\rho_{MOF}} \qquad \text{Eq. (2.15)}$$

This scaling factor can be determined twofold with a fairly good agreement: (i) either by theoretical modeling of experimental data (see **section 2.3.2**) or (ii) by using a series of calibration experiments (see **section 2.3.3**). Both methodologies are compared in the following paragraph to highlight their strength and deviations for the SC isotherm determination. To distinguish between the results, we name them Γ_{th} and Γ_{exp}. Please note that both parameters yield a similar result.

2.3.2 Determination of scaling factor Γ_{th} by theoretical calculations and fit

Knowing about the number and nature of binding sites in MOF-801 (**Supplementary Note 2**) allowed us to describe the total number of adsorbed water molecules (N_{H2O}) per asymmetric unit cell as a function of RH via five different equilibrium constants. The uptake as volume water (mL) per mass MOF-801 (g) was modeled as a function of the RH. Eq. 1.5 displays the relation as derived:

$$\frac{V_{H2O}}{m_{MOF}} = N_{H2O}(RH) \cdot 8.22 \qquad \text{Eq. (2.16)}$$

Since the ratio $\frac{A_{OH}}{A_{CH}}$ is also only dependent on the RH with

$$\frac{V_{H2O}}{m_{MOF}} \propto N_{H2O}(RH) \propto \frac{A_{OH}}{A_{CH}} \qquad \text{Eq. (2.17)}$$

the same fit model can be applied to approximate the measured ratio of Raman intensities

$$\frac{A_{OH}}{A_{CH}} = N_{H2O}(RH) \cdot f_{fit} \qquad \text{Eq. (2.18)}$$

By inserting Eq 2.15-2.18, we can connect the theoretical and experimental approach

$$N_{H2O}(RH) \cdot 8.22 = N_{H2O}(RH) \cdot f_{fit} \cdot \Gamma_{th} \cdot \frac{1}{\rho_{MOF}} \qquad \text{Eq. (2.19)}$$

and derive the following expression for Γ_{th}:

$$\Gamma_{th} = \frac{8.22 \cdot \rho_{MOF}}{f_{fit}} \qquad \text{Eq. (2.20)}$$

As described in the material section accompanying **Figure 4f**, the ratio of A_{OH}/A_{CH} at different RH was measured on seven different crystals. All data points were combined in one data set. The resulting data were fitted (Eq. 2.18) to extract f_{fit}, and the standard deviation of the fit.

With this, Γ_{th} was determined as $\Gamma_{th} = 0.0938 \pm 0.0041$.

2.3.3 Determination of scaling factor Γ_{exp} by calibration measurement

In comparison to the modeling approach, we equally pursued an experimental determination using an external standard procedure. We measured five different areas in completely dry MOF-801 and liquid water under identical experimental conditions (**Material section 3**, SC isotherm). Next, we determined the Raman peak strength for the CH stretch vibration in MOF-801 without water and the OH-stretch vibration of liquid water (**Supplementary Note 2.2**). For both samples completely occupying the confocal volume, which has an identical shape and size for both materials, we can derive the following linear scaling factor:

$$\Gamma_{exp}^{*} = \frac{A_{CH,cal}}{A_{OH,cal}} \qquad \text{Eq. (2.22)}$$

Light, however, is significantly scattered at the interface between air and the MOF crystal while this effect is negligible within the water. Due to the extensive scattering, the intensity of the laser excitation within the MOF calibration sample is lower than anticipated. Since water [12-14], as well as MOF-801 [10], barely absorb in the Vis/NIR range, we assign the decrease in transmission primarily to scattering and reflection. The incident laser light, as well as the created Raman photons, will be scattered differently, depending on their wavelength. This prohibits the estimation of the scattering by Rayleigh photons alone. To estimate the correction factor against this loss we determined the integrated transmission intensity of a spectrally broad light source in MOF-801 compared to water for 15 different areas (**Supplementary Figure S7**).

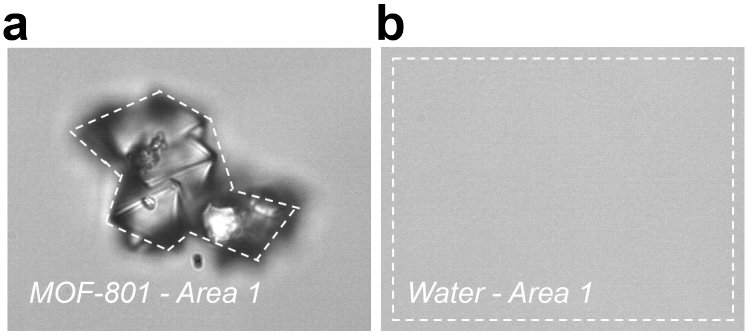

Supplementary Figure S7: Example of the estimation of the loss in Raman signal intensity due to scattering in MOF-801 crystals. *Bright-field images of (a) MOF-801 crystals and (b) water were acquired with the same settings (light source intensity, camera parameters, height over microscopy slide). The areas of interest were selected (inside of white dotted line), and the average intensity of the selected areas per pixel (I_{mean}) was calculated. In total, 15 areas for MOF-801 and 2 areas for water were analyzed.*

We derived the mean transmitted intensity per area $I_{mean,x}$ for both media and defined the correction factor $L_{scatter}$ between liquid water and MOF-801 as

$$L_{scatter} = \frac{I_{mean,MOF}}{I_{mean,H20}} \qquad \text{Eq. (2.23)}$$

The determined correction factor $L_{scatter}$ accounts for the reduction in excitation power and hence reduced amplitude of the linearly scaling Raman scattering process taking place in adsorbed water (when measured within MOF-801) compared to liquid water.

The measured scaling factor can therefore be described as

$$\Gamma_{exp} = \frac{A_{CH,cal}}{A_{OH,cal} \cdot L_{scatter}} \qquad \text{Eq. (2.24)}$$

Since the scattering loss is inducing a significantly higher uncertainty compared to all other contributions, the standard deviation of the 15 areas selected to determine $I_{mean,MOF}$ alone was applied to estimate the uncertainty of Γ_{exp}.

With Eq. 2.24, we could calculate $\Gamma_{exp} = 0.0837 \pm 0.0131$.

2.4 Uncertainty of water quantification and error propagation

2.4.1 General uncertainty of Raman Intensity

To derive the experimental error when determining the water content in MOF-801, we took the mean of all background-corrected spectra of a series with the length *i* of spectral pixels. Under the assumption that the background is spectrally independent, we calculated the standard deviation for each spectrum $\sigma_S(i)$ against the mean within a selected spectral region sel, where no Raman resonances are present ($x_{sel} = 2495 - 2625$ and $3760 - 4190$ cm^{-1} with $L(x_{sel})$ pixels; **Supplementary Figure S8**):

$$\sigma_S(i) = \sqrt{\frac{1}{L(x_{sel}) - 1} \cdot \sum_{j=1}^{L(x_{sel})} \left| x_{sel}(j) - x_{sel,mean}(j) \right|^2} \qquad \text{Eq. (2.25)}$$

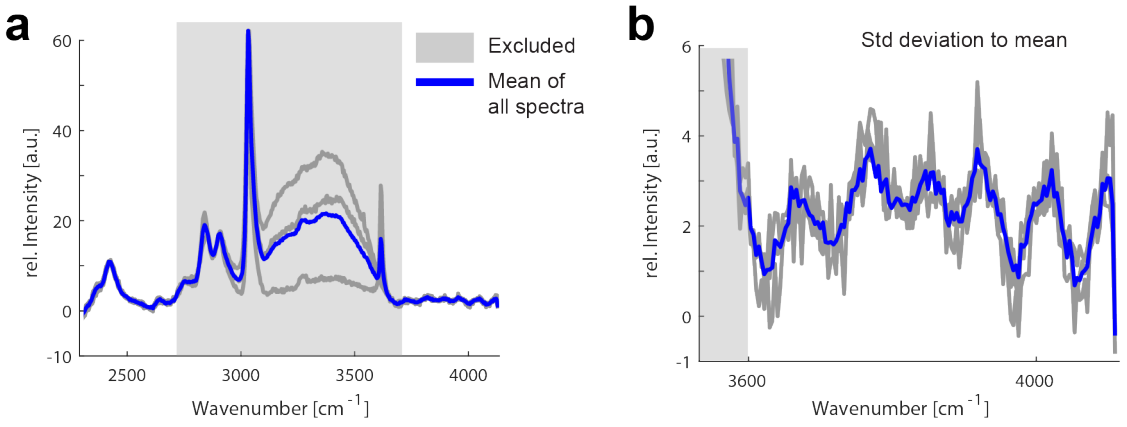

Supplementary Figure S8: Estimation of the white noise-induced measurement uncertainty. a) *Example series of Raman spectra for isotherm and kinetic curves (grey lines). While water significantly changes the Raman signature between 2800 and 3700 cm^{-1}, the spectral signature outside the grey area are hardly affected, only seen by changes in background level and structure. When calculating the mean of all spectra (blue), we derive the static background inherent to all spectra.* ***b)*** *When comparing the background region of every spectrum to the mean, we can approximate the white noise induced uncertainty as the standard deviation.*

The intensity $A_{OH}(i)$ of the adsorbed water peak is given as integral over the Raman resonance, *i.e.*, the sum over Raman signal. The associated error for $A_{OH}(i)$, $\sigma_{OH}(i)$ is

accumulating over the number of pixels N_{OH} in the integration range (*i.e.,* 3145 - 3665 cm^{-1}) and given using the constant, wavelength-independent error σ_S by

$$\sigma_{OH} = \sum_{i=3145\ cm^{-1}}^{3665\ cm^{-1}} \sigma_{OH}(i) = N_{OH} \cdot \sigma_S \qquad \text{Eq. (2.26)}$$

The error σ_{CH} of the intensity $A_{CH}(i)$ of the CH vibration in MOF-801 can be derived accordingly.

$$\sigma_{CH} = N_{CH} \cdot \sigma_S \qquad \text{Eq. (2.27)}$$

We assume no covariance between A_{OH} and A_{CH} yielding the propagated error σ_{noise} as [15]

$$\sigma_{noise} = \sigma_S \cdot \left|\frac{A_{OH}}{A_{CH}}\right| \cdot \sqrt{\left(\frac{N_{OH}}{A_{OH}}\right)^2 + \left(\frac{N_{CH}}{A_{CH}}\right)^2} \qquad \text{Eq. (2.28)}$$

2.4.2 Comparison of $\sigma_{rel,H2O}$, Γ_{th}, $\sigma_{\Gamma_{th}}$, Γ_{exp} and $\sigma_{\Gamma_{exp}}$

When comparing the determined scaling factors Γ_{th} and Γ_{exp}, we found an agreement of both values within the margin of error (**Supplementary Figure S9a**). This is a strong validation of the values since both methods followed fundamentally different approaches. That said, the experimentally derived calibration factor is smaller with an about four times higher standard deviation due to the scattering loss approximation. When determining $L_{scatter}$ (**Supplementary Note 2.3.3**), we found a roughly two-time higher transmission through the water compared to the MOF-801 crystals. The chosen method is likely overestimating the scattering, leading to the decreased scaling factor compared to the fit-derived value. But even a more precise estimation of the amount of scattered light would not significantly reduce the large standard deviation since every crystal has a wide variety of scattering possibilities, e.g., due to the exact measurement position in a crystal.

Therefore, the scaling factor used for the presented data of this work was the one derived from the theoretical approach:

$$\Gamma_{th} = 0.0938 \pm 0.0041. \qquad \text{Eq. (2.29)}$$

To determine the origin of the uncertainty of this scaling factor, we compared the noise-induced standard deviation σ_{noise} (**Supplementary Note 2.4.1**) for both scaling factors. For comparison, we expressed the values as uncertainty in percent of the respective data points:

$$\text{Uncertainty } \delta = (\text{standard deviation} / \text{data point value}) \cdot 100 \qquad \text{Eq. (2.30)}$$

Since the noise-induced uncertainty can vary between data points, we plotted the mean over 37 data points from 6 different SC isotherms.

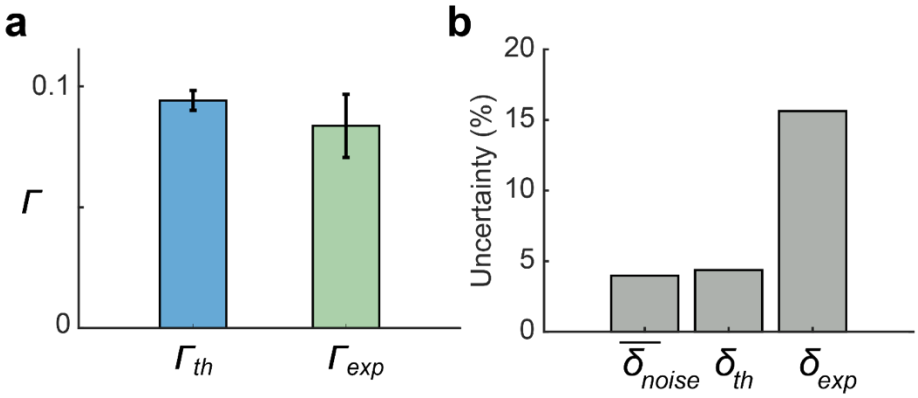

Supplementary Figure S9: Reliabiity of conversion factor. a) *Determination of the conversion factor Γ using the fit model (left) and calibration measurements (right). The error bars represent the mean value and standard deviation as specified in* ***Supplementary Note 2.3****.* ***b)*** *Comparison of the uncertainty in determining the conversion factor Γ. From left to right: $\overline{\delta_{noise}}$ is the uncertainty induced by spectral noise for the uptake-averaged over 37 data points. δ_{th} denotes the uncertainty of the scaling factor derived by fitting, while δ_{exp} denotes the one derived from the calibration measurements.*

It was found that the uncertainty of the approximated conversion factor Γ_{th} is nearly equal to the noise-induced uncertainty observed in Raman spectra, while the experimentally derived uncertainty Γ_{exp} is significantly higher (**Supplementary Figure S9b**). For Γ_{th}, this is a good indication that the selected method for the fit is a valid interpretation of the Raman spectra and the underlying uptake mechanism. Furthermore, these findings give encouraging indications that additional noise reduction by advanced chemometric methods, such as principal component analysis [16,17], can further enhance the robustness of our method.

Supplementary Note 3: SC-XRD on polycrystalline MOF-801 particles

Monocrystalline MOF-801. A MOF-801 single-crystal of 5 × 5 × 5 µm was taken from the synthesized batch and mounted on the diffractometer. The measured, raw data were processed with the Bruker APEX3 software package[18]. The data were first integrated using the SAINT V8.38A software and then corrected for absorption with SADABS 2016/2 routines[19].

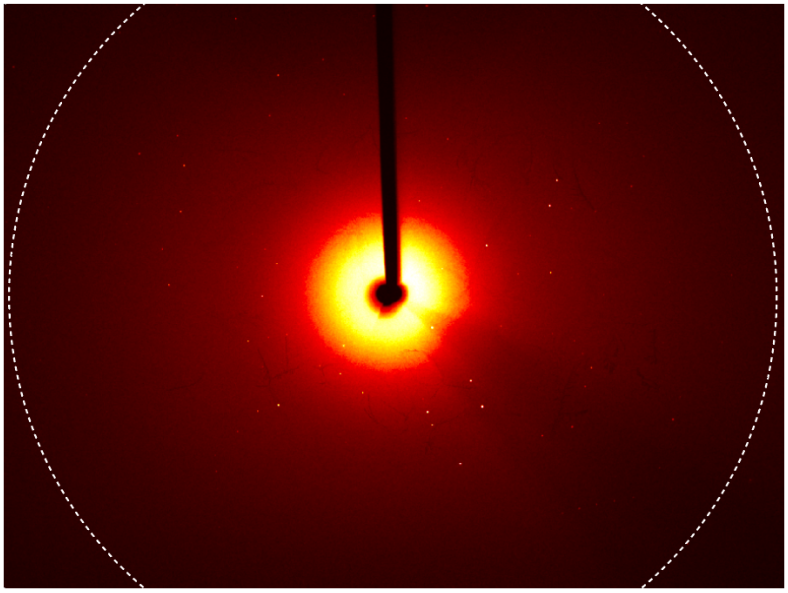

Supplementary Figure S10: SC-XRD example of a regular MOF-801 crystal. *The Circle represents the resolution of 0.8 Å.*

The structures were solved by intrinsic phasing (SHELXT-2018/03) and the refinement was done by full-matrix least-squares on F^2 (SHELXL-2018/03), using the Olex2 software package[20-22]. In line with literature, MOF-801 has a cubic unit cell with space group P_{n-3}.

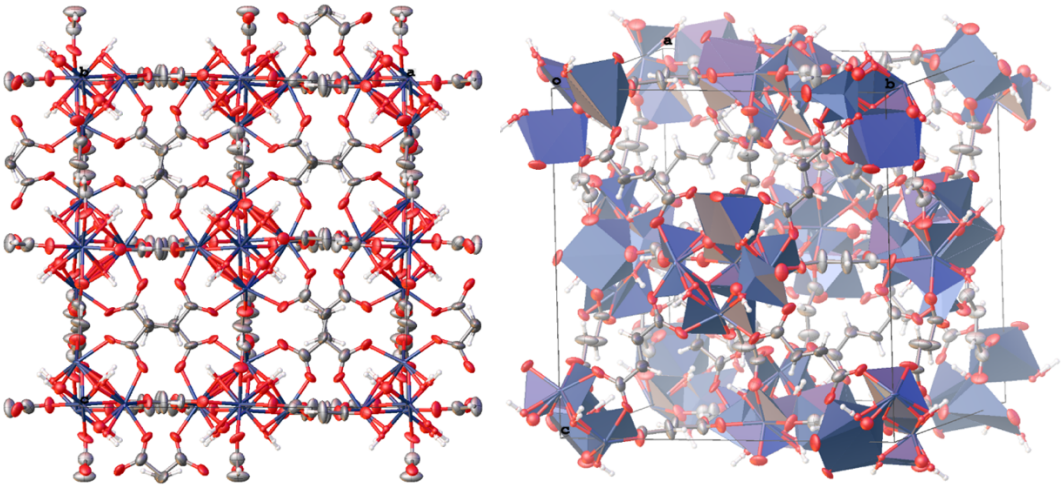

Supplementary Figure S11: Structure of MOF-801 single crystal. *Thermal Ellipsoids are drawn with 50% probability. Zr Oxide clusters are represented in dark blue, linker molecules in gray, and red elements sketch the oxygen atoms of the connecting carboxy groups of the fumarate linker.*

The data quality was influenced by the limited diffraction ability from the crystal. The resolution was cut off to 1 Å, and the R_{int} of the full data was 16.64%. The atoms of MOF-801 was refined anisotropically, except the μ-3 oxygen atoms always failed, mostly because the limited resolution is not able to distinguish the disorders clearly[23]. H5A and H6B were fixed by command HFIX 13 to fit the pseudo-tetrahedral geometry of oxygen. Despite the limited quality of the structural solution, the skeleton of the chemical structure clearly matched with the structure of MOF-801.

Polycrystalline Particles. A minor fraction of MOF-801 particles is polycrystalline (about 10% of particles per field of view in SEM). To characterize their nature, we carried out SXRD on several particles. Two representative examples are described in the following:

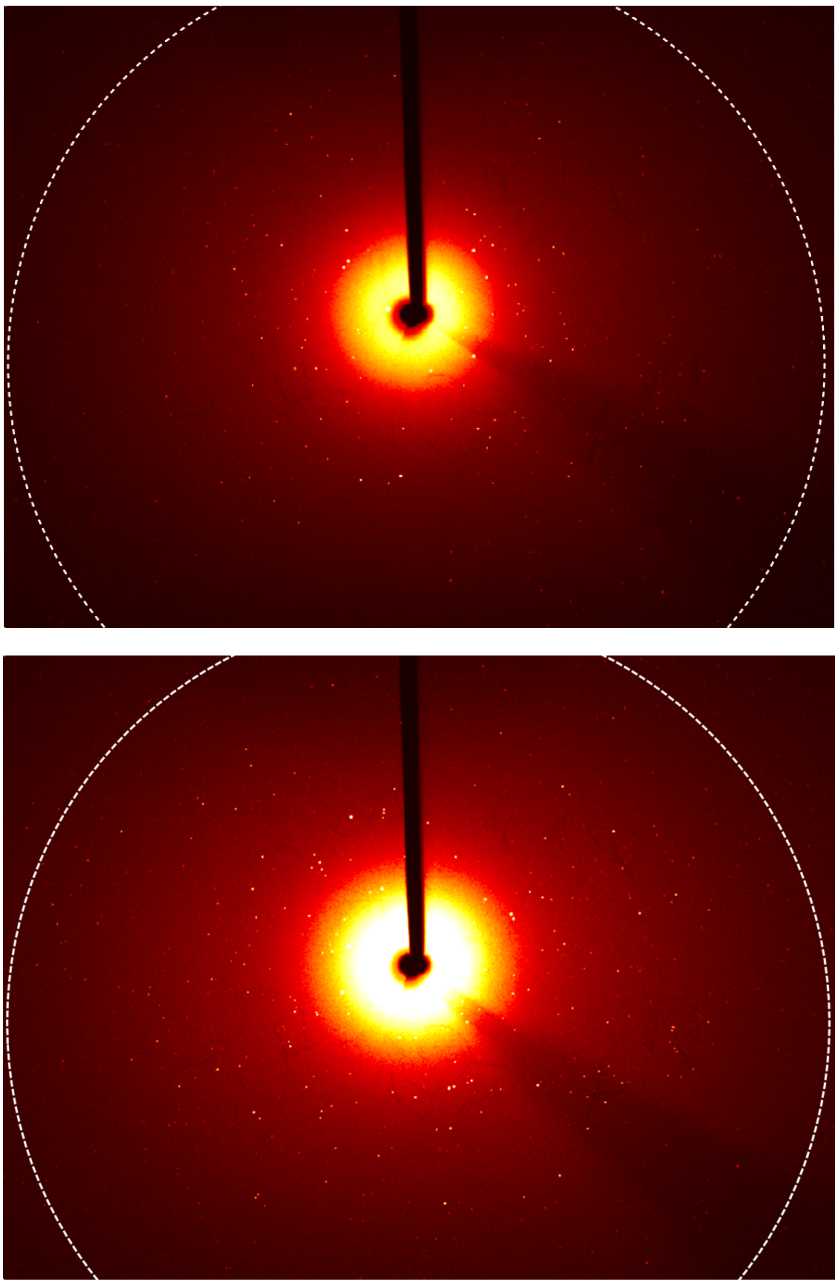

Supplementary Figure S12: SXRD examples of polycrystalline particles. *Electron diffraction pattern of polycrystalline sample 1 (top) and 2 (bottom) of MOF-801. The Circle represents the resolution of 0.8 Å.*

Polycrystalline sample 1 of MOF-801 was around 2 × 3 × 2 µm in size. Its diffraction pattern showed discrete diffraction peaks in the frames (**Supplementary Figure S12; top**), indicating that it was composed of a countable number of single-crystalline domains. The twin domains were searched with CELL_NOW and eventually, 8 domains of MOF-801 were identified (**Supplementary Table T2**). The five largest domains had sufficient numbers of diffractions to determine the Bravais lattice followed by unit cell refinements, while the last three domains did not.

Supplementary Table T2: *Summary of parameters of polycrystalline sample 1 from the crystallographic data.*

Domains	**Bravais Lattice**	**Unit cell [*a*, *b*, *c* / Å; *α*, *β*, *γ* / °]**	**Figure of Merit**	**Rotation axis (relative to domain 1)**	**Angle of rotation / °**
Domain 1	cP	*a* = 17.857(9)	0.230	-	-
Domain 2	cP	*a* = 17.836(5)	0.277	[-0.788 1.000 -0.954]	134.4
Domain 3	cP	*a* = 17.845(7)	0.281	[1.000 0.661 -0.378]	159.5
Domain 4	cP	*a* = 17.855(12)	0.328	[-0.505 1.000 0.507]	179.1
Domain 5	cP	*a* = 17.880(5)	0.366	[1.000 0.954 -0.584]	159.7
Domain 6	-	*a* = 17.799, *b* = 17.871, *c* = 17.871; *α* = 90.05, *β* = 89.72, *γ* = 90.28	0.431	[0.525 -0.984 1.000]	144.5
Domain 7	-	*a* = 17.799, b = 17.871, *c* = 17.871; *α* = 90.05, *β* = 89.72, *γ* = 90.28	0.504	[0.549 -0.832 1.000]	80.7
Domain 8	-	*a* = 17.799, *b* = 17.871, *c* = 17.871 *α* = 90.05, *β* = 89.72, *γ* = 90.28	0.192	0.926 -0.635 1.000	155.8

Polycrystalline sample 2 was around 8 × 3 × 2 μm in size and examined by SXRD. Similar to polycrystalline sample 1, the diffraction of polycrystalline sample 2 showed discrete diffraction peaks in the frames (**Supplementary Figure S12; bottom**), indicating it was composed of a countable number of single-crystalline domains. The twin domains were searched with CELL_NOW, and eventually, 10 domains that all matched the unit cell of MOF-801 were identified. The five largest domains had sufficient numbers of diffractions to determine the Bravais lattice followed by unit cell refinements, while the last 5 domains did not (**Supplementary Table T3)**.

Supplementary table T3: *Summary of parameters of polycrystalline sample 2 from the crystallographic data.*

Domains	**Bravais Lattice**	**Unit cell [*a*, *b*, *c* / Å; *α*, *β*, *γ* / °]**	**Figure of Merit**	**Rotation axis (relative to domain 1)**	**Angle of rotation / °**
Domain 1	cP	*a* = 17.879(9)	0.294	-	-
Domain 2	cP	*a* = 17.876(7)	0.352	[-0.195 1.000 -0.195]	155.0
Domain 3	cP	*a* = 17.879(12)	0.277	[1.000 0.304 0.460]	144.2
Domain 4	cP	*a* = 17.897(6)	0.267	[1.000 0.854 0.080]	176.1
Domain 5	cP	*a* = 17.867(11)	0.302	[1.000 -0.314 0.943]	173.2
Domain 6	-	*a* = 17.846, *b* = 17.875, *c* = 17.917; *α* = 89.94, *β* = 90.13, *γ* = 90.01	0.335	[1.000 0.456 0.441]	147.0
Domain 7	-	*a* = 17.846, *b* = 17.875, *c* = 17.917; *α* = 89.94, *β* = 90.13, *γ* = 90.01	0.397	[0.042 0.794 1.000]	57.0
Domain 8	-	*a* = 17.846, *b* = 17.875, *c* = 17.917; *α* = 89.94, *β* = 90.13, *γ* = 90.01	0.350	[0.472 1.000 -0.152]	163.9
Domain 9	-	*a* = 17.846, *b* = 17.875, *c* = 17.917; *α* = 89.94, *β* = 90.13, *γ* = 90.01	0.389	[-0.084 1.000 -0.478]	138.1
Domain 10	-	*a* = 17.846, *b* = 17.875, *c* = 17.917; *α* = 89.94, *β* = 90.13, *γ* = 90.01	0.365	[0.625 -0.639 1.000]	178.7

Supplementary Figures

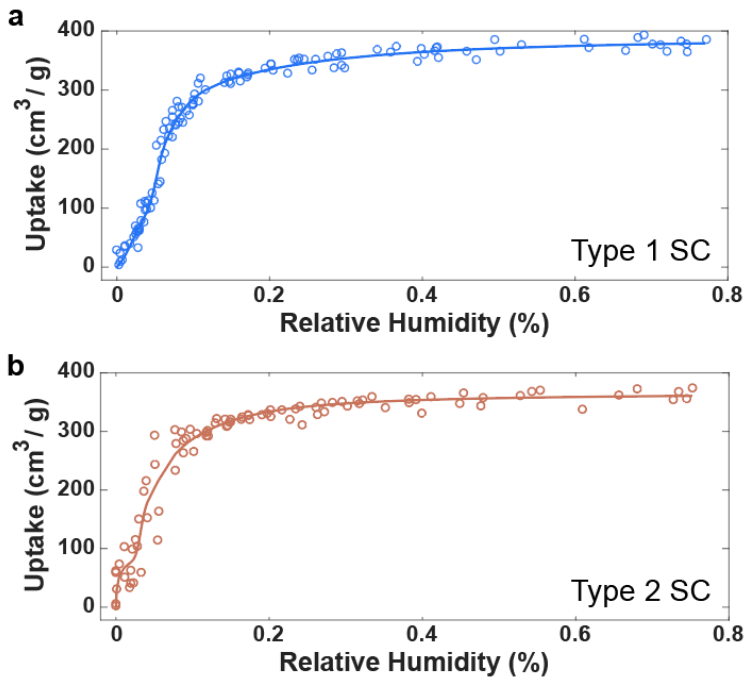

Supplementary Figure S13: Data to Figure 3a. *Overview plot of underlying data sets for SC isotherms of monocrystalline (Type 1) and polycrystalline (Type 2) MOF-801 particles. The colored lines represent the mean fit curve over N = 7 (Type 1) and N = 5 (Type 2) particles.*

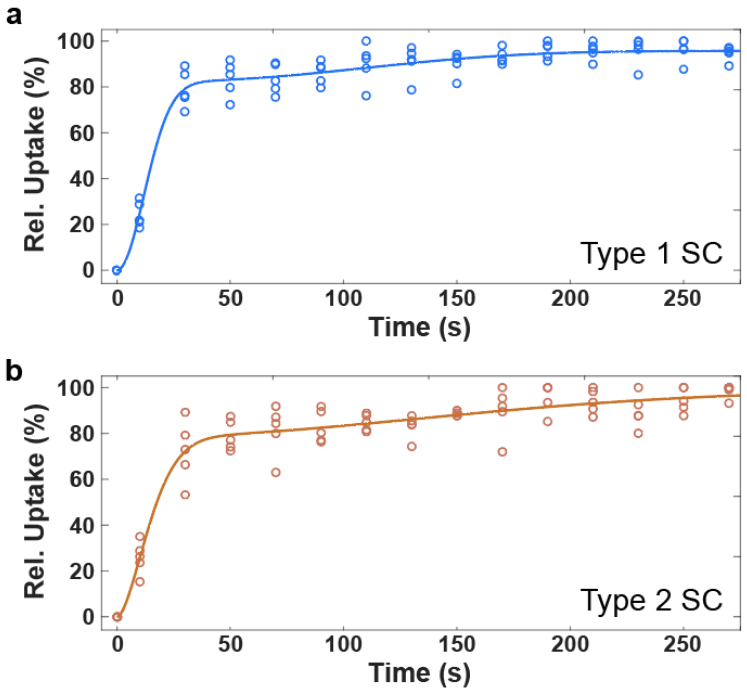

Supplementary Figure S14: Data to Figure 3c. *Overview plot of underlying data sets for SC kinetics data of monocrystalline (Type 1) and polycrystalline (Type 2) MOF-801 particles. The colored lines represent the mean fit curve over N = 5 particles each.*

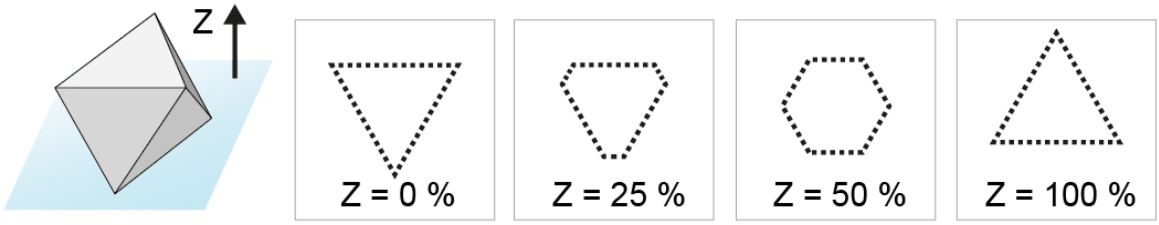

Supplementary Figure S15: *Apparent shape of an octahedral crystal at different imaging planes.*

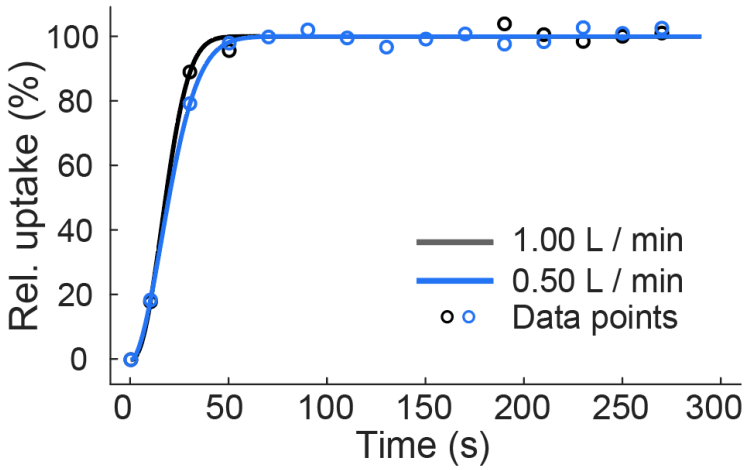

Supplementary Figure S16: Adsorption at 8%RH for different flow rates. *No significant difference in uptake kinetics was observed.*

Supplementary References

1 Avrami, M. Kinetics of Phase Change. II Transformation‐Time Relations for Random Distribution of Nuclei. *The Journal of Chemical Physics* **8**, 212-224, doi:10.1063/1.1750631 (1940).
2 Guo, B. *et al.* Study on CO(2) Capture Characteristics and Kinetics of Modified Potassium-Based Adsorbents. *Materials (Basel, Switzerland)* **13**, 877, doi:10.3390/ma13040877 (2020).
3 Martell, J. D., Milner, P. J., Siegelman, R. L. & Long, J. R. Kinetics of cooperative CO2 adsorption in diamine-appended variants of the metal-organic framework Mg2(dobpdc). *Chem. Sci.* **11**, 6457-6471, doi:10.1039/d0sc01087a (2020).
4 Furukawa, H. *et al.* Water adsorption in porous metal-organic frameworks and related materials. *J. Am. Chem. Soc.* **136**, 4369-4381, doi:10.1021/ja500330a (2014).
5 Buttersack, C. Modeling of type IV and V sigmoidal adsorption isotherms. *Phys Chem Chem Phys* **21**, 5614-5626, doi:10.1039/c8cp07751g (2019).
6 Long, D. A. *The Raman Effect: A Unified Treatment of the Theory of Raman Scattering by Molecules*. (John Wiley & Sons, Ltd, 2002).
7 Pelletier, M. J. & Pelletier, C. C. in *Raman, Infrared, and Near‐Infrared Chemical Imaging* 1-20 (2010).
8 Placzek, G. in *Handbuch der Radiologie VI* Vol. 2 (ed E Marx) 205 (Akademische Verlagsgesellschaft, 1934).
9 Nestor, J. R. & Lippincott, E. R. The effect of the internal field on Raman scattering cross sections. *Journal of Raman Spectroscopy* **1**, 305-318, doi:10.1002/jrs.1250010309 (1973).
10 Fathieh, F. *et al.* Practical water production from desert air. *Sci. Adv.* **4**, eaat3198, doi:10.1126/sciadv.aat3198 (2018).
11 Furukawa, H. *et al.* Water Adsorption in Porous Metal–Organic Frameworks and Related Materials. *J. Am. Chem. Soc.* **136**, 4369-4381, doi:10.1021/ja500330a (2014).
12 Mason, J. D., Cone, M. T. & Fry, E. S. Ultraviolet (250-550nm) absorption spectrum of pure water. *Appl. Opt.* **55**, 7163-7172, doi:10.1364/AO.55.007163 (2016).
13 Pope, R. M. & Fry, E. S. Absorption spectrum (380–700 nm) of pure water. II. Integrating cavity measurements. *Appl. Opt.* **36**, 8710-8723, doi:10.1364/AO.36.008710 (1997).
14 Curcio, J. A. & Petty, C. C. The Near Infrared Absorption Spectrum of Liquid Water. *J. Opt. Soc. Am.* **41**, 302-304, doi:10.1364/JOSA.41.000302 (1951).
15 Goodman, L. A. On the Exact Variance of Products. *Journal of the American Statistical Association* **55**, 708-713, doi:10.1080/01621459.1960.10483369 (1960).
16 Ramirez-Elias, M. G., Alda, J. & Gonzalez, F. J. Noise and Artifact Characterization of in Vivo Raman Spectroscopy Skin Measurements. *Appl. Spectrosc.* **66**, 650-655 (2012).
17 Zhang, X. *et al.* Method for Removing Spectral Contaminants to Improve Analysis of Raman Imaging Data. *Sci. Rep.* **7**, 39891, doi:10.1038/srep39891 (2017).
18 APEX3 V 8.38 v. 8.38 (Version 8.38, Madison, WI, 2018).
19 SADABS V 2016/2 (Version 2016/2, Madison, WI, 2014).
20 Sheldrick, G. M. A short history of SHELX. *Acta Crystallogr A* **64**, 112-122, doi:10.1107/S0108767307043930 (2008).
21 Sheldrick, G. M. Crystal structure refinement with SHELXL. *Acta Crystallogr C Struct Chem* **71**, 3-8, doi:10.1107/S2053229614024218 (2015).
22 Dolomanov, O. V., Bourhis, L. J., Gildea, R. J., Howard, J. A. K. & Puschmann, H. OLEX2: a complete structure solution, refinement and analysis program. *J. Appl. Crystallogr.* **42**, 339-341, doi:doi:10.1107/S0021889808042726 (2009).
23 Trickett, C. A. *et al.* Definitive molecular level characterization of defects in UiO-66 crystals. *Angew Chem Int Ed Engl* **54**, 11162-11167, doi:10.1002/anie.201505461 (2015).

A.3. Sponges as bioindicators for microparticulate pollutants?.

Environmental Pollution 268 (2021) 115851

Contents lists available at ScienceDirect

Environmental Pollution

journal homepage: www.elsevier.com/locate/envpol

Sponges as bioindicators for microparticulate pollutants?☆

Elsa B. Girard [a, 1], Adrian Fuchs [b], Melanie Kaliwoda [c], Markus Lasut [d], Evelyn Ploetz [b], Wolfgang W. Schmahl [a, c, e], Gert Wörheide [a, e, f, *]

[a] Department of Earth and Environmental Sciences, Ludwig-Maximilians-Universität München, 80333, Munich, Germany
[b] Department of Chemistry and Center for Nanoscience (CeNS), Ludwig-Maximilians-Universität München, 81377, Munich, Germany
[c] SNSB - Mineralogische Staatssammlung München, 80333, München, Germany
[d] Faculty of Fisheries and Marine Science, Sam Ratulangi University, Jalan Kampus Unsrat Bahu, Manado, 95115, Sulawesi Utara, Indonesia
[e] GeoBio-Center[LMU], Ludwig-Maximilians-Universität München, 80333, Munich, Germany
[f] SNSB - Bayerische Staatssammlung für Paläontologie und Geologie, 80333, Munich, Germany

ARTICLE INFO

Article history:
Received 7 June 2020
Received in revised form
14 September 2020
Accepted 12 October 2020
Available online 20 October 2020

Keywords:
Sponge
Marine pollution
Bioindicator
Microplastic

ABSTRACT

Amongst other threats, the world's oceans are faced with man-made pollution, including an increasing number of microparticulate pollutants. Sponges, aquatic filter-feeding animals, are able to incorporate fine foreign particles, and thus may be a potential bioindicator for microparticulate pollutants. To address this question, 15 coral reef demosponges sampled around Bangka Island (North Sulawesi, Indonesia) were analyzed for the nature of their foreign particle content using traditional histological methods, advanced light microscopy, and Raman spectroscopy. Sampled sponges accumulated and embedded the very fine sediment fraction (<200 μm), absent in the surrounding sand, in the ectosome (outer epithelia) and spongin fibers (skeletal elements), which was confirmed by two-photon microscopy. A total of 34 different particle types were identified, of which degraded man-made products, i.e., polystyrene, particulate cotton, titanium dioxide and blue-pigmented particles, were incorporated by eight specimens at concentrations between 91 and 612 particle/g dry sponge tissue. As sponges can weigh several hundreds of grams, we conservatively extrapolate that sponges can incorporate on average 10,000 microparticulate pollutants in their tissue. The uptake of particles, however, appears independent of the material, which suggests that the fluctuation in material ratios is due to the spatial variation of surrounding microparticles. Therefore, particle-bearing sponges have a strong potential to biomonitor microparticulate pollutants, such as microplastics and other degraded industrial products.

© 2020 Elsevier Ltd. All rights reserved.

1. Introduction

Microparticulate pollutants (later referred to as "micropollutants") are a threat to inhabitants of the world's oceans. Here, we define micropollutants as man-made substances, or products of their subsequent degradation, smaller than 5 mm in size. They are introduced into the environment and are potentially harmful to organisms, for instance as microplastics, textile fibers, and particulate toxins that leach from household and cosmetic products (Dris et al., 2016; Auta et al., 2017; Rochman 2018). Because traditional sieving techniques fail to assess the very fine particulate fraction (<200 μm) adequately (Lindeque et al., 2020), the main question driving this research is whether potential bioindicators for such anthropogenic micropollutants can be identified among marine organisms.

Sponges (Phylum Porifera) are aquatic benthic animals, which are geographically widely spread (Bell 2008). They consume mainly dissolved organic carbon (DOC), prokaryotes and ultraphytoplankton (<10 μm) by filtering fine particles from the ambient water (Yahel et al., 2006). They incorporate particles following two main paths (1) phagocytosis by choanocytes (i.e., cells that generate the water flow in the sponge body through the beating activity of their flagellum, organized in chambers): and (2) endocytosis through the exopinacoderm (i.e., external cells forming the outermost body layer) (Willenz and van de Vyver 1982; Teragawa 1986a; Hammel and Nickel 2014). Exopinacocytes may incorporate particles as big as 2 mm diameter, which deposited on the outside of the

☆ This paper has been recommended for acceptance by Maria Cristina Fossi.

* Corresponding author. Department of Earth and Environmental Sciences, Ludwig-Maximilians-Universität München, 80333, Munich, Germany.
E-mail address: woerheide@lmu.de (G. Wörheide).
[1] Naturalis Biodiversity Center, 2300 RA Leiden, The Netherlands.

https://doi.org/10.1016/j.envpol.2020.115851
0269-7491/© 2020 Elsevier Ltd. All rights reserved.

animal on the ectosome (Cerrano et al., 2002). Such microparticles are thought to subsequently be transported by ameboid mesohyl cells from the ectosome towards sites of skeletogenesis in non-spiculated demosponges (Teragawa 1986a). Foreign microparticles provide sponges with strength and support their growth (Teragawa 1985). They may also serve for protection (Burns and Ilan 2003) and anchorage to the substrate (Cerrano et al., 2002); Teragawa (1986b). However, mechanisms behind particle incorporation, retention and rejection in sponges are not fully understood yet. Nonetheless, we hypothesize that the fluctuation in material ratios incorporated by sponges is due to the spatial variation of surrounding microparticles; therefore, sponges may incorporate man-made micropollutants if present in their immediate environment and be viable models for biomonitoring such.

To address this issue, we carried out a combination of field and laboratory studies. The sampling of sponges was conducted in Indonesia since it is known to be a hotspot for land-based pollution in the middle of the Coral Triangle (Eriksen et al., 2014). We used histological methods, such as (nonlinear) light microscopy, as well as Raman spectroscopy for five poriferan species from Bangka Island (North Sulawesi, Indonesia) to address the following three questions: in which structure(s) do particles accumulate? what kind of particles do sponges incorporate (diversity)? do sponges have the potential to monitor microparticulate pollutants? Findings from this study contribute to fill a knowledge gap on particle incorporation by sponges, regarding accumulation areas and diversity of incorporated particles. Moreover, our study suggests that sponges are promising aquatic bioindicators for microparticulate pollutants, such as microplastics and other degraded industrial products.

2. Material and methods

2.1. Site of study and sample collection

The field work took place at Coral Eye Resort on the west coast of Bangka Island (Kabupaten Minahasa Utara, Perairan Likupang), Sulawesi Utara, Indonesia, between March 17th and April 12th, 2019, to assess the plastic contamination in marine sponges (research permit holder: Elsa Girard; SIP no.: 97/E5/E5.4/SIP/2019). The sampling area spanned approximately 7 km^2 and specimens were sampled at two different locations: Coral Eye house reef South and North from the jetty (Supplementary material Fig. S1; Tab. S1). Non-lethal sponge samples (n = 15) of fragments of maximum 8 cm^3 tissue were taken from five abundant sponge species (3 specimens collected per sponge species, later referred to as “triplicate”) known to naturally incorporate foreign microparticles. The sample collection was done at water depth between 1 and 3 m below the lowest tide using a stainless-steel diving knife. Collected samples were preserved in two aliquots: 96% ethanol for DNA barcoding and 4% formaldehyde for histology and spectroscopy. An *in situ* picture of each specimen was taken, showing the macromorphological features of the species. Molecular, histological and Raman spectroscopy analyses described below were performed on all 15 sponge samples.

In addition, one sand sample from Coral Eye Resort was collected for comparison in the intertidal zone near the jetty (later referred to as “beach sand”) using a polyethylene terephthalate (PET) plastic bottle. A random subsample of the sand was transferred into a 1.5 mL Eppendorf microtube (Eppendorf AG, Hamburg) using a metal spatula. The beach sand was prepared for Raman spectroscopy the same way as the sponge samples were (see below), going through bleaching, washing and filtration steps. Microparticles (<200 μm) were not extracted from the beach sand sample. Due to the small sand sample size (n = 1), it may potentially introduce a control bias.

2.2. Species identification

At the Molecular Geobiology and Paleobiology laboratory of the Department of Earth & Environmental Sciences, Paleontology & Geobiology, LMU Munich, the 15 sponge specimens collected from five different species were identified and confirmed to the genus using integrative taxonomy (Wörheide and Erpenbeck 2007; Voigt and Wörheide 2016). The DNA was extracted from the sponge samples using a DNA extraction kit (NucleoSpin® Tissue, Macherey-Nagel GmbH & Co. KG). DNA barcoding was conducted using a fragment of the 28S ribosomal DNA, a region amplified using universal primers via polymerase chain reaction (PCR) (Supplementary material Tab. S2). The DNA was sequenced with BigDyeTerminator v3.1. Sanger Sequencing was conducted at the Genomic Sequencing Unit of the LMU Munich, using an ABI 3730 (Erpenbeck et al., 2017).

Forward and reverse sequences were assembled and edited using CodonCode Aligner v3.7.1.2 (www.codoncode.com). Sequences of poriferan origins were identified with BLAST® for nucleotides using the NCBI database (https://blast.ncbi.nlm.nih.gov) and combined to the 28S sponge data set (Erpenbeck et al., 2016) available at the Sponge Genetree Server (www.spongegenetrees.org). The data set was largely reduced to concentrate on the important clades, by selecting only the nearby taxa (taxonomically classified) with the least genetic distance to the samples. Alignments were performed in MAFFT v7.427 (https://mafft.cbrc.jp/alignment/software/), default settings. Subsequently, a phylogenetic tree was calculated for 28S sequences in Seaview v4.6.3 (Gouy et al., 2010) under PhyML Generalized Time-Reversible model with the invariable site and gamma shape settings obtained via jmodeltest 2.1.10 v20160303 (Darriba et al., 2012), and included 100 bootstrap replicates (Guindon et al., 2010). Final barcoding data (alignments and trees) is stored on GitHub repository (https://github.com/PalMuc/PlasticsSponge).

2.3. Histological analysis

All 15 sponge samples that were initially fixed with 4% formaldehyde overnight were gradually dehydrated with ethanol at the Coral Eye Resort laboratory (Indonesia). At the laboratory in Munich, samples were prepared for thin sectioning in LR-white medium to preserve the original position of foreign particles within the tissue. Sections with a thickness ranging between 50 and 400 μm were cut depending on the specimen morphology, using a saw microtome (Leica SP1600). Sections were mounted on microscope slides using Eukitt Quick-hardening mounting medium. The histological analysis was conducted using a microscope Leica DMLB (Type 020−519.502 LB30 T BZ:00, Leica Mikroskopie & Systeme GmbH Wetzlar) with a mounted digital camera. Images of the same field of views were taken under brightfield and (cross-) polarized light illumination. The polarized light fields allowed a better recognition of the foreign particles in the sponge, embedded in the organic tissue. Field of views of the ectosome, mesohyl, skeletal structures and aquiferous system (i.e., canals and choanocyte chambers) were recorded for each specimen. The histological analysis also enabled the description of the sponge main morphological micro-features.

In addition to the assessment of particle accumulation areas, relative particle abundance and size were analyzed with ImageJ v1.52K (Schindelin et al., 2012). All tissue images utilized for the analysis were taken under the same settings (100 μm thin section, equal luminosity and magnification) to ensure comparability of the data. To measure the particle’s relative abundance, images were

translated into grayscale (8-bit) and the mean light intensity of ten random square areas (264.52 μm side length) were measured per structure and per sample. The mean light intensity is a numerical value generated by the software that allows for a comparison between areas and samples with an arbitrary unit (AU). Unpolarized light illumination was chosen for keratose sponges, because the spongin tissue from the skeletal fibers has a high transmission with little scattering comparable to the particles. On the contrary, (cross) polarized light illumination was used for heteroscleromorphs, to observe particles in these heavily spiculated specimens with high organic matter content. Images taken with polarized light were treated in a second step by inverting the gray scale in order to have dark particles on a pale background, similarly to the images taken with unpolarized light. Therefore, the lower the intensity value, the darker the area and the more particles are present. The particle size was also assessed and categorized with ImageJ: small (most particles <50 μm diameter), large (most particles > 50 μm diameter) or mix (presence of small and large particles at a similar fraction). The diameter corresponds to the longest axis of the particle. The data gathered from the particle distribution, abundance and size was analyzed in R v3.3.3 (R Core Team 2017). Primary data and R scripts are available on GitHub repository (https://github.com/PalMuc/PlasticsSponge).

2.4. Particle distribution with two-photon excitation

Histological sections of sponge tissue were analyzed by two-photon excitation (TPE) 3D imaging, to highlight the contrast between the highly fluorescent organic tissue from the sponges in opposition to the non-fluorescent mineral particles incorporated by the sponge. Samples were evaluated after histological preparation. For two-photon imaging, fresh sections of 170 μm thickness were prepared without staining and mounted on microscope slides using Eukitt Quick-hardening mounting medium. Brightfield pictures of the scanned area were taken before the experiment followed by a 3D scan of the specimen. Each 2D image had a range of 190 μm, an acquisition time of 180 s and a step size of 380 nm. The 3D step size between the 2D image planes and the total number of planes was chosen with respect to the object of interest and ranged from 10 to 21 planes with 0.5–3 μm steps.

Imaging was carried out on a confocal scanning microscope (TE 300; Nikon) with mounted bright-field illumination and camera. The two-photon excitation source was a fiber-based, frequency-double erbium laser (FemtoFiber dichro bioMP, Toptica Photonics) running at 774 nm. The laser power was 10 mW. The laser light was coupled into the microscope via a low pass dichroic mirror (HC BS 749 SP; AHF Analysetechnik) that separates laser excitation and fluorescence emission. Scanning of the sample in 3D was achieved by using a xyz piezo stage (BIO3.200; PiezoConcept). The laser excitation was focused onto the sample with a 60x (water) 1.20-NA plan apochromat objective (Plan APO VC 60× 1.2 NA, Nikon). The emission was collected by the same objective and passed afterwards through a bandpass filter (SP600; AHF). The emission was recorded on an APD detector (Count Blue; Laser Components) and its photons stream registered using a TCSPC card (TH260 pico dual; PicoQuant GmbH). The experiment was controlled using a home-written program written in C#. The confocal data was extracted and evaluated afterwards by PAM (Schrimpf et al., 2018) and ImageJ2 (Schindelin et al., 2012).

2.5. Raman spectroscopy

Raman spectroscopy was performed on all 15 sponge samples and the beach sand, and the analyses permitted the identification and quantification of particles on a filter and *in situ*, i.e., from thin sections (30–50 μm thick). As preparation for Raman measurements, all sponge samples were firstly subsampled, dried and weighed. The subsamples weighed between 2.2 and 11 mg. The sponge tissue and the beach sand was digested in 1.5 mL household bleach over 2–3 days, with a one-time bleach renewal. All samples were then washed with MilliQ water five times in a row. Particles left were filtered through a nitrocellulose membrane (Whatman™, 1 μm mesh size) with the aid of a vacuum pump. One hundred particles were randomly measured per sample (referred to as "random" search pattern). Furthermore, a maximum of ten additional particles per sample were measured on purpose depending on differences in color, shape and texture to assess the diversity of incorporated particles in lower abundance (referred to as "target" search pattern). In addition, the spectrum of white and a red sclerites of *Tubipora musica* (sample number GW1858, obtained from an individual grown in an aquarium at the Molecular Geobiology and Paleobiology laboratory) was measured to compare its red pigment signal to that of the red particles present in sponges.

Raman spectra were taken on a confocal Raman microscope (HORIBA JOBIN YVON XploRa ONE micro Raman spectrometer) at the SNSB–Mineralogical State Collection Munich. The Raman spectrometer used is equipped with a Raman edge longpass filter, a Peltier cooled CCD detector and three different lasers working at 532 nm (green), 638 nm (red) and 785 nm (near IR). Here, 532 nm excitation was used to perform the measurements, with a long working distance (LWD) objective magnification 100× (Olympus, series LMPlanFL N), resulting in a 0.9 μm laser spot size on the sample surface. The power required for high-quality spectra varied between 10% and 100% (i.e., respectively 0.879 mW and 8.73 mW ± 0.1 on the sample surface) depending on the type and size of measured particles. The diameter of pin-hole and the slit width were set to 300 and 100 μm, respectively. Each acquisition included two accumulations with an integration time of 8 s over a spectral range of 50–2000 cm^{-1} (ca. 35 s per measurement). Resulting Raman spectra were analyzed using LabSpec Spectroscopy Suite software v5.93.20, compiled in a table, visualized in R v3.3.3, manually sorted in Adobe Illustrator CS3, and compared with available spectra from RRUFF database (see: http://rruff.info/index.php) and published work (e.g., Zięba-Palus and Michalska (2014)). The statistical ANOSIM test (Analysis of Similarity) was performed in R v3.3.3, using 999 permutations in the vegan package (Oksanen et al., 2017) to assess the similarity in foreign particle assemblage composition between species, subclasses and sampling locations. Raman spectra and analysis scripts written in R used for the analysis are available on GitHub repository (https://github.com/PalMuc/PlasticsSponge).

2.6. Precautions against contaminants

To avoid contamination of the samples, latex gloves, glassware, cotton towel and dust-free wipers (Kimtech Science) were used when manipulating all 15 sponge samples at all times. All open manipulations done in Molecular Geobiology and Paleobiology laboratory at LMU, i.e., dissection and filtration of the samples, were conducted under a clean bench (BDK, Luft-und Reinraumtechnik GmbH). Eppendorf safe-lock tubes 1.5 mL (polypropylene) were used to centrifuge the subsamples during tissue digestion and subsequent washing steps. Consequently, a negative sample was included, undergoing the same steps as all samples from tissue digestion to particle filtration. Due to the airborne exposure of the samples in the field at Coral Eye Resort laboratory and the presence of fibers on the negative filter, all resulting fibers in this study were regarded as contaminants and therefore not taken into account. Only microparticles, excluding microfibers, were analyzed.

3. Results

Five particle-bearing species were particularly abundant around Bangka Island (Indonesia), and were sampled three times to generate the triplicates (n = 15). In order to determine the accumulation areas of foreign particles in coral reef sponges, the samples were taxonomically classified to the genus level into 5 clades: *Carteriospongia*, *Ircinia* I, *Ircinia* II, Tethyid I and Tethyid II (Supplementary material Fig. S2; Tab. S3) and histologically analyzed. Subsequently, the samples were examined with Raman spectroscopy to assess the diversity of incorporated particles.

3.1. Particle distribution

Thin sections provided an overview of the main structures and the distribution of particles within sponge bodies. Incorporated particles were located and identified with polarized light microscopy using TPE 3D imaging and Raman spectroscopy. No particles were found inside choanocyte chambers; only particles surrounding choanocyte chambers were observed in both Tethyid species. Therefore, no further statistical analysis was conducted on choanocyte chambers.

Foreign particles were observed by (nonlinear) light microscopy in the aquiferous system, the mesohyl, the ectosome and the fibrous skeleton, depending on the species (Figs. 1 and 2). Two-photon microscopy clearly confirmed that the incorporated particles were completely embedded in the surrounding tissue (Fig. 2, Supplementary material Fig. S3). All specimens incorporated particles in the mesohyl and the ectosome. Moreover, 73% of the specimens, independently of the skeletal material, had some particles in the aquiferous system; the clades *Ircinia* I did not contain particles in their canals. All specimens of the subclass Keratosa incorporated particles in their skeletal spongin fibers (e.g., Fig. 2D), whereas heteroscleromorphs did not because they have siliceous spicules instead of fibers as skeletal structures (Fig. 1).

Across all specimens, particles embedded in the mesohyl (e.g., Fig. 2A) were in lower abundance (the higher the light intensity, less dense the particle cover), in comparison to the density of particles accumulated in spongin fibers and/or the ectosome (Fig. 1). Moreover, thorough microscopy analyses revealed a majority of small particles (<50 μm) present in the mesohyl/aquiferous system and accumulated in the ectosome (Figs. 1 and 2). Larger particles (>50 μm) were observed in spongin primary fibers of keratose sponges (Figs. 1 and 2). Only specimens from the clade *Ircinia* I incorporated large particles in all three structures. The size of uptaken particles between *Ircinia* species differed although they belong to the same genus. In fact, the clade *Ircinia* II reflected *Carteriospongia*'s particle size pattern. Measured particles on the filters varied in size, with a diameter ranging from 5 μm to approximately 200 μm, which are equivalent in size to the particles measured *in situ* (Fig. 2). The size of the particle may therefore indicate in which structure particles might have been incorporated in relation to Fig. 1, for example, larger particles in Keratosa are more likely to accumulate in the fiber network than the mesohyl (Figs. 1 and 2). The fine fraction (<200 μm) was absent from the beach sand sample, where only coarse particles (>500 μm diameter) were observed.

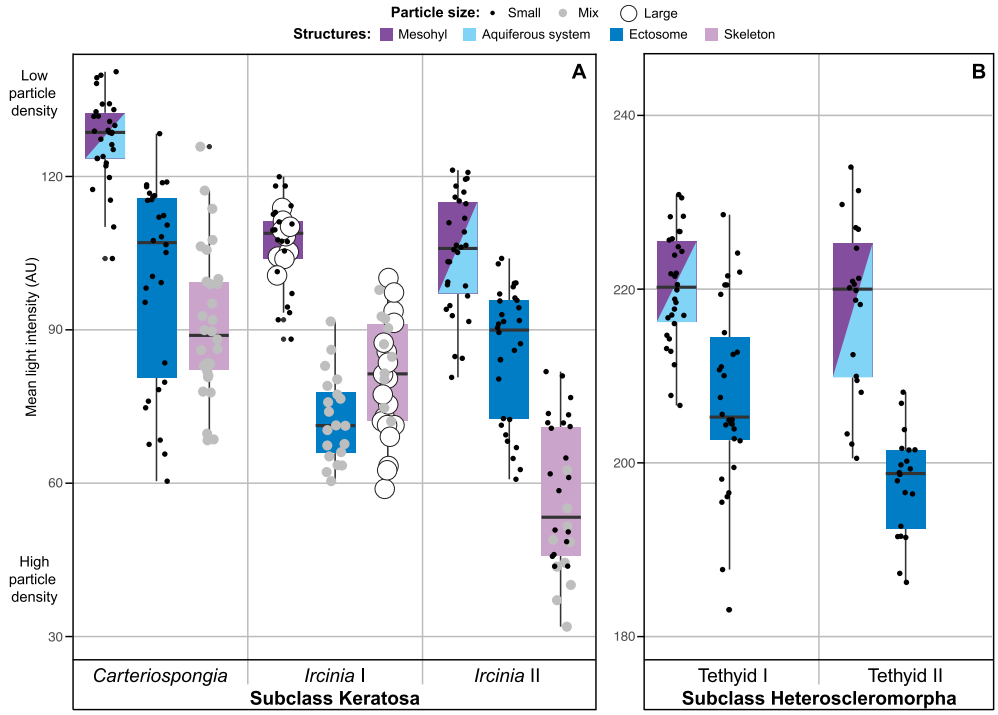

Fig. 1. Particle distribution amongst sampled sponges and their abundance in tissue structures as derived from brightfield imaging. A) Subclass Keratosa, B) subclass Heteroscleromorpha. The lower the intensity, i.e., absorption of the specimen body, the higher the number of particles in the structure; the aquiferous system was not differentiated from the mesohyl in cases where particles were present in the aquiferous system. Particle size is represented by the size and color of the dots (i.e., black small dots for a majority of particles < 50 μm, white large dots for a majority of particles > 50 μm and gray medium dots for a more or less equal presence of small and large particles). Color code: skeleton in lila, aquiferous system in cyan, mesohyl in purple, ectosome in blue. The box size corresponds to the 25th (bottom) and 75th (top) percentile of the data (known as the interquartile range) and the middle line shows the median (50th percentile). The error bars correspond to the smallest and largest value within 1.5 times the interquartile range below and above the 25th and 75thpercentile, respectively. The mean light intensity (y-axis) is given in an arbitrary unit (AU). Note: relative intensity within the same subclass can be compared, however not between the subclasses as the scale used was different. (For interpretation of the references to color in this figure legend, the reader is referred to the Web version of this article.)

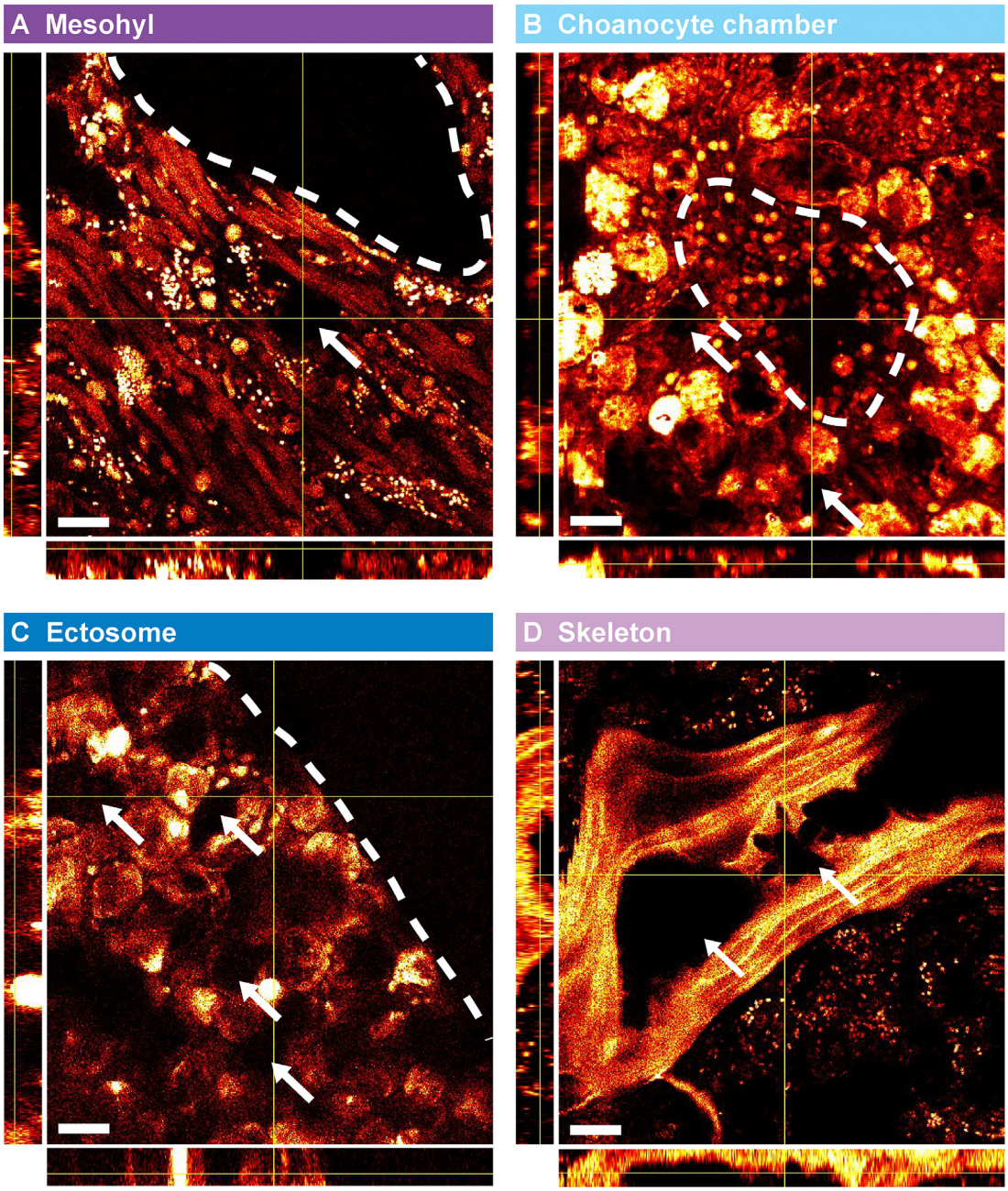

Fig. 2. Two-photon images of three-dimensional sponge tissue sections with embedded foreign particles. The auto-fluorescence of the organic tissue material serves as imaging contrast compared to inorganic particles that are non-fluorescent. XZ and YZ projections through the 3D image stack are depicted aside of each XY projection (brightfield images are shown in Supplementary material Fig. S3). Exogenous particles are embedded in the tissue (some examples are marked with white arrows) and are found A) in the mesohyl of *Ircinia* sp. (the canal is circled with a dashed line), B) surrounding the choanocyte chamber of Tethyid sp. (circled with a dashed line), C) at the ectosome of Tethyid sp. (the dashed line separates the outermost part of the sponge tissue), and D) in spongin fibers of *Carteriospongia* sp.. Z-scan ranges are 18 μm and scale bars are 20 μm.

3.2. Particle diversity

A total of 1686 particles were measured on 15 filters (between 103 and 110 particles per filter). Across all measured particles on the filters, 34 different spectra were identified, of which 22 were associated to a single material or pigment (aragonite, calcite, amorphous calcite, quartz, β-quartz, anatase, feldspar, graphite, magnetite, mackinawite, ferrosilite, cotunnite, hematite, riebeckite derivative, polystyrene, particulate cotton, carbon, *Argopecten irradians* shell, red biomineralization type I and II, blue pigment type I and II) (Fig. 3, Supplementary material Tab. S4). The 12 remaining spectra are polymineralic particles and were interpreted as a mixture of two different materials (e.g., aragonite + quartz). Our results also show a high variability and diversity of the scarce incorporated compounds between the different species, including particles derived from anthropogenic products (Supplementary material Tab. S5, S6).

3.2.1. Inorganic compounds

As illustrated in Fig. 3, calcite and aragonite (i.e., $CaCO_3$) showed similar vibrational bands around 150, 705 and 1085 cm^{-1}, but calcite had a band at ca. 280 cm^{-1}, whereas aragonite had one at ca.

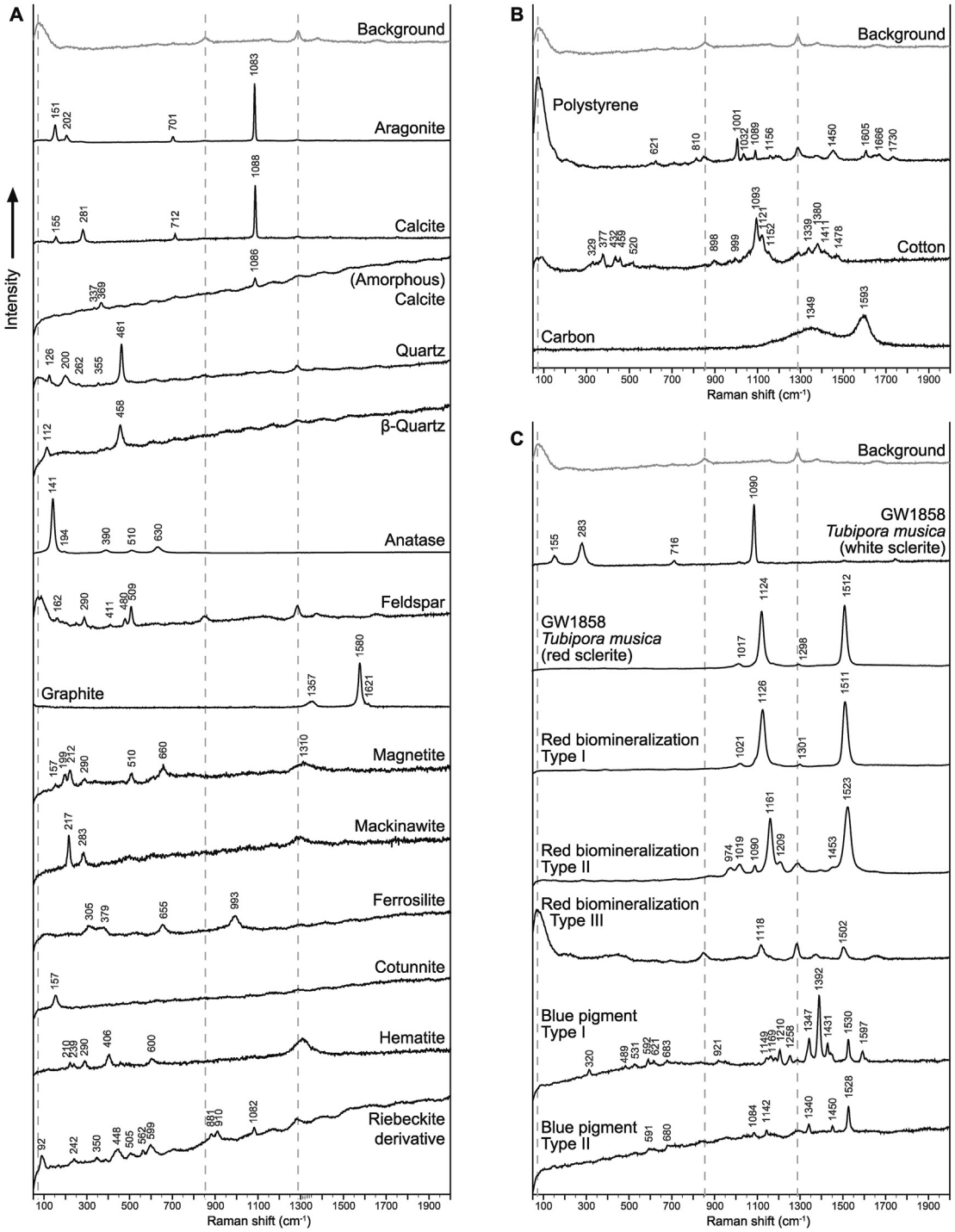

Fig. 3. Raman spectra of incorporated particles (n = 1686). Mix spectra are not included, as they are a combination of two different minerals illustrated above. A) inorganic spectra. B) organic spectra. C) spectra associated with pigments. Red biomineralization spectra are compared to GW1858 (octocoral *Tubipora musica* red and white sclerites). Numbers over the signatures indicate the highest point of each vibrational band. Dotted lines indicate bands corresponding to the background.

205 cm^{-1} due to their different crystallographic structures. Quartz was characterized with a vibrational band at 460 cm^{-1}, related to the Si—O—Si bond. Carbonate phosphate showed two weak vibrational bands at ca. 960 cm^{-1} (phosphate; PO_4^{3-}) and 1075 cm^{-1} (carbonate; CO_3^{2-}). Feldspar was distinguished by three vibrational bands: ca. 290, 480 and 510 cm^{-1} (silica; Si), and anatase by one main band at ca. 140 cm^{-1}. The D-band (ca. 1350 cm^{-1}) and G-band (ca. 1580 cm^{-1}) are indicative for carbon-based materials, such as carbon, graphene and graphite. Given the band shape and ratio between both lines (Roscher et al., 2019), we identified the compounds as carbon and graphite (Fig. 3).

3.2.2. Organic compounds

Polystyrene was measured for two particles during a random search pattern. Particles, such as particulate cotton and blue colored particles, were found during a target search pattern

(Supplementary material Tab. S5). Some of these materials potentially come from man-made products, which is discussed in detail below. One specimen of *Carteriospongia* sp. (4.6 mg dry weight) and one of *Ircinia* I (6.3 mg dry weight) contained polystyrene at a concentration of 0.217 and 0.159 particle/mg, respectively. Four specimens from the Genus *Iricnia* (4.8, 4.9, 6.3 and 6.5 mg dry weight, respectively) were found with particulate cotton at concentrations between 0.154 and 0.612 particle/mg.

3.2.3. Pigmented compounds

The Raman signature of a white and a red sclerite of *Tubipora musica* (GW1858) showed that the red pigment signal generally (peaks at 1326 and 1511 cm^{-1}) covers all vibrational bands of calcite (ca. 280 and 1085 cm^{-1}). However, this red pigment (type I), found also in red aragonitic particles (e.g., red type I + aragonite), did not overtake the vibrational bands of aragonite (ca. 150 and 1085 cm^{-1}), ubiquitous across all samples. A second and third red pigments were also detected with Raman spectroscopy, showing peaks at 1161 and 1523 cm^{-1} and at 1118 and 1502 cm^{-1}, respectively. Red pigment type III is slightly shifted compared to the type I and II (Fig. 3). Finally, blue-pigmented particles were observed on the filter of two specimens from the clade Tethyid I (11.0 and 8.5 mg dry weight, respectively) at a concentration of 0.091 (type I) and 0.118 (type II) particle/mg.

3.3. Mineral ratios

Aragonitic and calcitic particles were identified in all observed structures. Tethyid clades did not only incorporate minerals, but also a considerable amount of particulate organic matter (Fig. 2C and D). Keratosa specimens incorporated on average 68% aragonite and 25% calcite, whereas Heteroscleromorpha specimens had 59% and 30%, respectively (Fig. 4). The aragonite-calcite median ratio of Tethyid I was 1.875, Tethyid II 2.462, *Cartegiospongia* 2.680, *Ircinia* I 2.310 and *Ircinia* II 2.783. Although all specimens had a higher aragonite-calcite ratio on average than that of the beach sand (ratio = 1.735), no species had significantly different particle ratio compared to one another and to the sand sample (ANOSIM: $P = 0.067$) as well as between the subclasses (ANOSIM: $P = 0.392$) based on the Analysis of Similarity (Fig. 5C and D). Specimens were also compared on their aragonite-calcite ratio according to the location they were collected, i.e., Coral Eye house reef South or north. The Analysis of Similarity also indicates that the particle ratio did not significantly vary between the sampling sites (ANOSIM: $P = 0.620$) (Fig. 5E).

Other than aragonite and calcite, < 2% of quartz was measured across all clades, but it was not present in the beach sand. However, 4% of the coarse grains in the beach sand sample was feldspar, which was also identified in *Carteriospongia* and both Tethyid clades. Carbonate phosphate and titanium oxide (anatase) were respectively measured on *Ircinia* II and Tethyid II filters (Supplementary material Tab. S5). Anatase was found at concentrations of 0.208 and 0.345 particle/mg. Most abundant polymineralic particles observed across the samples were quartz + aragonite and quartz + anatase, although both of them found in low concentrations (Supplementary material Tab. S5). The Analysis of Similarity suggests that the species have no preference on the material to be incorporated, because the species did not have significantly different material assemblage composition (ANOSIM: $P > 0.05$).

4. Discussion

In this study, 15 demosponges (3 of *Carteriospongia* sp., 6 of *Ircinia* spp. and 6 of Tethyid spp.) were histologically analyzed and characterized with respect to their foreign particle content with light microscopy and Raman spectroscopy. The particle density was higher in the ectosome and spongin fibers of keratose sponges than

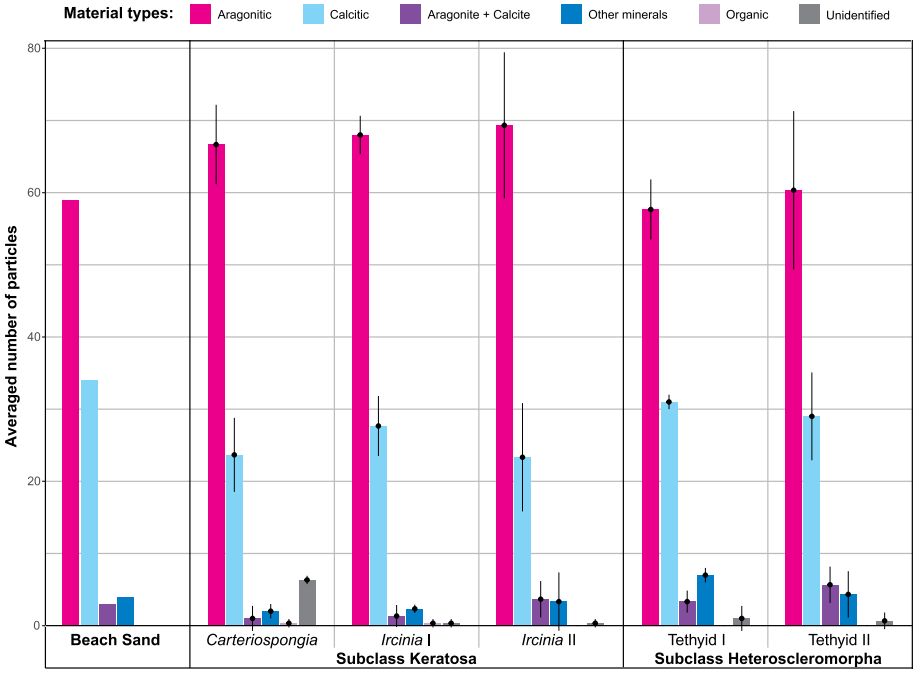

Fig. 4. Diversity of materials among sampled sponges. Particle diversity from resulting Raman measurements of 100 randomly selected particles per sample. Each species accounts for 3 samples, and particle counts were averaged per clade (pink: aragonitic; cyan: calcitic; purple: aragonite + calcite; blue: other minerals; lila: organic; gray: unidentified). Error bars represent the standard deviations in number of particles compared to the mean between the specimens of the same species. The category "Unidentified" results from low quality spectra, which could not be associated with any known material. (For interpretation of the references to color in this figure legend, the reader is referred to the Web version of this article.)

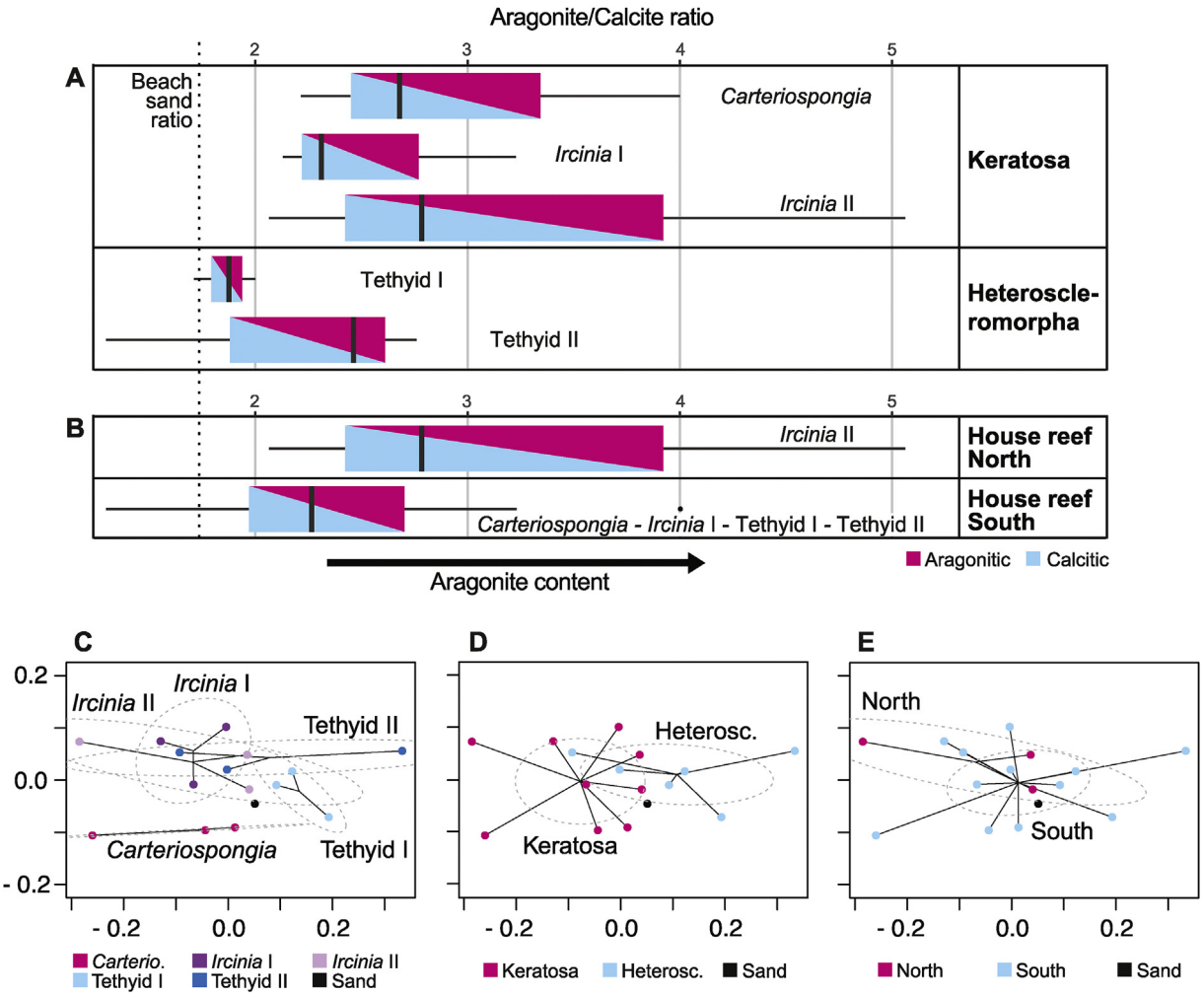

Fig. 5. Aragonite to calcite ratio A) at the species level and B) according to the sampling site. The beach sand sample ratio (1.735) is indicated with the dotted vertical line. The box size corresponds to the 25th (bottom) and 75th (top) percentile of the data (known as the interquartile range) and the middle line shows the median (50th percentile). The error bars correspond to the smallest and largest value within 1.5 times the interquartile range below and above the 25th and 75th percentile, respectively. Non-metric multidimensional scaling (NMDS) plots C) at the species level, D) at the subclass level and E) according to the sampling site, displaying the differences between the foreign particle assemblage composition. Dashed gray ellipses represent the 99% confidence interval. Note: the Analysis of Similarity indicates no significant differences between the samples at all three comparison levels (ANOSIM: $P > 0.05$).

in the mesohyl, and no particles were observed in choanocyte chambers. Embedded foreign particles were of larger size in keratose spongin fibers, whereas generally smaller than 50 μm in the mesohyl and the ectosome, as confirmed with TPE analysis. A wide range of different particles were present in low percentages on the filters (<3%), such as feldspar, quartz, carbonate phosphate, red pigments and composites. Moreover, several particles are most certainly of anthropogenic origin, i.e., particulate cotton, titanium dioxide, plastic and blue pigments, at densities between 0.091 and 0.612 particle/mg dry sponge tissue. No species preferentially incorporated particles of particular material type.

4.1. Incorporation of foreign particles

The capture and retention of foreign particles are common practice amongst sponges, especially noticeable within members of the subclass Keratosa, for instance species of the genus *Dysidea* embed particles in their spongin fibers (Willenz and van de Vyver 1982; Teragawa 1986a; Cerrano et al., 2007). The pathway most likely used to incorporate coarse particles in the core of spongin fibers is the endocytosis by exopinacocytes (Willenz and van de Vyver 1982; Teragawa 1986a). The diffusion of foreign particles through the ectosome towards the mesohyl in keratose specimens from Bangka Island suggests a particle transfer from the superficial region of the sponge towards the inner one. These findings indicate that the mesohyl serves as a transit zone for particle transport in keratose demosponges. Similar pathways are likely used by heteroscleromorph demosponges; however, patterns observed in our study show differences between accumulation areas. Indeed, Tethyid clades present a thick and dense ectosome hosting organic and inorganic particles of size equal to or smaller than 50 μm diameter. Similar particles also aggregate around choanocyte chambers, which indicates that particles are incorporated via both processes, i.e., captured by the exopinacocytes and absorbed or phagocytized by choanocytes. Consequently, sponges tend to select more voluminous particles (>50 μm) to support their skeleton in keratose demosponges and to retain smaller particles (<50 μm) in the ectosome in spiculated demosponges (Teragawa 1986b; Cerrano et al., 2007). Based on these findings, microparticulate pollutants are incorporated by sponges either in skeletal fibers or the ectosome, or both depending on the particle size and sponge species.

Other possible effects arise as sponges also incorporate micropollutants, for instance toxins associated with these microparticles can leach, impacting sponge development and pumping capacity (Hill et al., 2002). Likewise, microbial pathogens hitchhiking on, for example, microplastics may negatively affect sponges (Taylor et al., 2007), both of which will have a direct impact on the ecosystem they inhabit. Keratose demosponges may also use particulate micropollutants to build their skeleton and support their growth, creating temporary sinks or an expressway to enter the marine food chain through spongivores. On a more positive note, sponges likely host degrading bacteria able to remineralize certain micropollutants (Lee et al., 2001), taking the sponge loop theory to the next level.

4.2. Origins of micropollutants

A wide range of different materials was observed in sponges from Bangka Island. On the one hand, they are autochthonous and reflect geological formations, e.g., quartz and feldspar (Carlile et al., 1990; Kavalieris et al., 1992), and reef assemblages, e.g., tunicates and reef-building corals (Yamano et al., 2000; Bergamonti et al., 2011; Łukowiak 2012), of the surroundings. Indeed, slow weathering and erosion processes generate the detachment of particles that compose, together with the reef's coral sand production, most of today's Bangka Island sand. On the other hand, they are allochthonous and foreign to the natural environment, such as titanium dioxide, particulate cotton, blue-pigmented particles and microplastics.

4.2.1. Titanium dioxide

Titanium dioxide (TiO_2), i.e., anatase, brookite and rutile, can naturally accumulate in the sand subsequent to weathering of the titanium-bearing mineral ilmenite by underground water (Premaratne and Rowson 2003). At the same time, anatase is also used as a white pigment, i.e., PW6 (titanium white), in automotive paints (Zięba-Palus and Michalska 2014), pharmaceutical coatings (Alexander 2008), thermoplastic resin (Kitamura and Mitsuuchi 1996) and archeological paints (Middleton et al., 2005). That being said, none of the Raman vibrational bands measured in our study directly correspond to a white pigment. Nanoparticulate anatase, together with rutile, is also extensively used for its chemical properties and UVB protective behavior in sunscreens (Yue et al., 1997; Jaroenworaluck et al., 2006; Serpone et al., 2007). Hence, anatase particles found in sponges from Coral Eye house reef might as well come from the degradation of anthropogenic anatase-containing products, such as sunscreens, and not only from natural sources.

4.2.2. Blue pigments

Particles of highly similar blue color to the human eye were incorporated in two specimens of the clade Tethyid I. The blue pigments, however, showed two different Raman signatures. The main vibrational bands were also measured by Zięba-Palus and Michalska (2014) who identified those as from blue pigments used in car paints. The blue pigment Type I is most probably a mix between the pigment PV23 (dioxazine violet) and PB15 (phthalocyanine 15) and the blue pigment Type II PB15, according to the findings of Zięba-Palus and Michalska (2014). These synthetic organic pigments might also be used in marine coating or recreational painting (Bouchard et al., 2009). Because the Raman vibrational bands of the pigments overwrite that of its polymer composition, it is not possible to identify the nature of the particle. However, the pigment PB15 was previously recorded as a dye associated with microplastics isolated from the soft tissue of bivalves (van Cauwenberghe and Janssen 2014) and intertidal textile fibers (Girard et al., 2020).

4.2.3. Textiles and microplastics

High tides and winds bring large quantities of marine debris, including plastics and textiles, on to the shores of Bangka Island (EB Girard, personal observation; Giebel (2018) unpublished report). The litter lands on beaches, where the highest degradation rate of plastic has been reported (Andrady 2017). Coral Eye Resort volunteers clean the beach daily, however this is not done systematically all around the island yet, nor on proximal coast lines (EB Girard, personal observation). Not surprisingly then, eight microparticles were herein identified as particulate cotton ($n = 6$) or polystyrene ($n = 2$) in all sampled keratose species. Cotton fabric has also been reported to be the most observed fabric in environmental dust, as fibers in the atmosphere, but also in the intertidal zone (Dris et al., 2016, 2017; Girard et al., 2020). Nevertheless, some of these particles may also originate from the cloth made of cotton that was used to dry glass dishes to avoid plastic contamination of the samples. Polystyrene is one of the three most abundant microplastic materials reported at sea, together with polyethylene and polypropylene (Andrady 2017; Auta et al., 2017). Our results are further supported by the findings of Ling et al. (2017), who estimated that the concentration of microplastic particles in the sediment reaches up to 0.4 particle/mL in the southern coasts of Australia. The authors noticed a consistent microplastic concentration across 42 sampling sites. Moreover, microparticles of plastic were at highest concentration in a size range ca. 60–400 μm (Ling et al., 2017), which is concordant with the particle size incorporated by the sponge exopinacoderm. Because sponges can pump several decades to hundreds of liters per day (Leys et al., 2011) and microparticles deposit on their ectosome, Bangka specimens indeed incorporated microplastics.

4.3. Sponges as bioindicators

Sponges are potentially ideal local bioindicators because they are sessile animals and widely distributed across all aquatic habitats. In fact, the families of sponges occurring around Bangka island have previously been recorded from various other localities in Indonesia (van Soest 1989, 1990; Cerrano et al., 2002, 2006; Bell and Smith, 2004; de Voogd et al., 2006, 2009; 2009; de Voogd and Cleary, 2008; Becking et al., 2013; Calcinai et al., 2017a, b) (Supplementary material Fig. S4).

Our study confirms that sponges are efficient sediment traps, recording the diversity of the matter in the ambient water as they are able to register this diversity to the finest grain (<200 μm), otherwise difficult to recall solely based on sand samples (Janßen et al., 2017). Sponges have also been recognized as bioindicators for environmental stress (Carballo et al., 1996), water quality (Mahaut et al., 2013), and multiple pollutants, e.g., by heavy metals (Selvin et al., 2009; Venkateswara Rao et al., 2009) and polychlorobiphenyl (Perez et al., 2003). Furthermore, a recent study identified sponges as a good monitor to record more efficiently DNA of surrounding vertebrates than robotic samplers for environmental DNA (eDNA) (Mariani et al., 2019). Such biological monitors also provide information over a time window, whereas traditional net tows represent only a single point in time (Lindeque et al., 2020). Furthermore, in sediment traps, the fine fraction is washed away by currents, leading to biases in the actual particle diversity present in the sediment at a given location (Janβen et al., 2017).

4.3.1. Extrapolation to realistic micropollutant concentrations

Based on our results, sampled sponges did not preferentially incorporate particles of specific materials, which suggests that

fluctuation in material ratios is due to the spatial variation of surrounding microparticles. At a concentration higher than 0.1 particle/mg of dry sponge tissue, here from keratose demosponges (*Carteriospongia* sp. and *Icrinia* spp.) weighing ca. 6 mg (dry weight), we extrapolate that at least 10,000 microplastic particles can be incorporated by sponges weighing more than 100 g (dry weight). Similar approximations can derive from the results regarding abundance of blue-pigmented particles, particulate cotton and titanium dioxides in the spiculated demosponge Tethyid species. Because sponges can weigh several hundreds of grams (Reiswig, 1971; McMurray et al., 2008), they have the potential to accumulate non-negligible amounts of micropollutants. Sponges from museum collections have also been recently surveyed positively for fibrous microplastics (Modica et al., 2020). A larger screening of associated particles in sponge tissue, combined with carbonate dissolution, is likely to reveal more microplastics and other particles derived from anthropogenic products.

5. Conclusion

This study narrows the knowledge gap on particle incorporation processes and provides a first assessment on the particle diversity in sponges. Indeed, 34 particles of different nature were identified using Raman spectroscopy including micropollutants (i.e., polystyrene, particulate cotton, blue-pigmented particles, titanium dioxide). As sponges incorporate these micropollutants from their surroundings, a sample of sponge tissue may provide a unique estimate of the local micro-pollution available to the immediate fauna. Based on current knowledge and findings from this study, we conclude that particle-bearing sponges have the very promising potential to biomonitor micropollutants, such as particles putatively originating from anthropogenic products (e.g., microplastics). Whether sponges can disintegrate these micropollutants to the atomic or molecular level, and the effect this has on the immediately neighboring fauna is matter of future research.

Credit author statement

Elsa B. Girard, Conceptualization, Methodology, Validation, Investigation, Writing - original draft, Writing - review & editing, Visualization, Formal analysis. Arian Fuchs, Methodology, Validation, Investigation, Writing - original draft, Visualization, Formal analysis. Melanie Kaliwoda, Writing - original draft, Supervision, Resources. Markus Lasut, Project administration, Resources. Evelyn Ploetz, Writing - original draft, Writing - review & editing, Validation, Visualization, Supervision, Project administration, Resources, Funding acquisition. Wolfgang W. Schmahl, Resources. Gert Wörheide, Conceptualization, Methodology, Validation, Writing - original draft, Writing - review & editing, Supervision, Project administration, Resources, Funding acquisition

Declaration of competing interest

The authors declare that they have no known competing financial interests or personal relationships that could have appeared to influence the work reported in this paper.

Acknowledgements

This work is the result of a master thesis from the Master Program “Geobiology and Paleobiology” at the Department of Earth and Environmental Sciences of LMU München. We thank the Indonesian authorities for providing the research visa and permit (research permit holder: Elsa Girard; SIP no.: 97/E5/E5.4/SIP/2019) to conduct the research activities on Bangka Island, in collaboration with Sam Ratulangi University Manado (UNSRAT, Indonesia). We thank Dirk Erpenbeck, Oliver Voigt, Anna Clerici, Marco Perin, Stefanie Ries (providing the sand sample), Magdalena Wilde and Samuel Leivy Opa for helping during field work activities. We also thank the reviewers for their constructive comments, improving the article. A last word to acknowledge the No-Trash Triangle Initiative for tackling one of the big problems Earth is facing today.

Appendix A. Supplementary data

Supplementary data to this article can be found online at https://doi.org/10.1016/j.envpol.2020.115851.

Funding

The field work was funded by Coral Eye Resort (Marco Segre Reinach), the DAAD Hochschulpartnerschaft between the Zoologische Forschungsmuseum Alexander Koenig and Sam Ratulangi University Manado (Heike Wägele), Aqueis e.V. (MiriamWeber and Christian Lott), as well as the LMU (Gert Wörheide). Additional funding by the Center of NanoScience Munich (CeNS) and by the Deutsche Forschungsgemeinschaft (SFB1032, project B03); LMUexcellent; and PL 696/4–1) is gratefully acknowledged.

References

Alexander, R., 2008. Raman spectroscopy analysis of polymorphs. Photonics Media. https://www.photonics.com/Articles/Raman_Spectroscopy_Analysis_of_Polymorphs_/a33214. (Accessed 11 August 2019).
Andrady, A.L., 2017. The plastic in microplastics: a review. Mar. Pollut. Bull. 119, 12–22.
Auta, H.S., Emenike, C.U., Fauziah, S.H., 2017. Distribution and importance of microplastics in the marine environment: a review of the sources, fate, effects, and potential solutions. Environ. Int. 102, 165–176.
Becking, L.E., Cleary, D.F.R., de Voogd, N.J., 2013. Sponge species composition, abundance, and cover in marine lakes and coastal mangroves in Berau, Indonesia. Mar. Ecol. Prog. Ser. 481, 105–120.
Bell, J.J., 2008. The functional roles of marine sponges. Estuar. Coast Shelf Sci. 79, 341–353.
Bell, J.J., Smith, D., 2004. Ecology of sponge assemblages (Porifera) in the Wakatobi region, south-east Sulawesi, Indonesia: richness and abundance. J. Mar. Biol. Assoc. U. K. 84, 581–591.
Bergamonti, L., Bersani, D., Csermely, D., Lottici, P.P., 2011. The nature of the pigments in corals and pearls: a contribution from Raman spectroscopy. Spectrosc. Lett. 44, 453–458.
Bouchard, M., Rivenc, R., Menke, C., Learner, T., 2009. Micro-FTIR and micro-Raman full paper study of paints used by Sam Francis. e-PS 6, 27–37.
Burns, E., Ilan, M., 2003. Comparison of anti-predatory defenses of Red Sea and Caribbean sponges. II. Physical defense. Mar. Ecol. Prog. Ser. 252, 115–123.
Calcinai, B., Bastari, A., Bavestrello, G., et al., 2017a. Demosponge diversity from North Sulawesi, with the description of six new species. ZooKeys 105–150.
Calcinai, B., Bastari, A., Makapedua, D.M., Cerrano, C., 2017b. Mangrove sponges from Bangka island (North Sulawesi, Indonesia) with the description of a new species. J. Mar. Biol. Assoc. U. K. 97, 1417–1422.
Carballo, J.L., Naranjo, S.A., García-Gómez, J.C., 1996. Use of marine sponges as stress indicators in marine ecosystems at Algeciras Bay (southern Iberian Peninsula). Mar. Ecol. Prog. Ser. 135, 109–122.
Carlile, J.C., Digdowirogo, S., Darius, K., 1990. Geological setting, characteristics and regional exploration for gold in the volcanic arcs of North Sulawesi, Indonesia. J. Geochem. Explor. 35, 105–140.
Cerrano, C., Bavestrello, G., Boyer, M., et al., 2002. Psammobiontic sponges from the bunaken marine park (North Sulawesi, Indonesia): interactions with sediments. Proc 9th Int Coral Reef Symp 279–282.
Cerrano, C., Calcinai, B., Pinca, S., Bavestrello, G., 2006. Reef sponges as hosts of biodiversity: cases from North Sulawesi. Proc 10th Int Coral Reef Symp 208–213.
Cerrano, C., Calcinai, B., Di Camillo, C.G., et al., 2007. How and why do sponges incorporate foreign material? Strategies in Porifera. In: Custódio, M.R. (Ed.), Porifera Research : Biodiversity, Innovation and Sustainability. Museu Nacional, Rio de Janeiro, pp. 239–246.
Darriba, D., Taboada, G.L., Doallo, R., Posada, D., 2012. jModelTest 2: more models, new heuristics and parallel computing. Nat. Methods 9, 772.
de Voogd, N.J., Cleary, D.F.R., 2008. An analysis of sponge diversity and distribution at three taxonomic levels in the Thousand Islands/Jakarta Bay reef complex, West-Java, Indonesia. Mar. Ecol. 29, 205–215.
de Voogd, N.J., Cleary, D.F.R., Hoeksema, B.W., et al., 2006. Sponge beta diversity in the spermonde archipelago, SW Sulawesi, Indonesia. Mar. Ecol. Prog. Ser. 309,

131–142.
de Voogd, N.J., Becking, L.E., Cleary, D.F.R., 2009. Sponge community composition in the derawan islands, NE kalimantan, Indonesia. Mar. Ecol. Prog. Ser. 396, 169–180.
Dris, R., Gasperi, J., Saad, M., et al., 2016. Synthetic fibers in atmospheric fallout: a source of microplastics in the environment? Mar. Pollut. Bull. 104, 290–293.
Dris, R., Gasperi, J., Mirande, C., et al., 2017. A first overview of textile fibers, including microplastics, in indoor and outdoor environments. Environ. Pollut. 221, 453–458.
Eriksen, M., Lebreton, L.C.M., Carson, H.S., et al., 2014. Plastic pollution in the world's oceans: more than 5 trillion plastic pieces weighing over 250,000 tons afloat at sea. PloS One 9, e111913.
Erpenbeck, D., Voigt, O., Al-Aidaroos, A.M., et al., 2016. Molecular biodiversity of red sea demosponges. Mar. Pollut. Bull. 105, 507–514.
Erpenbeck, D., Aryasari, R., Benning, S., et al., 2017. Diversity of two widespread Indo-Pacific demosponge species revisited. Mar. Biodivers. 47, 1035–1043.
Girard, E.B., Kaliwoda, M., Schmahl, W.W., et al., 2020. Biodegradation of textile waste by marine bacterial communities enhanced by light. Environ Microbiol Rep. https://doi.org/10.1111/1758-2229.12856.
Gouy, M., Guindon, S., Gascuel, O., 2010. SeaView version 4: a multiplatform graphical user interface for sequence alignment and phylogenetic tree building. Mol. Biol. Evol. 27, 221–224.
Guindon, S., Dufayard, J.-F., Lefort, V., et al., 2010. New algorithms and methods to estimate maximum-likelihood phylogenies: assessing the performance of PhyML 3.0. Syst. Biol. 59, 307–321.
Hammel, J.U., Nickel, M., 2014. A new flow-regulating cell type in the Demosponge Tethya wilhelma – functional cellular anatomy of a leuconoid canal system. PloS One 9, e113153.
Hill, M., Stabile, C., Steffen, L.K., Hill, A., 2002. Toxic effects of endocrine disrupters on freshwater sponges: common developmental abnormalities. Environ. Pollut. 117, 295–300.
Janßen, A., Wizemann, A., Klicpera, A., et al., 2017. Sediment composition and facies of coral reef islands in the spermonde archipelago, Indonesia. Frontiers in Marine Science 4, 144.
Jaroenworaluck, A., Sunsaneeyametha, W., Kosachan, N., Stevens, R., 2006. Characteristics of silica-coated TiO2 and its UV absorption for sunscreen cosmetic applications. Surf. Interface Anal. 38, 473–477.
Kavalieris, I., van Leeuwen, T.M., Wilson, M., 1992. Geological setting and styles of mineralization, north arm of Sulawesi, Indonesia. J. Southeast Asian Earth Sci. 7, 113–129.
Kitamura, H., Mitsuuchi, M., 1996. Glass-reinforced thermoplastic resin compositions containing the anatase form of titanium dioxide as a white pigmenting agent. US Patent.
Lee, Y.K., Lee, J.H., Lee, H.K., 2001. Microbial symbiosis in marine sponges. J. Microbiol. 39, 254–264.
Leys, S.P., Yahel, G., Reidenbach, M.A., et al., 2011. The sponge pump: the role of current induced flow in the design of the sponge body plan. PloS One 6, e27787.
Lindeque, P.K., Cole, M., Coppock, R.L., et al., 2020. Are we underestimating microplastic abundance in the marine environment? A comparison of microplastic capture with nets of different mesh-size. Environ. Pollut. 114721.
Ling, S.D., Sinclair, M., Levi, C.J., et al., 2017. Ubiquity of microplastics in coastal seafloor sediments. Mar. Pollut. Bull. 121, 104–110.
Mahaut, M.-L., Basuyaux, O., Baudinière, E., et al., 2013. The porifera Hymeniacidon perlevis (Montagu, 1818) as a bioindicator for water quality monitoring. Environ. Sci. Pollut. Res. Int. 20, 2984–2992.
Mariani, S., Baillie, C., Colosimo, G., Riesgo, A., 2019. Sponges as natural environmental DNA samplers. Curr. Biol. 29, R401–R402.
McMurray, S.E., Blum, J.E., Pawlik, J.R., 2008. Redwood of the reef: growth and age of the giant barrel sponge Xestospongia muta in the Florida Keys. Mar Biol 155, 159–171.
Middleton, A.P., Edwards, H.G.M., Middleton, P.S., Ambers, J., 2005. Identification of anatase in archaeological materials by Raman spectroscopy: implications and interpretation. J. Raman Spectrosc. 36, 984–987.
Modica, L., Lanuza, P., García-Castrillo, G., 2020. Surrounded by microplastic, since when? Testing the feasibility of exploring past levels of plastic microfibre pollution using natural history museum collections. Mar. Pollut. Bull. 151, 110846.
Oksanen, Jari, Blanchet, F.Guillaume, Friendly, Michael, Kindt, Roeland, Legendre, Pierre, McGlinn, Dan, Minchin, Peter R., O'Hara, R.B., Simpson, Gavin L., Solymos, Peter, Henry, M., Stevens, H., Szoecs, Eduard, Wagner, Helene, 2017. vegan: community Ecology Package. Version R package version 2.4-5. https://CRAN.R-project.org/package=vegan.
Perez, T., Wafo, E., Fourt, M., Vacelet, J., 2003. Marine sponges as biomonitor of polychlorobiphenyl contamination: concentration and fate of 24 congeners. Environ. Sci. Technol. 37, 2152–2158.
Premaratne, W.A.P.J., Rowson, N.A., 2003. The processing of beach sand from Sri Lanka for the recovery of titanium using magnetic separation. Phys. Separ. Sci. Eng. 12, 13–22.
R Core Team, 2017. R: A Language and Environment for Statistical Computing. URL. R Foundation for Statistical Computing, Vienna, Austria, Version 3.3.3. https://www.R-project.org/.
Reiswig, H.M., 1971. In situ pumping activities of tropical Demospongiae. Mar Biol 9, 38–50.
Rochman, C.M., 2018. Microplastics research—from sink to source. Science 360, 28–29.
Roscher, S., Hoffmann, R., Ambacher, O., 2019. Determination of the graphene–graphite ratio of graphene powder by Raman 2D band symmetry analysis. Anal Methods 11, 1224–1228.
Schindelin, J., Arganda-Carreras, I., Frise, E., et al., 2012. Fiji: an open-source platform for biological-image analysis. Nat. Methods 9, 676–682.
Schrimpf, W., Barth, A., Hendrix, J., Lamb, D.C., 2018. PAM: a framework for integrated analysis of imaging, single-molecule, and ensemble fluorescence data. Biophys. J. 114, 1518–1528.
Selvin, J., Shanmugha Priya, S., Seghal Kiran, G., et al., 2009. Sponge-associated marine bacteria as indicators of heavy metal pollution. Microbiol. Res. 164, 352–363.
Serpone, N., Dondi, D., Albini, A., 2007. Inorganic and organic UV filters: their role and efficacy in sunscreens and suncare products. Inorg. Chim. Acta. 360, 794–802.
Taylor, M.W., Radax, R., Steger, D., Wagner, M., 2007. Sponge-associated microorganisms: evolution, ecology, and biotechnological potential. Microbiol. Mol. Biol. Rev. 71, 295–347.
Teragawa, C.K., 1985. Mechanical Function and Regulation of the Skeletal Network in Dysidea. Duke University, pp. 252–258.
Teragawa, C.K., 1986a. Sponge dermal membrane morphology: histology of cell-mediated particle transport during skeletal growth. J. Morphol. 190, 335–347.
Teragawa, C.K., 1986b. Particle transport and incorporation during skeleton formation in a keratose sponge: Dysidea etheria. Biol Bull 170, 321–334.
van Cauwenberghe, L., Janssen, C.R., 2014. Microplastics in bivalves cultured for human consumption. Environ. Pollut. 193, 65–70.
van Soest, R.W.M., 1989. The Indonesian sponge fauna: a status report. Neth. J. Sea Res. 23, 223–230.
van Soest, R.W.M., 1990. Shallow-water reef sponges of Eastern Indonesia. In: Rützler, K. (Ed.), New Perspectives in Sponge Biology. Smithsonian Institute Press, London, pp. 302–308.
Venkateswara Rao, J., Srikanth, K., Pallela, R., Gnaneshwar Rao, T., 2009. The use of marine sponge, Haliclona tenuiramosa as bioindicator to monitor heavy metal pollution in the coasts of Gulf of Mannar, India. Environ. Monit. Assess. 156, 451–459.
Voigt, O., Wörheide, G., 2016. A short LSU rRNA fragment as a standard marker for integrative taxonomy in calcareous sponges (Porifera: calcarea). Org. Divers. Evol. 16, 53–64.
Willenz, P.H., van de Vyver, G., 1982. Endocytosis of latex beads by the exopinacoderm in the fresh water sponge Ephydatia fluviatilis: an in vitro and in situ study in SEM and TEM. J. Ultra. Res. 79, 294–306.
Wörheide, G., Erpenbeck, D., 2007. DNA taxonomy of sponges—progress and perspectives. J. Mar. Biol. Assoc. U. K. 87, 1629–1633.
Yahel, G., Eerkes-Medrano, D.I., Leys, S.P., 2006. Size independent selective filtration of ultraplankton by hexactinellid glass sponges. Aquat. Microb. Ecol. 45, 181–194.
Yamano, H., Miyajima, T., Koike, I., 2000. Importance of foraminifera for the formation and maintenance of a coral sand cay: green Island, Australia. Coral Reefs 19, 51–58.
Yue, J., Dew, L.R., Bissett, D.L., 1997. Sunscreen composition. US Patent.
Zięba-Palus, J., Michalska, A., 2014. Characterization of blue pigments used in automotive paints by Raman spectroscopy. J. Forensic Sci. 59, 943–949.
Łukowiak, M., 2012. First record of late eocene ascidians (ascidiacea, tunicata) from southeastern Australia. J. Paleontol. 86, 521–526.

A.4. Schwamm drüber? Schwämme als Bioindikatoren für Mikroplastikverschmutzung in Gewässern.

Bild: LMU München

1 Plastikverschmutzung im Meer vor Nord-Sulawesi (Indonesien). (A) Müll wird am Strand von Bunaken Island (links) angespült und bleibt bei Hochwasser in den Mangroven hängen (rechts). (B) In kürzester Zeit lassen sich schnorchelnd Unmengen an Plastik einsammeln (links, Foto: Stefanie Ries), die vor der Küste im Ozean schwimmen (rechts).

Schwamm drüber?

Schwämme als Bioindikatoren für Mikroplastikverschmutzung in Gewässern // Meeresverschmutzung durch Plastik und insbesondere durch Mikroplastik schreitet ungebremst fort. Mit unabsehbaren Folgen. Münchener Wissenschaftler verwenden nun Schwämme als Bioindikatoren, um Art und Menge der Verschmutzung mit Mikroplastik in Gewässern zu bestimmen.

*ADRIAN FUCHS; **, ***ELSA B. GIRARD; *DR. EVELYN PLOETZ; **, ****, *****PROF. DR. GERT WÖRHEIDE

Der technologische Fortschritt seit Mitte des letzten Jahrhunderts ist eng verknüpft mit der Vielseitigkeit von Kunststoffen, umgangssprachlich „Plastik". Das Material ist sehr haltbar, lässt sich gut verarbeiten und ist daher aus unserem Alltag nicht mehr wegzudenken. Doch gerade die lange Haltbarkeit wird inzwischen, in Verbindung mit unzureichenden Recycling-Bemühungen, zu einem ernsten Problem. Während in Europa fortschrittliche Systeme der Müllverwertung und Trennung bereits weitreichend etabliert sind, befindet sich die organisierte Müllentsorgung z. B. in weiten Teilen Südostasiens erst im Aufbau. Der täglich produzierte Müll wird – sofern er lokal organisiert eingesammelt wird – verbrannt oder vergraben. Meist landet er jedoch aus Unachtsamkeit in Straßengräben und Flüssen, von wo er unweigerlich ins Meer wandert und anschließend z. B. am Strand teilweise wieder angeschwemmt wird (s. Abb. 1). Schätzungen zufolge landen aktuell auf diese Weise bis zu zehn Prozent der weltweiten Kunststoffproduktion in den Weltmeeren [1]. Im Jahr 2015 entsprach dies einer Menge von rund acht Millionen Tonnen Plastikmüll [2].

Mikroplastikverseuchung der Weltmeere

Während grober Plastikmüll, wie Flaschen und Verpackungsmaterial, unter großem technischem Aufwand wieder eingesammelt werden könnte, droht eine zunehmende Gefahr durch so genanntes Mikroplastik, d. h. durch Partikel kleiner als 5 mm. Mikroplastik gelangt zum einen – als primäres Mikroplastik – direkt ins Wasser, beispielsweise in Form von Polyethylenpartikeln aus Kosmetika und Reinigungsmitteln, aus Oberflächenbeschichtungen oder Kunststoffwachsen, die als Trennmittel eingesetzt werden. Die zweite, weitaus größere Quelle ist allerdings sekundäres Mikroplastik,

*Ludwig-Maximilians-Universität München, Department für Chemie und CeNS, Physikalische Chemie I, 81377 München, Tel: +49 89 2180 77571
**Ludwig-Maximilians-Universität München, Department für Geo- und Umweltwissenschaften, Paläontologie & Geobiologie, 80333 München
***Derzeitige Adresse: Naturalis Biodiversity Center, 2333CR Leiden, Niederlande
****Ludwig-Maximilians-Universität München, GeoBio-Center, 80333 München
*****SNSB-Bayerische Staatssammlung für Paläontologie und Geologie, 80333 München

welches durch die schrittweise Zersetzung von groben Plastikteilen, z. B. durch Reifenabrieb, durch den Einfluss von Sonne (UV-Strahlung) oder mechanisch durch Wellenbewegung und Gezeiten entsteht. Unmengen an Kleinstpartikeln werden hierbei kontinuierlich weiter zermahlen und in unterschiedlichem Feinheitsgrad in die Umwelt freigesetzt. Da Mikroplastik kaum organisch degradiert, landen die Partikel zunehmend in der Nahrungskette, beginnend bei Plankton, bis hin zu Algen, Krebsen und Fischen [3], in denen sie sich anreichern. Zudem haften diesen Partikeln vermehrt toxische Moleküle wie Alkyl- und Biphenole an, welche beispielsweise zur Herstellung von Flaschenverschlüssen oder Innenbeschichtungen von Konserven genutzt werden. Neben deren hormonsteuernden Eigenschaften, wirken sie bereits in geringen Mengen krebserregend [4] und gelangen wiederum über die Nahrungskette unerkannt auf unserem Speiseteller.

Mikroplastik quantifizieren und entsorgen

Umfassende Studien zur tatsächlichen Häufigkeit von Mikroplastik im Meer fehlen weltweit, auch da sowohl Identifizierung als auch Quantifizierung technisch komplex sind. Herkömmliche Methoden sind aktuell nicht in der Lage, Partikel im sub-Mikrometer-Bereich zu extrahieren und zu analysieren. Da ein negativer Effekt von Mikroplastik auf die Gesundheit nicht auszuschließen ist, ist es essenziell, alsbald Methoden zu dessen Identifizierung und Kartographierung und nachfolgend zur Rückgewinnung zu entwickeln. Für die Weltmeere würde man zweierlei benötigen: Sedimentfilter zum Sammeln von Mikropartikeln und eine Möglichkeit, zwischen natürlichen und menschengemachten Partikeln zu unterscheiden. Nachdem Bau und Verteilung von Millionen von Sedimentfiltern in den Weltmeeren utopisch ist, gilt es, nach alternativen Optionen zu suchen: Könnte man Schwämme (s. Abb. 2) als biologische Filteranlagen einsetzen? Könnten diese über die Art und das Ausmaß der Mikroplastik-Verschmutzung lokal Auskunft geben?

Bild: LMU München

2 Verschiedene Arten von Schwämmen (Phylum Porifera) wachsen vor Bangka Island (Nord-Sulawesi, Indonesien), darunter auch eine nicht identifizierte Art der Familie Tethyidae (links) und eine *Ircinia* sp. (rechts).

Lebewesen als Indikatoren für Umweltverschmutzung

Spezialisierte Lebewesen wie Schildkröten, Wasservögel oder Fische werden oftmals als Anzeiger ökologischer Verschmutzung bzw. der Wasserqualität herangezogen [5]. Im Fall von Mikroplastik ist dieser Ansatz allerdings nur bedingt geeignet: Um das aufgenommene Mikroplastik zu untersuchen, müssten die Tiere sterben. Muscheln, beispielsweise Austern, wiederum, sind meist auf Riffe beschränkt [6], und ihre Nahrungsbevorzugung ist sehr spezialisiert.

Schwämme hingegen sind Allrounder und weltweit verbreitet, von der Tiefsee bis hin zu Flüssen und Seen [7]. Diese natürlichen Filtrierer zeichnen sich durch ihr Wasserkanalsystem aus, mit dem sie täglich, angetrieben von so genann-

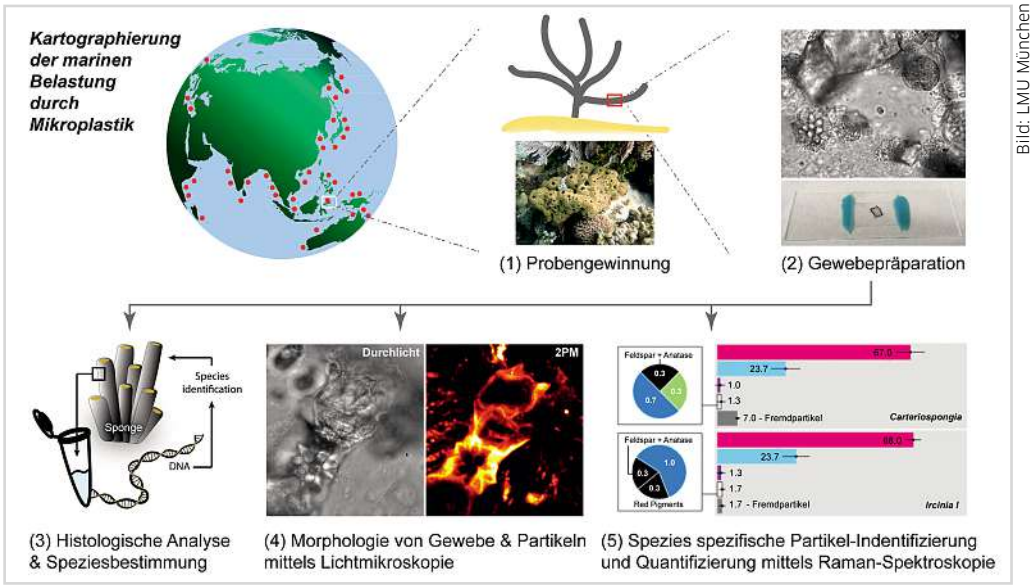

Bild: LMU München

3 Arbeitsschritte zur Bestimmung der lokalen Belastung durch Mikroplastik. Um die lokale Belastung zu bestimmen, werden Gewebeproben unterschiedlicher Schwammarten gesammelt (1) und anschließend im Labor aufbereitet (2). Zum einen wird eine Morphologie- und DNA-basierte Klassifizierung der Spezies, sowie histologische Untersuchung durchgeführt (3). Zum anderen werden die Gewebeproben bezüglich der aufgenommenen Anzahl und Größe der Partikel mittels Durchlicht- und Zweiphotonenmikroskopie (2PM) evaluiert (4). Im letzten Schritt werden Partikel vom Gewebe labortechnisch getrennt, mittels Raman-Spektroskopie bezüglich ihrer Zusammensetzung chemisch identifiziert, und anschließend statistisch in Größe und Zusammensetzung erfasst (5). Eine Kartographie könnte über eine weltweit angelegte Datenerfassung stattfinden.

ten Kragengeißelzellen (Choanozyten), ein Vielfaches ihres Körpervolumens an Umgebungswasser durch ihren Körper pumpen, um Nahrung (Kleinstpartikel wie Bakterien) aufzunehmen. Schwämme strudeln allerdings auch andere feinste Partikel, beispielsweise Sedimente, durch ihr Wasserkanalsystem und können solche bis zu einer Größe von 2 mm auch über ihre Außenseite aufnehmen. Dies geschieht bei einigen Schwämmen wohl auch zur strukturellen Stabilisation durch Einlagerung in Skelettfasern im Gewebe (Mesohyl). Zusätzlich zeichnen sich Schwämme durch eine hohe Lebensdauer sowie Resistenz gegen äußere Verletzungen aus, wie sie beispielsweise bei der Entnahme von Gewebeproben für die Analyse von Mikroplastik entstehen. Ihre Verbreitung und Artenvielfalt macht sie daher zum perfekten Indikator, um die örtlich aufkommenden Verschmutzungen durch Mikroplastik zu kartieren.

Bild: LMU München

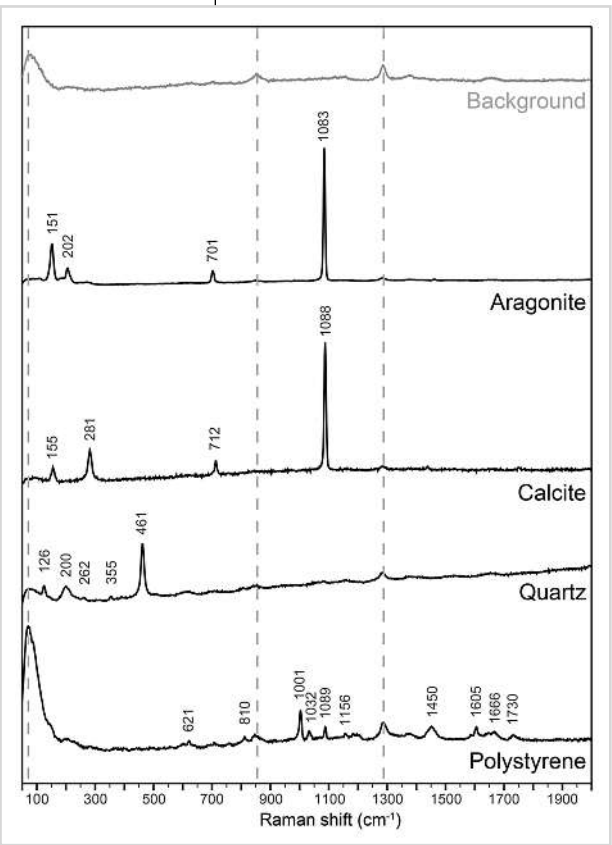

4 Raman-Spektren ausgewählter Partikel, die in Schwämmen aufgenommen wurden. Neben anorganischen Verbindungen wie Kalziumkarbonate (Kalzit, Aragonit) und Quarz, sind ebenso Plastikpartikel im Gewebe vorhanden.

Diese Eigenschaften haben sich nun Wissenschaftler der Universität München zu Nutze gemacht. Im Fachjournal Environmental Pollution berichten sie von einem empfindlichen und zuverlässigen Analyseverfahren, das aufgenommene Partikel in Schwämmen sowohl identifizieren, quantifizieren, als auch räumlich vermessen kann. Darüber hinaus konnten die Forschenden die Morphologie der in Gewebe eingebetteten Partikel erfolgreich determinieren [8]. Die Untersuchung wurde vor Nord-Sulawesi in Indonesien durchgeführt, in einem Gebiet, welches stark mit Plastikmüll im Meer belastet ist (s. Abb. 1).

Spezies-spezifische, lokale Mikroplastikanalyse

Um die aufgenommene Menge, die chemische Zusammensetzung der Partikel, und deren Morphologie sowie die primär aufnehmenden Spezies zu bestimmen, wurde ein fünfstufiges Verfahren entwickelt (s. Abb. 3). Zunächst wurden unterschiedliche Gewebeproben verschiedener Schwämme vor Ort im Korallenriff gesammelt. Diese Gewebeproben wurden anschließend untersucht, um Aufschluss über das Ausmaß der Mikroplastikverschmutzung zu erhalten sowie über die Spezies-spezifische ‚Vorliebe' für Kleinst-Plastikpartikel in Form und Zusammensetzung und deren Herkunft.

Im nächsten Schritt wurden die gesammelten Proben im Labor für die Analysen zur Artbestimmung (Morphologie, DNA Barcoding) vorbereitet, gefolgt von einer histologischen Präparation. Durchlichtmikroskopie sowie Zwei-Photonen-Mikroskopie wurden als neue Methoden zur Untersuchung von im Gewebe eingebetteten Partikeln, deren Form, Menge, Ausrichtung und Verteilung in verschiedenen Bereichen des Schwammes eingesetzt. Um die chemische Zusammensetzung und Häufigkeit von Mikroplastik und anderen anthropogenen Stoffen zu quantifizieren, wurde im letzten Schritt Raman-Spektroskopie verwendet [8, 9]. Raman-Spektroskopie kann Partikel ortsaufgelöst im Gewebe dokumentieren und deren chemische Zusammensetzung bestimmen. Um jedoch statistisch belastbare Zahlen über die Belastung der Schwämme mit Mikropartikeln zu erhalten, wurden definierte Mengen des Gewebes organisch aufgelöst, und die freigesetzten Partikel auf einer zweidimensionalen, anorganischen Filter-Matrix gesammelt. Nach schnellem Scan der Partikel-Position, wurde im letzten Schritt die Raman-Signatur, d. h. der chemische Fingerabdruck der einzelnen Partikel aufgenommen, identifiziert, klassifiziert und nach Häufigkeit pro Spezies aufgetragen.

Schwämme als marine Bioindikatoren

Um die Eignung von Schwämmen als marine Mikroplastik-Bioindikatoren zu testen, wurden Proben von 15 Schwämmen aus Korallenriffen vor Nord-Sulawesi (Indonesien) gesammelt, da dort das Problem der Verschmutzung durch Plastik besonders prominent ist [10]. Für die histologischen Untersuchungen wurden 15 Proben aus fünf verschiedenen Schwamm-Arten analysiert. Von jeder dieser Spezies wurden von drei Exemplaren unter Wasser im Korallenriff nicht-letale Proben entnommen und im Feld-Labor an Land für die weitere Analyse präpariert. Die beprobten Bereiche der Schwämme waren maximal bis zu 8 cm^3 groß und werden schnell vom Organismus regeneriert. Um die Partikelzusammensetzung in der Umgebung der Probestellen mit den späteren Ergebnissen der Partikelanalyse vergleichen zu können, wurde zusätzlich Sand des angrenzenden Strandes mit demselben Verfahren analysiert.

Ein Teil jeder entnommenen Gewebeprobe wurde direkt nach der Entnahme für das DNA Barcoding in 96 % Ethanol, ein weiterer Teil in 4 % Formaldehyd fixiert. Nach 24 Stunden Fixierung wurden die Formaldehyd-fixierten Proben gewebeschonend mit reinem Ethanol dehydriert. Ein Teil jeder Probe wurde dann im Labor in München für die bildgebende Analyse abgezweigt, während das restliche Gewebe mehrere Tage mit Bleiche behandelt wurde. Diese löste das Zellgewebe auf, sodass die eingelagerten Partikel freigelegt wurden. Ein Partikelfilter isolierte alle Teilchen grö-

ßer 1 µm für die Identifizierung mittels Raman-Spektroskopie. Das Gewebe für die 3D-Analyse wurde u. a. in 170 µm dünne Scheiben unterteilt und mit einem Fixierungsagenten auf Plastikbasis auf einen Objektträger aufgebracht.

Die 3D-Analyse der präparierten Gewebeschnitte wurde auf einem modifizierten Konfokalmikroskop durchgeführt. Die Anregung der Autofluoreszenz über Zwei-Photonen-Absorption erfolgte mit einem gepulsten Infrarotlaser. Organisches Gewebe gibt nach Anregung mit einem starken Infrarot-Laser Autofluoreszenz ab, während anorganische Mikropartikel als Negativ erscheinen. Die hohe axiale Auflösung zeigt klar, dass in allen Bereichen der beprobten Schwämme kleinere Partikel eingelagert sind. Es wurden ausgewählte Bereiche von 190 µm Breite und Länge und 18 µm Dicke untersucht. Die partikelbasierte Aufnahme der Raman-Spektren erfolgte zudem an einem kommerziellen Raman-Spektrometer. Die Aufnahmen deckten den spektralen Fingerprintbereich der potenziell organischen Proben zwischen 50 und 2.000 cm^{-1} ab. Die aufgenommenen Raman-Signaturen erlauben hierbei die chemische Identifizierung kleiner Partikel mit hoher räumlicher Auflösung ohne zusätzliche Markierungstechniken. Da anorganische Partikel im Allgemeinen und Mikroplastik im Besonderen als starke Raman-Streuer bekannt sind, eignet sich diese Spektroskopie-Methode zur Identifizierung der eingelagerten Materialien besonders gut.

Zunächst wurde die Aufnahme der Teilchen in Choanozytenkammern und Fasern sowie das Mesohyl mittels Zwei-Photonen-Mikroskopie untersucht (s. Abb. 5). In allen Bereichen wurde eine hohe Anzahl an anorganischen Partikeln nachgewiesen, umschlossen von organischem Gewebe. Die Schwämme nutzen diese v. a. zur Erhöhung ihrer strukturellen Stabilität, weshalb im Spongin-Skelett der beprobten Arten und dem Ektosom (äußerster Gewebebereich des Schwamms) eine hohe Teilchendichte beobachtet wurde. Interessanterweise wurden Partikel zwar rund um, aber nicht im Inneren von Choanozytenkammern lokalisiert. Dies ist insofern verwunderlich, als dass Schwämme in diesen Kammern vorwiegend Mikroplankton aus dem Meerwasser ausfiltern, gleiches wurde auch für anorganische Partikel erwartet. Wie und ob Schwämme zwischen organischer Nahrung und anderen Partikeln unterscheiden können, ist noch nicht abschließend geklärt. Die von den Autoren dieses Beitrags beobachtete hohe Häufung anorganischer Partikel außerhalb und ihre Abwesenheit innerhalb der Choanozytenkammern würde allerdings für eine Selektierung sprechen.

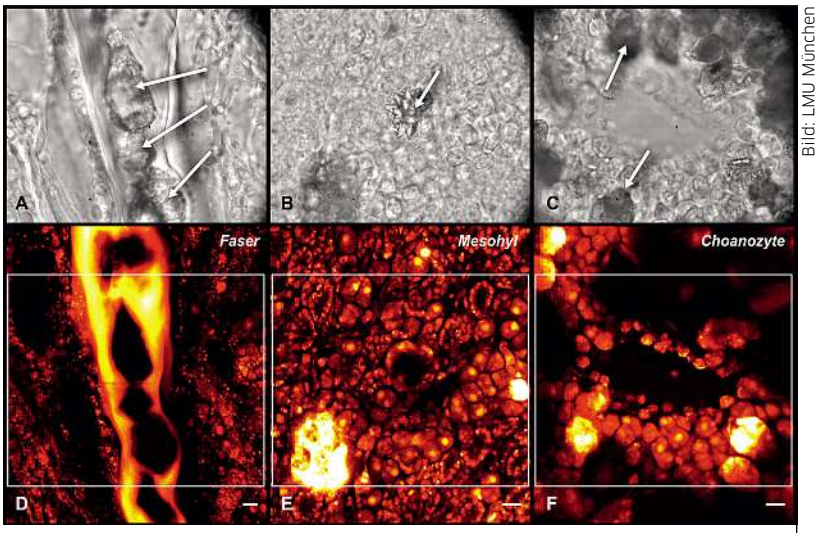

Bild: LMU München

5 Partikel sind im Gewebe eingeschlossen. Mittels Durchlicht- (oben) und Zwei-Photonen-Mikroskopie (unten) konnte nachgewiesen werden, dass Partikel unterschiedlicher Größen in allen Bereichen der Schwämme eingelagert und vom dortigen Gewebe komplett eingeschlossen wurden. (A+D) Spongin-Faser, (B+E) Mesohyl und (C+F) Choanozyten. Skalierung: 10 µm.

Markierungsfreie Identifizierung der Partikel

Um die eingelagerten Partikel zu identifizieren, wurden 1.686 Teilchen aus allen 15 Proben mittels Raman-Spektroskopie untersucht (s. Abb. 4). Dabei konnten 34 verschiedene Partikelarten identifiziert werden, größtenteils Kalziumkarbonate und Quarz, welche den Hauptbestandteil des Sediments in den Riffen um Bangka Island ausmachen. Zudem fanden sich Polystyrol und Farbpigmente – eindeutige Zeugen für die menschengemachte Verschmutzung des Meeres. Ausgehend von einer linearen Extrapolation der gefundenen Belastung durch Polystyrol-basierte Mikropartikel ist dabei eine Belastung von mindestens 10.000 Plastikteilchen pro 100 g trockenem Schwammgewebe zu erwarten. Zudem konnten keine signifikanten Unterschiede in der Zusammensetzung der eingelagerten Partikel gefunden werden, weder zwischen den untersuchten Spezies noch zur Sandzusammensetzung. Dies legt nahe, dass Schwämme (größtenteils unabhängig von ihrer Spezies) Mikropartikel unspezifisch in ihr Gewebe einlagern, was ihre Eigenschaft als ideale Partikelfilter verdeutlicht.

Kartographierung der Mikroplastikverschmutzung

Was Verbreitung und Auswirkung von Mikroplastik betrifft, gibt es noch viele unbeantwortete Fragen, aber die neuesten Ergebnisse legen nahe, dass die Untersuchung von Schwämmen als Bioindikatoren für die Belastung verschiedener Meeresregionen, aber auch von Flüssen und Seen, mit Mikroplastik geeignet sein könnte. Schwämme erlauben somit, mit geringem Aufwand eine zukünftige Kartierung der Mikroplastik-Belastung von Gewässern weltweit vorzunehmen. Diese Daten wären dann die essenzielle Grundlage, um nachhaltige, regionale und lokale Strategien für die Vermeidung von Plastikeintrag in aquatische Systeme zu entwickeln. ■

LP Tipp+

mehr zum Thema:

- Mehr zu diesem Thema sowie die **Literaturstellen** zum Beitrag finden Sie unter dem Stichwort „Mikroplastik“ auf www.laborpraxis.de.
- Die Jahrestagung der Wasserchemischen Gesellschaft **Wasser 2021** wird vom 10. bis 12. Mai 2021 online abgehalten (weitere Infos unter www.wasserchemische-gesellschaft.de).

A.5. Spatio-selective activation of nuclear translocation of YAP with light directs invasion of cancer cell spheroids.

iScience

CellPress
OPEN ACCESS

Article

Spatio-selective activation of nuclear translocation of YAP with light directs invasion of cancer cell spheroids

Bernhard Illes,[1] Adrian Fuchs,[1] Florian Gegenfurtner,[2] Evelyn Ploetz,[1] Stefan Zahler,[2] Angelika M. Vollmar,[2] and Hanna Engelke[1,3,4,*]

SUMMARY

The mechanical properties of the extracellular matrix strongly influence tumor progression and invasion. Yes-associated protein (YAP) has been shown to be a key regulator of this process translating mechanical cues from the extracellular matrix into intracellular signals. Despite its apparent role in tumor progression and metastasis, it is not clear yet, whether YAP activation can actively trigger the onset of invasion. To address this question, we designed a photo-activatable YAP (optoYAP), which allows for spatiotemporal control of its activation. The activation mechanism of optoYAP is based on optically triggered nuclear translocation of the protein. Activation of optoYAP induces downstream signaling for several hours and leads to increased proliferation in two- and three-dimensional cultures. Applied to cancer spheroids, optoYAP activation induces invasion. Site-selective activation of optoYAP in cancer spheroids strikingly directs invasion into the activated direction. Thus, nuclear translocation of YAP may be enough to trigger the onset of invasion.

INTRODUCTION

Yes-associated protein (YAP) is a key regulator of mechanosignaling. It translates mechanical cues from the extracellular matrix into intracellular signals (Dupont et al., 2011). This process is mediated via its localization within the cell: YAP is cytoplasmic on soft substrates and translocates into the nucleus upon sensing mechanical forces, e.g., by a stiff substrate (Dupont et al., 2011; Elosegui-Artola et al., 2017). In the nucleus, it activates downstream signaling. High nuclear YAP has been shown to be associated with invasion and altered matrix properties in tumors (Zanconato et al., 2016; Lin et al., 2015). However, due to lack of control over its translocation, it is not clear whether nuclear YAP is sufficient to induce invasion or whether it is rather just associated with invasion. YAP is able to induce symmetry breaks in cell collectives (Serra et al., 2019). We therefore hypothesized that it may be responsible for triggering the symmetry break, which is essential for the occurrence of invasive buds of a tumor and, subsequently, invasion. For a test of this hypothesis, we needed a local activation of YAP to ensure a sufficiently asymmetrical cue that induces the symmetry break. To obtain the necessary spatiotemporal control of YAP's translocation into the nucleus, we developed an optical control of YAP's nuclear translocation (Valon et al., 2017).

RESULTS

Photoactivation of YAP

In the cell, localization of YAP is regulated by several different processes, and the exact regulation principles are not entirely known yet (Pocaterra et al., 2020). To keep the interference with other signaling processes low and maximize the amount of control, we prepend a small (20 amino acids) photo-controlled nuclear localization signal (optoNLS) (Engelke et al., 2014), which we developed earlier, to YAP resulting in a photo-activatable YAP (optoYAP). The optoNLS is based on genetic insertion of a photocaged lysine (Gautier et al., 2010) (Fig. S1, S2) into a nuclear localization signal, which blocks nuclear import entirely (Engelke et al., 2014). Uncaging the lysine with light yields the functional signal and restores nuclear import. The small size of optoNLS and caging group minimizes their impact on protein function. To visualize protein localization and block nuclear import via diffusion by an increase in size, we use a YAP fused to two enhanced green fluorescent proteins (eGFPs). To

[1]Department of Chemistry and Center for NanoScience (CeNS), Ludwig-Maximilians-Universität München, Butenandtstraße 11, 81377 Munich, Germany

[2]Department of Pharmacy, Ludwig-Maximilians-Universität München, Butenandtstraße 5, 81377 Munich, Germany

[3]Institute of Pharmaceutical Sciences, Department of Pharmaceutical Chemistry, University of Graz, Humboldtstr. 46, 8010 Graz, Austria

[4]Lead contact

*Correspondence: hanna.engelke@uni-graz.at

https://doi.org/10.1016/j.isci.2021.102185

This is an open access article under the CC BY license (http://creativecommons.org/licenses/by/4.0/).

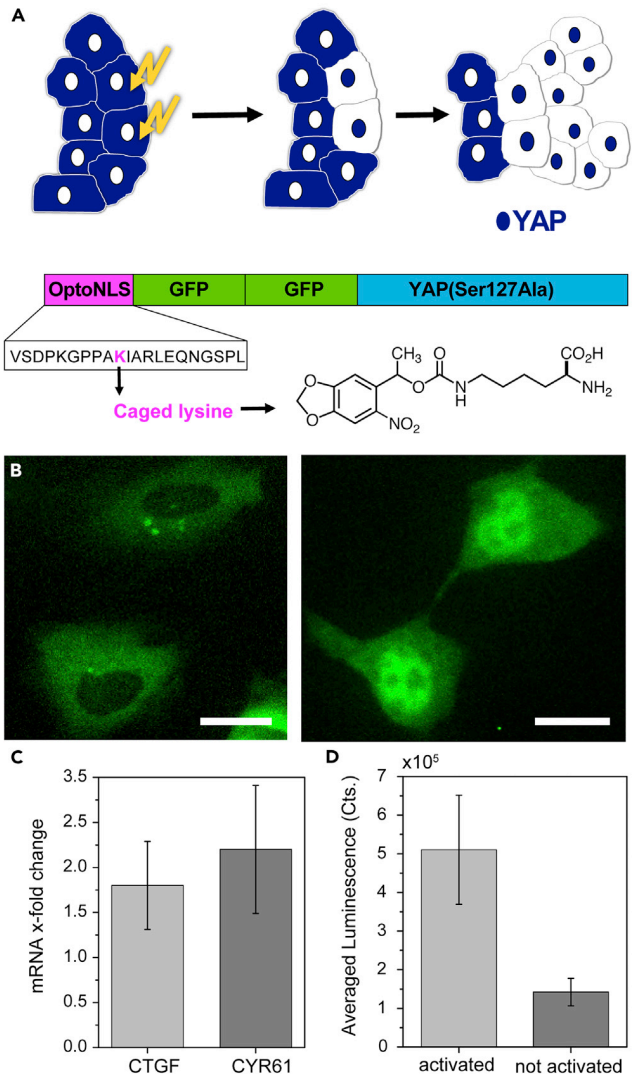

Figure 1. Photoactivation of YAP

(A) Schematics of optoYAP. OptoYAP is composed of the optoNLS with a caged lysine and two GFP prepended to YAP Ser127Ala. The optoNLS is activated by uncaging the lysine with light leading to nuclear localization of optoYAP followed by enhanced proliferation in the photo-activated area.

(B) HeLa cells transfected with optoYAP show YAP localization in the cytosol before activation. Approximately 30 min after photoactivation, optoYAP is localized in the nucleus. Scale bar = 30 μm.

(C) qPCR shows an increase in RNA levels of YAP downstream proteins CTGF and CYR61 (with GAPDH as gatekeeper).

(D) Yap functionality assay based on a TEAD luciferase reporter shows four times higher activity in activated samples compared to controls, which were not activated, confirming increased YAP activity. Data in (C) and (D) are represented as mean +/− standard deviation.

See also related Figures S1–S7

improve YAP detection we used a stabilized form of YAP, S127A that does not affect YAP regulation by mechanical signals (Figure 1A).

Figure 1B shows images of optoYAP-transfected cells. YAP was kept cytosolic either by serum depletion or mechanically by keeping the cells on a soft matrigel substrate. Before illumination, the entire optoYAP signal is cytosolic. Less than an hour after photoactivation, most of the optoYAP signal is located in the nucleus. This successful photo-activated translocation occurred independently of whether serum depletion or matrigel was used to prime cytosolic YAP with natural signaling. After successful nuclear translocation, functionality tests were

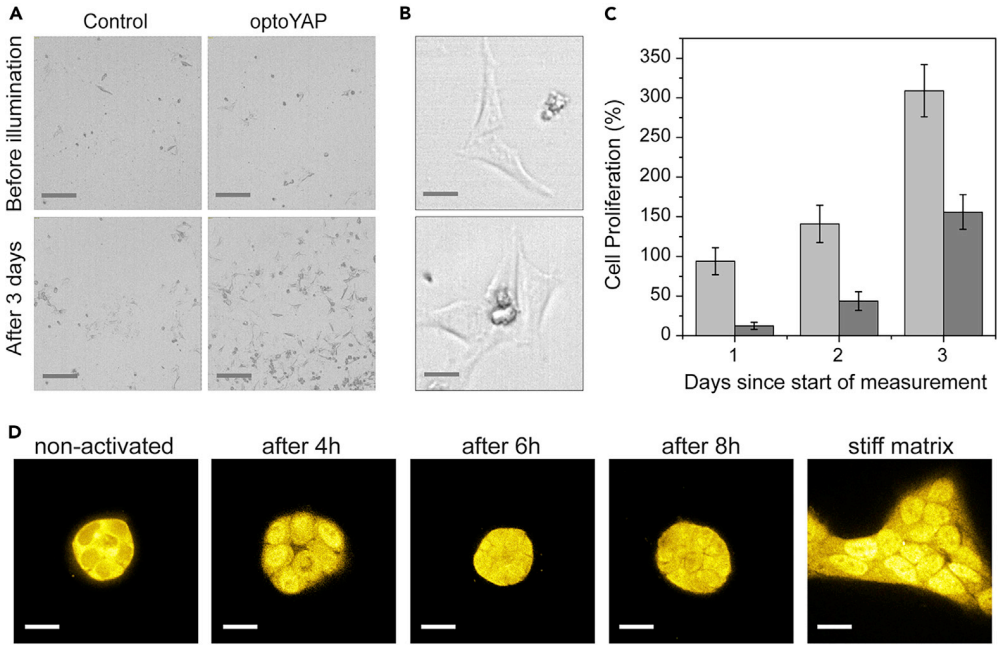

Figure 2. Proliferation and localization after optoYAP activation

(A) Proliferation of cells with optoYAP in FBS-depleted medium is strongly enhanced by photoactivation of optoYAP compared to controls without optoYAP. Scale bar: 200 μm.

(B) Higher magnification images of cells in FBS-depleted medium show no changes in morphology after photoactivation. Scale bar: 20 μm.

(C) Quantitative analysis of proliferation reveals a strong increase in the growth rate of photo-activated cells (light gray) compared to controls without optoYAP (dark gray) during the first day. This difference is amplified in the following days albeit at similar growth rates compared to the control. Note that growth rates on day 1 with activated optoYAP reach levels as known for proliferation under commonly used cell culture conditions (stiff substrate, medium supplemented with serum), which generally exhibit activated YAP. Data are represented as mean +/− standard deviation.

(D) Antibody staining of optoYAP transfected HeLa cells on matrigel before and after photoactivation. YAP is mainly cytosolic before activation; 4 h after activation it is located mainly in the nucleus, and at later time points, it returns to mainly cytosolic localization. For comparison, the nuclear localization of YAP in cells on a stiff matrix is shown. Scale bar: 20 μm.

See also related Figures S7–S12

performed to show that optoYAP is fully functional and able to activate downstream signaling in the nucleus. quantitative PCR (qPCR) of CCN1 (CYR61) and CCN2 (CTGF)—proteins, which are upregulated downstream of YAP activation (Totaro et al., 2018)—reveals an enhanced signal compared to controls after photoactivation of YAP on an RNA level (Figure 1C). On a protein level, a luciferase reporter (Dupont et al., 2011) responsive to YAP signaling clearly showed enhanced expression (Figures 1D and S3) upon photoactivation of optoYAP revealing functional YAP-responsive signaling. Kinetics of YAP translocation as well as kinetics and size of downstream effects upon mechanical or chemical stimulation varies strongly depending on cell type, stimulation method, ratio of nuclear to cytosolic YAP before stimulation, and many other factors (Elosegui-Artola et al., 2017; Yu et al., 2012; Gegenfurtner et al., 2018). Kinetics of optoYAP translocation (Figures S4 and S5) and downstream effects (Figures 1C, 1D, and S3) are in the same range as measured for other stimuli (Yu et al., 2012). The absence of permanent DNA damage due to the illumination was also confirmed (Figures S6 and S7).

Proliferation after optoYAP activation

Having thus established a functional, photo-activatable YAP, we next studied the influence of YAP activation on HeLa cells cultured on two-dimensional substrates (Figures 2A and S8). Inactivation of YAP via serum depletion on plastic substrates did not change cell morphology. Accordingly, photoactivation of optoYAP did not lead to changes in cell morphology either (Figure 2B). However, proliferation was significantly increased: while the number of control cells without YAP activation increased after 24 h by 12.5% only, the number of cells after photoactivation of optoYAP was enhanced much stronger by 94% (Figure 2C). Note that cells with photo-activated YAP reach proliferation levels known for standard culture conditions

on a plastic substrate in a medium supplemented with serum, which induce active YAP. Cells with inactivated YAP proliferate much slower. Mechanical inactivation of YAP via growth on a soft matrigel substrate leads to a round cell morphology. Upon photoactivation of YAP, interestingly, cells did not change morphology to the stretched shape found on stiff substrates (Figure S9). However, similarly to serum-depleted, activated cells, they showed increased proliferation compared to controls resulting in enhanced growth of cell spheroids on the matrigel (Figure S10). Thus, the different cell morphologies on stiff and soft substrates, respectively, do not stem from the difference in YAP activation. The results rather suggest them to be a direct consequence of mechanical forces or other signaling pathways.

Kinetics of YAP localization and downstream signaling

To further understand the effect of the photo-activated YAP on cells, we investigated the time course of proliferation. Figure 2C already suggests the strongest effect of YAP to happen during the first day, which is then amplified by the exponential growth. A logarithmic plot and analysis (Figure S11) confirm that the growth rate of activated cells is enhanced during the first day and returns to non-activated levels on day 2 and thereafter. On a molecular level, we find an increased amount of nuclear YAP after activation. While nuclear YAP can be clearly seen 4 h after activation, the amount of nuclear YAP is decreased after 6 h (Figures 2D and S12). Finally-8 h after activation it is almost back to cytosolic localization as in the non-activated state. A time course of the luciferase reporter assay also shows an increase in downstream signaling reaching a maximum around 4-6 h after illumination and decreasing afterward (Figure S3A). The time evolution of YAP's localization and downstream luciferase expression combined with the fact that proliferation is enhanced for one day suggests that activation of YAP as performed with our photoactivation induces a boost in downstream events, which lasts for several hours and vanishes over the course of a day.

YAP triggers directed growth in spheroids

Next, we investigated the effect of YAP activation on cell spheroids. To this end, spheroids were grown and embedded in collagen gels. In this three-dimensional model system, we also observed an increase in proliferation upon photoactivation of optoYAP in entire spheroids as shown in Figure 3A. Quantitative analysis (Figure 3B) reveals an increase in spheroid size by a factor of almost 4 (measured as the area of the z-projection including all connected invasive buds) over the course of three days after photoactivation of optoYAP, whereas controls hardly grew at all. Next to the enhanced size, YAP-activated spheroids also underwent morphological changes. YAP activation leads to an increased number of invading buds and network-like structures of invading cells as depicted in Figure 3A. These results already strongly suggest that activation of YAP can induce invasion.

Finally, we made use of the spatiotemporal control provided by the photoactivation. We used the spheroids in collagen gels and restricted optoYAP activation locally to a selected area of the spheroid. While non-activated controls grew symmetrically into all directions, strikingly, spatially selective activation of optoYAP was followed by invasion on the activated sites. Figure 3C shows the spherical non-illuminated spheroids and the invasive mass in the illuminated areas of photo-activated spheroids. Thus, local activation of YAP can induce a symmetry break and trigger invasion. Further microscopy studies of protein localization within the spheroids after photoactivation show the activated YAP 4 h after illumination (Figure 3D and see also Figure S13 for 3 days after illumination).

DISCUSSION

In conclusion, photoactivation of optoYAP in spheroids confirmed the hypothesis that YAP translocation into the nucleus is able to trigger invasion from the spheroids into the surrounding matrix. The results thus suggest YAP to be an important regulator of the onset of invasion. The developed optoYAP may also prove to be a useful tool for future investigations of the role of YAP in organ development, contact inhibition, and other processes in development and disease (Low et al., 2014).

Limitations of the study

As a tool, optoYAP is limited to irreversible activation due to the underlying photocleavage-based mechanism. Upon brief and non-toxic photoactivation (less than 1 min), it acts as "on-switch" of a functional YAP triggering downstream signaling for several hours with spatial control as provided by the light beam used for photoactivation. The temporal control is on the order of hours (30 min until full import, 8 h until recovery to mainly cytosolic YAP), which is not as fast as triggering YAP activation by applying force directly to the nucleus (Elosegui-Artola

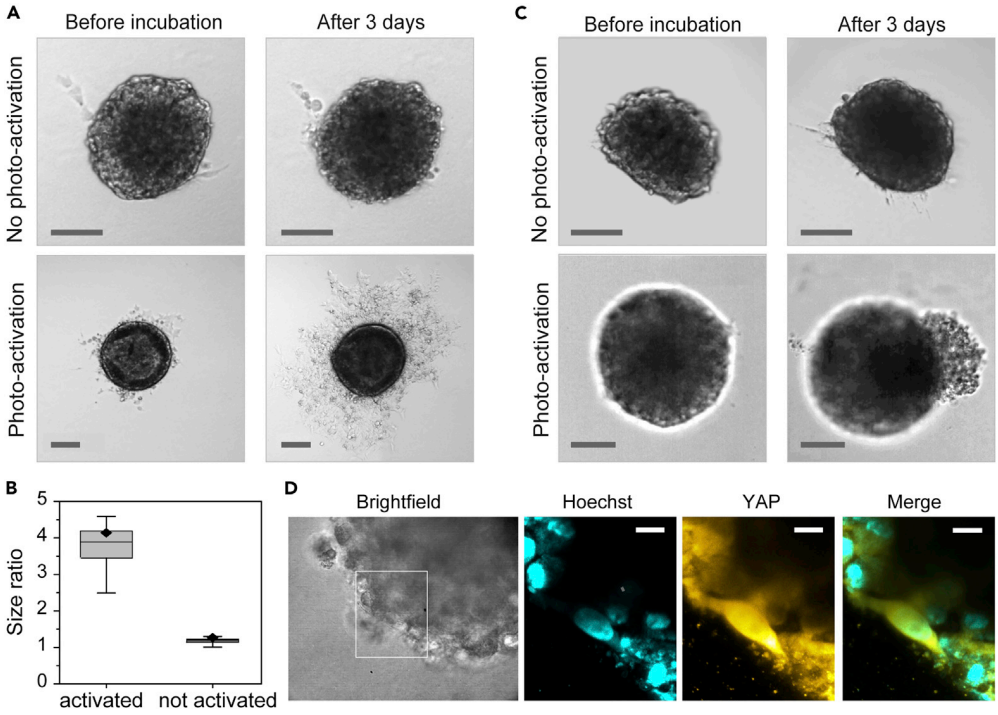

Figure 3. YAP triggers directed growth in spheroids

(A) HeLa spheroids in collagen gels transfected with optoYAP three days after photoactivation show increased invasion leading to a larger size of the spheroid compared to non-activated controls, which barely invade at all. Scale bars: 100 μm.

(B) Quantification of the average spheroid size change over three days. Activated samples (light gray) show a fourfold increase in their size (measured as area of the central plane) over three days while non-activated samples (dark gray) grew only by a factor of 1.2.

(C) Spatio-selective photoactivation of spheroids with optoYAP in collagen gels on the right side of the spheroid induces directed invasion on that side, while controls, which were not photo-activated, do not show directed growth. Scale bars: 100 μm.

(D) High resolution and fluorescence imaging of activated YAP in a cell in a spheroid. Scale bars: 5 μm.

See also related Figures S13–S15.

et al., 2017), but fast enough given the timescales of downstream events and the timescales of processes in development and diseases such as the described invasion. The optoYAP construct is still sensitive to other physiological stimuli. Thus, the efficiency of photoactivation strongly depends on depletion of nuclear YAP via physiological stimuli, such as substrate stiffness or serum depletion, prior to photoactivation. On a stiff substrate in presence of serum, optoYAP will be nuclear prior to photoactivation, and thus, photoactivation will have no significant effect. Upon successful depletion of nuclear YAP prior to activation, however, it can trigger efficient changes in downstream signaling as shown above. Successful depletion and subsequent photoactivation can be monitored by fluorescence of the GFP fused to optoYAP. Although our results are limited to cell culture—specifically HeLa and A431 cells (Figures 3, S14, and S15)—the underlying method of genetic insertion of an artificial amino acid has been applied to zebrafish (Liu et al., 2017) and mice (Ernst et al., 2016). Hence, in principle, the tool should be applicable to investigations in animals as well.

Resource availability

Lead contact

Further information and requests for resources and reagents should be directed to and will be fulfilled by the lead contact, Hanna Engelke (hanna.engelke@uni-graz.at).

Material availability

All unique reagents (optoYAP plasmid) generated in this study are available from the lead contact.

Data and code availability

Data and codes that support the findings of this study are available from the authors upon reasonable request.

METHODS

All methods can be found in the accompanying Transparent methods supplemental file.

SUPPLEMENTAL INFORMATION

Supplemental information can be found online at https://doi.org/10.1016/j.isci.2021.102185.

ACKNOWLEDGMENTS

We thank Valerie M. Weaver for helpful discussions and Jana Peliskova for experimental support. This study was funded by the Deutsche Forschungsgemeinschaft (Project ID 201269156 – SFB 1032, project B08 and B11, the excellence cluster NanoInitiative Munich and project PL 696/4-1) and by the Fritz Thyssen Stiftung.

AUTHOR CONTRIBUTIONS

B.I. and H.E. conceived and designed the study; B.I. performed experiments; A.F. and E.P. performed high-resolution microscopy of spheroids; F.G. performed DNA damage experiment and provided support with functionality assays; S.Z. and A.M.V. helped to design the experiments and provided support with functionality assays; H.E. supervised the study. All authors contributed to writing the manuscript.

DECLARATION OF INTERESTS

The authors declare no competing interests.

Received: October 28, 2020
Revised: January 14, 2021
Accepted: February 9, 2021
Published: March 19, 2021

REFERENCES

Dupont, S., Morsut, L., Aragona, M., Enzo, E., Giulitti, S., Cordenonsi, M., Zanconato, F., Le Digabel, J., Forcato, M., Bicciato, S., et al. (2011). Role of YAP/TAZ in mechanotransduction. Nature *474*, 179–183.

Elosegui-Artola, A., Andreu, I., Beedle, A., Lezamiz, A., Uroz, M., Kosmalska, A., Oria, R., Kechagia, J., Rico-Lastres, P., Le Roux, A., et al. (2017). Force triggers YAP nuclear entry by regulating transport across nuclear pores. Cell *171*, 1397–1410.e14.

Engelke, H., Chou, C., Uprety, R., Jess, P., and Deiters, A. (2014). Control of protein function through optochemical translocation. ACS Synth. Biol. *3*, 731–736.

Ernst, R., Krogager, T., Maywood, E., Zanchi, R., Beránek, V., Elliott, T., Barry, N., Hastings, M., and Chin, J. (2016). Genetic code expansion in the mouse brain. Nat. Chem. Biol. *12*, 776–778.

Gautier, A., Nguyen, D., Lusic, H., An, W., Deiters, A., and Chin, J. (2010). Genetically encoded photocontrol of protein localization in mammalian cells. J. Am. Chem. Soc. *132*, 4086–4088.

Gegenfurtner, F., Jahn, B., Wagner, H., Ziegenhain, C., Enard, W., Geistlinger, L., Rädler, J., Vollmar, A., and Zahler, S. (2018). Micropatterning as a tool to identify regulatory triggers and kinetics of actin-mediated endothelial mechanosensing. J. Cell Sci. *131*, jcs212886.

Lin, C., Pelissier, F., Zhang, H., Lakins, J., Weaver, V., Park, C., and LaBarge, M. (2015). Microenvironment rigidity modulates responses to the HER2 receptor tyrosine kinase inhibitor lapatinib via YAP and TAZ transcription factors. Mol. Biol. Cell *26*, 3946–3953.

Liu, J., Hemphill, J., Samanta, S., Tsang, M., and Deiters, A. (2017). Genetic code expansion in zebrafish embryos and its application to optical control of cell signaling. J. Am. Chem. Soc. *139*, 9100–9103.

Low, B., Pan, C., Shivashankar, G., Bershadsky, A., Sudol, M., and Sheetz, M. (2014). YAP/TAZ as mechanosensors and mechanotransducers in regulating organ size and tumor growth. FEBS Lett. *588*, 2663–2670.

Pocaterra, A., Romani, P., and Dupont, S. (2020). YAP/TAZ functions and their regulation at a glance. J. Cell Sci. *133*, jcs230425.

Serra, D., Mayr, U., Boni, A., Lukonin, I., Rempfler, M., Challet Meylan, L., Stadler, M., Strnad, P., Papasaikas, P., Vischi, D., et al. (2019). Self-organization and symmetry breaking in intestinal organoid development. Nature *569*, 66–72.

Totaro, A., Panciera, T., and Piccolo, S. (2018). YAP/TAZ upstream signals and downstream responses. Nat. Cell Biol. *20*, 888–899.

Valon, L., Marín-Llauradó, A., Wyatt, T., Charras, G., and Trepat, X. (2017). Optogenetic control of cellular forces and mechanotransduction. Nat. Commun. *8*, 14396.

Yu, F., Zhao, B., Panupinthu, N., Jewell, J., Lian, I., Wang, L., Zhao, J., Yuan, H., Tumaneng, K., Li, H., et al. (2012). Regulation of the Hippo-YAP pathway by G-protein coupled receptor signaling. Cell *150*, 780–791.

Zanconato, F., Cordenonsi, M., and Piccolo, S. (2016). YAP/TAZ at the roots of cancer. Cancer Cell *29*, 783–803.

iScience, Volume *24*

Supplemental information

Spatio-selective activation of nuclear translocation of YAP with light directs invasion of cancer cell spheroids

Bernhard Illes, Adrian Fuchs, Florian Gegenfurtner, Evelyn Ploetz, Stefan Zahler, Angelika M. Vollmar, and Hanna Engelke

Transparent Methods

1. Plasmid construction of optoYAP

1.1 PCR

Plasmids for optoYAP and optoYAP(Ser127Ala) were obtained as follows: GFP was subcloned into a GFP-hYAP1 plasmid on a pEGFP backbone to yield a 2xGFP-YAP fusion. Subsequently, the optoNLS from the optoNLS-TEV plasmid (Engelke et al., 2014) was prepended. Finally, the mutation Ser127Ala was introduced using the QuikChange kit (Agilent). All cloning steps except for the mutation were performed using standard protocols of the sequence and ligation independent cloning method (SLIC), which has been introduced by Li et al. (Li et al., 2007; Li et al., 2012). QuikChange was performed according to the manufacturer's manual.

The PAG plasmid for the insertion of the photocaged lysine was a gift from the Deiters lab (Engelke et al., 2014).

Primers for Cloning:
2xGFP-YAP:
Insert Forward ACAGGATCCCCGCATCTAGGCGCCGGCCGGATCCT
Vector Reverse: CCGGCCGGCGCCTAGATGCGGGGATCCTGTACAAT
Vector Forward: GCCAACCTGCCGGCCATGGATCCCGGGCAGCAGCC
Insert Reverse CTGCCCGGGATCCATGGCCGGCAGGTTGGCAGCGC

optoYAP:
Insert Reverse: GCCCTTGCTCACCATGCCACGGCTCTTGGTATATA
Vector Forward: ACCAAGAGCCGTGGCATGGTGAGCAAGGGCGAGGA
Insert Forward: CTACCGGTCGCCACCCCGGTCGCCACCATGGTGAG
Vector Reverse: CATGGTGGCGACCGGGGTGGCGACCGGTAGCGCTA

Primer for QuikChange to optoYAP(S127A):
Forward: TCGAGCTCATgCCTCTCCAGC
Reverse: ACATGCTGTGGAGTCAGG

1.2 OptoYAP Sequencing

Plasmid sequencing was performed by *Eurofins Genomics*.
Primers were ordered from *Metabion.*

Mutation Sequencing Primer:
GCTCTTCAACGCCGTCATGAAC

2. Synthesis and characterization of the caged Lysine

Synthesis of the caged lysine was performed as described in Gautier et al., 2010: 1-(6-Nitrobenzo[d][1,3]dioxol-5-yl)ethanol (500 mg, 2.36 mmol) and Na_2CO_3 (247 mg, 2.36 mmol) were added to THF (5 mL) and cooled to 0 °C under stirring. Next, triphosgene (701 mg, 2.36 mmol) was added to the suspension and the reaction was kept stirring overnight at RT. The reaction was centrifuged to remove Na_2CO_3 and the liquids were subsequently evaporated without heating. The residue was dried under vacuum, to yield a greyish solid (644 mg, 2.36 mmol). NMR confirms the successful synthesis of 1-(6-nitrobenzo[d][1,3]dioxol-5-yl)ethyl carbonochloridate (Fig. S1).

*N*ε-Boc-lysine (500 mg, 2.02 mmol) was dissolved in THF/1 M NaOH (aq.) (1:4 mixture, 8 mL total) under stirring and the solution was cooled to 0 °C. Next 1-(6-nitrobenzo[d][1,3]dioxol-5-yl)ethyl carbonochloridate (496 mg, 1.82 mmol) was added and the reaction was stirred overnight, at RT. The aqueous layer was washed with Et_2O (5 mL) and subsequently acidified with ice-cold 1 M HCl (20 mL) to pH 1 and then extracted with EtOAc (30 mL). The organic layer was dried over Na_2SO_4, filtered, and the volatiles were evaporated, leaving a yellow foam. The yellow foam was dissolved in DCM:TFA (1:1 mixture, 14 mL total) and the reaction was allowed to stir for 40 min. The volatiles were subsequently evaporated and the residue was redissolved in MeOH (5 mL) and precipitated into Et_2O (250 mL), yielding a white solid (679 mg, 1.42 mmol). NMR confirmed the successful synthesis of (2*S*)-2-(*tert*-Butoxycarbonylamino)-6-[1-(6-nitrobenzo[d][1,3]dioxol-5-yl)ethoxy]carbonylaminohexanoic acid which will be called caged lysine from now on (Fig. S2). For use on cells 100 mg of the caged lysine were dissolved in 1 mL H_2O and filtered with a 0.2 µm syringe filter to avoid contamination.

3. Cell Culture and optoYAP Functionality Assays

All cell experiments were prepared in a *Hera-Safe* cell culture unit from *Heraeus*. The cells were incubated in *Hera Cell incubators* also from *Heraeus*. The cells were cultured in DMEM with 10% FBS and 1% Penicillin/Streptomycin at 37°C/5% CO_2.

Experiments in which cells were not embedded in collagen gels or seeded on matrigel were performed in FBS-free DMEM to keep YAP in the cytosol prior to the photo-activation.

Experiments with cells in collagen gel or on matrigel were performed in the presence of FBS as the gels were sufficiently soft to prevent a nuclear localization of YAP even in the presence of FBS.

Cells were either seeded into *ibidi* 8-well, 6-well plates, or *Corning* 96-well plates.

Standard cell numbers for experiments were 5000 cells per well unless noted otherwise.

3.1 Transfection experiments

Transfections of cells in 8-wells plates were carried out by preparing an Optimem solution containing optoYAP plasmid (1 ug/100 µL), PAG plasmid (1 ug/100 µL) and the Xtreme Gene 9 Transfection reagent (3 µl/100 µL). After mixing carefully by tapping against the tube, the solution was then incubated at RT for 20 min. For each 8-well 10 µL of the transfection mixture were used and 3 µL of the caged Lysine were added before incubation. For the luciferase assay (1 ug/100 µL) of the 8xGTIIC-luciferase plasmid was added as well.

Transfections in 96 well plates used 5 µL of the transfection mixture and 1 µL of the caged lysine per well.

The transfection procedure for single cells and spheroids was carried out in the same manner.

3.2 Photo-activation

For non-directed photo-activation of optoYAP a *Spectroline E-Series* UV lamp (365 nm, 0.6mW/mm²) was used to illuminate the sample for 20 s. For directed photo-activation a laser (405 nm, integrated in a *Zeiss Observer SD* spinning disk confocal microscope) or LED (365 nm, integrated in a *Nikon Eclipse Ti-E*) regulated to the same output as the UV lamp was used to illuminate the sample for 20 s.

3.3 Spheroid formation

To form spheroids, 500 cells were seeded in each well (100 µL DMEM) of a 96-well plate with ultra-low adhesion and incubated at 37°C/5%CO_2 until the spheroids reached the desired size. Spheroids used for experiments had a diameter of 200-300 µm for HeLa spheroids and 100-150 µm for A431 spheroids. For transferring the spheroids into gels disposable plastic pipettes were used.

3.4 Cell Spheroid/Collagen Gel preparation

150 µL of collagen (8.36 mg/mL) were prepared in a 1.5 mL Eppendorf-tube on ice and 47.5 µL PBS and 2.5 µL 1M NaOH, both pre-cooled to 0°C on ice, were added for each well of an ibidi 8-Well plate. The reagents were mixed by pipetting up and down before applying them to the well. Aggregates were carefully aspirated with a pipette and transferred to the gels (2 per well) for a total volume of 400 µL. The spheroids were incubated for 24 h at 37°C/5%CO_2 before transfection.

3.5 Spheroid Growth Rate

To compare the growth rate of activated and inactivated optoYAP transfected spheroids, collagen embedded spheroids were imaged before activation of optoYAP and then again after three days of incubation after activation. As a control, non-activated spheroids were measured as well. The growth analysis was performed using *Fiji* by comparing 2D projections of the total area covered by spheroids and cell outgrowths before and after incubation.

3.6 RNA extraction for qPCR

RNA Extraction, purification and cDNA synthesis was carried out according to the instructions provided in the RNeasy Mini Kit from *QIAGEN*.

3.7 Luciferase Functionality Assays

HeLa cells were seeded in a 96-well plate with 5000 cells per well and then transfected with optoYAP and 8xGTIIC-luciferase plasmid. After an incubation of 24 hours, optoYAP was activated and after an additional 24 the *Bright-Glo Luciferase Assay* from *Promega* was carried out according to the instructions provided in the manual. The assays were performed on a *Berthold Tristar² LB 942*. 8xGTIIC-luciferase was a gift from Stefano Piccolo (Addgene plasmid # 34615 ; http://n2t.net/addgene:34615 ; RRID:Addgene_34615)

3.8 Proliferation Assay

500 HeLa cells were seeded into each well of a 96-well plate in media without FBS and then transfected with optoYAP after 24 hours. After an additional 24 hours, half of the wells were illuminated with UV light at 365 nm to photo-activate optoYAP. The remaining wells served as the control and were not treated with UV. Afterward, cell images were recorded every 24 hours to observe cell proliferation with and without activation of optoYAP.

4. Fluorescence imaging and staining

4.1 Confocal laser scanning microscopy

High-magnification brightfield and fluorescence microscopy was carried out utilizing a *Zeiss Observer SD* spinning disk confocal microscope with a Yokogawa CSU-X1 spinning disc unit, an oil objective with 63x magnification. For excitation, a 488 nm (GFP) and 561 nm (YAP) were used. Emission was filtered with a BP 525/50 and LP 690/50 filter, respectively. The setup was heated to 37°C and a CO_2 source was provided to keep the atmosphere at 5% for living samples. The images were recorded and processed with the *Zen* software by *Zeiss*.

4.2 High-Throughput Brightfield imaging

The proliferation assay and general spheroid growth quantification measurements were performed with the *ImageXpress Micro XLS* from *Molecular Devices* using an objective with 10x magnification and the resulting images were evaluated with the *MetaXpress* software.

Further image data analysis was performed with *ImageJ*/*Fiji* (Schindelin et al., 2012). Specific analysis methods are described at the respective assays.

4.3 High-resolution Fluorescence Confocal Microscopy

Imaging was carried out on a confocal scanning microscope (TE 300; Nikon) with mounted bright-field illumination and camera. The two-photon excitation source for Hoechst staining was a fiber-based, frequency-doubled erbium laser (FemtoFiber dichro bioMP; Toptica Photonics) running at 774 nm. The excitation laser line for YAP staining was a DPSS CW laser running at 561 nm (Cobolt Jive 50, Cobolt AB). The laser powers were 3.3 mW at 774 nm and 2.9 µW at 561, measured in front of the microscope entrance. The laser light was coupled into the microscope via a dichroic mirror (Penta Line zt405/488/561/640/785rpc; AHF Analysetechnik) that separates laser excitation and fluorescence emission. Scanning of the sample in 3D was achieved by using an xyz piezo stage (BIO3.200; PiezoConcept). The laser excitation was focused onto the sample with a 60x (water) 1.20-NA plan apochromat objective (Plan APO VC 60x 1.2 NA, Nikon). The emission was collected by the same objective and spectrally separated by a 647-nm dichroic mirror (BS 647 SP; AHF Analysentechnik). The emission was recorded with two APD detectors (Count Blue; Count Red; Laser Components) and its photons stream registered using a TCSPC card (TH260 pico dual; PicoQuant GmbH). The filter sets for the red APD were: 710/130 bandpass fluorescence filter (HQ 710/130 M; AHF Analysetechnik) and a 750 shortpass (FES0750; Thorlabs GmbH) to additionally block the 774 nm laser line. The filter sets for the blue APD were: 692/40 bandpass fluorescence filter (692/40 BrightLine HC; AHF Analysetechnik) and a 680 shortpass (HC 680/SP; AHF Analysentechnik) to additionally block the 774-nm laser line. The experiment was controlled using a home-written program written in C#. The confocal data was extracted and evaluated afterward by PAM (Schrimpf et al., 2018) and ImageJ2 (Schindelin et al., 2012).

4.4 Antibody Staining

Primary and secondary antibodies for were purchased *as stated in the following list.*

List of used antibodies:
YAP

- YAP1 polyclonal rabbit antibody; PA1-46189 *Thermo Fisher Scientific.*
- Donkey anti-Rabbit IgG (H+L) Highly Cross-Adsorbed Secondary Antibody, Alexa Fluor 546; A-10040 *Thermo Fisher Scientific.*

RPA2

- *RPA32/RPA2 mouse monoclonal antibody; ab2175, Abcam*
- *Goat anit-Mouse* IgG (H+L) Highly Cross-Adsorbed Secondary Antibody, Alexa Fluor 488; A-11001 *Thermo Fisher Scientific.*

gH2A.

- *gH2A.X rabbit antibody; 2577 Cell Signaling Technology*
- *Goat anit-Rabbit* IgG (H+L) Highly Cross-Adsorbed Secondary Antibody, Alexa Fluor 647; A-21245 *Thermo Fisher Scientific.*

4.5 2D Antibody Staining

HeLa cells were seeded on matrigel to prevent the nuclear localization of YAP and transfected with optoYAP 24h after seeding. 24 hours after transfection, cells were illuminated with UV light (365 nm) for 20 s. After another 6-24 h cells were washed with PBS (pH 7.4) before being fixed with 4% PFA for 10 min. Afterwards, cells were washed three times with PBS for 5 min each. Cells were then permeabilized with Triton X-100 (0.15% in PBS) for 10 min and washed with PBS for 5 min an additional three times. Cells were blocked with 1% BSA containing glycine for 30 min before primary antibodies were applied diluted in PBS with 1% BSA (1 µg antibody per well). After 1 h of incubation, at room temperature (or overnight at 4°C) the cells were washed 5 min with PBS three times. Next, the secondary antibodies were applied diluted in 1% BSA. After one hour of incubation the sample was washed again and Hoechst was applied before imaging.

4.6 3D Antibody Staining

HeLa spheroids embedded into collagen were fixed with 4% PFA for 40 minutes and washed with PBS twice for 20 minutes. The cells were permeabilized for 20 minutes with 0.5% Triton X-100 in PBS and subsequently washed with PBS for 30 minutes. The cells were blocked with 1% BSA in PBS overnight. Primary antibodies were diluted 1:100 with 1% BSA in PBS and cells were incubated for 72 hours. Prior to incubation with secondary antibodies (1:200 in 1% BSA), the cells were washed twice with PBS for 30 minutes. The cells were incubated with secondary antibodies for 48 hours. Afterwards, the cells were washed with PBS for 30 minutes and Hoechst 33342 (0.5 µg/ml) for 40 minutes. Prior to imaging, the cells were washed again with PBS for 30 minutes. Finally, the PBS was renewed and kept in the reservoirs during confocal microscopy.

Supplemental Figures

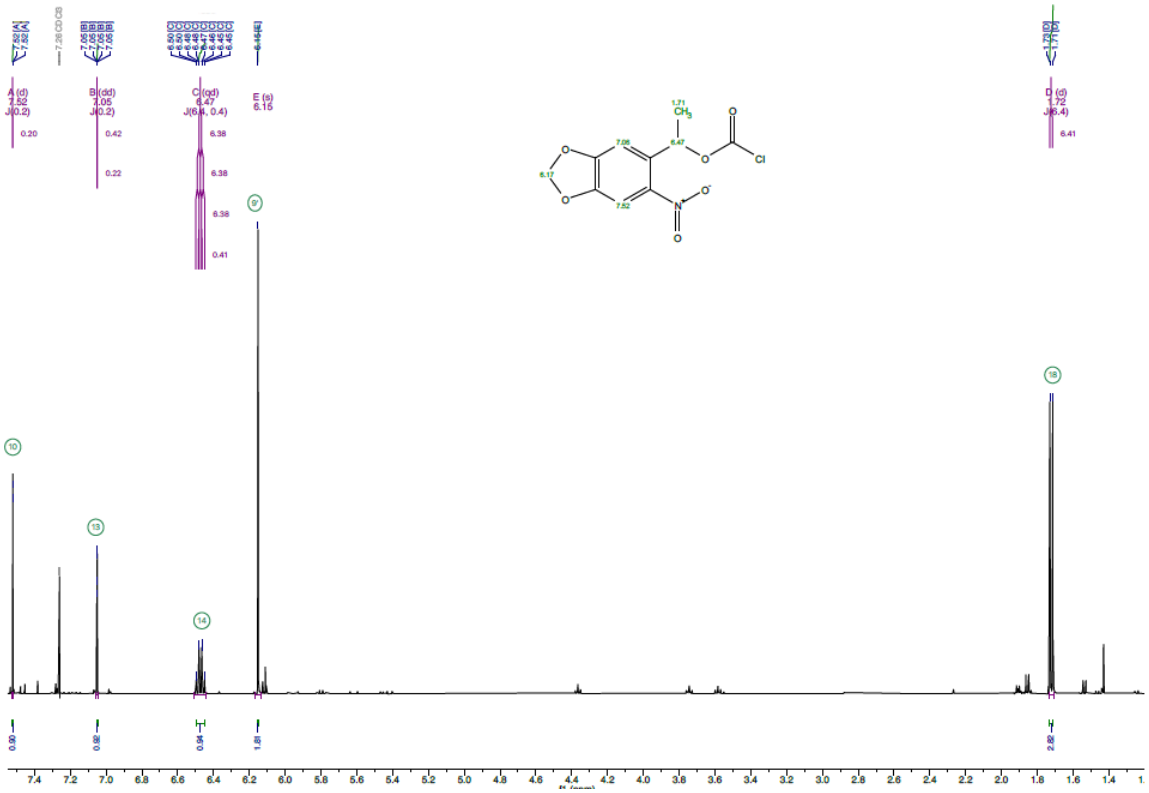

Fig. S1: NMR spectrum of 1-(6-nitrobenzo[d][1,3]dioxol-5-yl)ethyl-carbonochloridate. Related to Figure 1. It is obtained as an intermediate product of the synthesis of the caged lysine. ^{1}H NMR (400 MHz, CDCl3): _ (ppm) = 7.52 (d, J = 0.2 Hz, 1 H, H-7), 7.05 (dd, J = 0.2 Hz, 1 H, H-4), 6.47 (qd, J = 6.4, 0.4 Hz 1 H, H-1'), 6.15 (s, 2 H, H-2), 1.72 (d, J = 6.4 Hz, 3 H, H-2').

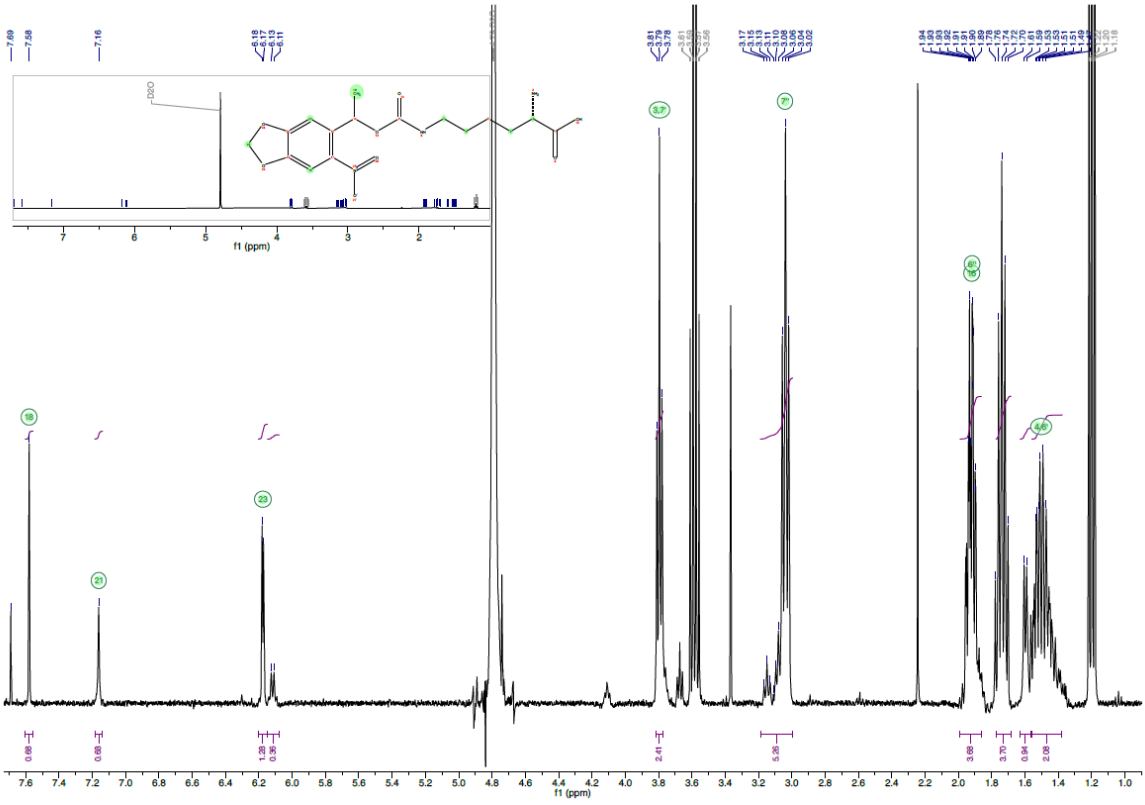

Fig. S2: NMR spectrum of the caged lysine ((2S)-2-(tert-Butoxycarbonylamino)-6-[1-(6-nitrobenzo[d][1,3]dioxol-5-yl)ethoxy]carbonyl-aminohexanoic acid). Related to Figure 1. ^{1}H NMR (400 MHz, CDCl3): _ (ppm) = 7.58 (s, 1 H, H-7”), 7.16 (s, 1 H, H-4”), 6.18 (d,J =3.5 Hz, 2 H, H-2”), 6.12 (d, J = 6.4 Hz 1 H, H-1’), 3.79 (t, J = 6.1 Hz, 2 H), 3.19 – 3.00 (m, 5 H),1.92 (m, 3 H), 1.62 – 1.38 (m, 3 H).

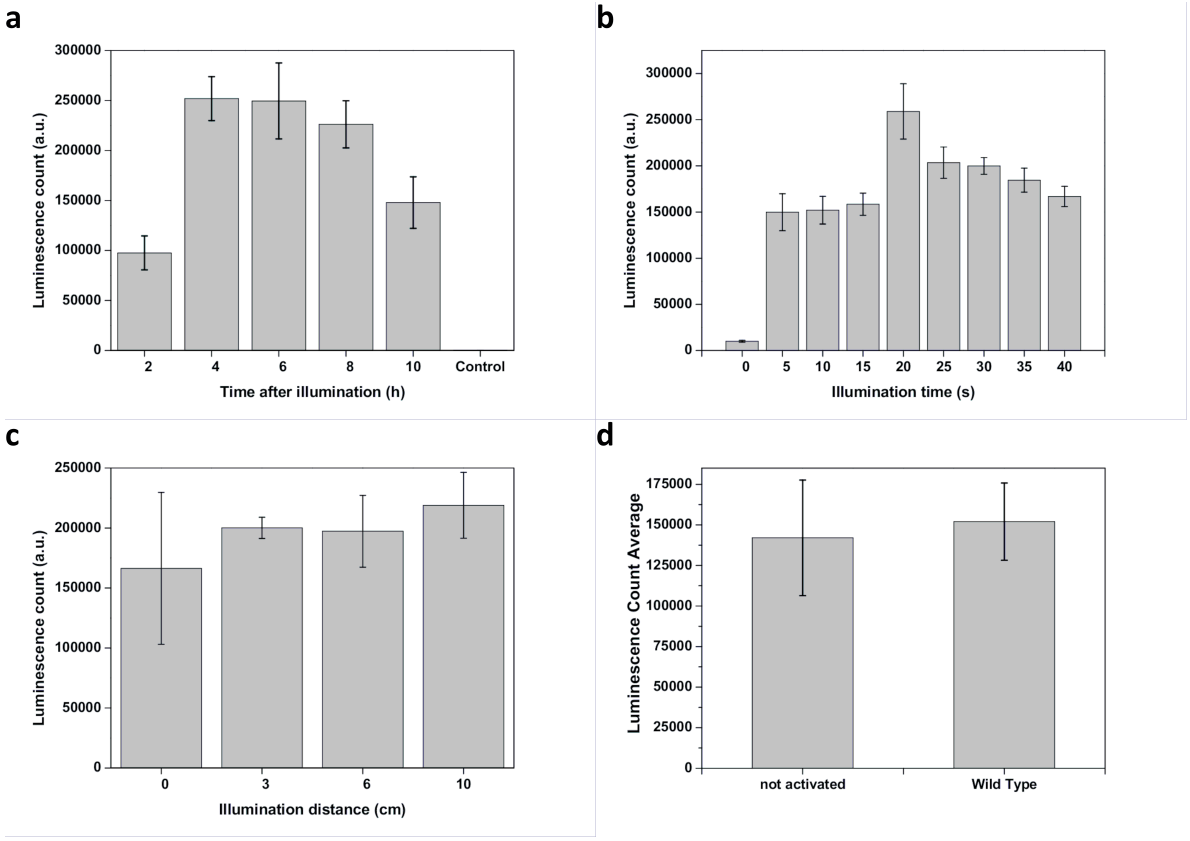

Fig. S3: Luciferase Functionality Assay. Related to Figure 1. a) Time-dependence of optoYAP activity. The observed luciferase count, and thus optoYAP activity, is time-dependent. Measurements taken at different time points after illumination show a clear maximum in activity at 4 to 6 h after photo-activation with a steady decline afterward. b) Dependence of optoYAP activity on illumination time. To gauge the effect of variations in illumination time on optoYAP activity, transfected HeLa cells were illuminated for different time periods to photo-activate optoYAP. Subsequently, the corresponding luciferase activity was recorded. The results show a clear peak in luciferase count and thus YAP activity at an illumination time of 20 seconds. c) Distance dependence of the photo-activation: The distance between light source and sample during photo-activation and thus the power needed to activate optoYAP was investigated. Photo-activation was performed at the indicated distances between light source and sample and the subsequent luciferase activity was recorded. While there was a slight deviation in recorded luminescence in case of full contact of the UV light to the sample (0 cm distance), no significant differences could be observed for larger distances. The luciferase activity shows thus little sensitivity to deviations in light intensity of the UV light source. d) Comparison of luciferase activity of optoYAP transfected, non-activated cells (not activated) and cells that were not transfected with optoYAP and not activated (Wild Type) shows that optoYAP transfection does not influence downstream signaling significantly prior to photoactivation. Data in all figures are represented as mean +/- standard deviations of triplicates.

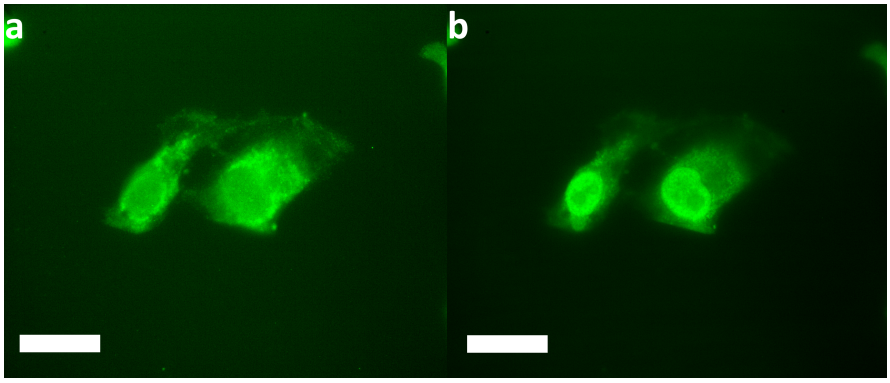

Fig. S4: optoYAP translocation. Related to Figure 1. optoYAP transfected HeLa cells on a thin layer of matrigel before (a) and 30 min (b) after illumination. Scale bar: 20 µm.

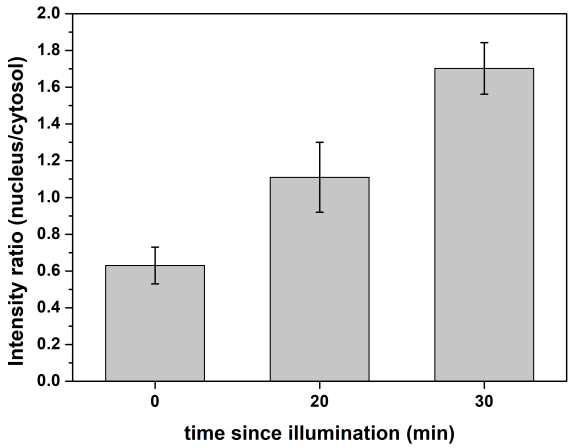

Fig. S5: Kinetics of optoYAP translocation. Related to Figure 1. Intensity ratio of (nucleus/cytosol) of optoYAP in HeLa cells in 2D cell culture at different times after optoYAP activation. Prior to activation the optoYAP signal is localized in the cytosol, but gradually translocates into the nucleus upon activation. Note: images are not background corrected for analysis, thus leading to an intensity ratio above zero before illumination, and above 1 after illumination. Data are represented as mean +/- standard deviations of triplicates.

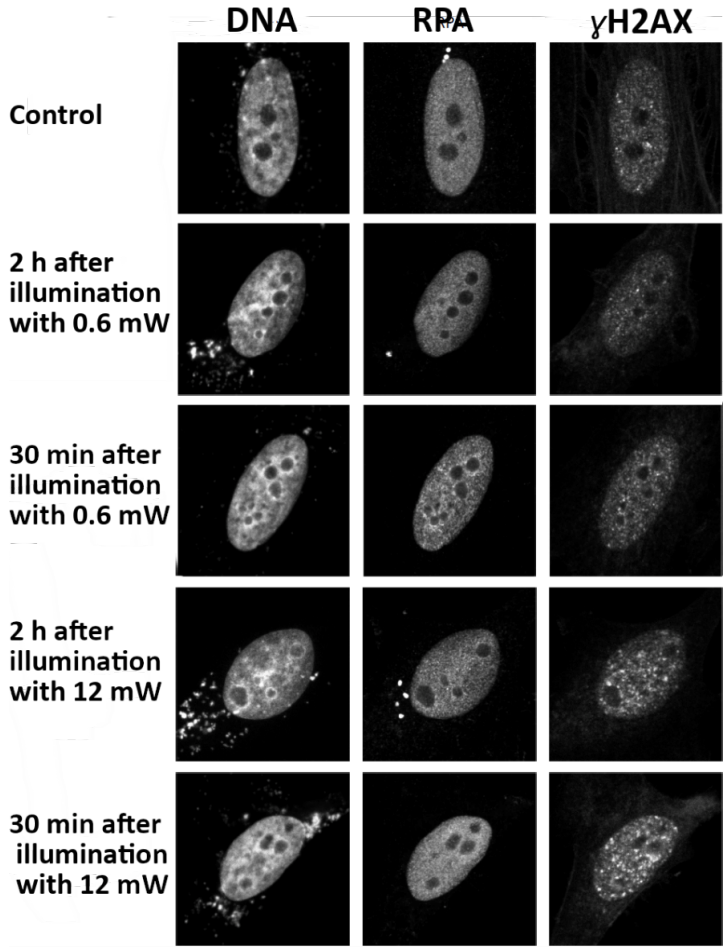

Fig. S6: Assessment of the damage caused during photo-activation with 20 s UV light (365 nm) illumination. Related to Figure 1. HeLa cells were seeded on an 8-well microscopy slide and transfected with optoYAP. After photo-activation at different intensities the damage to the cells was investigated with markers for DNA and as a marker of DNA damage with the DNA damage repair proteins RPA and γH2AX. Comparing the activated samples to a transfected non-activated control shows that the higher intensity leads to some DNA damage (visible by an increase in RPA and γH2AX signal) that is almost repaired after 2 h. The lower intensity of 0.6 mW leads to negligible DNA damage, which cannot be detected anymore after 2h. Thus, this intensity was chosen for all experiments.

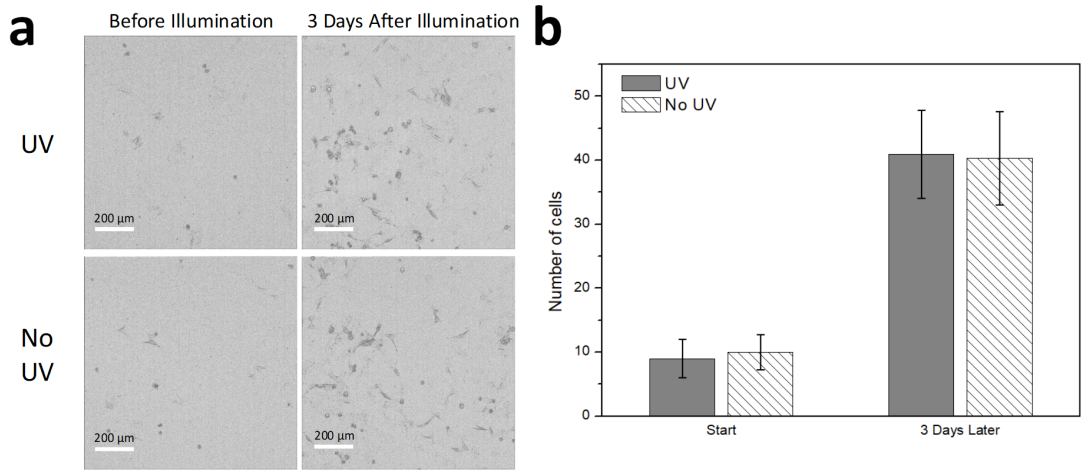

Fig. S7: Effect of UV illumination on proliferation. Related to Figure 1 and 2. Proliferation of cells is not affected by the illumination used for optoYAP activation. a) Brightfield microscopy images of cells at the time of illumination and 3 days later. The upper row was illuminated with UV as used for optoYAP activation and the lower row serves as control, which was not illuminated. Scale bar: 200 µm. b) Quantitative analysis of the number of cells at the time point of UV-illumination and 3 days later compared to controls, which were not illuminated, shows that proliferation is not influenced by the UV used for photo-activation. Data are represented as mean +/- standard deviation.

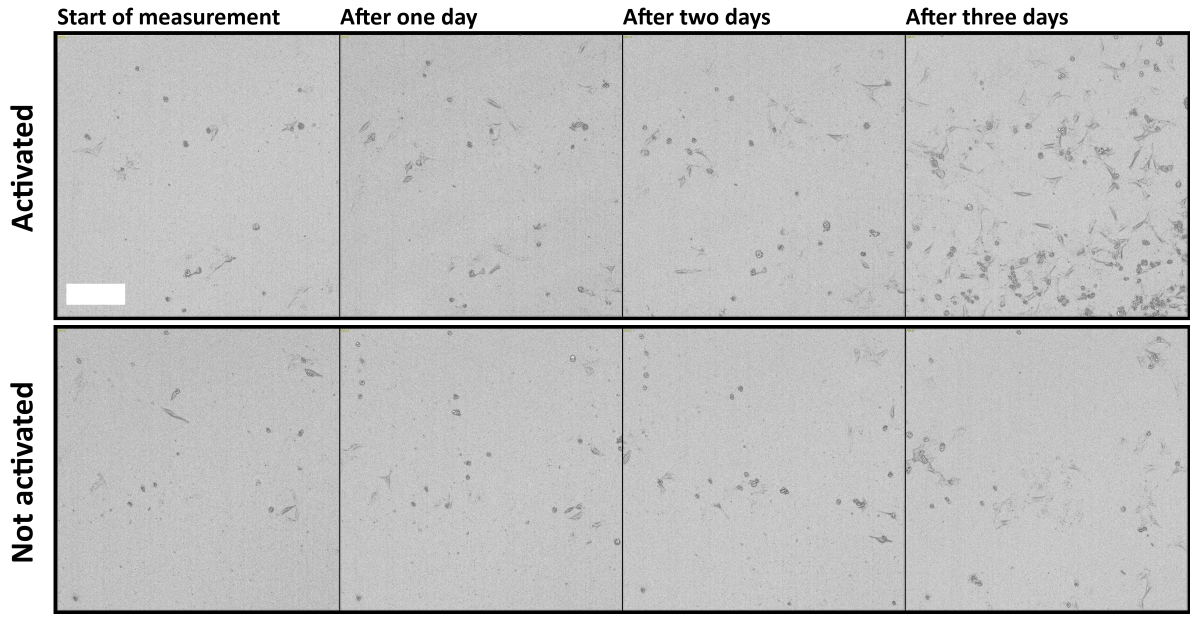

Fig. S8: Proliferation assay on optoYAP-transfected HeLa cells. Related to Figure 2. Time is measured after optoYAP activation. The upper row shows activated cells, the lower row non-activated controls. The images show a clear increase in overall growth upon optoYAP activation. Scale bar: 200 µm.

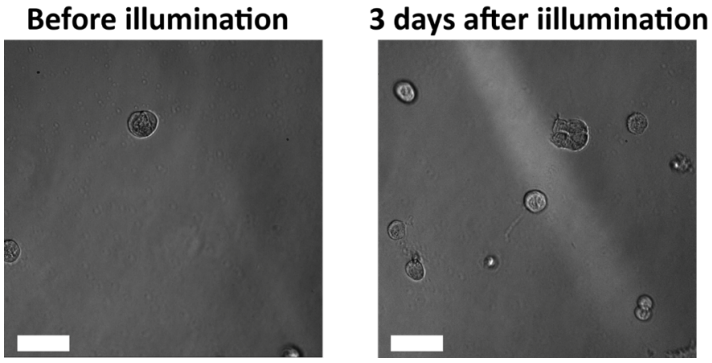

Fig. S9: Morphology of optoYAP transfected HeLa cells on matrigel. Related to Figure 2. OptoYAP transfected HeLa cells on a layer of matrigel before and three days after photo-activation. Cell morphology of transfected cells on matrigel did not change after photo-activation even after several days of incubation. Scale bar: 200 µm.

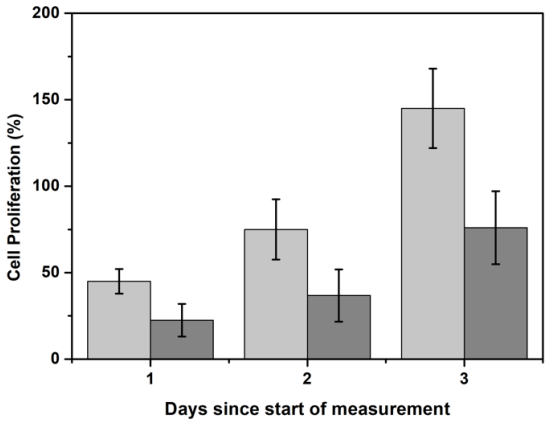

Fig. S10: Effect of optoYAP activation on proliferation on matrigel. Related to Figure 2. Cell proliferation of activated (light grey) and non-activated (dark grey) optoYAP transfected HeLa cells on matrigel in presence of FBS. The overall growth rate on matrigel is about a factor of two smaller in comparison to cell proliferation on a plastic substrate without FBS. Yet, likewise, the activated samples show a strongly increased proliferation compared to the non-activated samples. Data are represented as mean values +/- standard deviations of triplicates.

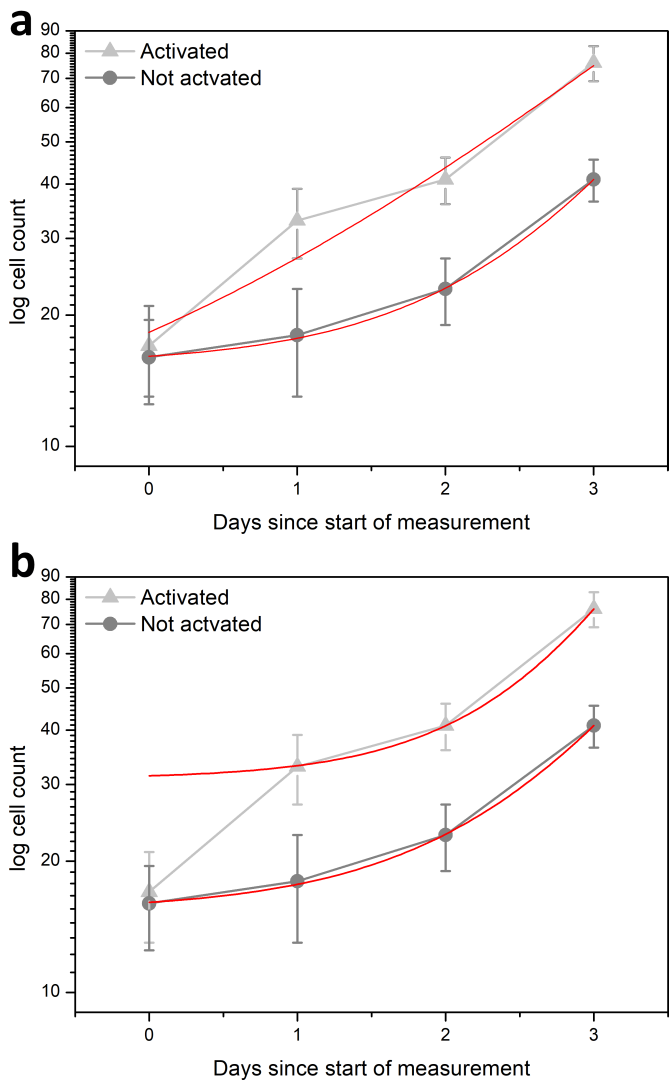

Fig. S11: Analysis of effect of optoYAP activation on proliferation. Related to Figure 2. Logarithmic plot of the cell count with exponential fits. a) Fitting exponential growth curves to the data yields an average growth rate of 0.49/d for activated and 0.31/d for non-activated cells indicating the increase in growth upon optoYAP activation. However, due to the apparent reduction in growth rate of the activated sample after day 1 the fit is only a rough approximation. b) Fitting only the last three data points of the activated sample yields a fit of much better quality and a growth rate of 0.27/d, which is very similar to that of non-activated cells. The strong deviation of the first data point from this curve shows the strongly increased growth during the first 24 h of the experiment. This leads to the conclusion that the observed difference between activated and non-activated samples mainly stems from the cell proliferation of the first day of observation, while the proliferation returns to normal growth rates after the first day. Data are represented as mean values +/- standard deviations of triplicates.

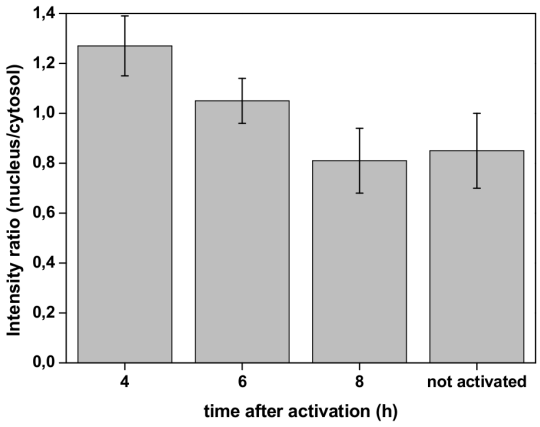

Fig. S12: Intensity ratio of (nucleus/cytosol) for YAP (via antibody staining) in HeLa cells on matrigel at different times after optoYAP activation. Related to Figure 2. 4 h after incubation YAP is in the nucleus followed by a decrease in the ratio of nuclear/cytosolic YAP. Note: images are not background corrected for analysis, thus leading to an intensity ratio above zero before illumination, and above 1 after illumination. Specifically due to the cell morphology on matrigel, the nuclear background signal is quite high. Data are represented as mean +/- standard deviations.

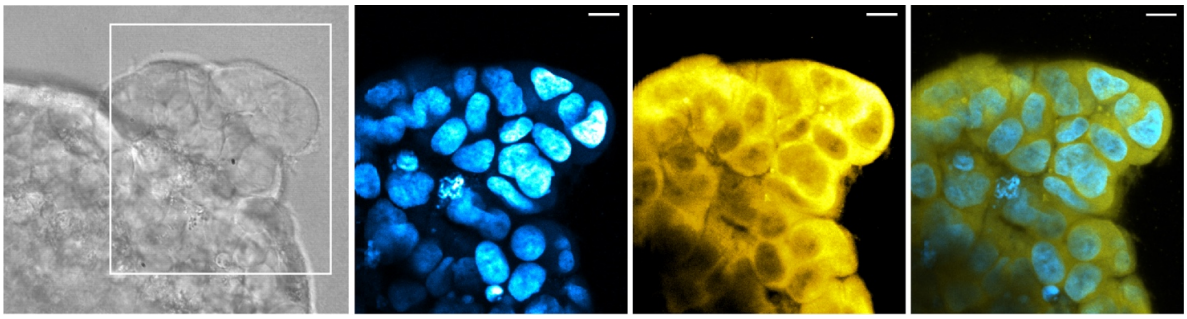

Fig. S13: High resolution confocal microscopy image of the inside of a fixed HeLa spheroid transfected with optoYAP. Related to Figure 3. The spheroid is embedded in a collagen gel and was completely illuminated for activation. The spheroid was fixed 3 days after activation. YAP appears concentrated in the cytosol. Scale bars: 5 µm.

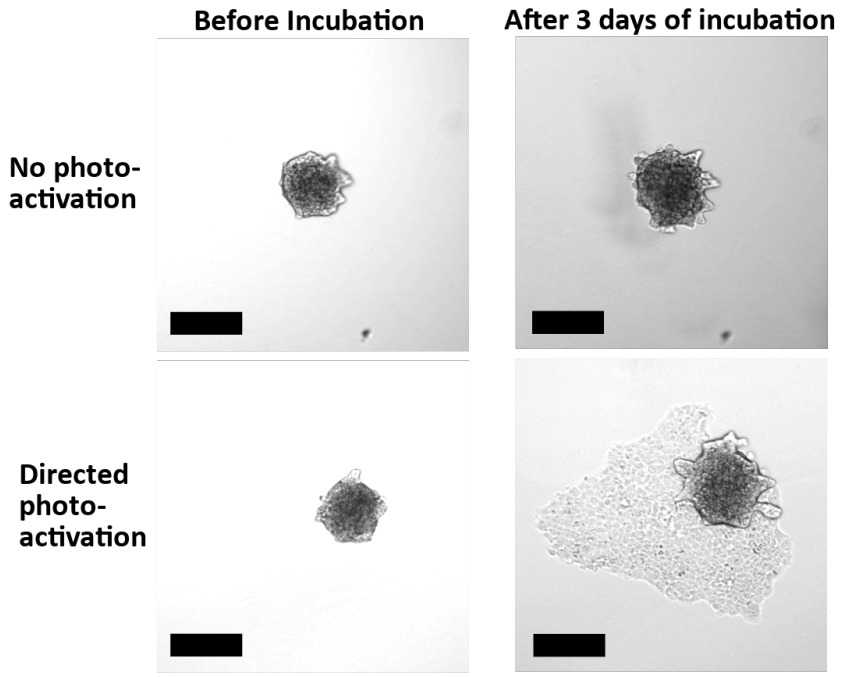

Fig. S14: optoYAP transfected A431 spheroids embedded into collagen gel. Related to Figure 3. To investigate if the effects of optoYAP activation can also be observed in other cell lines, A431 spheroids were transfected according to the same protocol described for HeLa spheroids and selectively activated. The treated A431 spheroids showed similar results to those obtained from HeLa spheroids: non-activated samples exhibit no discernible invasive behavior aside from general growth of the spheroid, while activated samples show significant invasion starting from the activated area. Scale bars: 150 μm.

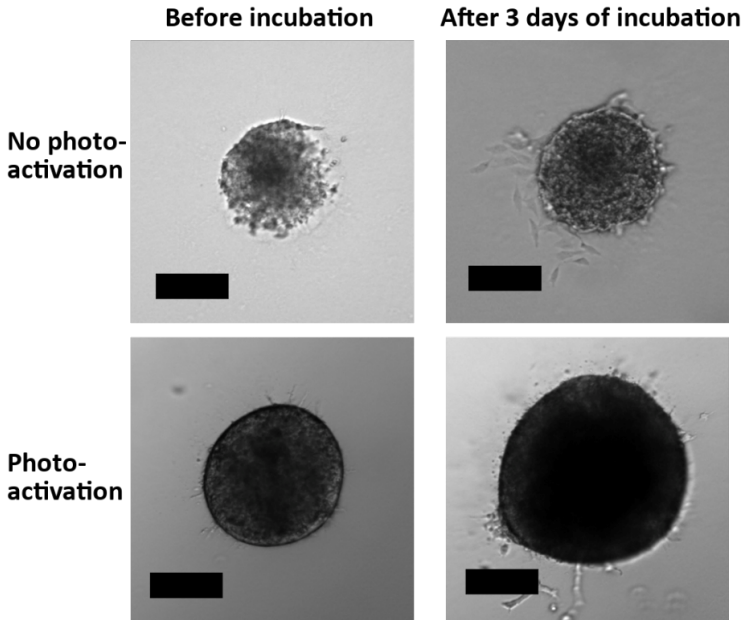

Fig. S15: Non-transfected HeLa spheroids embedded in collagen gel. Related to Figure 3. To investigate if the observed behaviors of the treated HeLa spheroids are indeed caused by optoYAP, non-transfected HeLa spheroids were used as controls and activated the same way as optoYAP. Neither the activated nor the non-activated samples show invasive behavior comparable to that of the optoYAP transfected spheroids. The only discernible difference between before and after incubation is an increase in overall spheroid size in both cases – with and without activation. Scale bars: 100 μm.

Supplemental references

Engelke, H., Chou, C., Uprety, R., Jess, P. and Deiters, A. (2014). Control of protein function through optochemical translocation. *ACS Synth Biol* 3, 731-736.

Li, M.Z. and Elledge, S.J. (2007). Harnessing homologous recombination in vitro to generate recombinant DNA via SLIC. *Nat. Methods* 4, 251-256.

Li, M.Z. and Elledge, S.J. (2012). SLIC: a method for sequence- and ligation-independent cloning. *Methods Mol. Biol.* 852, 51-59.

Schindelin, J., Arganda-Carreras, I., Frise, E., Kaynig, V., Longair, M., Pietzsch, T., Preibisch, S., Rueden, C., Saalfeld, S., Schmid, B. et al. (2012). Fiji: an open-source platform for biological-image analysis. *Nat. Methods* 9, 676-682.

Schrimpf, W., Barth, A., Hendrix, J. and Lamb, D.C. (2018). PAM: A Framework for Integrated Analysis of Imaging, Single-Molecule, and Ensemble Fluorescence Data. *Biophys. J.* 114, 1518-1528.

A.6. Chemical synthesis of the fluorescent, cyclic dinucleotides cthGAMP

ChemBioChem

Research Article
doi.org/10.1002/cbic.202200005

Chemistry Europe
European Chemical Societies Publishing

www.chembiochem.org

Chemical Synthesis of the Fluorescent, Cyclic Dinucleotides c[th]GAMP

Simon Veth[+],[a] Adrian Fuchs[+],[a] Dilara Özdemir[+],[a] Clemens Dialer,[a] David Jan Drexler,[b] Fabian Knechtel,[a] Gregor Witte,[b] Karl-Peter Hopfner,[b] Thomas Carell,*[a] and Evelyn Ploetz*[a]

The cGAS-STING pathway is known for its role in sensing cytosolic DNA introduced by a viral infection, bacterial invasion or tumorigenesis. Free DNA is recognized by the cyclic GMP-AMP synthase (cGAS) catalyzing the production of 2′,3′-cyclic guanosine monophosphate-adenosine monophosphate (2′,3′-cGAMP) in mammals. This cyclic dinucleotide acts as a second messenger, activating the stimulator of interferon genes (STING) that finally triggers the transcription of interferon genes and inflammatory cytokines. Due to the therapeutic potential of this pathway, both the production and the detection of cGAMP via fluorescent moieties for assay development is of great importance. Here, we introduce the paralleled synthetic access to the intrinsically fluorescent, cyclic dinucleotides 2′3′-c[th]GAMP and 3′3′-c[th]GAMP based on phosphoramidite and phosphate chemistry, adaptable for large scale synthesis. We examine their binding properties to murine and human STING and confirm biological activity including interferon induction by 2′3′-c[th]GAMP in THP-1 monocytes. Two-photon imaging revealed successful cellular uptake of 2′3′-c[th]GAMP in THP-1 cells.

Introduction

The innate immune system of eukaryotes is one of the first defense lines against invading pathogens.[1] To detect pathogens, the discrimination of molecular patterns from "self" (host) and "nonself" (e.g., microorganisms) is a fundamental process and relies on an array of pattern recognition receptors (PRRs). These PRRs are cell surface or intracellular receptors that distinguish pathogen-associated molecular patterns (PAMPs) from endogenous host patterns.[2] In addition to PAMPs, some PRRs recognize damage-associated molecular patterns (DAMPs) such as host-derived signals of cellular stress.[3] During the last decade, a cyclic dinucleotide (CDN) 2′,3′-cyclic guanosine monophosphate-adenosine monophosphate (2′3′-cGAMP, **1**) was identified to be crucially involved in transmitting innate immune system signaling (Figure 1a).[4]

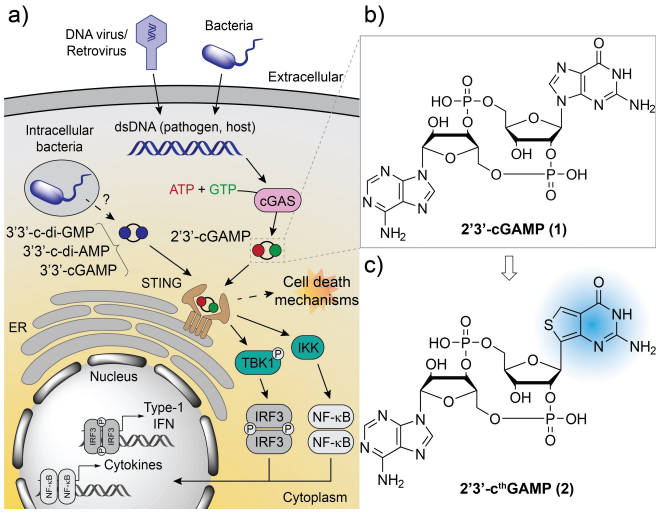

Figure 1. Biological role of CDNs. a) Molecular activation and regulation of the cGAS-cGAMP-STING pathway leading to interferon activation, inflammatory response and potential cell death. b) Structure of the CDN 2′3′-cGAMP. c) Chemical structure of the fluorescent analogue 2′3′-c[th]GAMP (**2**).

CDNs are found in vertebrates and prokaryotes alike and play an important role as second messengers.[5] While the CDNs from bacterial origin (e.g., 3′3′-c-di-GMP, 3′3′-c-di-AMP, 3′3′-cGAMP) are based on two canonical 3′-5′ phosphodiester bonds,[6] the only CDN found in mammalian cells possesses a mixed 2′-5′ and 3′-5′ phosphodiester linkage (2′3′-cGAMP).[4]

2′3′-cGAMP plays a crucial role in the cyclic GMP-AMP synthase (cGAS)-stimulator of interferon genes (STING) pathway, which has emerged as a critical mechanism for coupling the sensing of double-stranded DNA (dsDNA) in the cytosol to the induction of innate immune defense programs. cGAS, an

[a] S. Veth,[+] A. Fuchs,[+] D. Özdemir,[+] Dr. C. Dialer, F. Knechtel, Prof. T. Carell, Dr. E. Ploetz
Department of Chemistry and Center for NanoScience (CeNS)
Ludwig-Maximilians-Universität München
Butenandtstr. 5–13, 81377 Munich (Germany)
E-mail: thomas.carell@cup.uni-muenchen.de
evelyn.ploetz@cup.uni-muenchen.de
[b] Dr. D. J. Drexler, Dr. G. Witte, Prof. K.-P. Hopfner
Gene Center and Department of Biochemistry
Ludwig-Maximilians-Universität München
Feodor-Lynen-Straße 25, 81377 Munich (Germany)
[+] These authors contributed equally to this work.

Supporting information for this article is available on the WWW under https://doi.org/10.1002/cbic.202200005

© 2022 The Authors. ChemBioChem published by Wiley-VCH GmbH. This is an open access article under the terms of the Creative Commons Attribution Non-Commercial License, which permits use, distribution and reproduction in any medium, provided the original work is properly cited and is not used for commercial purposes.

© 2022 The Authors. ChemBioChem published by Wiley-VCH GmbH

enzyme belonging to the family of DNA sensors, recognizes a broad repertoire of DNA species of both foreign (e.g., pathogens) and self-origin.[7] Upon binding to dsDNA in the cytosol, cGAS from bacteria are sensed by STING at the endoplasmic reticulum (ER),[8] triggering a signaling cascade by recruiting the kinases TBK1 and IKK, which results in the activation of interferon regulatory factor 3 (IRF3) and NF-κB.[9] IRF3 and NF-κB consecutively induce the expression of type-1 interferons (IFN), inflammatory cytokines and other interferon-stimulated genes (ISGs),[10] leading to a DNA-driven immune response. Depending on signaling strength, STING also results in the activation of other cellular processes such as apoptosis and necroptosis.[11]

The modification of CDNs with fluorescently active moieties holds great promises for the development of novel activity assays and emissive probes for following these key compounds *in vivo*, in order to deepen our fundamental understanding on the life cycle of CDNs, including biosynthesis, distribution, and degradation or recycling. For instance, a fluorescently labeled ATP analogue based on 2-aminopurine (2AP) was used in the cGAS-catalyzed formation of a fluorescent CDN (fGAMP) to characterize the length-dependency of cGAS activity.[12]

Depending on the desired application a drawback of many emissive nucleoside analogues, including the most prevalently used 2AP, could be their significant quenching upon incorporation into oligonucleotides and CDNs.[13] The group of Yitzhak Tor developed a highly emissive RNA alphabet (thA, thG, thU, thC) with unparalleled structural isomorphicity to the native purine and pyrimidine bases derived from thieno[3,4-*d*]-pyrimidine as the heterocyclic nucleus. Besides excellent structural isomorphicity, good quantum yield ($\phi = 0.46$) and long excited-state lifetime (14.8 ns) were reported for thG in H_2O. Moreover, thG was found to show strong visible emission compared to 2AP even if "sandwiched" by two potential quenching guanosine residues in an oligonucleotide.[14]

In 2019, the enzymatic synthesis of a 2′3′-CDN bearing the thG base (2′3′-cthGAMP, **2**; Scheme 1) among 32 other CDNs was published focusing on the substrate specificity of cGAS derived from human, mouse and chicken as well as immunostimulatory properties in human peripheral blood mononuclear cells (PBMCs).[15] One year later, the enzymatic synthesis of thG-modified derivatives of bacterial 3′3′-c-di-GMP (3′3′-c-di-thGMP and 3′3′-c-thGGMP) were reported, highlighting their application in enzymatic assays and ability to induce a type-1 IFN response in THP-1 cells.[16] Cell experiments require large scales of the fluorescent, structural isomorph cGAMP mimics, which are hard to achieve by enzymatic pathways. To date, the organic synthesis of these compounds, as well as their application for cellular assays and fluorescent characterization *in vivo*, are missing.

Herein, we report the paralleled synthetic access to the cyclic dinucleotides 2′3′-cthGAMP and 3′3′-cthGAMP (Scheme 1) based on phosphoramidite and phosphate chemistry, suited for large scale synthesis. We highlight the differences in affinity of these CDNs to human and murine STING and focus on the scope and limitations of 2′3′-cthGAMP for *in vivo* studies in THP-1 cells using two-photon excitation microscopy.

Results and Discussion

Synthesis

The paralleled synthesis of 2′3′-cthGAMP (**2**) and 3′3′-cthGAMP (**3**) is depicted in Scheme 1. Starting from the 5′-dimethoxytrityl (DMTr)- and dimethylformamidino (dmf)-protected thG nucleoside **4** (for synthetic details see Shin et al.),[14] TBS-protection did yield a regioisomeric mixture of the 3′-OTBS (**5**) and 2′-OTBS (**6**) protected nucleosides. Following a modified procedure from Ching et al.,[17] these were converted to the corresponding phosphoramidites using commercially available 2-cyanoethyl *N*,*N*,*N*′,*N*′-tetraisopropylphosphorodiamidite and pyridinium trifluoroacetate. The resulting 2′- and 3′-phosphoramidites were not isolated but instead the diisopropylamine functionality was directly displaced by allyl alcohol with the aid of 5-(benzylthio)-1*H*-tetrazole (BTT) activator followed by the *t*-BuOOH-mediated oxidation of the P(III)- to the P(V)-species and DMTr-deprotection in 3% dichloroacetic acid (DCA). In total, the four-step reaction sequence allowed to generate the allyl- and cyanoethyl-protected 2′-phosphate (**7**) and 3′-phosphate (**8**) in 56% yield. In a similar reaction sequence, commercially available DMT-2′-O-TBS-rA(Bz) phosphoramidite was then coupled to the free 5′ OH groups of **7** and **8** with the aid of BTT activator, followed by oxidation and DMTr deprotection as described before. The resulting linear coupled dinucleotides were isolated in moderate yields, possessing the desired 2′3′- (**9**) and 3′3′- (**10**) connectivity. The deprotection of the allyl group with sodium iodide in refluxing acetone gave the alkoxides, which were cyclized using *N*-methylimidazole as nucleophilic catalyst, 2,4,6-triisopropylbenzenesulfonyl chloride (TPSCl) as condensing agent and molecular sieves (4 Å) as moisture scavenger to yield **11** and **12** in 49% yield over two steps. To minimize the formation of undesired side products by dimer formation, the cyclization reaction was carried out in dilute conditions (4 mM referred to starting material) to promote the intramolecular reaction. Treatment of **11** and **12** with a 1:1 mixture of ammonium hydroxide and methanol followed by triethylammonium fluoride resulted in the deprotection of the nucleobase protecting groups (dmf, Bz), β-cyanoethyl and silyl groups. After precipitation in cold acetone the resulting crude product was purified by reverse-phase HPLCs to separate and purify 2′3′-cthGAMP (**2**) and 3′3′-cthGAMP (**3**) in 13% yield for each CDN. The correct phosphodiester connectivity was NMR spectroscopically verified by ^{1}H-^{31}P-HMBC measurements (see Supporting Information).

Biochemical characterization

With both target compounds in hands, we focused on evaluating their binding properties to murine and human STING. At first, we employed differential scanning fluorimetry (DSF) to determine the binding affinity of synthetic and natural CDNs to STING proteins by evaluating the difference in melting temperature of the STING protein with and without ligand (Supporting Figure S5.1). While 2′3′-cthGAMP shows reduced

© 2022 The Authors. ChemBioChem published by Wiley-VCH GmbH

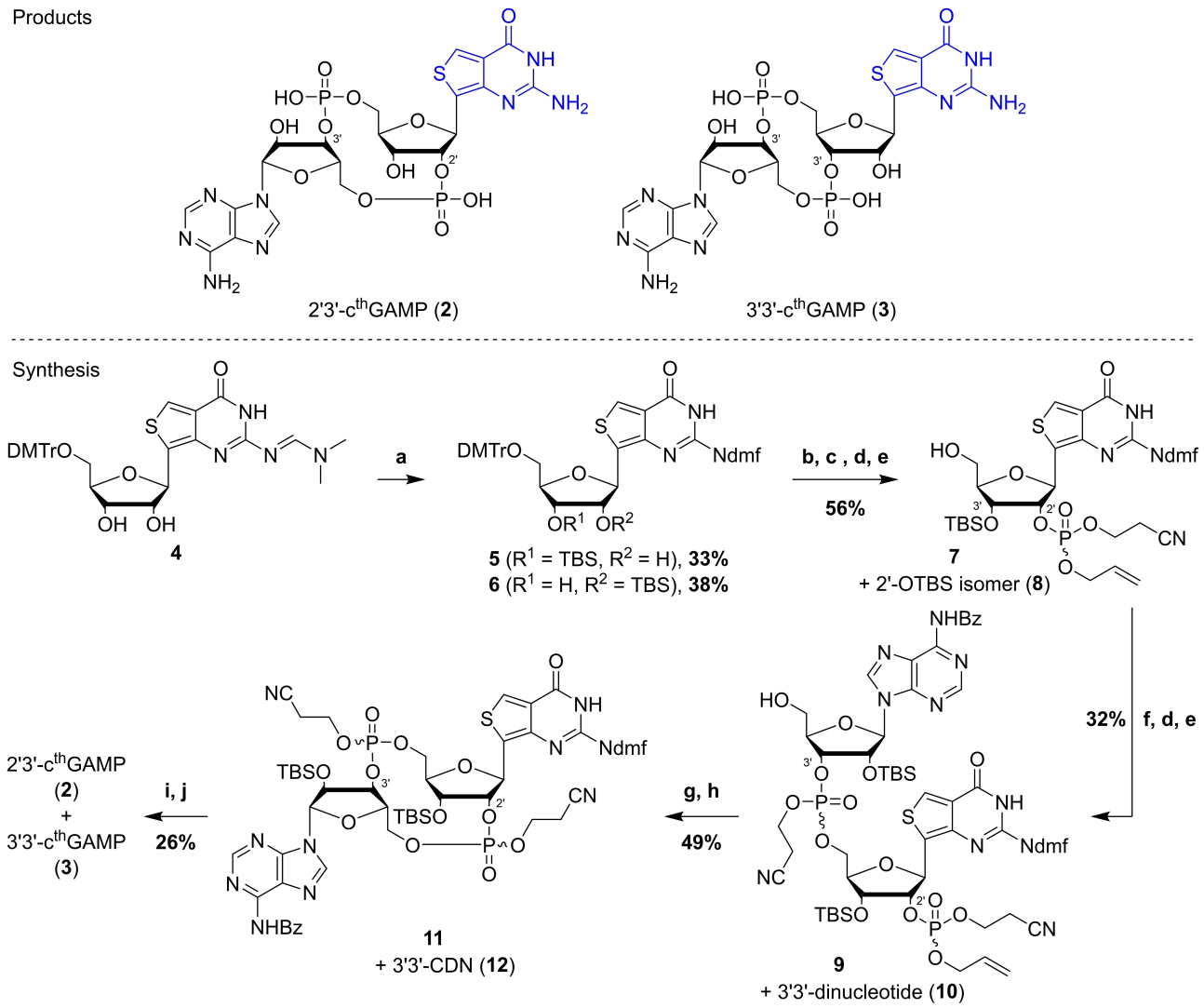

Scheme 1. Paralleled synthesis of 2′3′-c[th]GAMP and 3′3′-c[th]GAMP. Products 2′3′-c[th]GAMP (**2**) and 3′3′-c[th]GAMP (**3**) and synthetic overview. a) TBSCl, imidazole, pyridine; b) 2-cyanoethyl *N,N,N′,N′*-tetraisopropylphosphorodiamidite, pyridinium trifluoroacetate, MeCN; c) BTT, allyl alcohol; d) *t*-BuOOH, then $NaHSO_3$; e) 3% DCA in DCM; f) DMT-2′-O-TBS-rA(Bz) phosphoramidite, BTT, MeCN; g) NaI, acetone; h) TPSCl, N–Me-imidazole, THF; i) NH_4OH, MeOH; j) $NEt_3 \cdot 3HF$, THF, then HPLC.

binding-affinity compared to natural 2′3′-cGAMP, the thermal shift assays revealed, that 3′3′-c[th]GAMP (**3**) does not possess favorable binding affinity to neither murine nor human STING. As a consequence, we focused on the characterization and application of 2′3′-c[th]GAMP (**2**) in the later part of this publication.

Using isothermal titration calorimetry (ITC; Figure 2), we found that 2′3′-c[th]GAMP (**2**) is a less potent binder than natural 2′3′-cGAMP ($k_D = \sim 4$ nM).[18] It shows a 120- and 4000-fold reduced affinity to murine STING (mSTING; $k_D = 455$ nm) and human STING (hSTING; $k_D = 15$ μm). The thermodynamic parameters highlight, that the binding of 2′3′-c[th]GAMP to both receptors is exergonic ($\Delta G_{mSTING} = -36.3$ kJ/mol, $\Delta G_{hSTING} = -27.9$ kJ/mol), however with opposite trend for enthalpy and entropy: binding to mSTING is favorable in terms of entropy ($-T\Delta S_{mSTING} = -59.3$ kJ/mol) and endothermic ($\Delta H_{mSTING} = 23.4$ kJ/mol). In contrast, binding to hSTING was found to be

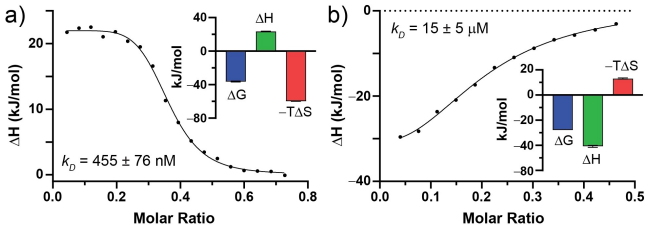

Figure 2. Binding to STING as measured by ITC. ITC curves and thermodynamic parameters for 2′3′-c[th]GAMP (**2**) bound to a) murine STING and b) human STING.

exothermic ($\Delta H_{hSTING} = -40.8$ kJ/mol) but entropically unfavorable ($-T\Delta S_{hSTING} = 13.1$ kJ/mol). Unlike the endothermic binding process of natural 2′3′-cGAMP to hSTING[18], the data suggests that binding of 2′3′-c[th]GAMP might not trigger a full conforma-

© 2022 The Authors. ChemBioChem published by Wiley-VCH GmbH

tional change in STING and, hence, a stabilized enclosure of the ligand. This observation would be in line with the reduced affinity of the synthetic compound.

Despite its reduced affinity, we set out next to investigate, whether binding of 2′3′-cthGAMP still activates STING signaling and consecutively interferon production. For this, we monitored the expression of the reporter gene Lucia luciferase in THP-1 Dual™ wild type (THP-1 monocytes) cells, which is under the control of the ISG54 promoter in conjunction with five IRF-stimulated response elements. Secretion of luciferase and hence activation of the IFN pathway was quantified by monitoring its luminescence in response to 2′3′-cGAMP and 2′3′-cthGAMP after transfection. 2′3′-cthGAMP showed a ~5-fold reduced but significant IRF activation compared to the natural compound (Supporting Information Figure S2).

Uptake in THP-1 cells

Having verified the biological potency of 2′3′-cthGAMP, we continued with THP-1 monocyte cells and monitored the uptake and effect on immune cells by following the fluorescent signature of the synthetic molecule *in vivo*. As reported, the 2′3′-cthGAMP features a broad absorption in the UV below 360 nm with a maximum around 315 nm (Figure 3a). Being excited at 310 nm, a blue photoluminescence was observed. The emission spectrum has a width of more than 200 nm, starting around 380 nm upwards with an emission maximum around 470 nm (Figure 3a). Since excitation sources in the UV and blue spectral range cause high background when being used for imaging cells due to scattering and autofluorescence, we employed two-photon imaging[19] using a pulsed laser excitation at 774 nm (Supporting Information Figure S5.3a–b). The fluorescence emission of 2′3′-cthGAMP (**2**) in water between 400–650 nm clearly showed a quadratic dependence on the exciting laser power (Supporting Information Figure S5.3c) confirming the nonlinear nature of the two-photon excitation.

Figure 3b (upper panels) shows the emitted autofluorescence of two THP-1 Dual™ cell lines, wild type (wt) and STING knock-out (STING KO), after two-photon excitation in the spectral range between 417 and 477 nm. Upon the addition of 2′3′-cthGAMP (**2**) to THP-1 wt cells, we expected an increase in overall brightness due to the intrinsic fluorescence of the compound. Instead, we observed a significant change in cell morphology combined with a strong decrease in emission (Figure 3c, upper panel, N = 91/129). In contrast, THP-1 STING-KO cells (Figure 3b, lower panel), which do not enter the consecutive immune response cascade, showed no morphological changes but only a slight swelling of the cell volume. Here, a significant increase in fluorescence intensity after 2′3′-cthGAMP uptake was monitored (Figure 3c, lower panel, N = 85/72). Both observations suggest, that 2′3′-cthGAMP is successfully taken up by both cell lines, however with different biological response: while cellular accumulation of 2′3′-cthGAMP leads to the expected brightness increase in THP-1 STING KO cells due to unavailability of the STING receptor and hence missing cellular response, the uptake in THP-1 wt cells triggered downstream

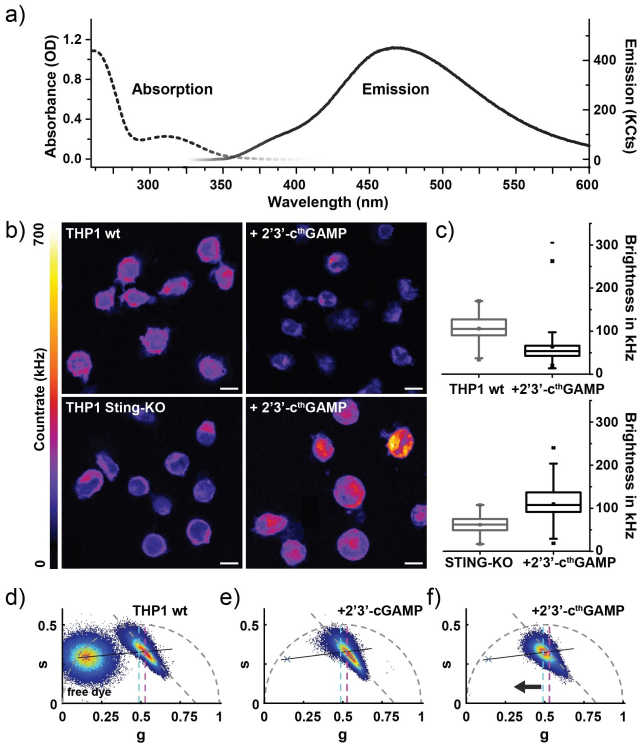

Figure 3. Fluorescence microscopy probing the cellular uptake of 2′3′-cthGAMP in THP-1 cells. a) Absorption (dotted line) and emission spectrum (solid line) of 52 μM 2′3′-cthGAMP in water after excitation at 310 nm. b-c) Two-photon images (b) and average cell brightness (c) of THP-1 wt cells (upper panel) and THP-1 STING-KO cells (lower panel) in absence and presence of 2′3′-cthGAMP. 2′3′-cthGAMP is biologically active in THP-1 wt cells leading to morphological changes and brightness decrease. In contrast, uptake of 2′3′-cthGAMP in STING knockout cells leads to a fluorescence increase. The emission was recorded between 417–477 nm and evaluated on average for 70–130 cells per condition. d–f) Phasor analysis of the average lifetime observed for THP-1 wt cells before (d) and after uptake of 50 μM 2′3′-cGAMP (e) and 200 μM 2′3′-cthGAMP (f). d) Phasor representation of the fluorescence signature of THP-1 wt cells and free 2′3′-cthGAMP in cell medium. The angled dotted line (grey) marks the multicomponent autofluorescent background in THP-1 wt cells. The center positions of the populations before (pink) and after (cyan) addition of 2′3′-cthGAMP (f) is marked with dotted lines. e) The addition of the non-fluorescent compound cGAMP triggers a shift in cellular autofluorescence towards shorter lifetimes and reduced brightness. f) The addition of 2′3′-cthGAMP leads to an off-axis shift towards free 2′3′-cthGAMP (along the black line), confirming the successful uptake.

processes due to activity of 2′3′-cthGAMP. Consecutive changes in cellular environment could affect the autofluorescent background, but also alter the photochemistry of the environmentally sensitive 2′3′-cthGAMP compound (see Supporting Information Figure S5.4.) by cellular interactions, leading to a decrease in fluorescence (if we anticipate the short time-window for free 2′3′-cthGAMP diffusion before binding to STING).

The autofluorescence signature of THP-1 overlaps with the emission spectrum of 2′3′-cthGAMP (**2**). To investigate whether the fluorescence increase observed for THP-1 STING KO cells can be directly linked to the uptake of 2′3′-cthGAMP (**2**), we evaluated the time-correlated single photon counting (TCSPC) data available for each image pixel in addition to the recorded

© 2022 The Authors. ChemBioChem published by Wiley-VCH GmbH

brightness information. At first, we recorded two-photon images of free dye only in solution for comparison and calibration (Supporting Information Figure S5.4a-b). By analyzing the exponential decay of the TCSPC histograms, we found an approximately mono-exponential behavior (on long timescales) of 16.8 ns for 2′3′-cthGAMP in water, similar to thG in water (14.8 ns).[14] In buffers, however, we observed a shortened lifetime of 6.2 ns in PBS and even 4.3 ns in THP-1 cell medium (Supporting Information Figure S5.4a). Due to this complex behavior and the multi-exponential nature of cellular autofluorescence, we expanded the lifetime evaluation using the phasor approach[20], which graphically translates the fluorescence lifetime decay into Fourier space (see Supporting Information Note 4.4 for details). This technique enables the detection of small contributions to a multi-component lifetime mixture.[20a] Here, mono-exponential decays will be observed on an arc of radius 0.5 with long lifetime components near the origin (0,0), while short lifetimes are expected to contribute near (1,0). On the other side, multi-exponential decay pathways or fluorescence decays of mixed species are expected inside the circle. They are composed of weighted linear compositions of the contributing mono-exponential species along the arc and obtained by vectorial addition of the weighted contributions by each fluorescence species (Supporting Information Figure S4.2d–f).

When analyzing the TCSPC data by the phasor approach, 2′3′-cthGAMP in PBS and cell medium is characterized by a bi-exponential, long-lived lifetime lying close to the left half-circle (Supporting Information Figure S5.4b), compared to the single-exponential signature of Atto532 in PBS on the circle. For the uptake of the fluorescent 2′3′-cthGAMP into THP-1 cells, we expect a mix between the signature of the fluorescent analogue and the autofluorescence of the cell line. The uptake should be seen by a shift of the cellular autofluorescence signature towards the population of the free dye, while for the natural, non-fluorescent 2′3′-cGAMP no change should occur.

THP-1 wt cells show a short-lived, multi-exponential autofluorescence of about 1.85 ns. Their population lies in the right half-circle compared to the longer-lived signature of the free 2′3′-cthGAMP in cell medium (Figure 3d). The addition of the natural analog 2′3′-cGAMP to THP-1 cells triggers a change in morphology and autofluorescent background. This change is evident by a shift along the grey dotted line towards shorter lifetimes and concomitantly reduced brightness. Besides a decrease of the average lifetime from 1.85 to 1.75 ns (Figure 3e), no shift towards the free 2′3′-cthGAMP compound (along the black line) was observed. Upon addition of 2′3′-cthGAMP, however, a clear shift towards the free fluorescent analog is observed (Figure 3f), as marked for the center position of cellular autofluorescent in absence (pink) and presence of 2′3′-cthGAMP (cyan). The cellular uptake of 2′3′-cthGAMP leads to an increase in average lifetime (2.05 ns) although a simultaneous reduction in autofluorescence background and lifetime is observed. For the STING KO line an identical behavior was detected (Supporting Information Figure 5.4c). Both findings, the brightness increase (Figure 3c, lower panel) as well as the lifetime shift towards the pure compound (Figure 3f) give clear evidence, that 2′3′-cthGAMP was taken up into THP-1 monocytes.

Conclusion

In summary, we report the first organic synthesis of 2′3′-cthGAMP (**2**) and 3′3′-cthGAMP (**3**), which feature the fluorescent thG base. The described synthetic strategy - involving phosphoramidite and phosphate chemistry - provides direct access to large quantities of both immunostimulants and enabled us to carry out cell feeding experiments with 2′3′-cthGAMP (**2**) as well as subsequent two-photon microscopy on THP-1 cells. While biochemical as well as cell-based assays confirmed the biologically activity of the synthetically derived compound, we further verified its presence in cells using fluorescence imaging and lifetime. Moreover, our observations show that the fluorescence lifetime of 2′3′-cthGAMP (**2**) is highly dependent on its environment suggesting a complex photochemistry for CDNs in general including the synthesized compound. While suitable for two-photon excitation microscopy, the cellular application of the fluorescent 2′3′-cGAMP analogue including intracellular tracking and downstream monitoring is strongly dependent on the autofluorescence of the chosen cell line, which creates an additional cell dependent detection limit. The decreased binding affinity of 2′3′-cthGAMP (**2**) to human STING in combination with high EC50 values[15] indicate substantial shortcomings which need to be addressed in the future. Nevertheless, as second messengers with diverse roles in both prokaryotes and eukaryotes, both fluorescent cthGAMP analogues may well serve for enzymatic assays/screening assays for inhibitors of CDN metabolism enzymes facilitating the development of therapeutics that target the cGAS-STING signaling pathway.

Experimental Section

Detailed experimental procedures during the synthesis and characterization of the fluorescent dinucleotides, protein purification of murine and human STING receptors, cell culturing, and advanced fluorescence microscopy are provided in the Supporting Information.

Acknowledgements

We thank Don C. Lamb for support and access to his laboratory facilities. Funding by the Center of NanoScience Munich (CeNS), the European Union's Horizon 2020 research and innovation programme under the Marie Sklodowska-Curie grant agreement No 861381 to T.C. and the Deutsche Forschungsgemeinschaft (RTG1721 Project A4 and TRR237 Project A9 to K.P.H.; RTG1721 Project A10 to G.W.; SFB1032, Project-ID 201269156, A05 to T.C. / B03 and PL 696/4-1 to E.P.) is gratefully acknowledged. Open Access funding enabled and organized by Projekt DEAL.

© 2022 The Authors. ChemBioChem published by Wiley-VCH GmbH

Conflict of Interest

The authors declare no conflict of interest.

Data Availability Statement

The data that support the findings of this study are available from the corresponding author upon reasonable request.

Keywords: cGAMP · imaging agents · STING pathway · fluorescent analogues · two-photon fluorescence lifetime imaging

[1] R. Medzhitov, C. A. Janeway, Jr., *Cell* **1997**, *91*, 295–298.
[2] S. Gordon, *Cell* **2002**, *111*, 927–930.
[3] K. Schroder, J. Tschopp, *Cell* **2010**, *140*, 821–832.
[4] A. Ablasser, M. Goldeck, T. Cavlar, T. Deimling, G. Witte, I. Röhl, K.-P. Hopfner, J. Ludwig, V. Hornung, *Nature* **2013**, *498*, 380–384.
[5] a) O. Danilchanka, J. J. Mekalanos, *Cell* **2013**, *154*, 962–970; b) L. Sun, J. Wu, F. Du, X. Chen, Z. Chen, *Science* **2013**, *339*, 786–791; c) U. Römling, M. Y. Galperin, M. Gomelsky, *Microbiol. Mol. Biol. Rev.* **2013**, *77*, 1–52.
[6] a) R. M. Corrigan, J. C. Abbott, H. Burhenne, V. Kaever, A. Gründling, *PLoS Path.* **2011**, *7*, e1002217; b) B. W. Davies, R. W. Bogard, T. S. Young, J. J. Mekalanos, *Cell* **2012**, *149*, 358–370; c) P. Ross, H. Weinhouse, Y. Aloni, D. Michaeli, P. Weinberger-Ohana, R. Mayer, S. Braun, E. de V-room, G. A. van der Marel, J. H. van Boom, M. Benziman, *Nature* **1987**, *325*, 279–281; d) G. Witte, S. Hartung, K. Büttner, K. P. Hopfner, *Mol. Cell* **2008**, *30*, 167–178.
[7] A. Decout, J. D. Katz, S. Venkatraman, A. Ablasser, *Nat. Rev. Immunol.* **2021**, *21*, 548–569.
[8] H. Ishikawa, G. N. Barber, *Nature* **2008**, *455*, 674.
[9] a) S. Liu, X. Cai, J. Wu, Q. Cong, X. Chen, T. Li, F. Du, J. Ren, Y.-T. Wu, N. V. Grishin, Z. J. Chen, *Science* **2015**, *347*, aaa2630; b) R. Fang, C. Wang, Q. Jiang, M. Lv, P. Gao, X. Yu, P. Mu, R. Zhang, S. Bi, J.-M. Feng, Z. Jiang, *J. Immunol.* **2017**, *199*, 3222.
[10] J. Wu, N. Dobbs, K. Yang, N. Yan, *Immunity* **2020**, *53*, 115–126.e115.
[11] a) M. F. Gulen, U. Koch, S. M. Haag, F. Schuler, L. Apetoh, A. Villunger, F. Radtke, A. Ablasser, *Nat. Commun.* **2017**, *8*, 427; b) J. Sarhan, B. C. Liu, H. I. Muendlein, C. G. Weindel, I. Smirnova, A. Y. Tang, V. Ilyukha, M. Sorokin, A. Buzdin, K. A. Fitzgerald, A. Poltorak, *Cell Death Differ.* **2019**, *26*, 332–347.
[12] L. Andreeva, B. Hiller, D. Kostrewa, C. Lässig, C. C. de Oliveira Mann, D. J. Drexler, A. Maiser, M. Gaidt, H. Leonhardt, V. Hornung, K.-P. Hopfner, *Nature* **2017**, *549*, 394.
[13] a) J. Zhou, Y. Zheng, B. T. Roembke, S. M. Robinson, C. Opoku-Temeng, D. A. Sayre, H. O. Sintim, *RSC Adv.* **2017**, *7*, 5421–5426; b) R. W. Sinkeldam, N. J. Greco, Y. Tor, *Chem. Rev.* **2010**, *110*, 2579–2619.
[14] D. Shin, R. W. Sinkeldam, Y. Tor, *J. Am. Chem. Soc.* **2011**, *133*, 14912–14915.
[15] B. Novotná, L. Vaneková, M. Zavřel, M. Buděšínský, M. Dejmek, M. Smola, O. Gutten, Z. A. Tehrani, M. Pimková Polidarová, A. Brázdová, R. Liboska, I. Štěpánek, Z. Vavřina, T. Jandušík, R. Nencka, L. Rulíšek, E. Bouřa, J. Brynda, O. Páv, G. Birkuš, *J. Med. Chem.* **2019**, *62*, 10676–10690.
[16] Y. Li, A. Fin, A. R. Rovira, Y. Su, A. B. Dippel, J. A. Valderrama, A. M. Riestra, V. Nizet, M. C. Hammond, Y. Tor, *ChemBioChem* **2020**, *21*, 2595–2598.
[17] S. M. Ching, W. J. Tan, K. L. Chua, Y. Lam, *Bioorg. Med. Chem.* **2010**, *18*, 6657–6665.
[18] X. Zhang, H. Shi, J. Wu, X. Zhang, L. Sun, C. Chen, Z. J. Chen, *Mol. Cell* **2013**, *51*, 226–235.
[19] A. Fuchs, P. Mannhardt, P. Hirschle, H. Wang, I. Zaytseva, Z. Ji, O. M. Yaghi, S. Wuttke, E. Ploetz, *Adv. Mater.* **2021**, *34*, 2104530.
[20] a) G. I. Redford, R. M. Clegg, *J. Fluoresc.* **2005**, *15*, 805; b) M. A. Digman, V. R. Caiolfa, M. Zamai, E. Gratton, *Biophys. J.* **2008**, *94*, L14-L16; c) G. Weber, *J. Phys. Chem.* **1981**, *85*, 949–953; d) D. M. Jameson, E. Gratton, R. D. Hall, *Appl. Spectrosc. Rev.* **1984**, *20*, 55–106.

Manuscript received: January 4, 2022
Revised manuscript received: February 12, 2022
Accepted manuscript online: February 21, 2022
Version of record online: ■■, ■■■

© 2022 The Authors. ChemBioChem published by Wiley-VCH GmbH

RESEARCH ARTICLE

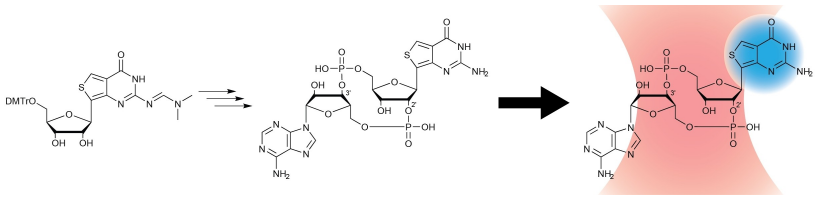

S. Veth, A. Fuchs, D. Özdemir, Dr. C. Dialer, Dr. D. J. Drexler, F. Knechtel, Dr. G. Witte, Prof. K.-P. Hopfner, Prof. T. Carell, Dr. E. Ploetz**

Chemical Synthesis of the Fluorescent, Cyclic Dinucleotides cthGAMP

The cyclic dinucleotide (CDN) 2′3′-cGAMP is an essential second messenger for the innate immune system of mammals. The organic synthesis of an intrinsically fluorescent mimic provided large quantities for cell feeding studies, examination of biological activity and two-photon excitation microscopy.

ChemBioChem

Supporting Information

Chemical Synthesis of the Fluorescent, Cyclic Dinucleotides $c^{th}GAMP$

Simon Veth[+], Adrian Fuchs[+], Dilara Özdemir[+], Clemens Dialer, David Jan Drexler, Fabian Knechtel, Gregor Witte, Karl-Peter Hopfner, Thomas Carell,* and Evelyn Ploetz*

TABLE OF CONTENTS

1. EXPERIMENTAL SECTION

1.1 Chemicals

Reagents were purchased from *Sigma-Aldrich*, *Acros Organics*, *TCI Europe*, *Link Technologies* and *Alfa Aesar*, were stored under nitrogen and were used without further purification unless otherwise specified. Dry solvents were purchased from *Acros Organics*, were stored under argon over molecular sieves and used as received applying standard *Schlenk* techniques. HPLC grade solvents were purchased from VWR. Water was purified by a *Milli-Q Plus* system from *Merck Millipore*.

Chemicals used include acetic acid (HOAc), allyl alcohol, BTT activator, 2-cyanoethyl *N*,*N*,*N*',*N*'-tetraisopropylphosphorodiamidite, dichloroacetic acid (DCA), 2-[4-(2-hydroxyethyl)piperazine-1-yl]ethanesulfonic acid (HEPES; Sigma Aldrich), imidazole, 1-methylimidazole, methoxytrimethylsilane, pyridinium trifluoroacetate, silica gel, sodium bisulfite, sodium hydrogen carbonate, sodium iodide, sodium sulfate, triethylamine (NEt_3), triethylamine trihydrofluoride ($NEt_3 \cdot 3HF$) 2,4,6-triisopropyl-benzolsulfonylchloride, and tert-Butyldimethylsilyl chloride (TBSCl), *tert*-Butyl hydroperoxide (*t*-BuOOH).

Dry solvents comprise acetone, acetonitrile (MeCN), deuterated chloroform-d ($CDCl_3$), dichloromethane (DCM), ethylacetate (EtOAc), iso-hexane (iHex), methanol (MeOH), pyridine, tetrahydrofuran (THF), toluene, were stored (if necessary) under septum and used without further purification.

For cell culture, we used Roswell Park Memorial 1640 medium (RPMI 1640; ThermoFisher Scientific), L-Alanyl-L-Glutamine (Sigma Aldrich), Pen-Strep (Sigma Aldrich), HEPES (1M, Sigma Aldrich), Lipofectamine™ RNAiMAX (Thermo Fischer), and Poly-D-Lysine (PDL, Sigma Aldrich), which were stored at 4^0C and used only under sterile conditions. Antibiotics, including blasticidin, Normocin™, and Zeocin™ were purchased from Invivogen and kept at -20^0C. Fetal Bovine Serum (FBS, Pan Biotech), Quanti-Luc™ (Invivogen) were aliquoted and stored at -20^0C as well. Phosphate buffered saline (PBS, Sigma Aldrich) was kept at room temperature.

1.2 Methods and Characterization

Photophysical characterization by UV-Vis and Fluorescence spectroscopy: UV-Vis spectra of compounds were recorded using a spectrophotometer (Implen Nanophotometer N60). The weight purity of CDNs was measured by UV spectroscopy using the estimated extinction coefficient at maximum absorbance, i.e. 25050 M^{-1} cm^{-1} at 256 nm for 2'3'- or 3'3'-cGAMP and 4150 M^{-1} cm^{-1} at 321 nm for 2'3'- or 3'3'-c^{th}GAMP. Fluorescence based measurements were performed on a FLS 1000 Fluorimeter (Edinburgh Instruments). Emission and excitation spectra were recorded on a photon multiplier tube (PMT 900 detector, Hamamatsu) by exciting the sample with a 450 W Xenon lamp, an excitation/emission slit width of 1 nm and 0.5 nm steps with 1 s of dwell time.

Infrared (IR) spectroscopy: IR spectroscopy was performed on an FT-IR spectrometer (PerkinElmer Spectrum BX FT-IR) with a diamond-ATR (ATTenuated Total Reflection) mode Samples were applied directly on the ATR unit. The range of analysis was 4500 to 600 cm^{-1}.

TLC: All reactions were monitored with analytical TLC (*Merck* silica gel 60 F254).

RP-HPLC: Separations and purifications by reversed-phase HPLC were carried out with an *Agilent Technologies 1260 Infinity II* machine consisting of *1260 Quat Pump VL*, *1260 man. Inj.* and *1260 MWD* using a *VP 250/10 NUCLEODUR 100-5 C18ec* column (*Macherey-Nagel*). The flow rate applied was 0.5 mL/min.

RP-LCMS: LC-MS and low resolution ESI-MS were measured on a *Dionex* micro UHPLC-System (mobile phase: water and acetonitrile with 0.01 % formic acid) using a *Hypersil Gold* C18 selectivity column (100 × 2.1 mm) coupled to a *MSQ Plus* single-quadrupole mass spectrometer.

NMR spectroscopy: NMR spectra were measured on a Bruker Ascend 400 or Bruker ARX 600 at room temperature operating at 400 MHz or 600 MHz for 1H-nuclei and at 101 or 151 MHz for 13C-nuclei. For 29Si-NMR and 31P-NMR measurements, 80 MHz or 162 MHz measurements respectively, were performed.
The chemical shift (δ) in the NMR spectra is reported in parts per million (ppm) and referenced to the residual solvent signal. Measurements were performed in $CDCl_3$ or D_2O. The spectra were referenced to the residual protons and carbons of the solvent (CDCl3: $\delta(^1H)$ = 7.26 ppm; $\delta(^{13}C)$ = 39.52 ppm; D_2O $\delta(^1H)$ = 4.79 ppm). All spectra were analyzed with the software *MestReNova* from *Mestrelab Research*.

Mass spectroscopy: High resolution mass spectra (HRMS) were recorded on a Thermo Finnigan MAT 95 (EI) and a Thermo Finnigan LTQ FTCR (ESI)

Isothermal titration calorimetry: ITC measurements were carried out on a Malvern PEAQ-ITC system with 52 µM (mSTING) or 251 µM (hSTING) protein in ITC-buffer (20 mM HEPES pH 7.5, 150 mM NaCl) in the cell. Compound **2** was titrated in a concentration of 200 µM (mSTING) into the cell by 19 injections of 2 µL or in a concentration of 600 µM (hSTING) into the cell by 13 injections of 3 µL, spaced 150 seconds apart, at 25 °C. The results were analyzed using the MicroCal PEAQ-ITC analysis software provided with the instrument. All titrations were repeated to confirm robustness of the assay.

Nano differential scanning fluorimetry: Thermal melting experiments of STING constructs were performed using a Tycho NT.6 instrument (NanoTemper Technologies). In brief, the samples were heated up in a glass capillary and while heating, the internal fluorescence at 330 nm and 350 nm was recorded. Data analysis, data smoothing, and calculation of derivatives was done using the internal evaluation features of the NT.6 instrument. All measurements were repeated to confirm robustness of the assay.

2. SYNTHESIS STEPS AND CHARACTERIZATION OF C-THGAMP

Unless otherwise specified, all reactions were magnetically stirred under an N_2 atmosphere. Reactions vessels were dried under high vacuum at 550 °C prior to use. Synthesis of c-thGAMPs was verified by a set of different techniques, including RP-HPLC, 1H-NMR, 13C-NMR, 29Si-NMR, Infrared spectroscopy, ESI-HRMS and ESI-LRMS.

2.1. Preparation of 5'-*O*-DMTr-N^2-DMF-2'-*O*-TBS-thguanosine (6) and 5'-*O*-DMTr-N^2-DMF-3'-*O*-TBS-thguanosine (5)

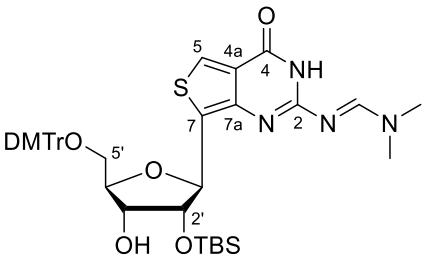

6

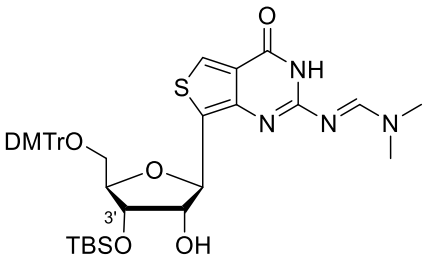

5

To a stirred solution of 5'-*O*-DMTr-N^2-DMF-thguanosine (**4**, 4.60 g, 7.00 mmol, 1.0 eq.) in dry pyridine (125 mL), imidazole (0.95 g, 14.1 mmol, 1.0 eq.) and TBSCl (1.59 g, 10.5 mmol, 1.5 eq.) were added and the reaction mixture was stirred under nitrogen atmosphere for 16 hours at rt. The reaction was quenched by the addition of MeOH (15 mL), all volatile components were removed *in vacuo* and the residue was co-evaporated with toluene (2 x 100 mL). The crude product was purified by column chromatography (silica gel, *i*Hex/EtOAc, 4:1 → 2:1 → 1:1 → 1:3 → 1:4 → EtOAc) to yield the title compounds (3.84 g, 4.98 mmol, 71%) as a colorless foam. The product was a mixture of the 2'-*O*-TBS regioisomer **6** and 3'-*O*-TBS regioisomer **5** inseparable by flash column chromatography and was used without further purification.

For analysis of **5** and **6** a small sample was purified by preparative RP-HPLC (isocratic elution, 80% MeCN in H_2O for 30 min, R_t(**6**) = 11.4 – 14.2 min, R_t(**5**) = 16.0 – 19.4 min).

2.1.1. Compound 6 (2'-O-TBS)

R_f = 0.58 (DCM/MeOH, 10:1).

^{1}H-NMR (400 MHz, $CDCl_3$): δ/ppm = 8.68 (s, 1H, H-dmf), 8.66 (s, 1H, N*H*), 8.16 (s, 1H, H-5), 7.55 – 7.51 (m, 2H, Ph-*o*-C*H*), 7.44 – 7.38 (m, 4H, MeO-Ph-*o*-C*H*), 7.30 – 7.25 (m, 2H, Ph-*m*-C*H*), 7.23 – 7.17 (m, 1H, Ph-*p*-C*H*), 6.84 – 6.80 (m, 4H, MeO-Ph-*m*-C*H*), 5.63 (d, ^3J = 6.9 Hz, 1H, H-1'), 4.45 (dd, ^3J = 6.9 Hz, ^3J = 4.9 Hz, 1H, H-2'), 4.18 – 4.15 (m, 1H, H-4'), 4.16 – 4.14 (m, 1H, H-3'), 3.784 (s, 3H, OCH_3), 3.780 (s, 3H, OCH_3), 3.50 (dd, ^2J = 10.2 Hz, ^3J = 2.5 Hz, 1H, H_a-5'), 3.19 (dd, ^2J = 10.2 Hz, ^3J = 3.5 Hz, 1H, H_b-5'), 3.13 (s, 3H, CH_3-dmf), 3.08 (s, 3H, CH_3-dmf), 2.88 (d, ^3J = 3.1 Hz, 1H, OH-3'), 0.83 (s, 9H, SiC(CH_3)$_3$), -0.03 (s, 3H, Si(CH_3)$_2$), -0.16 (s, 3H, Si(CH_3)$_2$).

^{13}C-NMR (100.6 MHz, $CDCl_3$): δ/ppm = 159.7 (C-4), 158.54 (MeO-*C*-Ph), 158.52 (MeO-*C*-Ph), 157.9 (*C*H-dmf), 153.8 (C-2), 147.9 (C-7a), 145.1 (Ph-*C*C), 136.31 (MeO-Ph-*C*C), 136.11 (MeO-Ph-*C*C), 130.30 (2x MeO-Ph-*o*-*C*H), 130.26 (2x MeO-Ph-*o*-*C*H), 128.9 (C-7), 128.4 (2x

Ph-*o*-*C*H), 127.9 (2x Ph-*m*-*C*H), 126.8 (Ph-*p*-*C*H), 125.9 (C-5), 125.4 (C-4a), 113.23 (2x MeO-Ph-*m*-*C*H), 113.21 (2x MeO-Ph-s*m*-*C*H), 86.2 (*C*Ph(Ph-OMe)$_2$), 84.0 (C-4'), 79.6 (C-2'), 77.0 (C-1'), 73.0 (C-3'), 64.3 (C-5'), 55.3 (2x O*C*H$_3$), 41.3 (*C*H$_3$-dmf), 35.1 (*C*H$_3$-dmf), 25.8 (SiC(*C*H$_3$)$_3$), 18.1 (Si*C*(CH$_3$)$_3$), -4.8 (Si(*C*H$_3$)$_2$), -5.1 (Si(*C*H$_3$)$_2$).

^{29}Si-NMR (80 MHz, CDCl$_3$): *δ*/ppm = 23.5.

IR (ATR): $\tilde{\nu}$/cm^{-1} = 2929, 2248, 1679, 1629, 1572, 1508, 1250, 1112, 835, 729.

ESI-HRMS calculated for $[C_{41}H_{50}N_4O_7SSi + H]^+$: 771.3242, found: 771.3243.

calculated for $[C_{41}H_{50}N_4O_7SSi - H]^-$: 769.3096, found: 769.3105.

2.1.2. Compound 5 (3'-*O*-TBS)

***R*$_f$** = 0.55 (DCM/MeOH, 10:1).
^{1}H-NMR (400 MHz, CDCl$_3$): *δ*/ppm = 9.03 (s, 1H, N*H*), 8.61 (s, 1H, H-dmf), 8.12 (s, 1H, H-5), 7.52 – 7.47 (m, 2H, Ph-*o*-C*H*), 7.41 – 7.35 (m, 4H, MeO-Ph-*o*-C*H*), 7.29 – 7.24 (m, 2H, Ph-*m*-C*H*), 7.22 – 7.17 (m, 1H, Ph-*p*-C*H*), 6.83 – 6.79 (m, 4H, MeO-Ph-*m*-C*H*), 5.53 (d, ^3J = 7.0 Hz, 1H, H-1'), 4.31 (dd, ^3J = 5.3 Hz, ^3J = 3.3 Hz, 1H, H-3'), 4.24 (dd, ^3J = 7.0 Hz, ^3J = 5.3 Hz, 1H, H-2'), 4.11 (dd, ^3J = 6.9 Hz, ^3J = 3.3 Hz, 1H, H-4'), 3.775 (s, 3H, OC*H*$_3$), 3.773 (s, 3H, OC*H*$_3$), 3.42 (dd, ^2J = 10.3 Hz, ^3J = 3.4 Hz, 1H, H$_a$-5'), 3.14 (dd, ^2J = 10.3 Hz, ^3J = 3.9 Hz, 1H, H$_b$-5'), 3.12 (s, 3H, C*H*$_3$-dmf), 3.05 (s, 3H, C*H*$_3$-dmf), 0.88 (s, 9H, SiC(C*H*$_3$)$_3$), 0.06 (s, 3H, Si(C*H*$_3$)$_2$), -0.02 (s, 3H, Si(C*H*$_3$)$_2$).

^{13}C-NMR (100.6 MHz, CDCl$_3$): *δ*/ppm = 159.7 (C-4), 158.50 (MeO-*C*-Ph), 158.49 (MeO-*C*-Ph), 157.8 (*C*H-dmf), 154.1 (C-2), 146.3 (C-7a), 144.9 (Ph-*C*C), 136.2 (MeO-Ph-*C*C), 136.0 (MeO-Ph-*C*C), 130.2 (4x MeO-Ph-*o*-*C*H), 129.5 (C-7), 128.3 (2x Ph-*o*-*C*H), 127.9 (2x Ph-*m*-*C*H), 126.8 (Ph-*p*-*C*H), 125.4 (C-4a), 125.1 (C-5), 113.19 (2x MeO-Ph-*m*-*C*H), 113.18 (2x MeO-Ph-*m*-*C*H), 86.2 (*C*Ph(Ph-OMe)$_2$), 84.0 (C-4'), 78.3 (C-1'), 77.8 (C-2'), 73.7 (C-3'), 63.5 (C-5'), 55.3 (2x O*C*H$_3$), 41.3 (*C*H$_3$-dmf), 35.1 (*C*H$_3$-dmf), 25.9 (SiC(*C*H$_3$)$_3$), 18.3 (Si*C*(CH$_3$)$_3$), -4.5 (Si(*C*H$_3$)$_2$), -4.6 (Si(*C*H$_3$)$_2$).

^{29}Si-NMR (80 MHz, CDCl$_3$): *δ*/ppm = 22.3.

IR (ATR): $\tilde{\nu}$/cm^{-1} = 2930, 2247, 1680, 1629, 1572, 1508, 1258, 1111, 832, 725.

ESI-HRMS calculated for $[C_{41}H_{50}N_4O_7SSi + H]^+$: 771.3242, found: 771.3239.

calculated for $[C_{41}H_{50}N_4O_7SSi - H]^-$: 769.3096, found: 769.3107.

2.2. Peparation of *N*^{2}-DMF-3'-*O*-PO(Oallyl,OCE)-2'-*O*-TBS-thguanosine (8) and *N*^{2}-DMF-2'-*O*-PO(Oallyl,OCE)-3'-*O*-TBS-thguanosine (7)

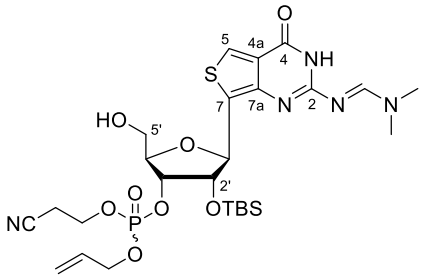

8

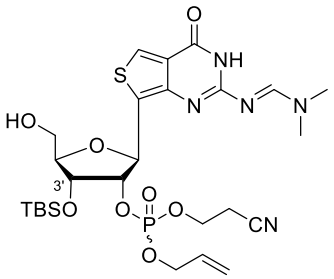

7

To a stirred solution of **5** and **6** (2.30 g, 2.98 mmol, 1.0 eq.) in dry DCM (23.1 mL), 2-cyanoethyl *N*,*N*,*N*',*N*'-tetraisopropylphosphorodiamidite (1.14 mL, 3.58 mmol, 1.2 eq.) was added under argon atmosphere at rt. After stirring for 10 min pyridinium trifluoroacetate (1.14 mL, 3.58 mmol, 1.2 eq.) was added and the reaction mixture was stirred for additional 3 h. The reaction progress was monitored by TLC. After full conversion allyl alcohol (1.01 mL, 14.9 mmol, 5.0 eq.) and BTT activator (0.3 M in MeCN, 19.9 mL, 5.96 mmol, 2.0 eq.) were added and the reaction mixture was stirred for 90 min. The intermediate products were oxidized by addition of *t*-BuOOH (5.5 M in decane, 1.60 mL, 8.94 mmol, 3.0 eq.) and further stirring for 30 min. The reaction mixture was cooled to 0 °C and the reaction was quenched by the addition of an aqueous solution of $NaHSO_3$ (500 mg/mL, 3.74 mL, 17.8 mmol, 6.0 eq.). The resulting yellow suspension was diluted with EtOAc (100 mL) and washed with brine (100 mL). The aqueous layer was extracted with EtOAc (3 x 50 mL) and the combined organic layers were dried over Na_2SO_4, filtered and concentrated *in vacuo*.
The residue was dissolved in DCM (48.0 mL) and H_2O (0.54 mL) and a solution of DCA (6% v/v in DCM, 48.0 mL) was added. The resulting red solution was stirred for 15 min at rt and quenched by the addition of sat. aq. $NaHCO_3$ solution (200 mL). The resulting yellow suspension was diluted with EtOAc (500 mL) and H_2O (200 mL), the layers were separated and the aqueous layer was extracted with EtOAc (2 × 300 mL). The combined organic layers were dried over Na_2SO_4, filtered and concentrated under reduced pressure. The crude product was purified by column chromatography (silica gel, DCM/MeOH, 49:1 → 19:1) to yield the title compounds (1.32 g, 2.06 mmol, 69%) as a yellow foam. The product was a mixture of 4 isomers: 2 diastereomers of **8 (a/b)** and 2 diastereomers of **7 (a/b)**, inseparable by flash column chromatography and was used without further purification.

For analysis of **8a/8b** and **7a/7b** a small sample was purified by preparative RP-HPLC (gradient elution, 30% to 60% MeCN in H_2O over 45 min, R_t(**8a**) = 24.5 – 26.0 min, R_t(**8b**) = 26.4 – 28.8 min, R_t(**7a**) = 31.2 – 32.7 min, R_t(**7b**) = 33.3 – 35.8 min).

2.2.1. Diastereomer 8a (2'-*O*-TBS)

R_f = 0.41 (DCM/MeOH, 10:1).
R_t (RP-LCMS) = 5.91 min (gradient elution, 5 % to 80 % MeCN in H_2O over 7 min).
^{1}H-NMR (400 MHz, $CDCl_3$): *δ*/ppm = 8.99 (s, 1H, N*H*), 8.39 (s, 1H, H-dmf), 8.09 (s, 1H, H-5), 6.03 – 5.91 (m, 1H, OCH_2CH=CH_2), 5.56 (bs, 1H, OH-5'), 5.44 – 5.37 (m, 1H, OCH_2CH=CH_2), 5.32 – 5.28 (m, 1H, OCH_2CH=CH_2), 5.09 – 5.03 (m, 1H, H-2'), 4.95 – 4.91 (m, 1H, H-3'), 4.93 (d, ^3J = 8.8 Hz, 1H, H-1'), 4.65 – 4.58 (m, 2H, OCH_2CH=CH_2), 4.40 – 4.36 (m, 1H, H-4'), 4.34 – 4.26 (m, 2H, OCH_2CH_2CN), 3.84 (dd, ^2J = 12.5 Hz, ^3J = 2.3 Hz, 1H, H_a-5'), 3.71 (d, ^2J = 12.5 Hz, 1H, H_b-5'), 3.15 (s, 3H, CH_3-dmf), 3.07 (s, 3H, CH_3-dmf), 2.81 – 2.76 (m, 2H, OCH_2CH_2CN), 0.75 (s, 9H, $SiC(CH_3)_3$), -0.16 (s, 3H, $Si(CH_3)_2$), -0.28 (s, 3H, $Si(CH_3)_2$).

^{13}C-NMR (100.6 MHz, $CDCl_3$): *δ*/ppm = 159.4 (C-4), 158.1 (*C*H-dmf), 155.3 (C-2), 146.4 (C-7a), 132.1 (d, OCH_2CH=CH_2), 126.3 (C-4a), 125.4 (C-5), 124.5 (C-7), 119.1 (OCH_2CH=CH_2), 116.4 (OCH_2CH_2CN), 85.0 (d, C-4'), 80.7 (d, C-3'), 79.1 (C-1'), 75.1 (d, C-2'), 69.0 (d, OCH_2CH=CH_2), 63.0 (C-5'), 62.1 (d, OCH_2CH_2CN), 41.2 (CH_3-dmf), 35.1 (CH_3-dmf), 25.7 ($SiC(CH_3)_3$), 19.7 (d, OCH_2CH_2CN), 18.2 ($SiC(CH_3)_3$), -5.0 ($Si(CH_3)_2$), -5.3 ($Si(CH_3)_2$).

^{29}Si-NMR (80 MHz, $CDCl_3$): *δ*/ppm = 23.0.

^{31}P-NMR (162 MHz, $CDCl_3$): *δ*/ppm = −1.5 - −1.8 (m).

IR (ATR): $\tilde{\nu}$/cm^{-1} = 3191, 2929, 1681, 1630, 1565, 1463, 1421, 1257, 1022, 726.

ESI-LRMS calculated for $[C_{26}H_{40}N_5O_8PSSi + H]^+$: 642.2, found: 642.4.

ESI-HRMS calculated for $[C_{26}H_{40}N_5O_8PSSi + H]^+$: 642.2177, found: 642.2180.

calculated for $[C_{26}H_{40}N_5O_8PSSi + Na]^+$: 664.1996, found: 664.2003.

2.2.2. Diastereomer 8b (2'-*O*-TBS)

R_f = 0.41 (DCM/MeOH, 10:1).
R_t (RP-LCMS) = 6.08 min (gradient elution, 5 % to 80 % MeCN in H_2O over 7 min).
^{1}H-NMR (400 MHz, $CDCl_3$): *δ*/ppm = 9.01 (s, 1H, N*H*), 8.36 (s, 1H, H-dmf), 8.06 (s, 1H, H-5), 6.01 – 5.88 (m, 1H, OCH_2CH=CH_2), 5.57 (bs, 1H, OH-5'), 5.41 – 5.35 (m, 1H, OCH_2CH=CH_2), 5.30 – 5.25 (m, 1H, OCH_2CH=CH_2), 5.04 – 4.98 (m, 1H, H-2'), 4.93 – 4.88 (m, 1H, H-3'), 4.92 (d, ^3J = 8.8 Hz, 1H, H-1'), 4.64 – 4.58 (m, 2H, OCH_2CH=CH_2), 4.39 – 4.36 (m, 1H, H-4'), 4.28 – 4.21 (m, 2H, OCH_2CH_2CN), 3.83 (dd, ^2J = 12.5 Hz, ^3J = 2.3 Hz, 1H, H_a-5'), 3.71 (d, ^2J = 12.5 Hz, 1H, H_b-5'), 3.12 (s, 3H, CH_3-dmf), 3.04 (s, 3H, CH_3-dmf), 2.79 – 2.74 (m, 2H, OCH_2CH_2CN), 0.73 (s, 9H, $SiC(CH_3)_3$), -0.18 (s, 3H, $Si(CH_3)_2$), -0.31 (s, 3H, $Si(CH_3)_2$).

^{13}C-NMR (100.6 MHz, $CDCl_3$): *δ*/ppm = 159.3 (C-4), 158.0 (*C*H-dmf), 155.3 (C-2), 146.4 (C-7a), 132.1 (d, OCH_2CH=CH_2), 126.3 (C-4a), 125.2 (C-5), 124.5 (C-7), 119.2 (OCH_2CH=CH_2), 116.4 (OCH_2CH_2CN), 85.0 (d, C-4'), 80.7 (d, C-3'), 79.1 (C-1'), 75.1 (d, C-2'), 69.0 (d, OCH_2CH=CH_2), 63.0 (C-5'), 62.0 (d, OCH_2CH_2CN), 41.1 (CH_3-dmf), 35.0 (CH_3-dmf), 25.7 ($SiC(CH_3)_3$), 19.8 (d, OCH_2CH_2CN), 18.1 ($SiC(CH_3)_3$), -5.1 ($Si(CH_3)_2$), -5.4 ($Si(CH_3)_2$).

^{29}Si-NMR (80 MHz, $CDCl_3$): *δ*/ppm = 22.9.

^{31}P-NMR (162 MHz, $CDCl_3$): *δ*/ppm = −1.6 - −1.9 (m).

IR (ATR): $\tilde{\nu}$/cm^{-1} = 3397, 2929, 1681, 1631, 1566, 1422, 1280, 1259, 1023, 726.

ESI-LRMS calculated for $[C_{26}H_{40}N_5O_8PSSi + H]^+$: 642.2, found: 642.4.

ESI-HRMS calculated for $[C_{26}H_{40}N_5O_8PSSi + H]^+$: 642.2177, found: 642.2180.

calculated for $[C_{26}H_{40}N_5O_8PSSi + Na]^+$: 664.1996, found: 664.2003.

2.2.3. Diastereomer 7a (3'-*O*-TBS)

R_f = 0.41 (DCM/MeOH, 10:1).
R_t (RP-LCMS) = 6.30 min (gradient elution, 5 % to 80 % MeCN in H_2O over 7 min).
^{1}H-NMR (400 MHz, $CDCl_3$): δ/ppm = 8.81 (s, 1H, N*H*), 8.57 (s, 1H, H-dmf), 8.09 (s, 1H, H-5), 5.76 – 5.65 (m, 1H, OCH_2CH=CH_2), 5.56 – 5.49 (m, 1H, H-2'), 5.27 (d, ^3J = 6.9 Hz, 1H, H-1'), 5.22 – 5.16 (m, 1H, OCH_2CH=CH_2), 5.15 – 5.11 (m, 1H, OCH_2CH=CH_2), 4.48 (dd, ^3J = 4.6 Hz, ^3J = 3.0 Hz, 1H, H-3'), 4.32 – 4.27 (m, 2H, OCH_2CH=CH_2), 4.18 – 4.08 (m, 1H, OCH_2CH_2CN), 4.11 – 4.07 (m, 1H, H-4'), 4.02 – 3.94 (m, 1H, OCH_2CH_2CN), 3.87 (dd, ^2J = 12.4 Hz, ^3J = 2.3 Hz, 1H, H_a-5'), 3.64 (dd, ^2J = 12.4 Hz, ^3J = 1.8 Hz, 1H, H_b-5'), 3.18 (s, 3H, CH_3-dmf), 3.05 (s, 3H, CH_3-dmf), 2.70 – 2.54 (m, 2H, OCH_2CH_2CN), 0.93 (s, 9H, $SiC(CH_3)_3$), 0.14 (s, 3H, $Si(CH_3)_2$), 0.12 (s, 3H, $Si(CH_3)_2$).

^{13}C-NMR (100.6 MHz, $CDCl_3$): δ/ppm = 159.2 (C-4), 158.6 (*C*H-dmf), 155.1 (C-2), 146.5 (C-7a), 131.8 (d, OCH_2CH=CH_2), 126.3 (C-4a), 125.5 (C-5), 124.3 (C-7), 118.7 (OCH_2CH=CH_2), 116.3 (OCH_2CH_2CN), 86.3 (C-4'), 79.4 (d, C-2'), 77.6 (d, C-1'), 72.9 (d, C-3'), 68.7 (d, OCH_2CH=CH_2), 62.5 (C-5'), 61.9 (d, OCH_2CH_2CN), 41.3 (*C*H$_3$-dmf), 35.1 (*C*H$_3$-dmf), 25.9 ($SiC(CH_3)_3$), 19.6 (d, OCH_2CH_2CN), 18.3 ($SiC(CH_3)_3$), -4.5 ($Si(CH_3)_2$), -4.7 ($Si(CH_3)_2$).

^{29}Si-NMR (80 MHz, $CDCl_3$): δ/ppm = 22.1.

IR (ATR): $\tilde{\nu}$/cm^{-1} = 3438, 2929, 1682, 1630, 1568, 1423, 1352, 1260, 1032, 838.

ESI-LRMS calculated for $[C_{26}H_{40}N_5O_8PSSi + H]^+$: 642.2, found: 642.4.

ESI-HRMS calculated for $[C_{26}H_{40}N_5O_8PSSi + H]^+$: 642.2177, found: 642.2176.

calculated for $[C_{26}H_{40}N_5O_8PSSi + Na]^+$: 664.1996, found: 664.1999.

2.2.4. Diastereomer 7b (3'-*O*-TBS)

R_f = 0.41 (DCM/MeOH, 10:1).
R_t (RP-LCMS) = 6.43 min (gradient elution, 5 % to 80 % MeCN in H_2O over 7 min).
^{1}H-NMR (400 MHz, $CDCl_3$): δ/ppm = 8.87 (s, 1H, N*H*), 8.59 (s, 1H, H-dmf), 8.09 (d, ^4J = 1.1 Hz, 1H, H-5), 5.86 – 5.75 (m, 1H, OCH_2CH=CH_2), 5.55 – 5.48 (m, 1H, H-2'), 5.30 – 5.24 (m, 1H, OCH_2CH=CH_2), 5.29 (d, ^3J = 6.9 Hz, 1H, H-1'), 5.22 – 5.18 (m, 1H, OCH_2CH=CH_2), 4.53 – 4.45 (m, 1H, OCH_2CH=CH_2), 4.48 – 4.45 (m, 1H, H-3'), 4.37 – 4.29 (m, 1H, OCH_2CH=CH_2), 4.11 – 4.08 (m, 1H, H-4'), 4.00 – 3.85 (m, 2H, OCH_2CH_2CN), 3.87 (dd, ^2J = 12.4 Hz, ^3J = 2.0 Hz, 1H, H_a-5'), 3.65 (dd, ^2J = 12.4 Hz, ^3J = 1.7 Hz, 1H, H_b-5'), 3.19 (s, 3H, CH_3-dmf), 3.06 (s, 3H, CH_3-dmf), 2.59 – 2.42 (m, 2H, OCH_2CH_2CN), 0.92 (s, 9H, $SiC(CH_3)_3$), 0.14 (s, 3H, $Si(CH_3)_2$), 0.12 (s, 3H, $Si(CH_3)_2$).

^{13}C-NMR (100.6 MHz, $CDCl_3$): δ/ppm = 159.2 (C-4), 158.7 (*C*H-dmf), 155.2 (C-2), 146.5 (C-7a), 131.9 (d, OCH_2CH=CH_2), 126.3 (C-4a), 125.5 (C-5), 124.5 (C-7), 118.8 (OCH_2CH=CH_2), 116.3 (OCH_2CH_2CN), 86.3 (C-4'), 79.5 (d, C-2'), 77.7 (d, C-1'), 72.9 (d, C-3'), 68.8 (d,

OCH_2CH=CH_2), 62.5 (C-5'), 61.9 (d, O$CH_2$$CH_2$CN), 41.4 ($CH_3$-dmf), 35.2 ($CH_3$-dmf), 25.9 (SiC($CH_3$)$_3$), 19.5 (d, O$CH_2$$CH_2$CN), 18.3 (Si$C$($CH_3$)$_3$), -4.5 (Si($CH_3$)$_2$), -4.8 (Si($CH_3$)$_2$).

^{29}Si-NMR (80 MHz, $CDCl_3$): δ/ppm = 22.0.

IR (ATR): $\tilde{\nu}$/cm^{-1} = 3410, 2928, 1685, 1631, 1571, 1424, 1352, 1261, 1116, 1034.

ESI-LRMS calculated for $[C_{26}H_{40}N_5O_8PSSi + H]^+$: 642.2, found: 642.4.

ESI-HRMS calculated for $[C_{26}H_{40}N_5O_8PSSi + H]^+$: 642.2177, found: 642.2176.

calculated for $[C_{26}H_{40}N_5O_8PSSi + Na]^+$: 664.1996, found: 664.1999.

2.3. *N*6''-Bz-2'''-*O*-TBS-adenosin-3'''-5'-*O*,*O*-PO(OCE)-*N*^{2}-DMF-3'-*O*-PO(Oallyl,OCE)-2'-*O*-TBS-thguanosine (10) and *N*6''-Bz-2'''-*O*-TBS-adenosin-3'''-5'-*O*,*O*-PO(OCE)-*N*^{2}-DMF-3'-*O*-PO(Oallyl,OCE)-2'-*O*-TBS-thguanosine (9)

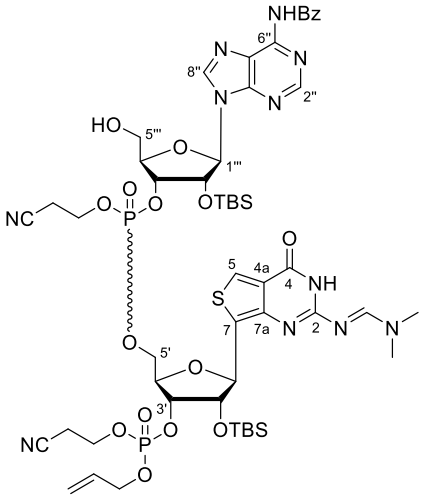

10

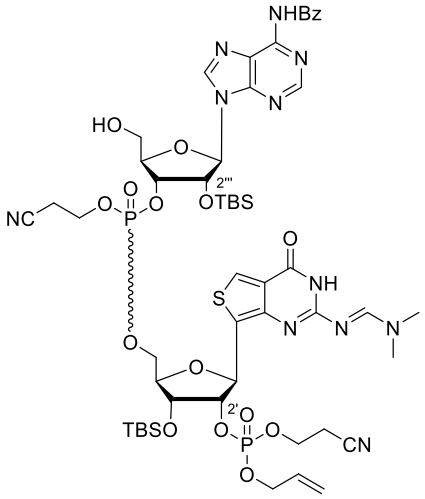

9

To a stirred solution of the diastereomeric mixture of **7** and **8** (1.32 g, 2.06 mmol, 1.0 eq.) in dry MeCN (12.7mL), a solution of DMT-2'-O-TBS-rA(Bz) phosphoramidite (2.24 g, 2.27 mmol, 1.10 eq.) in dry MeCN (1.00 mL) was added under argon atmosphere at rt. After stirring for 10 min BTT activator (0.3 M in MeCN, 13.7 mL, 4.12 mmol, 2.0 eq.) was and the reaction mixture was stirred for additional 90 min at rt. The intermediate products were oxidized by addition of *t*-BuOOH (5.5 M in decane, 1.12 mL, 6.18 mmol, 3.0 eq.) and further stirring for 30 min. The reaction mixture was cooled to 0 °C and the reaction was quenched by the addition of an aqueous solution of $NaHSO_3$ (500 mg/mL, 2.57 mL, 12.4 mmol, 6.0 eq.). The resulting yellow suspension was diluted with EtOAc (50 mL) and washed with brine (50 mL). the aqueous layer was extracted with EtOAc (3 x 25 mL) and the combined organic layers were dried over Na_2SO_4, filtered and concentrated under reduced pressure.
The residue was dissolved in DCM (18.2 mL) and H_2O (0.21 mL) and a solution of DCA (6% v/v in DCM, 18.2 mL) was added. The resulting red solution was stirred for 15 min at rt and quenched by the addition of sat. aq. $NaHCO_3$ solution (100 mL). The resulting yellow suspension was diluted with EtOAc (300 mL) and H_2O (100 mL), the layers were separated and the aqueous layer was extracted with EtOAc (2 × 300 mL). The combined organic layers were dried over Na_2SO_4, filtered and concentrated *in vacuo*. The crude product was purified by column chromatography (silica gel, DCM/MeOH, 49:1 → 19:1) to yield the title compounds (1.61 g, 1.29 mmol, 63%) as a yellow foam. The product was a mixture of 8 isomers: 4 diastereomers of **10** and 4 diastereomers of **9**, inseparable by flash column chromatography and was used without further purification.

For analysis of **10** and **9** a small sample was purified by preparative RP-HPLC (gradient elution, 30% to 60% MeCN in H_2O over 45 min, R_t(**10**) = 21.9 – 22.9 min, R_t(**9**) = 36.4 – 37.3 min). For compounds **10** and **9** a single diastereomer was isolated for analysis.

2.3.1. Compound 10 (3',3'-Dimer)

R_f = 0.27 (DCM/MeOH, 10:1).
R_t (RP-LCMS) = 7.31, 7.45 min (gradient elution, 5 % to 80 % MeCN in H_2O over 7 min).
^{1}H-NMR (400 MHz, $CDCl_3$): δ/ppm = 9.25 (bs, 1H, A-N*H*), 8.80 (s, 1H, H-2''), 8.65 (s, 1H, H-dmf), 8.57 (bs, 1H, G-N*H*), 8.133 (s, 1H, H-5), 8.128 (s, 1H, H-8''), 8.06 – 8.01 (m, 2H, Bz-*o*-C*H*), 7.64 – 7.58 (m, 1H, Bz-*p*-C*H*), 7.56 – 7.50 (m, 2H, Bz-*m*-C*H*), 6.01 – 5.89 (m, 1H, OCH_2CH=CH_2), 5.94 (d, ^3J = 7.8 Hz, 1H, H-1'''), 5.50 (d, ^3J = 4.9 Hz, 1H, H-1'), 5.42 – 5.36 (m, 1H, OCH_2CH=CH_2), 5.30 – 5.26 (m, 1H, OCH_2CH=CH_2), 5.25 – 5.18 (m, 1H, H-2'''), 5.09 – 5.03 (m, 1H, H-3'''), 4.89 – 4.83 (m, 1H, H-3'), 4.66 – 4.60 (m, 2H, OCH_2CH=CH_2), 4.59 – 4.52 (m, 1H, H-2'), 4.57 – 4.50 (m, 1H, H-4'''), 4.51 – 4.45 (m, 1H, H_a-5'), 4.46 – 4.40 (m, 1H, H_b-5'), 4.45 – 4.40 (m, 1H, H-4'), 4.37 – 4.27 (m, 2H, A-OCH_2CH_2CN), 4.35 – 4.25 (m, 2H, G-OCH_2CH_2CN), 3.96 – 3.87 (m, 1H, H_a-5'''), 3.85 – 3.76 (m, 1H, H_b-5'''), 3.18 (s, 3H, CH_3-dmf), 3.08 (s, 3H, CH_3-dmf), 2.83 – 2.76 (m, 2H, G-OCH_2CH_2CN), 2.81 – 2.69 (m, 2H, A-OCH_2CH_2CN), 0.84 (s, 9H, G-SiC(CH_3)$_3$), 0.73 (s, 9H, A-SiC(CH_3)$_3$), 0.03 (s, 3H, G-Si(CH_3)$_2$), -0.05 (s, 3H, G-Si(CH_3)$_2$), -0.11 (s, 3H, A-Si(CH_3)$_2$), -0.33 (s, 3H, A-Si(CH_3)$_2$).

^{13}C-NMR (100.6 MHz, $CDCl_3$): δ/ppm = 164.5 (aryl-C*C*ONH), 159.4 (C-4), 157.8 (*C*H-dmf), 154.2 (C-2), 152.4 (C-2''), 150.5 (C-6''), 150.4 (C-4''), 147.4 (C-7a), 143.4 (C-8''), 133.6 (aryl-*C*CONH), 133.1 (Bz-*p*-*C*H), 131.9 (d, OCH_2CH=CH_2), 129.0 (2x Bz-*o*-*C*H), 128.0 (2x Bz-*m*-*C*H), 127.0 (C-4a), 126.0 (C-7), 125.9 (C-5), 124.4 (C-5''), 119.6 (OCH_2CH=CH_2), 116.6 (G-OCH_2CH_2*C*N), 116.5 (A-OCH_2CH_2*C*N), 90.4 (C-1'''), 86.1 (C-4'''), 79.7 (C-4'), 79.4 (C-1'), 79.3 (C-3'''), 77.1 (d, C-3'), 77.0 (d, C-2'), 73.5 (d, C-2'''), 69.3 (d, OCH_2CH=CH_2), 68.1 (C-5'), 62.6 (C-5'''), 62.4 (d, G-OCH_2CH_2CN), 62.3 (d, A-OCH_2CH_2CN), 41.4 (*C*H_3-dmf), 35.3 (*C*H_3-dmf), 25.8 (SiC(*C*H_3)$_3$), 25.7 (SiC(*C*H_3)$_3$), 19.9 (d, G-O*C*H_2CH_2CN), 19.8 (d, A-O*C*H_2CH_2CN), 18.2 (G-Si*C*$(CH_3)_3$), 18.1 (A-Si*C*$(CH_3)_3$, -4.7 (G-Si(*C*H_3)$_2$), -4.8 (G-Si(*C*H_3)$_2$), -4.9 (A-Si(*C*H_3)$_2$), -5.5 (A-Si(*C*H_3)$_2$).

^{29}Si-NMR (80 MHz, $CDCl_3$): δ/ppm = 22.5 (G-TBS), 25.1 (A-TBS).

^{31}P-NMR (162 MHz, $CDCl_3$): δ/ppm = −1.5 - −1.7 (m, 1P, G-P), −2.0 - −2.3 (m, 1P, G-P).

IR (ATR): $\tilde{\nu}$/cm^{-1} = 3150, 2931, 1684, 1630, 1572, 1458, 1347, 1255, 1031, 838.

ESI-LRMS calculated for $[C_{52}H_{73}N_{11}O_{15}P_2SSi_2 + H]^+$: 1242.4, found: 1242.7.

ESI-HRMS calculated for $[C_{52}H_{73}N_{11}O_{15}P_2SSi_2 + H]^+$: 1242.4095, found: 1242.4120.

calculated for $[C_{52}H_{73}N_{11}O_{15}P_2SSi_2 - H]^-$: 1240.3949, found: 1240.3960.

2.3.2. Compound 9 (2',3'-Dimer)

R_f = 0.27 (DCM/MeOH, 10:1).
R_t (RP-LCMS) = 7.58, 7.63 min (gradient elution, 5 % to 80 % MeCN in H_2O over 7 min).
^{1}H-NMR (400 MHz, $CDCl_3$): δ/ppm = 9.25 (d, ^3J = 2.2 Hz, 1H, A-N*H*), 8.94 (s, 1H, H-dmf), 8.80 (s, 1H, H-2''), 8.70 (bs, 1H, G-N*H*), 8.11 (s, 1H, H-8''), 8.08 (s, 1H, H-5), 8.06 – 8.02 (m, 2H, Bz-*o*-C*H*), 7.64 – 7.59 (m, 1H, Bz-*p*-C*H*), 7.55 – 7.50 (m, 2H, Bz-*m*-C*H*), 5.99 – 5.84 (m, 1H, OCH_2CH=CH_2), 5.92 (d, ^3J = 7.8 Hz, 1H, H-1'''), 5.68 (d, ^3J = 2.6 Hz, 1H, H-1'), 5.49 – 5.43 (m, 1H, H-2'), 5.39 – 5.36 (m, 1H, OCH_2CH=CH_2), 5.30 – 5.26 (m, 1H, OCH_2CH=CH_2), 5.24 – 5.19 (m, 1H, H-2'''), 5.10 – 5.05 (m, 1H, H-3'''), 4.66 – 4.55 (m, 2H, OCH_2CH=CH_2), 4.59 – 4.53 (m, 1H, H-4'''), 4.46 – 4.40 (m, 1H, H_a-5'), 4.34 – 4.27 (m, 1H, H_b-5'), 4.36 – 4.27 (m, 2H, A-OCH_2CH_2CN), 4.27 – 4.21 (m, 1H, H-4'), 4.25 – 4.19 (m, 1H, H-3'), 4.19 – 4.11 (m, 2H, G-OCH_2CH_2CN), 3.99 – 3.91 (m, 1H, H_a-5'''), 3.87 – 3.87 (m, 1H, H_b-5'''), 3.24 (s, 3H, CH_3-dmf), 3.08 (s, 3H, CH_3-dmf), 2.81 – 2.71 (m, 2H, A-OCH_2CH_2CN), 2.71 – 2.61 (m, 2H, G-OCH_2CH_2CN), 0.93 (s, 9H, G-SiC(CH_3)$_3$), 0.74 (s, 9H, A-SiC(CH_3)$_3$), 0.15 (s, 3H, G-Si(CH_3)$_2$), 0.12 (s, 3H, G-Si(CH_3)$_2$), -0.08 (s, 3H, A-Si(CH_3)$_2$), -0.33 (s, 3H, A-Si(CH_3)$_2$).

^{13}C-NMR (100.6 MHz, $CDCl_3$): δ/ppm = 164.5 (aryl-C*C*ONH), 159.3 (C-4), 159.1 (*C*H-dmf), 154.6 (C-2), 152.5 (C-2''), 150.7 (C-6''), 150.6 (C-4''), 146.1 (C-7a), 143.2 (C-8''), 133.6 (aryl-*C*CONH), 133.1 (Bz-*p*-*C*H), 132.0 (d, OCH_2*C*H=*C*H_2), 129.1 (2x Bz-*o*-*C*H), 128.1 (2x Bz-*m*-*C*H), 126.0 (C-4a), 125.9 (C-7), 125.8 (C-5), 124.5 (C-5''), 119.2 (OCH_2CH=*C*H_2), 116.5 (G-OCH_2CH_2*C*N), 116.4 (A-OCH_2CH_2*C*N), 90.7 (C-1'''), 86.3 (C-4'''), 81.1 (d, C-2'), 80.4 (C-4'), 79.13 (C-1'), 79.08 (C-3'''), 73.4 (d, C-2'''), 71.6 (d, C-3'), 69.1 (d, O*C*H_2CH=CH_2), 68.6 (C-5'), 62.6 (C-5'''), 62.5 (d, A-OCH_2*C*H_2CN), 62.2 (d, G-OCH_2*C*H_2CN), 41.4 (*C*H_3-dmf), 35.2 (*C*H_3-dmf), 25.9 (G-SiC(*C*H_3)$_3$), 25.6 (A-SiC(*C*H_3)$_3$), 19.9 (d, G-O*C*H_2CH_2CN), 19.7 (d, A-O*C*H_2CH_2CN), 18.2 (G-Si*C*$(CH_3)_3$), 18.0 (A-Si*C*$(CH_3)_3$, -4.4 (G-Si(*C*H_3)$_2$), -4.88 (G-Si(*C*H_3)$_2$), -4.93 (A-Si(*C*H_3)$_2$), -5.5 (A-Si(*C*H_3)$_2$).

^{29}Si-NMR (80 MHz, $CDCl_3$): δ/ppm = 23.4 (G-TBS), 25.1 (A-TBS).

^{31}P-NMR (162 MHz, $CDCl_3$): δ/ppm = −2.2 (A-P), −2.5 (G-P).

IR (ATR): $\tilde{\nu}$/cm^{-1} = 3145, 2931, 1684, 1630, 1573, 1458, 1349, 1255, 1034, 839.

ESI-LRMS calculated for $[C_{52}H_{73}N_{11}O_{15}P_2SSi_2 + H]^+$: 1242.4, found: 1242.7.

ESI-HRMS calculated for $[C_{52}H_{73}N_{11}O_{15}P_2SSi_2 + H]^+$: 1242.4095, found: 1242.4122.

calculated for $[C_{52}H_{73}N_{11}O_{15}P_2SSi_2 - H]^-$: 1240.3949, found: 1240.3964.

2.4. Preparation of 3',3'-cthGAMP (3) and 2',3'-cthGAMP (2)

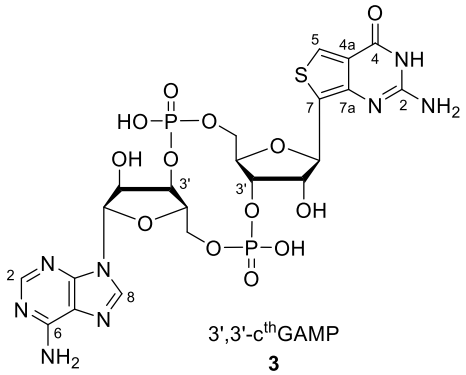

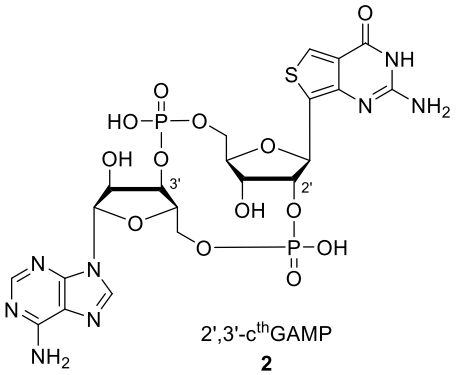

The cyclization and deprotection protocol starting from a mixture of **9** and **10** required three major steps: 1) allyl deprotection, 2) cyclization and 3) final deprotection. The characterization of intermediate products was limited to RP-LCMS und ESI-LRMS mostly.

1) Allyl deprotection

A stirred suspension of a mixture of **9** and **10** (538 mg, 0.433 mmol, 1.0 eq.) and sodium iodide (649 mg, 4.33 mmol, 10 eq.) in dry acetone (20 mL) under argon atmosphere was heated to 56 °C in the dark for 3 h. The reaction mixture was allowed to cool to rt and all volatile components were removed under reduced pressure. The residue was purified by column chromatography (silica gel, DCM/MeOH, 19:1 → 9:1 → 4:1) to yield the allyl-deprotected dinucleotides (367 mg, 0.305 mmol, 70%) as a yellow solid. The isolated product was a mixture of 4 isomers.

R_f = 0.32 (DCM/MeOH, 4:1).
R_t (RP-LCMS) = 6.52, 6.58, 6.72, 6.77 min (gradient elution, 5 % to 80 % MeCN in H_2O over 7 min).
ESI-LRMS calculated for $[C_{49}H_{69}N_{11}O_{15}P_2SSi_2 + H]^+$: 1202.4, found: 1202.7.

ESI-HRMS calculated for $[C_{49}H_{69}N_{11}O_{15}P_2SSi_2 - H]^-$: 1200.3636, found: 1200.3645.

2) Cyclization

The allyl-deprotected dinucleotides (367 mg, 305 µmol, 1.0 eq.) were dissolved in dry THF (72 mL) and 4 Å MS, 1-methylimidazole (1.22 mL, 15.3 mmol, 50 eq.) and 2,4,6-triisopropyl-benzolsulfonylchloride (4.62 g, 15.3 mmol, 50 eq.) were added. The reaction mixture was stirred under argon atmosphere for 25 h at rt. The reaction progress was monitored by RP-LCMS. After full conversion, the reaction was quenched by the addition of H_2O (23.1 mL). After stirring for an additional hour, the solution was concentrated *in vacuo*, diluted with brine (100 mL) and extracted with EtOAc (200 mL) and DCM (3 × 200 mL). The combined organic layers were dried over Na_2SO_4, filtered and concentrated under reduced pressure. The crude product was purified by column chromatography (silica gel, DCM/MeOH, 49:1 → 97:3 → 19:1) to yield the protected cyclic dinucleotides **11** and **12** (177 mg, 149 µmol, 49%) as a yellow solid. The isolated product was a mixture of 8 isomers.

R_f = 0.28 (DCM/MeOH, 19:1).

***R*$_t$** (RP-LCMS) = 7.38, 7.50 min (gradient elution, 5 % to 80 % MeCN in H_2O over 7 min).
ESI-LRMS calculated for $[C_{49}H_{67}N_{11}O_{14}P_2SSi_2 + H]^+$: 1184.4, found: 1184.4.

3) Final deprotection

The protected cyclic dinucleotides **11** and **12** (33.0 mg, 27.9 µmol) were dissolved in MeOH (5 mL) and ammonium hydroxide solution (28-30% NH_3, 5 mL) was added. The reaction mixture was stirred for 16 h at room temperature. The reaction progress was monitored by RP-LCMS. After full conversion, all volatile components were removed under reduced pressure and the residue was co-evaporated with pyridine (3 × 20 mL). The crude product was used in the next step without further purification.

***R*$_t$** (RP-LCMS) = 4.87, 5.40 min (gradient elution, 5 % to 80 % MeCN in H_2O over 7 min).
ESI-LRMS calculated for $[C_{33}H_{52}N_8O_{13}P_2SSi_2 + H]^+$: 919.2, found: 919.5.

The crude product was dissolved in dry pyridine (1 mL) and dry THF (2 mL). After dropwise addition of NEt_3 (0.56 mL) and $NEt_3{\cdot}3HF$ (0.56 mL, 3.41 mmol, 50 eq.) the reaction mixture was stirred for 48 h at room temperature. The reaction progress was monitored by RP-LCMS. After full conversion, the reaction was quenched by the addition of methoxytrimethylsilane (1.4 mL) and all volatile components were removed *in vacuo*. The solid residue was dissolved in MeOH (0.5 mL), the crude product was precipitated by the addition of cold acetone (15 mL) and collected by centrifugation. The products 3',3'-cthGAMP (**3**, 2.5 mg, 3.62 µmol, 13%) and 2',3'-cthGAMP (**2**, 2.5 mg, 3.62 µmol, 13%) were separated and purified by two RP-HPLCs as follows:
First preparative RP-HPLC: Isocratic and gradient elution, 0% buffer B for 5 min, then 0% to 40% buffer B in buffer A over 25 min; buffer A: 0.1 M NEt_3/HOAc in H_2O, buffer B: 0.1 M NEt_3/HOAc in MeCN/H_2O (4:1): R_t(**3**) = 13.6 – 14.1 min and R_t(**2**) = 15.5 – 16.5 min.

Second preparative RP-HPLC: Isocratic and gradient elution, 0% MeCN+0.1% TFA for 5 min, then 0% to 40% MeCN+0.1% TFA in H_2O+0.1% TFA over 18 min: R_t(**3**) = 12.5 – 13.1 min and R_t(**2**) = 13.6 – 14.6 min.

2.4.1. 3',3'-cthGAMP (3)

^{1}H-NMR (800 MHz, D_2O): *δ*/ppm = 8.65 (s, 1H, A_H-2), 8.51 (s, 1H, G_H-5), 8.46 (s, 1H, A_H-8), 6.28 (s, 1H, A_H-1'), 5.58 (d, ^3J = 2.6 Hz, 1H, G_H-1'), 4.97 – 4.91 (m, 1H, G_H-3'), 4.91 – 4.85 (m, 1H, A_H-3'), 4.83 – 4.78 (m, 1H, A_H-4'), 4.61 – 4.58 (m, 1H, G_H-2'), 4.54 – 4.49 (m, 1H, A_H-2'), 4.46 – 4.43 (m, 1H, G_H-4'), 4.44 – 4.40 (m, 1H, G_H$_a$-5'), 4.27 – 4.22 (m, 1H, A_H$_a$-5'), 4.14 – 4.08 (m, 1H, G_H$_b$-5'), 4.07 – 4.01 (m, 1H, A_H$_b$-5').

^{13}C-NMR (100.6 MHz, D_2O): *δ*/ppm = 157.7 (G_C-4), 151.2 (G_C-2), 149.9 (A_C-6), 147.6 (A_C-4), 144.8 (A_C-8), 142.0 (A_C-2), 132.6 (G_C-5), 132.3 (G_C-7a), 120.3 (G_C-4a), 119.4 (G_C-7), 118.8 (A_C-5), 90.0 (A_C-1'), 79.9 (A_C-2'), 78.1 (G_C-4'), 76.9 (G_C-1'), 73.8 (A_C-4'), 73.4 (G_C-3'), 72.6 (G_C-2'), 70.3 (A_C-3'), 63.3 (A_C-5'), 62.2 (G_C-5').

^{31}P-NMR (162 MHz, D_2O): *δ*/ppm = −1.1 - −1.3 (m, 1P, A_C-5'-P), −1.5 - −1.8 (m, 1P, G_C-5'-P).

ESI-HRMS calculated for $[C_{21}H_{24}N_8O_{13}P_2S + H]^+$: 691.0732, found: 691.0740.

calculated for $[C_{21}H_{24}N_8O_{13}P_2S - H]^-$: 689.0586, found: 689.0585.

The connectivity of the phosphodiesters was verified by ^{1}H-^{31}P-HMBC measurements:

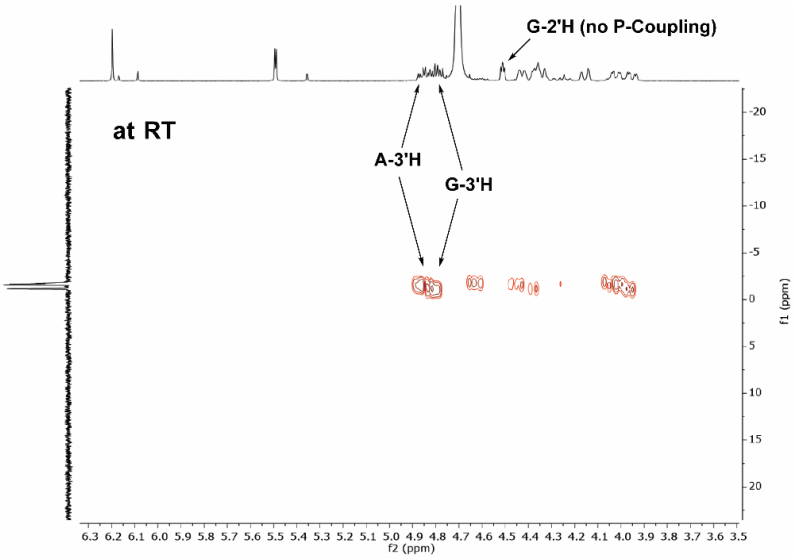

2.4.2. 2',3'-cthGAMP (2)

^{1}H-NMR (800 MHz, D_2O): *δ*/ppm = 8.44 (s, 1H, A_H-2), 8.31 (s, 1H, A_H-8), 7.77 (s, 1H, G_H-5), 6.11 (s, 1H, A_H-1'), 5.40 (s, 1H, G_H-1'), 4.89 – 4.83 (m, 1H, A_H-3'), 4.85 – 4.79 (m, 1H, A_H-2'), 4.72 – 4.64 (m, 1H, G_H-2'), 4.52 – 4.46 (m, 1H, A_H-4'), 4.48 – 4.42 (m, 1H, G_H-4'), 4.40 – 4.37 (m, 1H, A_H_a-5'), 4.38 – 4.32 (m, 1H, G_H_a-5'), 4.30 – 4.24 (m, 1H, G_H-3'), 4.08 (dd, ^{2}J = 11.8 Hz, ^{3}J = 4.4 Hz, 1H, G_H_b-5'), 4.03 (dd, ^{2}J = 11.7 Hz, ^{3}J = 4.1 Hz, 1H, A_H_b-5').

^{13}C-NMR (100.6 MHz, D_2O): *δ*/ppm = 156.0 (G_C-4), 153.1 (G_C-2), 149.8 (A_C-6), 147.0 (A_C-4), 145.0 (A_C-8), 142.0 (A_C-2), 130.7 (G_C-5), 129.9 (G_C-7a), 123.6 (G_C-7), 120.0 (G_C-4a), 118.5 (A_C-5), 90.9 (A_C-1'), 81.7 (G_C1'), 80.4 (A_C-4'), 78.5 (G_C-3'), 75.8 (G_C-4'), 73.6 (A_C-2'), 71.2 (G_C-2'), 70.0 (A_C-3'), 62.2 (A_C-5'), 61.9 (G_C-5').

^{31}P-NMR (162 MHz, D_2O): *δ*/ppm = −1.6 - −1.9 (2P).

ESI-HRMS calculated for $[C_{21}H_{24}N_8O_{13}P_2S + H]^+$: 691.0732, found: 691.0743.

calculated for $[C_{21}H_{24}N_8O_{13}P_2S - H]^-$: 689.0586, found: 689.0585.

The connectivity of the phosphodiesters was verified by ^{1}H-^{31}P-HMBC measurements:

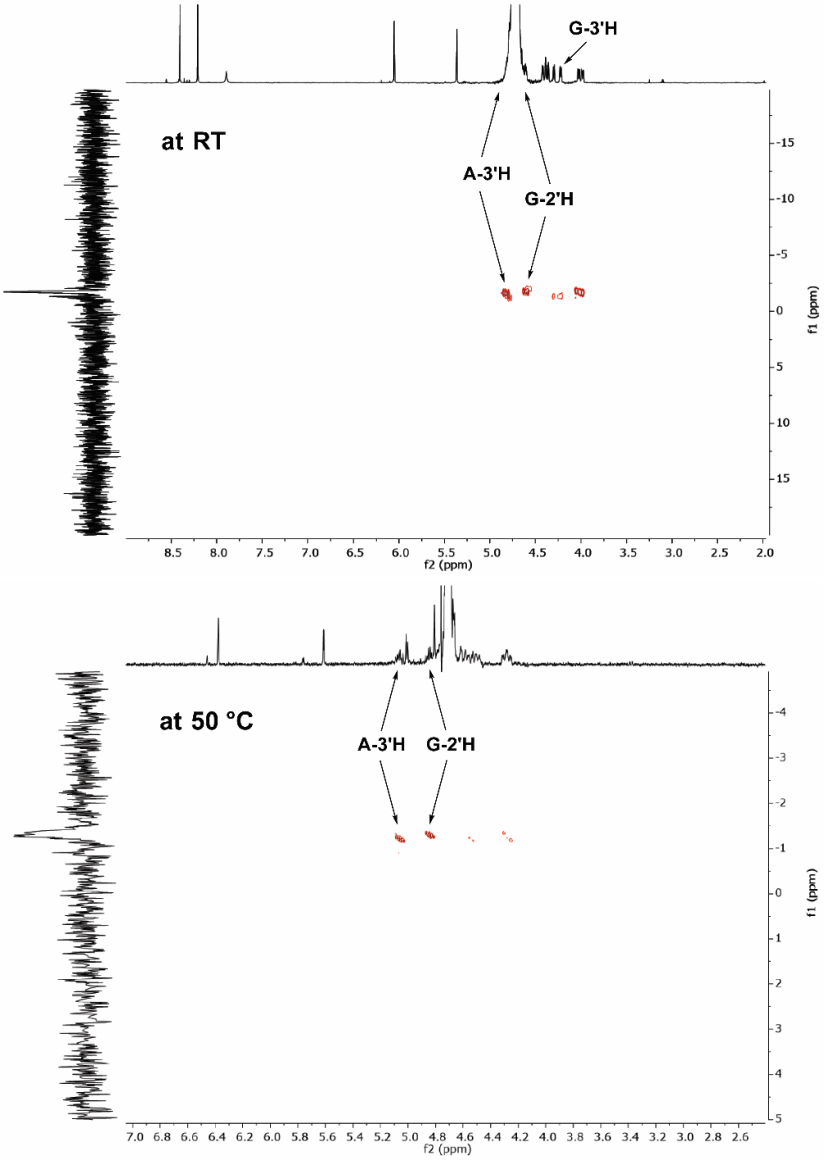

3. CELL CULTURE

3.1. Culturing of THP-1 wt and THP-1 STING-KO cell lines

THP-1-Dual™ wt cells and THP-1-Dual™ STING-KO cells were purchased from Invivogen. Both cell lines were cultured in initial growth medium containing RPMI 1640 (Sigma Aldrich), 20% FBS (for ESC, Pan Biotech), 25 mM HEPES (1M, Sigma Aldrich), 2 mM L-Alanyl-L-Glutamine (Sigma Aldrich), 100 µg/ml Normocin™ (Invivogen), Pen-Strep (100 U/ml-100 µg/ml, Sigma Aldrich) upon manufacturer's instructions. After the cells were passaged twice, they were cultured in maintaining medium (same as growth medium but with 10% FBS) with selective antibiotics blasticidin and Zeocin™ (Invivogen). The cells were cultured between $4x10^5$ and $1.5x10^6$ cells/mL. For experiments a test medium was used which contained no Normocin™, blasticidin, or Zeocin™. The cells were cultured in humidity saturated 37°C, 5% CO_2 containing incubators (Heracell 150 CO_2 incubator) and handled in sterile conditions.

3.2. Preparation of Poly-D-Lysin - coated Slides

18 mm diameter glass cover slides (Carl Roth) were placed in 12-well plates (VWR) in sterile conditions. Poly-D-Lysin (PDL; Sigma Aldrich) was prepared in sterile ddH_2O to an end concentration of 0.1 mg/mL and applied on the cover slides with the adjusted amount of 40 L/cm^2. The incubation last for 30 minutes under saturated humidity at 37°C and 5% CO_2 within the incubator. The slides were washed twice with ddH_2O, incubated for 5 minutes during each washing step in the incubator. Before use, the slides were dried at least for two hours in a laminal hood. All steps were performed in sterile conditions.

3.3. Feeding compounds to THP-1 cells

For a feeding of 24 hours, approximately 100.000 cells per well/condition in a 96-well plate were used. The compounds were added according to the desired concentration in test medium - reaching an end volume of 100 µL of test medium, i.e. medium without Normocin™. The concentration of the compounds was measured prior to each feeding via the UV-Vis spectrophotometer (Implen Nanophotometer N60) applying the extinction coefficient on Beer-Lambert law.

3.4. Immobilization of THP-1 cells for TPE imaging

A volume of 100 µL medium containing fed or unfed cells, respectively, was transferred on the dried cover slides and incubated for 20 minutes under saturated humidity at 37°C in the incubator containing 5% CO_2. After the cells were observed immobile on the slides under the microscope, the medium was washed away with sterile PBS for 5 minutes in the incubator. The samples were fixed with 4% paraformaldehyde in water, for 15-20 minutes on the bench. The slides were washed three times with PBS for 5 minutes and mounted on a microscope slide wit Fluoroshield™ mounting medium without DAPI (Sigma Aldrich).

3.5. Interferon activation in THP-1 wt cells

Cells described above have a luciferase reporter for interferon production, which is measured by Quanti-Luc™, following supplier's recommendations. The cells were transfected with Lipofectamine™ RNAiMAX according to supplier's protocol. 100.000 cells per well were used. The amount of compound transfected was calculated to give 200 nM 2'3'-cGAMP (**1**) and 1,1 µM 2'3'-cthGAMP (**2**) end concentrations in the well. An empty transfection with no compound served as an indicator of the effect of transfection on interferon production. 48 hours after transfection, 20 µl of the cell medium was transferred to an opaque white 96-well plate in

technical duplicates and 50 µl Quanti-Luc was injected to then measure the luminescence of the well via a Tecan Microplate Reader as relative light units (RLUs).

3.6. Cloning, expression and purification

Human STING AA139-379 and mouse STING AA138-378 constructs employed for ITC studies were cloned, expressed and purified according to previous studies.[1] The plasmids were used to transform E. coli Rosetta (DE3) protein expression strain cells (Novagen). The cells were grown in 1 L of Turbo BrothQ media (Molecular Dimensions) supplemented with Kanamycin (50 mg/mL) and Chloramphenicol (34 mg/mL) at 37°C to an OD_{600} = 1.3 and expression was induced by adding IPTG to a final concentration of 0.2 mM.

4. TWO-PHOTON EXCITATION IMAGING AND LIFETIME ANALYSIS OF C^{TH}GAMP IN THP-1 CELLS

Fluorescence imaging was carried out with two-photon excitation (TPE) imaging at constant laser power to first compare the mean brightness per cell area of THP-1cells (wild type and STING knock-out) in the presence and absence of CDNs. To prove the presence of CDNs in cells, we additionally performed lifetime analysis.

4.2. Brightfield and Confocal laser scanning microscopy

Imaging was carried out on a home-built, multimodal confocal scanning microscope with bright-field illumination and camera.[2] Briefly, a two-photon excitation source was a fiber-based, frequency-double erbium laser (FemtoFiber dichro bioMP; Toptica Photonics) running at 774 nm served as two-photon excitation. The laser light was coupled into the microscope via a low pass dichroic mirror (HC BS 749 SP; AHF Analysetechnik) that separates laser excitation and fluorescence emission. Scanning of the sample was achieved by using a xyz piezo stage (BIO3.200; PiezoConcept). The laser excitation was focused onto the sample with a 60x (water) 1.20-NA plan apochromat objective (Plan APO VC 60x 1.2 NA, Nikon). The emission was collected by the same objective and passed afterwards through a dichroic filter (HC BS 614 SPUV; AHF Analysentechnik). After spectrally dividing the emission signal, the green channel (< 610 nm) was filtered with a 447/60 bandpass (447/60 BrightLine HC; AHF Analysentechnik) for CDN detection and the red channel > 610 nm with a 620/60 bandpass filter (620/60 ET Bandpass; AHF Analysentechnik) for cellular auto-fluorescence. To ensure blocking of the excitation laser wavelength, an additional 780 notch filter (BNF-785-OD4-11M; Opti-Grate) was mounted in the red channel (> 610 nm). The emission was recorded on two APD detectors (< 610 nm: Count Blue; > 610 nm: Count Red; Laser Components) and its photon streams registered using a TCSPC card (TH260 pico dual; PicoQuant GmbH). The experiment was controlled using a home-written program written in C#. The confocal data was extracted and evaluated afterwards by PAM[3] and Fiji[4]. Lifetime data was analyzed using the Phasor approach.[5]

Brightfield pictures of the scanned area were taken before the experiment followed by a confocal scan. Each 2D image had a range of 100 µm, an acquisition time of 180 s and a step size of 200 nm. The laser power was 2.28 mW. For brightness comparison, the sum over triplets was compared to avoid scanning artefacts and increase statistics.

4.3. Brightness analysis

For comparing the brightness quantitatively, it was necessary to determine the mean brightness of all measured cells. The data analysis process carried out in Fiji[4] is exemplary shown for one data set in **Supplementary Fig. S4.1**. After cumulating over three scans (step 1), the resulting images were converted into binary images (step 2), with a threshold of 7 kHz. The binary image enables the automatic cell detection and analysis using the 'Analyze Particles' plugin (step 3), in order to distinguish between inner and outer cell area in the scan image and define the region of interests (ROI). The overlay between the map of ROIs and the averaged scan image is depicted after step 4. The average brightness, volume, size and shape per cell is extracted afterwards within the ROIs (step 5). Since only cells contribute to the average brightness, the results can be compared between the different conditions (see **Fig. 4c**).

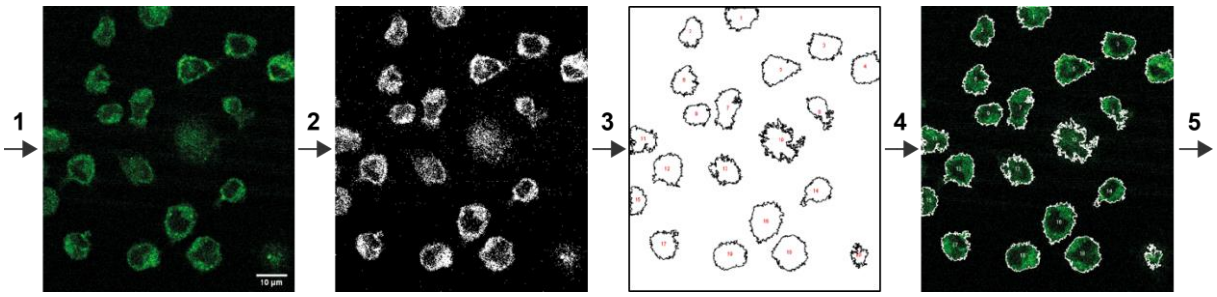

Figure S4.1: Brightness analysis of fluorescence imaging data*. Step 1: Accumulate scan images. Step 2: Conversion into binary image. Step 3: Identification of cells including their size and shape. Step 4: Application of ROI on cumulated image. Step 5: Determination of average fluorescence per cell area.*

4.4. Phasor analysis of fluorescence lifetime

Fluorescence lifetime imaging exploits the time a fluorophore spends in an excited state before emitting a photon in order to distinguish and characterize the local micro-environment. After a molecule is electronically excited to a higher energy level S_n by absorbing a photon, it will return to the electronic ground state S_0 via different decay (radiative and/or non-radiative) pathways. In the ensemble, the molecule relaxes to the ground state via different decay paths whose likelihood is statistically given by their decay rate k_i. Fluorescence refers to the radiative process occurring from the lowest excited electronic state S_1. The observed time the molecule needs for its emissive return to the electronic ground state is called lifetime τ. It is equal to the temporal decay of the observed fluorescence $I(t)$ to which it is linked via

$$I(t) = I_0 \cdot e^{-t/\tau} \qquad \text{and} \qquad 1/\tau = \sum k_i \qquad \text{Eq. (1)}$$

The precise likelihood for the accessible pathways, and hence detected fluorescence lifetime depends on multiple factors, not only the molecule but also its local environment. The fluorescent signal will hence show differences in the exponential decay (**Figure S4.2a**).

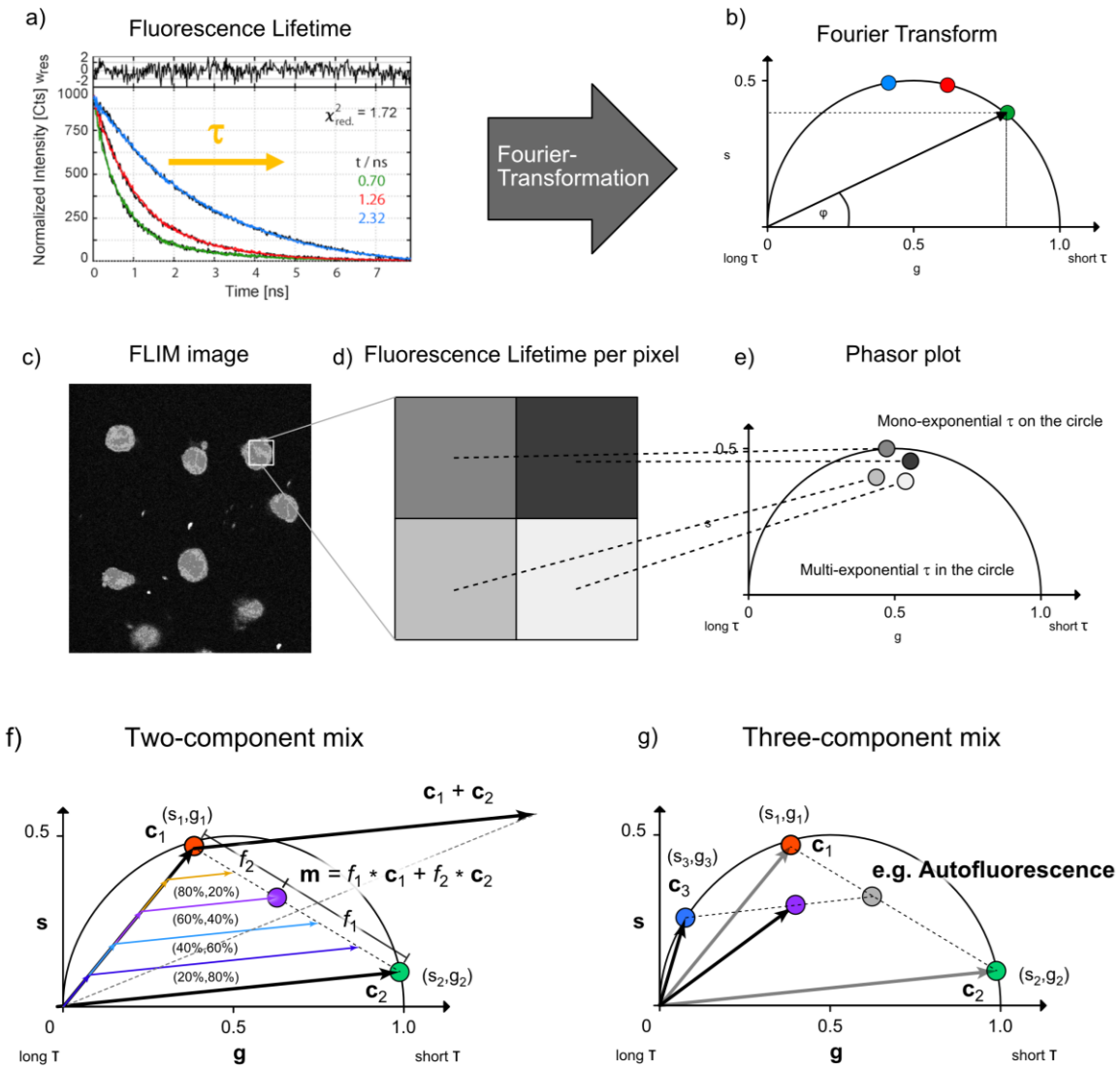

***Figure S4.2: Phasor analysis of fluorescence Lifetime imaging data**. **a)** Fluorescence lifetime decays with different durations. **b)** Phasor-Transformation of lifetimes. **c)** FLIM image (color-coded according to the lifetime extracted from the phasor plot). **d)** Conversion of lifetime information derived from the phasor analysis in **e)** into pixel 'brightness' within the FLIM image. **e)** Phasor plot of the pixel wise lifetimes measured in a confocal fluorescence microscope image with TCSPC. **f)** Theoretical phasor plot for a two-component mix, e.g., the cellular autofluorescence. The mixture (purple dot) is located on the weighted vector connecting the pure species. **g)** Theoretical phasor plot of a three-component mix upon addition of a third fluorescent species with long lifetime. The purple population would be observed as mixed population between all components, i.e. as mixed population connecting the signatures of the THP-1 autofluorescence and the the added compound 2'3'-cthGAMP.*

Fluorescence lifetimes can be determined in the temporal domain by exponential fitting. For samples with complex photo-chemistry or mixtures of fluorescent species with different lifetimes, a phasor transformation[6] is employed to unravel the underlying lifetime components. Based on time-correlated single-photon counting (TCSPC), the histogram of the photon arrival times is transformed into Fourier space. The phasor coordinates g and s of the phasor plot (**Figure S4.2b**) equals the sine and cosine Fourier components of the transformation and are derived using the following relations

$$g(\omega) = \int_0^T I(t) \cdot \cos(n\omega t)\, dt \Big/ \left(\int_0^T I(t) dt \right) \quad \text{Eq. (2a)}$$

$$s(\omega) = \int_0^T I(t) \cdot \sin(n\omega t)\, dt \Big/ \left(\int_0^T I(t) dt \right) \quad \text{Eq. (2b)}$$

in which T is repetition frequency of the data acquisition and n and ω the harmonic and angular frequency of excitation. The values of g range between 0 and 1, while s scales 0 and 0.5. The coordinates (g, s) per decay are shown in polar coordinates, where m is the modulus of the phasor and φ the phase. In the phasor transformation, mono-exponential fluorescent decays appear on the universal semicircle with decreasing lifetime from left to right (as shown in **Figure S4.2a-b** qualitatively for the decays and data points depicted in blue, red and green).

In Fluorescence Lifetime Imaging (FLIM), the lifetime for each individual pixel of an image is analyzed (**Figure S4.2c-d**). Using the phasor approach on FLIM measurements allows for a graphical visualization of the detected lifetimes per pixel and prevents the need of a complex fit-based analysis.[5b, 7] In this case, the sine and cosine Fourier components of the lifetime decay for every pixel of the image are calculated, resulting in the i times j pairs of phasor coordinates $g_{i,j}$ and $s_{i,j}$

$$g_{i,j}(\omega) = \int_0^T I_{i,j}(t) \cdot \cos(\omega t - \varphi_{Inst})\, dt \Big/ \left(m_{Inst} \cdot \int_0^T I_{i,j}(t) dt \right) \quad \text{Eq. (3a)}$$

$$s_{i,j}(\omega) = \int_0^T I_{i,j}(t) \cdot \cos(\omega t - \varphi_{Inst})\, dt \Big/ \left(m_{Inst} \cdot \int_0^T I_{i,j}(t) dt \right) \quad \text{Eq. (3b)}$$

$I_{i,j}(t)$ refers to the number of photon counts in the photon arrival histogram at time bin t at the corresponding pixel (i, j). For FLIM, the frequency ω corresponds to $2\pi/T$, with T being the repetition timescale of the lifetime decay histogram (here 12.4 ns). The phase shift and demodulation due to the instrument response function are corrected by φ_{Inst} and m_{Inst}. They are determined from a calibration measurement of samples with known lifetime (such as a solution of Atto532 in PBS (Atto-Tec) with a lifetime of 3.8 ns).

The phasor coordinates g and s of a population allow for determining the phase (τ_φ) and modulation (τ_m) lifetime according to

$$\tau_\varphi(\omega) = \frac{1}{\omega} \cdot \frac{s}{g} \quad \text{Eq. (4a)}$$

$$\tau_m(\omega) = \frac{1}{\omega} \cdot \sqrt{\frac{1}{g^2+s^2} - 1} \quad \text{Eq. (4b)}$$

As a result, samples with a pure mono-exponential decay are located directly on the semi-circle of the phasor plot (**Figure S4.2e** or **S4.2b**). For this case, the phase and modulation state the same value and show the correct lifetime. In mixed populations, lifetime times add up according to the weighted abundance of each compound. The mixture of two species lies on a straight line connecting the phasors of the pure species (**Figure S4.2f**), as observed in the case of the autofluorescence of THP-1 cells that is dominated by two lifetime species. In the case of three or more components *k* (**Figure S4.2g**), the mix is located inside the *k*–sided polygon where the corners are given by the pure lifetime species. This holds in particular true for multi-exponential species. In order to derive a single apparent lifetime, the mean phase and

modulation were calculated for all pixels above a threshold of ~300 photons. The lifetime of the sample then consists of the arithmetic average of the different lifetimes.

Lifetime analysis via the software PAM – PIE analysis in MATLAB:

The lifetime data is analyzed by a self-written program PAM – PIE analysis in MATLAB[3]. At first the calibration sample Atto532 is loaded into the program and set as reference (known lifetime of 3.8ns). Following, the measurements of the different cells are evaluated. For the phasor plots, an averaging of the photons by 3x3 matrix was calculated.

5. SUPPLEMENTAL FIGURES

Figure S5.1

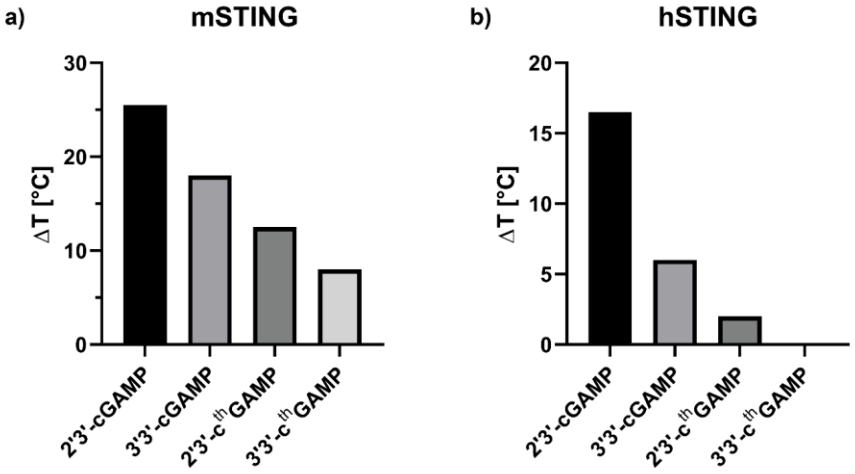

Figure S5.1: Binding affinity of CDNs to the STING receptor in humans and mice*. For monitoring the binding of CDNs to* ***a)*** *murine and* ***b)*** *human STING, differential scanning fluorimetry was performed using 10 µM mSTING/hSTING with 500 µM OF ligand. The physiological compounds 2'3'-cGAMP and 3'3'-cGAMP were used as control.*

Figure S5.2

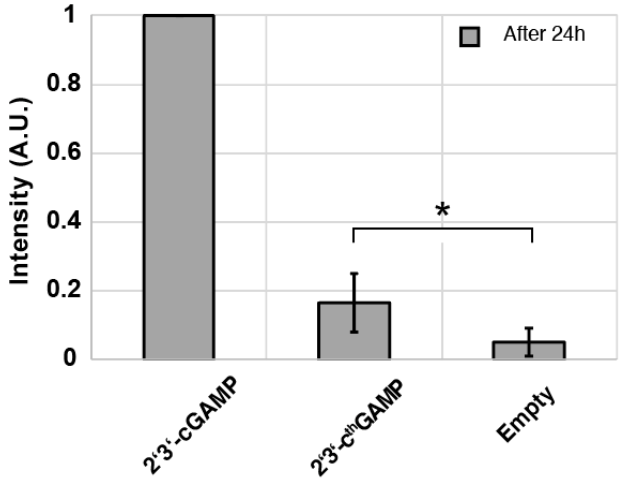

Figure S5.2: Interferon activation by 2'3'-cGAMP and 2'3'-cthGAMP. *Both CDN are biologically active and lead to interferon production. By quantifying the expressed luciferase-based reporter for interferon activation, a 4-fold lower activation was found for 2'3'-c[th]GAMP and compared to 2'3'-cGAMP. The mean values and standard deviations represent the average of biological repeats with n = 4. The interferon induction is significant at a level of 0.05 according to a two-sample t-test.*

Figure S5.3

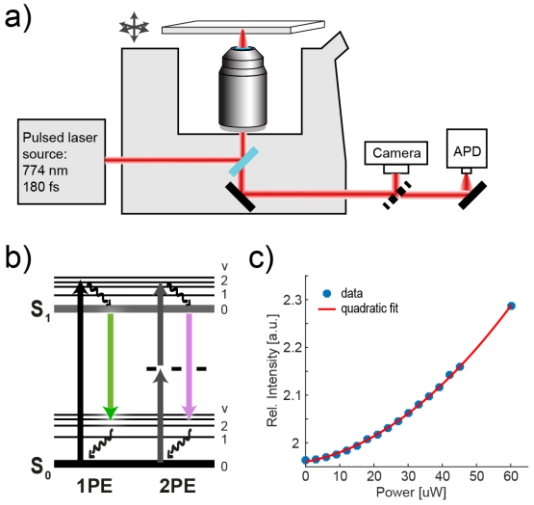

Figure S5.3: Two-photon microscopy. a) *Experimental setup with two-photon excitation at 774 nm for confocal fluorescence microscopy including lifetime information.* ***b)*** *Energy diagram of fluorescence with direct and two-photon excitation.* ***c)*** *Fluorescence emission of 2 mM of 2'3'-cthGAMP in water between 400 and 650 nm as function of laser power. The quadratic dependence confirms a two-photon dependence of the excitation for the molecule.*

Figure S5.4

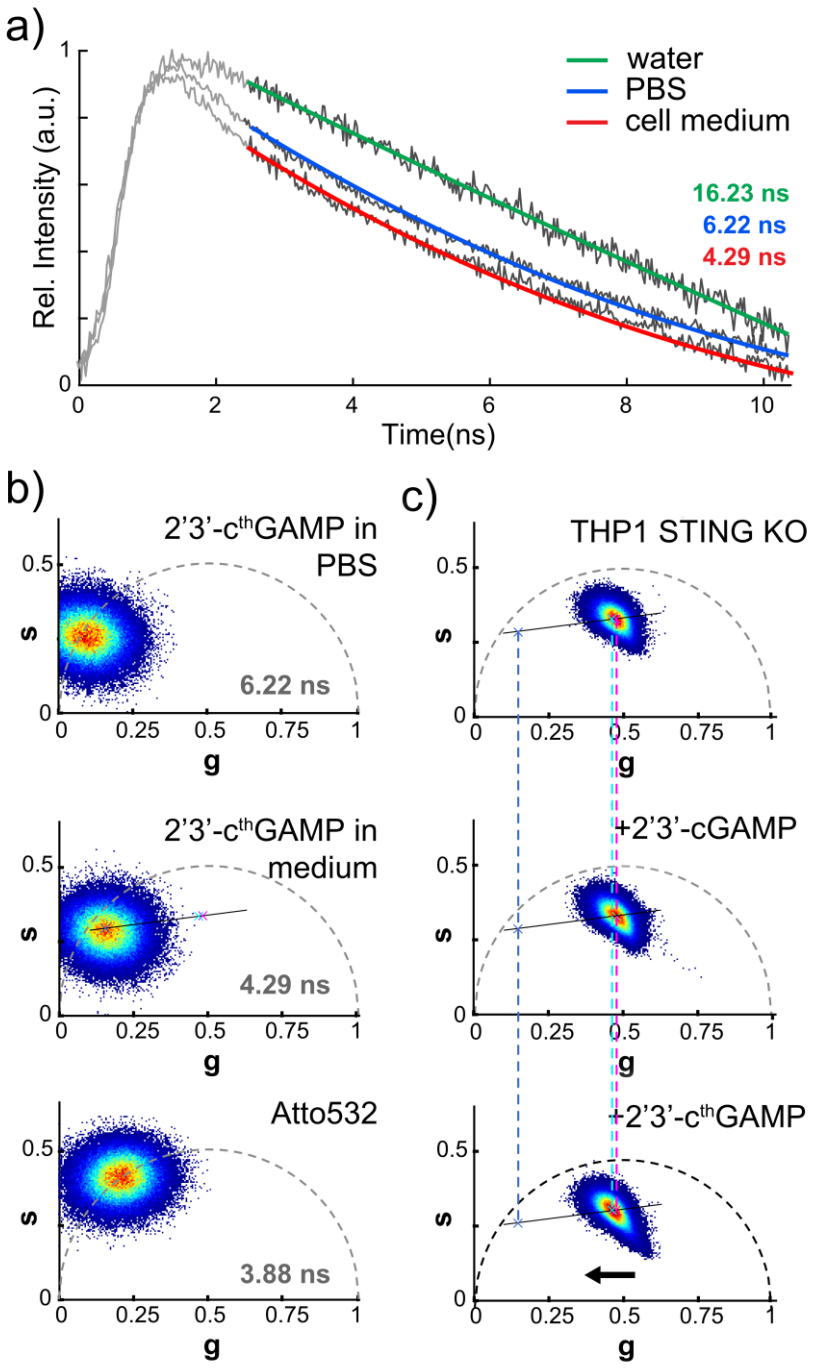

Figure S5.4: Calibrations for FLIM measurements. a) *Fluorescence decay of 200 nM 2'3'-cthGAMP in water, PBS and cell medium. Increasing salinity leads to fluorescence quenching.* ***b)*** *Phasor analysis for determining the fluorescence lifetime of 200 nM 2'3'-cthGAMP in PBS (top) and cell medium (middle) and 1 µM Atto532 (bottom).* ***c)*** *Phasor analysis of the fluorescence lifetime distribution of THP-1 STING KO cells in medium only (top), in presence of 2'3'-cGAMP (middle) and in presence of 2'3'-cthGAMP (bottom). Upon addition of fluorescent 2'3'-cthGAMP the average detected lifetime shifts towards the population of the pure 2'3'-cthGAMP in solution (visualized by the black bar connecting the pure 2'3'-cthGAMP and the autofluorescence). For 2'3'-cGAMP neither a shift in the phasor plot nor change in lifetime is observed. Color bar encodes from blue to red (i.e. from lowest to highest occurrence).*

6. SUPPLEMENTAL REFERENCES

[1] T. Cavlar, T. Deimling, A. Ablasser, K.-P. Hopfner, V. Hornung, *The EMBO Journal* **2013**, *32*, 1440-1450.

[2] A. Fuchs, P. Mannhardt, P. Hirschle, H. Wang, I. Zaytseva, Z. Ji, O. M. Yaghi, S. Wuttke, E. Ploetz, *Adv. Mater.* **2021**, 2104530.

[3] W. Schrimpf, A. Barth, J. Hendrix, D. C. Lamb, *Biophys. J.* **2018**, *114*, 1518-1528.

[4] J. Schindelin, I. Arganda-Carreras, E. Frise, V. Kaynig, M. Longair, T. Pietzsch, S. Preibisch, C. Rueden, S. Saalfeld, B. Schmid, J.-Y. Tinevez, D. J. White, V. Hartenstein, K. Eliceiri, P. Tomancak, A. Cardona, *Nat. Methods* **2012**, *9*, 676-682.

[5] a) G. I. Redford, R. M. Clegg, *J. Fluoresc.* **2005**, *15*, 805; b) M. A. Digman, V. R. Caiolfa, M. Zamai, E. Gratton, *Biophys. J.* **2008**, *94*, L14-L16.

[6] a) G. Weber, *J. Phys. Chem.* **1981**, *85*, 949-953; b) D. M. Jameson, E. Gratton, R. D. Hall, *Appl. Spectrosc. Rev.* **1984**, *20*, 55-106.

[7] S. Ranjit, L. Malacrida, D. M. Jameson, E. Gratton, *Nat. Protoc.* **2018**, *13*, 1979-2004.